COPIE 5

CONTROLLED SOLIDIFICATION OF
FE - MN BASE ALLOYS

THE CONTROLLED SOLIDIFICATION
OF
FE - MN BASE ALLOYS

by

MICHEL ROBERT HONE, B.A., B.A.Sc., M.Sc.

A thesis Submitted to the Faculty of Graduate Studies
and Research in Partial Fulfilment of the
Requirements for the Degree of
Doctor of Philosophy

McMaster University
October 1970

DOCTOR OF PHILOSOPHY (1970)
(Metallurgy)

McMASTER UNIVERSITY
Hamilton, Ontario.

TITLE: The Controlled Solidification of Fe-Mn Base Alloys

AUTHOR: Michel Robert Hone, B.A. (Université de Montréal)
B.A.Sc. (Université de Montréal)
M.Sc. (McMaster University)

SUPERVISOR: Dr. G.R. Purdy

NUMBER OF PAGES: xxv, 359

SCOPE AND CONTENTS:

Experiments were carried out on the solidification of iron-manganese alloys containing sulphur and carbon. The alloys were solidified under controlled conditions in a travelling furnace constructed especially for the investigation. Qualitative and quantitative metallography and electron-probe microanalysis were used to determine the solidification structure, dendrite arm spacings, solute concentration profiles and inclusion compositions. The results were interpreted in the light of existing knowledge and concepts especially developed for the purpose of this investigation.

ACKNOWLEDGEMENTS

I am grateful to Dr. G.R. Purdy for directing my thesis project; to Drs. J.S. Kirkaldy and A.E. Hamielec for serving on my Ph.D. committee; to Dr. S.V. Subramanian for help with the metallography; to Mr. H. Walker for assistance with the electron-probe microanalysis; to Mr. T. Bryner for technical support in all phases of the investigation; to Messrs. J.B. Gilmour, I. Jin, P.N. Smith and D.E. Stephens for their advice; to Dr. A. Hone for reviewing the manuscript; to Mrs. L. Mayrand-Hone for drafting the figures and proof-reading the final copy; to Mrs. H. Blevins for typing the thesis; and finally to the National Research Council of Canada, the Steel Company of Canada Limited and the American Iron and Steel Institute for their financial support.

CONTENTS

CONTENTS (Cont'd)

CONTENTS (Cont'd)

CONTENTS (Cont'd)

LIST OF SYMBOLS

A'	Proportionality constant
A_θ	Proportionality constant
a	Length of subsystem
a_i^ϕ	Activity of species i in the ϕ phase
B_H, B_L	Proportionality constants
C	Solute concentration
C'	Initial distribution of solute in a system
C_0, C_{01}, C_{02}, C_{0i}	Average concentration of solute in an alloy
C_a	Concentration of solute at $z = a$
C_b	Solute content of bulk liquid
C_L, C_{L1}, C_{L2}	Solute concentration at a given point in the liquid phase
C_L^*, C_{L1}^*, C_{L2}^*	Solute concentrations in the liquid phase at a solid-liquid interface
C_L^τ	Solute concentration in the liquid during initial transient state solidification
C_m	Minimum concentration in a dendrite
C_M	Maximum concentration in a dendrite
C_S	Solute concentration at a given point in the solid phase
C_S^*, C_{S1}^*, C_{S2}^*	Solute concentrations in the solid phase at a solid-liquid interface

LIST OF SYMBOLS (Cont'd)

C_u	Solute concentration at which an undercooled melt nucleates
D	Solute diffusivity
D_0	Pre-exponential factor
D_{11}, D_{22}, D_{ii}	Constant on-diagonal diffusion coefficients
D_{12}, D_{21}, D_{ij}	Constant off-diagonal diffusion coefficients
$\widetilde{D}_{12}, \widetilde{D}_{21}$	Variable off-diagonal diffusion coefficients
D_L	Solute diffusivity in the liquid phase
D_S	Solute diffusivity in the solid phase
d	Dendrite arm spacing
d_1	Primary dendrite arm spacing
d_2	Secondary dendrite arm spacing
d_θ	Width of the cells at breakdown for a particular orientation θ
E	Activation energy
f_0, f_1, f_2, f_i	Closure functions
G	Temperature gradient in the liquid phase
G'	Temperature gradient in the solid phase
G_L	Interfacial liquidus gradient
g	Solidified fraction of the system
H	Heat unit
$h,\ h_i$	Heats of fusion

LIST OF SYMBOLS (Cont'd)

I_S	Segregation index or ratio
I_S^x	Segregation index along [x] path
I_S^+	Segregation index along [+] path
J_t	Interfacial solute flux
K	Thermal conductivity
$k_0^T, k_1^T, k_2^T, k_i^T$	Equilibrium partition coefficients for solvent 0, and solutes 1, 2 and i in a ternary system
$\bar{k}_0, \bar{k}_1, \bar{k}_2, \bar{k}_i$	Estimates of equilibrium partition coefficients for solvent 0, and solutes 1, 2 and i
k_1, k_2, k_i	Equilibrium partition coefficients for solutes 1, 2 and i.
k_e	Effective partition coefficient for solute
k_0	Equilibrium partition coefficient for solute
L	Length unit
M	Mass unit
M_L, M_{L1}, M_{L2}	Amount of solute entering liquid phase
M_S, M_{S1}, M_{S2}	Amount of solute entering solid phase
M_τ	Amount of solute entering a given phase
M_∞	Total amount of solute in a given phase after an infinite time
m, m_1, m_2, m_i	Binary liquidus slopes (including sign)
m_1^T, m_2^T	Partial slopes (including sign) of a ternary liquidus surface

LIST OF SYMBOLS (Cont'd)

q	Small arbitrary number
R	Universal gas constant
r_o	Initial radius of interdendritic volume
r_c	Radius of curvature
T	Temperature
T_e	Equilibrium solidification temperature
T_{MS}	Temperature at which martensite starts to form
T_u	Solidification temperature of an undercooled melt
$T_i^{\alpha\beta}$	Temperature of α - β transformation of pure species i
t	Time
t_f	Local solidification time
V	Growth velocity of dendrite tip or solid-liquid interface
V'	Cooling rate
V_I	Terminal flotation velocity of inclusions
v_L	Volume of liquid
x_i^{ϕ}	Mole fraction of species i in the ϕ phase
z, Z	Distance coordinates
z_1	Distance of a solid-liquid interface measured from initially solidified end of a segregation cell

LIST OF SYMBOLS (Cont'd)

z_2	Distance of a point in the liquid phase ahead of a solid-liquid interface
z_3	Distance of a solid-liquid interface measured from finally solidified end of a segregation cell
z_c	Characteristic distance
α_{ij}^{ϕ}	Darken interaction parameter in ϕ phase
α_L	Homogeneity criterion for liquid phase
α_S	Homogeneity criterion for solid phase
Γ_i	Ratio of activity coefficients of species i
γ_i^{ϕ}	Activity coefficient of species i in ϕ phase
$\gamma_i^{0\phi}$	Henry's law coefficient of species i in ϕ phase
ΔC	Concentration difference
$\Delta g_i^{\alpha\beta}$	Free enthalpy of formation of one mole of pure species i from the α to β state
Δg_M^{ϕ}, Δg_m^{ϕ}	Free enthalpies of mixing for ϕ solution
$\Delta h_i^{\alpha\beta}$	Enthalpy of α to β transformation of species i
$\Delta s_i^{\alpha\beta}$	Entropy of α to β transformation of species i
ΔT	Undercooling
ΔZ_0	Increment in the advance of a solid-liquid interface
δ	Thickness of the diffusion-limited layer
ϵ_{ij}^{ϕ}	Wagner interaction parameter in ϕ phase

LIST OF SYMBOLS (Cont'd)

ζ_i	Adjustable parameter for solute i
η_i	Adjustable parameter for solute i
θ	Contact angle
λ	One-half of dendrite arm spacing
$\mu_i^{0\phi}$	Molar free enthalpy of pure species i in ϕ phase
μ_i^{ϕ}	Partial molar free enthalpy of species i in the ϕ phase
μ_S^{ϕ}	Molar free enthalpy of solution ϕ
ν	Viscosity
ξ	Jackson's interface roughness factor
ρ_a	Radius of dendrite arm
ρ_r	Radius of dendrite root
ρ_t	Radius of dendrite tip
σ_{SL}, σ_{SI}, σ_{LI}, σ_{SP}, σ_{LP}	Surface free enthalpies of the interface between solid and liquid, solid and inclusion, liquid and inclusion, solid and particle, and liquid and particle
τ	Small interval of time
ϕ	Dimensionless coefficient
Φ	Diameter of inclusion
ψ_I	Density of inclusion
ψ_M	Density of metal
ω	Gravity constant

LIST OF TABLES

LIST OF TABLES (Cont'd)

LIST OF FIGURES

LIST OF FIGURES (Cont'd)

LIST OF FIGURES (Cont'd)

LIST OF FIGURES (Cont'd)

LIST OF FIGURES (Cont'd)

LIST OF FIGURES (Cont'd)

LIST OF FIGURES (Cont'd)

LIST OF FIGURES (Cont'd)

LIST OF FIGURES (Cont'd)

LIST OF FIGURES (Cont'd)

CHAPTER 1

INTRODUCTION

The research project described in this thesis was undertaken to contribute to the understanding of the solidification behaviour of some ferrous alloys, in the expectation that it would be useful to the technology of modern steel casting, heat treating and steel refining processes.

The project was aimed in particular at the following aspects of the solidification of multi-component iron alloys:

i) the solidification morphology, i.e., the qualitative solute distribution and crystallography of a solidified system as a function of alloy composition and growth conditions;

ii) the periodicity in the spacing of dendritic arms as influenced by alloy composition and growth conditions;

iii) the quantitative distribution of solutes in a given cell; and

iv) the distribution, morphology and composition of inclusions formed during solidification.

Earlier work on solidification was directed at solving problems of immediate concern and did not produce a clear understanding of solidification and related phenomena. In recent years, however, researchers have taken a more fundamental outlook and have sought to use high purity materials and exercise closer experimental control.

In the present research, several theoretical treatments which bear on the understanding of the solidification of multi-component alloys were undertaken with the object of establishing a strong basis for the discussion of experimental observations. The experiments covered the solidification of iron-manganese alloys containing lesser amounts of sulphur and/or carbon, systems of obvious technological interest. The alloys were solidified under controlled conditions in a travelling furnace especially constructed for this investigation. Qualitative and quantitative metallography and electron-probe microanalysis were used to determine the solidification structure, dendrite arm spacings, solute concentration profiles and inclusion compositions.

CHAPTER 2

REVIEW OF LITERATURE

This chapter begins with a review of the essential equilibrium and kinetic data in the Fe - Mn - S - C - O systems required in the application of the theory outlined in Chapter 4, and in the interpretation of the experimental results. The literature on the general solidification process in ferrous systems is then discussed as well as the portion of the information on low melting-point metals and transparent materials which has direct bearing on the solidification of high-temperature materials. Special topics such as the influence of inclusions on solid-state transformations, constitutional supercooling, transitions in segregation structure, dendrite arm spacing, the influence of carbon on microsegregation and a review of directional solidification experiments are then presented.

2.1 - REVIEW OF DIFFUSION DATA

Diffusion data for manganese, sulphur, oxygen and carbon in liquid, delta and gamma iron, and in sulphides are required for the study of solidification kinetics in the Fe - Mn - S - O - C systems. Selected data from the literature are summarized in Table 2.1.1. The given values of D_0 and E refer to the pre-exponential and activation energy terms for the following empirical representation of the data:

$$D = D_0 \exp(-E/RT) \qquad (2.1.1)$$

where R is the universal gas constant and T, the absolute temperature.

In cases where published data were in tabular form, the D_0 and E values were obtained by the least-squares technique. The recent work of REYNIK (1969) suggests that the variation of diffusivity is linear with absolute temperature in liquid systems, i.e.:

$$D = a_1 + a_2T \qquad (2.1.2)$$

where a_1 and a_2 are constants.

However, no attempt was made in the present study to convert liquid diffusion data to this form.

For convenience in predicting and interpreting the results of this study the data of Table 2.1.1 have been plotted in Figures 2.1.1 and 2.1.2.

2.2 - REVIEW OF CONSTITUTION DATA

The constitution of the Fe - Mn - MnS - FeS system — the portion of the Fe - Mn - S system pertaining to the solidification of Fe - Mn base alloys — will be reviewed in this section.

Figure 2.2.1 shows a wire diagram of the Fe - Mn - MnS - FeS system. The binary Fe - Mn, Mn - MnS and Fe - FeS systems were constructed from the data collated by HANSEN (1958) and

ELLIOT (1965), and the FeS - MnS pseudo-binary from the data of CHAO et al. (1964). The various binary reactions involving liquids and the temperature of occurrence are listed below the figure.

German research in the mid 1930's roughly established the shape of the liquidus surfaces shown in Figure 2.2.2. A liquid-liquid miscibility gap is delimited by the horizontal loop originating at the Mn - MnS monotectic, and by the vertical loop which is the locus of the critical points. One eutectic trough originates near the Mn - MnS eutectic, runs close to the Fe - Mn binary plane, up to a temperature maximum in the Fe corner and joins the two other troughs at a ternary eutectic point in the FeS corner.

In Figure 2.2.3, the intersections of liquidus surfaces appear as projections on the composition plane. The arrows on the projections indicate the direction of decreasing temperature. MEYER and SCHULTE (1934) found that the liquid-liquid miscibility gap limit has a temperature maximum of approximately 1600°C at point J in the iron corner and another maximum at point H near the MnS corner of the diagram. The work of VOGEL and HOTOP (1937) suggests that the temperature maximum of eutectic trough EDC, D, occurs around 1510°C and that the minimum point I on the miscibility gap contour occurs around 1370°C.

The ternary equilibria of the Fe - Mn -MnS - FeS system from 980 to 1620°C are qualitatively described by a series of isotherms given in Figure 2.2.4. These isotherms are based on the work of CLARK (1964), NAKAO (1967) and SMITH (1970) but have been simplified somewhat for clarity by assuming that the Fe - Mn binary has a continuous series of liquid and solid solutions; in other words, it is assumed that iron-base alloys solidify directly to metastable γFe rather than to the stable δFe phase; these simplifications eliminate, in particular, the δFe + L_1 = γFe peritectic and the δFe = γFe + L_2 metatectic reactions. Between approximately 2400°C and 1620°C, the melting point of βMnS, the isotherms consist of a $L_1 + L_2$ miscibility gap. An isotherm typical of the situation slightly below 1620°C is shown in Figure 2.2.4-a, where in addition to the miscibility gap there exists a small L_2 + βMnS field.

Many new phase fields appear between 1600°C, the temperature of the maxima in the boundary of the miscibility gap, and 1580°C, the Mn - MnS monotectic temperature as shown in Figure 2.2.4-b. The L_1 + βMnS region is centered on the maximum point (point J in Figure 2.2.3) and separates two 3-phase fields, $L_1 + L_2$ + βMnS and $L_1 + L_2'$ + βMnS. Therefore the γFe + L_1 phase field shown in Figure 2.2.4-d contacts the L_1 + βMnS field rather than the $L_1 + L_2$ or $L_1 + L_2$ + βMnS fields and gives rise to the isotherm shown in Figure 2.2.4-e. The shrinking $L_1 + L_2$ region heralds the appearance of the type of isotherm studied in detail by CLARK (1964), NAKAO (1967) and SMITH (1970), presented in Figure 2.2.4-f. In Figure 2.2.4-g, the γFe + L_1' field has disappeared. Figure 2.2.4-h is one of the last stages of freezing before the remaining liquid reaches the ternary eutectic composition. The last stages of freezing are detailed in Figures 2.2.4-i to -l where the relevant portions of the isotherm have been magnified for the sake of clarity. The ternary eutectic $L_2 = \gamma Fe + \beta MnS + \gamma FeS$ is assumed to occur at approximately 980°C.

A quantitative survey of the 1300°C isotherm from the work of SMITH (1970) is shown in Figure 2.2.5.

MEYER and SCHULTE (1934) have determined the influence of other elements such as C, Cu, Ni, P and Si on equilibria in the Fe - Mn - S system. These elements shift the miscibility gap towards the Fe corner and enhance the desulphurization of a melt. These elements would be expected to produce a similar effect on the eutectic trough EDC , Figure 2.2.3, since they raise the activity of sulphur in the solution. DAHL et al. (1966), LICHY et al. (1965) and YEO (1967) have explained in this manner the enhanced primary separation of βMnS in the presence of additions to the basic Fe - Mn - S melt.

2.3 - REVIEW OF THE SOLIDIFICATION PROCESS

Solidification, very briefly, is a process by which a solid grows at the expense of a liquid. Alloy solidification occurs in one of three modes, according to the rate at which the transformation occurs. Equilibrium solidification occurs at extremely low transformation rates and is a limiting case of non-equilibrium solidification; the participating phases are homogeneous and the compositions are given by tie points on the relevant constitution diagram. Non-equilibrium solidification occurs at higher transformation rates; the phases are not homogeneous; equilibrium may or may not obtain at the solid-liquid interface. Diffusionless solidification takes place at still higher transformation rates and is in fact a limiting case of non-equilibrium solidification; equilibrium does not obtain at the interface during the transformation and the participating phases are homogeneous. An example of diffusionless solidification of an alloy has been given by COLE (1969).

Only equilibrium and non-equilibrium solidification need be examined in detail for the purposes of this investigation. This is done in the two following sections.

2.3.1 - EQUILIBRIUM SOLIDIFICATION

Equilibrium solidification occurs at a rate such that the participating phases have a quasi-uniform composition. One interesting feature of this solidification mode is that the products at a given temperature can be predicted from the average composition of the alloy, provided, of course, that the constitution diagram is known. In this section, equilibrium solidification is illustrated in terms of the Fe - Mn - S system.

It is clear from Figure 2.2.4 that only small variations in the average composition of iron-base Fe - Mn - S alloys are required to yield very different solidification products. For example, if the average composition of an alloy falls in the γFe + βMnS + L_1' region of Figure 2.2.4-e, equilibrium solidification produces primary γFe and the remaining liquid L_1' precipitates γFe and βMnS. The latter becomes impoverished in iron as solidification proceeds. If the average composition of an alloy containing slightly less manganese falls within the γFe + βMnS + L_2 region, the solidification products are primary γFe and a liquid L_2 which precipitates γFe and a βMnS phase which, in contradistinction to the previous case, becomes enriched in iron as the amount of remaining liquid decreases. If the average composition falls within the eutectic triangle shown in Figure 2.2.5-1, the final solidification products are γFe, γFeS and βMnS. The presence of eutectic mixture in cell boundaries is believed to be a factor in the occurrence of "hot shortness" which refers to the inability of a steel to withstand a hot-working treatment without breaking up (KIESSLING, 1968). Upon melting, at 980°C, the eutectic causes a partial decohesion of the structure.

If the average composition of the alloy lies within the limits of miscibility gap $L_1 + L_2$, Figure 2.2.4-d, the metal-rich phase L_1

precipitates a sulphur-rich liquid L_2. If it lies between the limits of the miscibility gap and the eutectic trough, cooling causes the precipitation of primary βMnS of cubic structure and medium grey colour. Discussion of the solidification process in quaternary and higher-order Fe - Mn base alloys such as Fe - Mn - S - O and Fe - Mn - S - C is hampered by the lack of equilibrium data and the conceptual difficulties involved in treating four-and five-dimensional phase space. A possible approach is to view multi-component solidification in terms of modifications of ternary constitution diagrams such as Fe - S - O (HILTY and CRAFTS, 1952, 1954) or Fe - Mn - S, illustrated in Section 2.2. For convenience, however, the discussion will be continued in Section 2.3.3 in connection with the formation of inclusions.

2.3.2 - NON-EQUILIBRIUM SOLIDIFICATION

Alloys are most often solidified under non-equilibrium rather than equilibrium conditions, i.e., there are concentration gradients on either one or both sides of the solid-liquid interface. This lack of uniformity leads to segregation. The present research is concerned mainly with the type of segregation taking place in volumes of material smaller than the volume of an ingot by several orders of magnitude, namely, microsegregation. In the present section, the controversial area of microsegregation attending the casting of ingots will be reviewed and discussed in terms of theoretical microsegregation models.

In the case of steel castings, which are the ultimate concern of the present investigation, the prevailing structure is dendritic or cellular-dendritic in nature. It is apparent from previous investigations that there are two stages in the process of dendritic solidification:

i) an initial stage, during which a dendritic skeleton is formed, and

ii) a final stage during which the liquid pools between the arms of the dendritic skeleton solidify.

Growth theories for each stage have been proposed by various investigators. An attempt is made in the following to present the theories and indicate the conditions under which each is valid.

It is convenient at this point to define parameters and terms which occur frequently in this study.

The equilibrium partition coefficient, k_0, is defined as the ratio of solute content in the solid at the interface, C_S^*, to the solute content in the liquid at the interface, C_L^*, and is given by the relevant phase diagram. The effective partition coefficient, k_e, is defined as the ratio of C_S^* to the solute content of the bulk liquid, C_b. As usual, the discussion shall be limited to the case where k_0 and k_e are equal or less than unity. These definitions are illustrated in Figures 4.2.6. The average concentration of solute in an alloy is denoted C_0, the minimum concentration in a segregation cell, C_m, and the maximum concentration, C_M.

A dendrite arm is that portion of a crystal which extends into the liquid phase in the course of solidification. A dendrite is composed of dendrite arms which are crystallographically interrelated; in cubic systems these arms are mutually perpendicular or parallel to each other. A dendritic grain comprises a single dendrite and the material entrapped between the arms. As illustrated in Figure 2.3.1-a, the first arm to extend into the liquid is termed primary arm; an arm which grows perpendicularly from the primary arm is termed secondary arm; an arm which grows perpendicularly from the secondary arm is termed tertiary arm; and so on and so forth. As will be seen in this work, a dendritic system can be, at least in part, plate-like. This type of structure occurs when various dendrite arms coalesce at early stages of solidification. As shown in Figure 2.3.1-b, plates parallel to primary and secondary arms are termed primary plates; plates parallel to secondary and tertiary arms, secondary plates; plates parallel to tertiary and quaternary arms, tertiary plates, and so on . . . .

The term "segregation cell" or "cell" is used sometimes in this investigation to denote the region of a specimen in which the solute concentration rises from a minimum to a maximum.

INITIAL SOLIDIFICATION STAGE

For the initial solidification stage, FLEMINGS (1964), BRODY and FLEMINGS (1966), BOWER et al. (1966), FLEMINGS (1967) considered that the composition of the bulk liquid in front of the dendrite tips remained close to the average initial liquid composition during solidification.

BOWER et al. studied the solidification of an Al - 4.5 wt% Cu alloy and found that for dendrite tip velocities of 0.005 to 0.05 cm/sec and gradients of 3 to 50°C/cm, the temperature measured at the dendrite tips was equal to the liquidus temperature within experimental accuracy.

The work of SUBRAMANIAN et al (1968-b) on Fe - 10 wt% As alloys, cooled at 18°C/min before the start of solidification and presumably under very low temperature gradients, showed that initial dendrite growth occurred with little supercooling and with the solid composition close to k_0C_0.

On the other hand, several investigators concluded that a substantial solute build-up existed ahead of the growing dendrites during the initial formation of the dendritic array, so that the dendrite compositions were intermediate between k_0C_0 and C_0. KOHN and PHILIBERT (1960) furnace-cooled Al-2 wt% Cu alloys at 6°C/min and interrupted the solidification process by immersing the crucible in water. Electron-probe microanalysis revealed that the solute composition along the axis of a given dendrite arm was close to $k_0 C_0$ and remarkably constant. Several other investigators, ZAITSEVA (1955), de BEAULIEU and PHILIBERT (1958), PHILIBERT and de BEAULIEU (1959), ZHURENKOV and GOLIKOV (1964) and PHILIBERT et al. (1965) observed the constancy of C_m in the dendrite arms of as-cast steels. In order to account for the constancy of C_m, KOHN and PHILIBERT suggested a freezing mechanism whereby a solute-enriched layer surrounds the growing dendrite and allows a steady-state solidification process to occur at a constant temperature. They analysed the variation of copper concentration through a solid-liquid interface and indeed found evidence for the existence of an enriched layer of solute on the liquid side of the interface. SUBRAMANIAN et al. (1968-a) stated, on the basis of their work, that the solute enrichment detected by KOHN and PHILIBERT was a "classical illustration" of a quenching "artefact". However, as pointed out later by KOHN (1967), the extent of the layer was rather large for an "artefact". It should also be pointed out that the work of SUBRAMANIAN et al. was performed on Fe - As and Fe - As - Cr alloys where the partition coefficient of arsenic in iron ($k_0 \approx 0.3$) is greater than that of copper in aluminium [$k_0 \approx 0.17$ by the phase diagram from the compilation of LYMAN (1948) and $k_0 \approx 0.10$ by the thermodynamic calculations of KOHN and PHILIBERT (1960)]; their experiments were therefore considerably less sensitive in detecting the difference between a quenching "artefact" and a true solute enrichment during growth.

DOHERTY and MELFORD (1966) also found evidence of solute enrichment in the liquid at the solid-liquid interface in their work on Fe - 1 wt%C - 1.5 wt% Cr alloys. They were unable to prove that the solute distribution found after the quenching operation was identical to that present during the unperturbed solidification period. However, they detected a depletion of solute in the dendrite arm and an accumulation in the region of the interface, while the solute content of the liquid remote from the interface remained unchanged, and concluded that the interfacial solute enrichment was a genuine effect.

BÄCKERUD and CHALMERS (1969) measured the growth temperature of dendrite tips in the binary alloy system Al - Cu as a function of the rate of formation of the solid phase. In Al - 4 wt% Cu alloys, the dendrite tip temperature, as measured by the arrest temperature in cooling curves, was depressed about 3°C at a rate of heat extraction of approximately 100°C/min. The effect is quite small; moreover, BÄCKERUD and CHALMERS pointed out that a significant part of the under cooling was possibly due to the curvature of the dendrite tips.

DOHERTY and FEEST (1967) investigated the distribution of solute during the initial stages of dendritic solidification in Cu - Ni alloys. They first redetermined the relevant portion of the Cu - Ni phase diagram by microanalysis of specimens quenched after equilibration in the solid-liquid region. The temperature of initial dendritic growth was then measured by thermal analysis and found to lie approximately $8^{o}C$ below the redetermined liquidus, a result which pointed to a significant solute enrichment of the liquid ahead of the growing dendrites.

There are observations on a variety of systems which suggest that both dendrite growth mechanisms may be valid and that a given mechanism operates under a given set of growth conditions. These are:

i) microsegregation is more severe in the equiaxed than in the columnar grains, that is, the segregation index $I_s = C_M/C_m$ is invariably higher in the equiaxed grains of a casting.

ii) The minimum concentration in the dendrite axis, C_m, is lower in the equiaxed grains than in the columnar grains.

This first appeared as a result of the earlier quantitative studies of microsegration in low-alloy steels [FINNISTON and FEARNEHOUGH (1951), CATTIER et al. (1953), KOHN (1954), WARD (1958), de BEAULIEU and PHILIBERT (1958), CRUSSARD et al. (1959), PHILIBERT and BIZOUARD (1959), PHILIBERT and de BEAULIEU (1959), KOHN and PHILIBERT (1960)]. The work of CLAYTON et al. (1961) also showed that there was a relationship between microsegregation and macrostructure, at least in small (100 lb) ingots of 0.3 wt% C steels containing significant amounts of chromium, manganese, nickel, molybdenum and silicon. DOHERTY and MELFORD (1966) studied the mechanism of solidification in commercial killed-steel ingots using 1 wt% C - 1.5 wt% Cr steel as a model material. They found that C_m was less than C_0 in the equiaxed dendrites but was greater than k_0C_0 and concluded that the greater segregation in equiaxed grains was due to their slower growth rate. Further studies by MELFORD and GRANGER (1967) on the same steel confirmed the previous results. DOHERTY and FEEST (1967) studied the solute distribution in small castings of Ni - 60 wt% Cu alloys and found that the copper content in the axis of equiaxed dendrites was lower than in the axis of columnar dendrites. Also the segregation index $I_s = C_M / C_m$ was always greater in equiaxed than in columnar regions.

Caution should be exercised in drawing conclusions about the mode of solidification based on measured values of C_m, since diffusion of solute in the solid during and after solidification may significantly alter the value of C_m. BRODY and FLEMINGS (1966) showed that diffusion of solute in the solid during solidification can be neglected if the parameter $\alpha_S \equiv D_S t_f / \lambda^2$ is much less than unity, where D_S is the diffusion coefficient of solute in the solid;

t_f, the local solidification time; and a, one half the dendrite arm spacing. Back-diffusion was encountered by FLEMINGS (1964) in his work on an Al - 4.5 wt% Cu alloy: the minimum solid composition increased from about 0.7 wt% Cu to 1.3 wt% Cu during the course of solidification. Another example is due to SUBRAMANIAN et al. (1968-b). They studied the distribution of arsenic in an Fe - 10 wt% as alloy during solidification and established that the process of back diffusion of solute into the dendrite arms was sufficiently fast for most of the solidification process to occur close to equilibrium.

A theoretical analysis of the solute distribution around a growing dendrite has been given by BOLLING and TILLER (1961). They treated the dendrite tip as an ellipsoid of revolution growing into a melt in which the heat and solute transport occurred by diffusion from the solid into the liquid. One result of practical value is the relation they derived between the minimum solute concentration in the dendrite axis, C_m, and the growth parameters and conditions:

$$k_e C_0 = C_m = \frac{k_0 C_0}{1 + (1 - k_0)\beta \exp(\beta) \operatorname{expi}(\beta)} \qquad (2.3.1)$$

where:
$$\beta \equiv V\rho_t / 2D_L \qquad (2.3.2)$$

and:
$$\operatorname{expi}(-\beta) \equiv \int_{\beta}^{\infty} \frac{\exp(-t)}{t}\, dt \qquad (2.3.3)$$

In these equations, V is the dendrite tip velocity;

D_L is the solute diffusivity in the liquid; ρ_t is the dendrite tip radius. It is seen that C_m approaches k_0C_0 for small values of β, and C_0 for large values of β. The theory thus indicates that both types of dendritic growth, i.e., with and without solute enrichment of the liquid, are possible, and as a result, the experimental evidence presented above is not necessarily in conflict.

DOHERTY and MELFORD (1966) showed that the effects of structure, composition and cooling rate on microsegregation can be interpreted in terms of Equation 2.3.1. They attributed the greater segregation in equiaxed regions to slower growth rate, a reduction of V independent of ρ_t or D_L. They observed that carbon increases the segregation of chromium in steel by reducing the value of C_m and accounted for this by considering the effect of carbon on the equilibrium partition coefficient of chromium and the dendrite tip radius. They found the value of C_m insensitive to variations in the cooling rate and explained this effect by considering that the finer dendrite spacing found at higher values of V tends to maintain the product $V\rho_t$ constant.

FINAL SOLIDIFICATION STAGE

As in the case of the initial stage of solidification, there are several theories concerning the final stage of solidification during which the liquid pools between the arms of the dendritic skeleton solidify.

One theory considers that the ratio of solute concentration in the solid at the interface, C_S^*, to that at any point in the liquid, C_L, is given by the equilibrium partition coefficient, k_0. This approach was taken by many investigators including GULLIVER (1922), SCHEUER (1931), HAYES and CHIPMAN (1939), SCHEIL (1942), McFEE (1947), PFANN (1952) and FLEMINGS et al. (1960) and shall be discussed in more detail in Section 4.2.1. Assuming that:

i) the partition coefficient k_0 is independent of alloy composition;

ii) there is no back-diffusion of solute from the interface into the second phase;

iii) the composition of the liquid phase is uniform;

iv) the solidification is unidirectional,

then C_S^* is given by:

$$C_S^* = k_0 C_0 (1-g)^{k_0-1} \qquad (2.3.4)$$

where g is the fraction solidified.

BOWER et al. (1966) argued that the magnitude of the concentration differences in the liquid pools between the dendrite arms, and hence the validity of the third assumption, depended on the parameter $\alpha_L \equiv D_L t_f / \lambda^2$, where D_L is the diffusion coefficient of solute in the liquid; t_f, the local solidification time, and λ, one-half the dendrite arm spacing. When α_L is much greater than unity, the concentration differences in the interdendritic liquid are small.

In order to account for the effects of back diffusion of solute, they derived approximate expressions similar to Equation 2.3.4. For a constant rate of thickening of dendrite plates, the relevant expression is:

$$C_S^* = k_0 C_0 \left[1 - \frac{g}{1 + \alpha_S k_0} \right]^{k_0 - 1} \qquad (2.3.5)$$

and for a parabolic rate of thickening,

$$C_S^* = k_0 C_0 \left[1 - (1 - 2\alpha_S k_0)\, g \right]^{\frac{k_0 - 1}{1 - 2\alpha_S k_0}} \qquad (2.3.6)$$

where $\alpha_S \equiv D_S t_f / \lambda^2$ as before. Using these uniform liquid models, as well as a more accurate finite-difference solution, they calculated several characteristics of a cast Al - Cu alloy, such as the weight fraction nonequilibrium second phase in the structure, and found good agreement with the values measured experimentally, provided a conversion factor of 0.32 was applied to the measured dendrite arm spacing. However, KIRKWOOD and EVANS (1967) pointed out that the need for a correction factor could be obviated by choosing a diffusion coefficient about an order of magnitude larger. In effect, the recent work of MURPHY (1961) indicates that, at the temperature of interest, the diffusion coefficient of copper in aluminium may be about an order of magnitude larger than the coefficient reported by BEERWALD (1943) and used in the work of BOWER et al.(1966).

TILLER et al.(1953) and SMITH et al. (1955) have quantitatively examined the segregation of solute in the presence of concentration gradients in the liquid assuming no convection in the liquid, negligible diffusion in the solid, a constant value of the partition coefficient k_0 and a constant growth velocity.

Considering the solidification of a long but finite specimen of average solute content C_0, the initial layer of solid to form has a solute concentration of k_0C_0 and the concentration of solute in the liquid adjacent to the interface rises as solute is rejected. The increase in concentration continues until the solute concentration in the solid adjacent to the interface reaches a value equal to the average concentration of the liquid, C_0. This point marks the end of the transient region and the beginning of the steady-state region in which the distribution of solute in the liquid ahead of the interface remains constant. The relation between solute concentration in the solid phase and distance in the initial transient region is:

$$C_S = \frac{C_0}{2} \left\{ 1 + \mathrm{erf}\sqrt{(V/2D_L)z_1} + (2k_0 - 1) \exp\left[-k_0(1-k_0)(R/D_L)z_1\right] \mathrm{erfc}\left[\frac{(2k_0-1) \quad (V/D_L)z_1}{2}\right]\right\} \qquad (2.3.7)$$

A simpler but approximate relation is:

$$C_S = C_0 \left\{ (1-k_0) \left[1 - \exp(-k_0 (V/D_L) z_1) \right] + k_0 \right\} \tag{2.3.8}$$

In these equations, V is the interface velocity, D_L the solute diffusion coefficient in the liquid and z_1, the distance measured from the beginning of the specimen. The advantage of using the latter relation is that it has a simple characteristic distance

$$z_c = D_L / k_0 V \tag{2.3.9}$$

which is approximately the length of the initial transient region.

In the steady-state region, the concentration of solute in the solid is, of course,

$$C_s = C_0 \tag{2.3.10}$$

The solute distribution in the liquid ahead of the interface is given by:

$$C_L = C_0 \left[1 + \frac{1 - k_0}{k_0} \exp\left(- \frac{V}{D_L} z_2 \right) \right] \tag{2.3.11}$$

where z_2 is the distance into the liquid from the interface. The characteristic distance of this distribution is

$$z_c = D_L / V \tag{2.3.12}$$

When the interface is less than a distance approximately D_L/V from the end of the specimen, the solute in the liquid phase reflects on the final boundary, builds up and causes both solid and liquid interface concentrations to increase. The concentration in the solute rises from the value C_0 to a much higher value in the manner given by:

$$C_S = C_0 \left\{ 1 + 3\,\frac{1 - k_0}{1 + k_0}\ \exp\left(-2\left(\frac{V}{D_L}\right) z_3\right) + 5\,\frac{(1 - k_0)(2 - k_0)}{(1 + k_0)(2 + k_0)} \right.$$

$$\exp\left(-6\left(\frac{V}{D_L}\right) z_3\right) + \ldots\ (2n + 1)\,\frac{(1 - k_0)(2 - k_0)\ldots(n - k_0)}{(1 + k_0)(2 + k_0)\ldots(n + k_0)}$$

$$\left. \exp\left(-n(n + 1)\left(\frac{V}{D_L}\right) z_3\right) \ldots\ldots \right\} \qquad (2.3.13)$$

where z_3 is the distance measured from the end of the specimen.

These calculations assume that C_S goes to C_0 before the solute distribution in the liquid impinges upon the limit of the segregation cell under consideration, or equivalently, before it begins interacting with the solute distribution of an adjacent cell. It is possible, in practice, that the steady-state regime during which Equation 2.3.10 holds may not be attained. However, TILLER (1959) showed that the true concentration in the solid would be between the upper limits $C_S^{max}(z_3)$ calculated by Equation 2.3.13 and a lower limit $C_S^{min}(z_3)$ calculated by treating the initial transient distribution in the liquid as a steady-state distribution with an interface concentration of aC_0/k_0 and a bulk concentration of aC_0. Presumably the factor "a" could be determined by equating the value of C_S to aC_0 when the solute distribution in the liquid for the initial transient impinges upon the cell boundary. An approximate expression for this distribution was derived by TILLER et al. (1953):

$$C_L^{\tau} = C_0 \left\{ \frac{1-k_0}{k_0} \left[1 - \exp\left(- k_0 \frac{V}{D_L} z_1 \right) \right] \exp\left(- \frac{V}{D_L} z_2 \right) + 1 \right\} \qquad (2.3.14)$$

where z_1 is the distance of the interface from the beginning of the crystal and z_2 is the distance of a point in the liquid as measured from the interface.

COATES et al. (1968) extended the analysis of TILLER et al. (1953) for steady-state distributions of solute in the liquid phase to ternary systems:

$$C_{L_1} = a_{10} + a_{11} \exp\left(\frac{-V}{U_1} z_2 \right) + a_{12} \exp\left(\frac{-V}{U_2} z_2 \right) \qquad (2.3.15)$$

$$C_{L_2} = a_{20} + a_{21} \exp\left(\frac{-V}{U_1} z_2 \right) + a_{22} \exp\left(\frac{-V}{U_2} z_2 \right) \qquad (2.3.16)$$

where C_{L_1} and C_{L_2} are the solute concentrations in the liquid at a distance z_2 from the interface moving at constant velocity V, and

$$a_{10} = C_{01} \qquad (2.3.17)$$

$$a_{20} = C_{02} \qquad (2.3.18)$$

$$a_{11} = \left[D_{12} C_{02} \left(\frac{1-k_2^T}{k_2^T} \right) + \tfrac{1}{2} (D_{11} - D_{22} + D^*) \, C_{01} \left(\frac{1-k_1^T}{k_1^T} \right) \right] / D^* \qquad (2.3.19)$$

$$a_{12} = C_{01} \left(\frac{1-k_1^T}{k_1^T} \right) - a_{11} \qquad (2.3.20)$$

$$a_{21} = \left[D_{21} C_{01} \left(\frac{1-k_1^T}{k_1^T} \right) - \tfrac{1}{2} (D_{11} - D_{22} - D^*) \, C_{02} \left(\frac{1-k_2^T}{k_2^T} \right) \right] / D^* \qquad (2.3.21)$$

$$a_{22} = C_{02}\left(\frac{1-k_2}{k_2^T}\right) - a_{21} \qquad (2.3.22)$$

$$U_1 = \tfrac{1}{2}(D_{11} + D_{22} + D^*) \qquad (2.3.23)$$

$$U_2 = \tfrac{1}{2}(D_{11} + D_{22} - D^*) \qquad (2.3.24)$$

$$D^* = \left[(D_{11} - D_{22})^2 + 4\, D_{12} D_{21} \right]^{\frac{1}{2}} \qquad (2.3.25)$$

where C_{01} and C_{02} are the solute concentrations in the bulk liquid; k_1^T and k_2^T, the equilibrium partition coefficients; D_{11} and D_{22}, the on-diagonal diffusion coefficients; and D_{12} and D_{21}, the off-diagonal diffusion coefficients. Each of these expressions reduces to Equation 2.3.11 if diffusional interaction is ignored, i.e., if $D_{12} = D_{21} = 0$.

Ternary expressions for the initial and final transient solute distributions have not been developed.

There is experimental evidence for the existence of concentration gradients in the liquid during interdendritic solidification, especially in rapidly cooled specimens. KOHN and PHILIBERT (1960) determined the phosphorus distribution in a Fe - 1.1 wt% P alloy solidified by aspiration into a cold refractory tube, using an electron-probe microanalyser. The phosphorus distributions clearly had the shape of braces suggesting the existence of the three characteristic periods of solidification described by Equations 2.3.7, 2.3.10 and 2.3.13. SHARP (1967) solidified an Al - 2 wt% Cu alloy in a capillary tube of 1 mm bore and quenched in the solute distribution in the liquid ahead of the solid-liquid interface. The electron-probe results clearly show a transient peak superposed on an approximately exponential solute profile which would be expected for diffusion-controlled solidification.

The work of WEINBERG (1963) and COLE and WINEGARD (1964-65) suggests that convective mixing in liquids is quite efficient in volumes of characteristic dimensions larger than 1000 microns. As a result, the solute accumulation in large volumes of liquid can be reduced by convection, in which case the solute profile exhibits a steep solute gradient next to the interface and a uniform solute concentration in the liquid remote from the interface. A theoretical analysis of this case by BURTON et al. (1953) showed that the effective partition coefficient k_e was related to the equilibrium partition coefficient k_0 by:

$$k_e = \frac{k_0}{k_0 + (1-k_0)\exp(-V\delta/D_L)} \tag{2.3.26}$$

where δ is the thickness of the diffusion-limited layer. As pointed out by HELLAWELL (1967), the value of k_e calculated from Equation 2.3.26 rises from k_0 to 1 in the range

$$0.1 < V\delta/D_L < 10 ,$$

for $\delta/D \approx 10^2 - 10^3$ sec/cm, that is, in the range of solidification velocities

$$0.3\ \text{cm/hr} < V < 300\ \text{cm/hr}\ ,$$

which includes most cases encountered in practice.

2.3.3-INCLUSION FORMATION

Over the years, steelmakers have made correlations between the habit, structure, type, parameter and composition of solidification products, i.e., endogenous inclusions, and the alloy content of various melts. However, as a review of pertinent literature will demonstrate, the understanding of inclusion formation is far from adequate and many discrepancies remain in spite of a massive research effort.

The only inclusions of concern in this study are oxy-sulphides, although it should be noted that other types, namely phosphides, selenides, nitrides and carbides, are known to precipitate from complex melts (SIMS, 1963). As a result of extensive investigations SIMS and DAHLE (1938) classified oxy-sulphides in cast steels into three types according to their morphology:

Type I: Large, globular inclusions.

Type II: Small, thin or bead-like inclusions in a formation.

Type III: Massive, irregular and angular inclusions.

The three types have been sketched in Figure 2.3.2 after the work of KIESSLING et al. (1963).

While researchers agree that there are three distinct inclusion types, there is considerable controversy over the location of the inclusions relative to the segregation cell boundaries or to the primary grain boundaries. The present study suggests several reasons for this uncertainty:

i) the $\delta \rightarrow \gamma$ and $\gamma \rightarrow \alpha$ transformations in iron-base alloys erase the primary cell boundaries,

ii) attempts to reveal segregation by chemical methods are frustrated by the low solute content of industrially important alloys and

iii) experiments to reveal segregation by heat treating alloys containing carbon are often inconclusive because the inclusions influence the $\gamma \rightarrow \alpha$ transformation.

Various theories have been advanced to explain the formation mechanism and location of the inclusion types. According to SIMS and DAHLE (1938) all three inclusion types were located on primary cell or grain boundaries. Type I sulphides precipitated in medium-carbon, low-alloy, silicon-deoxidised steels, where the oxygen concentration was relatively high ($>$ 0.008 - 0.01 wt%) and there was almost no metallic aluminium residue. The inclusions were large since they precipitated early in the solidification process and their spherical form indicated that they precipitated as liquids in a liquid metal. They were liquids because of the presence of iron sulphide, and manganese, iron and silicon oxide. Type II inclusions were formed when the oxygen content was below 0.008 - 0.01 wt%, as a result of using strong deoxidisers such as aluminium, titanium or zirconium. SIMS and DAHLE were of the opinion that lowering the oxygen level:

i) increased the solubility of the sulphide phase in the steel so that the last liquid to freeze was sulphur-rich and solidified as a eutectic, and

ii) lowered the interfacial tension of the sulphur rich dendritic concentrate so that it spread as a continuous film among the primary crystals of iron.

Type III inclusions were formed when excess amounts of aluminium or zirconium were added to a steel (SIMS, 1959). They were crystalline and therefore precipitated as solids or at least solidified before the iron matrix. They had an intercrystalline location but did not appear to be part of a eutectic. SIMS suggested that the sulphide-rich liquid from which the inclusions precipitated broke up into pools as a result of high interfacial tension.

MARICH and PLAYER (1969) studied the formation of both iron and manganese sulphide inclusions in melts containing less than 0.02 wt% impurities. They produced Type I, II and III inclusions simply by varying the oxygen content in the range 0.0010 - 0.010 wt%. Both iron and manganese inclusions were found to undergo essentially the same shape changes. In melts containing

0.001 wt% 0, the inclusions were faceted (Type III); in melts containing 0.003 wt% 0, the inclusions were whole or pinched-off films around the iron grains (Type II); in melts containing 0.01 wt% 0, the inclusions were globular in shape (Type I). MARICH and PLAYER agree with SIMS and DAHLE (1938) on the mode of formation of Type I and Type II inclusions. However, they discussed the transition from Type III to Type II inclusions in terms of the effect of oxygen on JACKSON's ξ factor (JACKSON, 1959). At low oxygen levels, they proposed that ξ is large so that the solid inclusion grows with a faceted interface (Type III). At higher levels, ξ is small and the inclusion grows with a rough interface (Type II).

DAHL et al. (1966) studied the conditions for the occurrence of the various types of sulphide inclusions in melts containing about 0.2 wt% S. Type I inclusions formed at oxygen contents of 0.02 wt% and over. While the inclusions appeared to be randomly distributed, they were in fact located exclusively in zones of positive segregation as revealed by OBERHOFFER's etch. Both Type I and Type II inclusions were present for oxygen contents in the range 0.02 - 0.01 wt%. For oxygen contents below 0.01 wt% DAHL et al. observed only Type II inclusions. They also demonstrated, as did MARICH and PLAYER (1969), that the formation of Type III inclusions did not require the presence of aluminium in the melt. Type III inclusions formed with the addition of over 8 wt% silicon or 3 wt% carbon. If the two elements were present, only approximately 2 wt% carbon and 2 wt% silicon were needed. Increasing the aluminium concentration of a low carbon steel in the absence of silicon did not lead to the formation of Type III inclusions but rather mixed aluminium — manganese sulphides. It appeared that aluminium led to the formation of Type III inclusions only in the presence of significant amounts of carbon and silicon. In this respect, the optimal aluminium concentration was 0.05 - 0.3 wt% when the carbon and silicon contents were of the order of 0.1 - 0.4 wt%.

Unlike SIMS and DAHLE (1938) and MARICH and PLAYER (1969) who attributed the change in the types of inclusions to surface tension effects, DAHL et al. (1966) interpreted their results in terms of constitution diagrams. They discussed the formation of Type I inclusions in terms of an isopleth of the Fe - MnS - MnO diagram shown in Figure 2.3.3-a. For a melt of composition C_0, primary iron precipitates, followed by the liquid L_2. Upon further cooling, the liquid L_1 rich in iron precipitates more iron. The sulphur-rich liquid then precipitates solid MnS, solid MnO and MnO and Fe. This ternary eutectic is normally not visible because of the low oxygen levels associated with Type I inclusions. In order to explain the formation of Type II inclusions DAHL et al. employed the quasi-binary Fe - MnS system shown in Figure 2.3.3-b. For alloy compositions such as C_0, primary iron precipitates and the liquid becomes enriched in manganese and sulphur. When the liquid composition reaches the eutectic composition, MnS sulphides precipitate at cell boundaries. The angular nature and uniform distribution of Type III inclusions led DAHL et al. to explain their formation in terms of the quasi-binary Fe - MnS system shown in Figure 2.3.3-c. The addition of carbon and silicon to a melt increases the activity of the sulphur which is thermodynamically equivalent to reducing the solubility of the sulphide in the melt. The melting point of iron decreases and the miscibility gap shifts towards the iron corner. For low alloy melts, the composition C_0 is located to the left of the eutectic point, and such melts produce Type II inclusions as seen previously. Type III inclusions are formed at higher carbon and silicon concentrations because C_0 is located to the right of the eutectic so that primary MnS precipitates and grows. Aluminium decreases the solubility of sulphur and lowers the melting point of iron but not sufficiently, according to DAHL et al., to explain the formation of Type III sulphides in the presence of carbon and silicon. They argued that aluminium has a specific role which consists of fixing the oxygen which may be present in the MnS phase, thereby promoting the primary precipitation of solid MnS.

YEO (1967) looked into the effect of oxygen on the machinability of resulphurized steels containing nominally 0.1 wt% C, 1.0 wt% Mn and 0.25 wt% S. He found that deoxidation suppressed the formation of large random sulphide inclusions (Type I) and caused the steel to solidify with a eutectic structure in which the inclusions were comparatively small (Type II). He proposed (independently, it seems) an explanation very similar to that of DAHL et al. (1966) for the formation of Type I and Type II inclusions. However, in contradistinction to SIMS (1959) and DAHL et al. (1966), YEO states that Type I inclusions are randomly distributed.

If the explanation of DAHL et al. (1966) for the formation of Type I inclusions is accepted, it is clear that the position of the miscibility gap in the Fe - Mn - S - O system just above the liquidus temperature of a steel melt is most important in determining whether or not Type I inclusions are formed, and if so, in what quantity. BOOTH and CHARLES (1969) investigated the two-phase region of liquid immiscibility in the Fe - Mn - S - O system by analysis of levitation melted and splat-cooled specimens. The distribution of the metal phase compositions is reproduced in Figure 2.3.4. The alloys were equilibrated at temperatures which varied about the 1520°C mark. The oxygen concentrations of the metal phase was approximately 0.1 wt%. These results are given here because of the potential usefuln ess to the present investigation on the formation of inclusions.

The effect of solidification rate on the formation of sulphide inclusions in Fe - Mn - S alloys containing different amounts of carbon, silicon and aluminium studied by MOOHLA and BEECH (1969) using metallographic and microradiographic techniques. An increase in solidification rate generally caused a transition from Type I or Type III to Type II inclusions. MOOHLA and BEECH qualitatively explained their results using the constitution diagram approach of DAHL et al. (1966) and the fact that higher solidification rates favour a greater proportion of non-equilibrium eutectic They found by microradiography that both Type II and Type III inclusions were located in the interdendritic spaces. They speculated that Type III inclusions were formed in the liquid, pushed ahead of the solid-liquid interface and trapped in the dendrite arms. No details were given on the location of Type I inclusions.

LICHY et al. (1965) also reported that the form of the sulphide in as-cast steel was strongly affected by solidification rate. High rates invariably produced small globular sulphides whereas low rates yielded a variety of inclusion forms depending on the type of addition employed. Although LICHY and co-workers did not quote the precise location and type of the small globular sulphides, it is presumed that they were eutectic Type II inclusions, in agreement with the results of MOOHLA and BEECH (1969).

2.4 - INFLUENCE OF INCLUSIONS ON SOLID-STATE TRANSFORMATIONS

In the course of this investigation, a number of interactions between inclusions and solid-state reactions were encountered. This section is a review of observations reported in this area.

It was pointed out in Section 2.3.1 that inclusions of (Fe, Mn) S, which precipitate during the solidification of Fe - Mn -S alloys, reject iron and become enriched in manganese during subsequent cooling. A number of investigators have discussed this phenomenon (WHITELEY, 1937; KIRKALDY et al. (1963); KIESSLING and LANGE (1963); SALMON COX and CHARLES (1965); KIESSLING and WESTMAN (1966). The calculations of KIRKALDY et al. demonstrated the tendency for manganese to diffuse to the sulphide phase: using thermodynamic data on the free enthalpy of formation of FeS and MnS and assuming ideality of the Fe - Mn and FeS - MnS solutions, they calculated the equilibrium content of an FeS - MnS inclusion and found that in a low-carbon steel containing 0.8 wt% Mn an inclusion would contain 50 - 88 wt% MnS at 1500°C, 89-98 wt% at 1227°C and 99 - 100 wt% at 927°C, the temperatures being typical of solidification, soaking and finish of rolling respectively. As a result of the manganese transfer, the matrix surrounding the inclusion is depleted in manganese, unless, of course, the system is allowed to attain equilibrium. The existence of a manganese-depleted region, predicted by WHITELEY (1937), has been determined by DELORME et al. (1961), KIRKALDY et al. (1963), SALMON COX and CHARLES (1965), LEGER and DETREZ (1965), PHILIBERT et al. (1965), KIESSLING and WESTMAN (1966), and others using electron probe microanalysis. It is interesting to note in passing that DELORME et al., LEGER and DETREZ and PHILIBERT et al. attributed the depletion to a dendritic solidification mechanism rather than a solid-state redistribution of manganese during cooling. SALMON COX and CHARLES studied manganese depletion adjacent to iron-manganese sulphides in relation to the macrostructure of a $3\frac{1}{2}$ ton ingot containing 0.2 wt% C, 0.8 wt% Mn, 0.2 wt% S. They observed that the depletion varied in extent and in regard to the minimum manganese concentration. In the columnar zone, the manganese depletions were low ($\sim$ 0.2 wt%) and extended for distances up to 20 microns. Depletions were not detected around many inclusions. In the branched columnar, inverted V segregate, and equiaxed zones the depletions were more pronounced ($\sim$ 0.4 wt%) and extended for 30 microns. The concentration around a two-phase iron/manganese sulphide inclusion in the equiaxed zone was almost zero for a distance of a few microns.

Regardless of the mechanism, the matrix in the immediate vicinity of the inclusion is depleted in manganese and hence its physical properties may differ significantly from those of the bulk matrix. In particular, during the austenite-ferrite transformation, ferrite would be expected to nucleate first in the depleted regions, since manganese favours the formation of γ_{Fe}, causing the rejection of carbon to the surroundings and formation of pearlite further away in the bulk matrix.

DELORME et al. (1961) in their study of banding in forged steels, found that sulphides in steels containing 1.42 wt% Mn and 0.008 wt% S (high manganese, low sulphur) were in the pearlitic bands indicating that nucleation of ferrite occurred in the manganese-depleted dendrite cores. The sulphides in alloys containing 1.11 wt% Mn and 0.050 wt% S (high manganese, high sulphur) were located in the ferritic bands. DELORME and co-workers argued that ferrite tended to nucleate in the interdendritic regions depleted in manganese by the enhanced precipitation of manganese sulphides. The sulphides in alloys containing 0.7 wt% Mn and 0.008 wt% S (moderately high manganese, low sulphur) were located in both the pearlitic and ferritic bands.

TURKDOGAN and GRANGE (1968) investigated microsegregation in steels containing 1.5 wt% Mn, 0.05 wt% S and 0.25 wt% C and found, as DELORME et al., that the sulphide precipitates were surrounded by the ferrite phase. They noted and discussed the effect of cooling rate over the temperature range of the gamma-alpha transformation range on the extent of ferrite precipitation around the sulphide inclusions relative to the amount formed within the dendrite cores. At sufficiently low transformation rates, carbon appeared to have sufficient time to diffuse in the dendritic cell and suppress the formation of ferrite in the low-manganese dendrite cores. As a result, massive ferrite regions appeared around the inclusions. At higher transformation rates, they argued, carbon rejected from the ferrite layer could not diffuse away fast enough, retarding the growth of ferrite but leaving unhindered the nucleation and growth of ferrite in the low-manganese dendrite cores. Hence the locations of the ferrite and pearlite regions were inverted with respect to the previous case. It is interesting to note that TURKDOGAN and GRANGE concluded that in both as-cast and annealed steels the sulphide inclusions act as nuclei for the precipitation of the ferrite phase during decomposition of austenite, without alluding to the existence of a manganese-depleted region around the inclusions.

2.5 - TRANSITIONS IN SEGREGATION STRUCTURE

It is clear from the preceding sections that periodic microsegregation occurs as a result of non-planar solidification. It follows that this review would be incomplete without consideration of the work on criteria for transitions in segregation structure.

As solidification proceeds in an alloy system where the partition coefficient k_0 is less than 1, solute material is rejected from the solid and builds up at the solidification front as indicated in Figure 2.5.1. Since every point in the liquid has a definite concentration of solute, it also has a definite liquidus temperature. As shown in Figure 2.5.2, the liquidus temperature rises from that at the interface, where it equals to a good approximation the actual temperature, to the value associated with the average liquid concentration. If the actual temperature gradient is lower than the liquidus temperature gradient, the actual temperature at every point in the shaded region is below its equilibrium temperature and the liquid in this region is said to be constitutionally supercooled.

The constitutional supercooling principle was devised by RUTTER and CHALMERS (1953) to explain the formation of a cellular solidification front. The principle was put on a quantitative basis by TILLER et al. (1953) for binary systems and extended to ternary systems by COATES et al. (1968). Their analyses yielded a parameter useful in the design and interpretation of solidification experiments, namely, the ratio of temperature gradient to solidification rate, G/V, for which a planar/cellular transition occurs in the structure for a given average solute concentration.

The constitutional supercooling principle states that if the temperature gradient G at a solid-liquid interface is less than the interfacial liquidus gradient G_L, then a planar interface is unstable and breaks down. In other words, the system is incipiently unstable if:

$$G = G_L \tag{2.5.1}$$

The value of G_L is obtained by considering the two solute distributions ahead of a moving planar interface and referring to the appropriate phase diagram. The general instability criterion in ternary systems is explicitly given by:

$$\frac{G}{V} < \frac{(m_1^T \tilde{D}_{22} - m_2^T \tilde{D}_{21})\, C_{01}\, (k_1^T - 1)/k_1^T}{\tilde{D}_{11}\tilde{D}_{22} - \tilde{D}_{12}\tilde{D}_{21}} + \frac{(m_2^T \tilde{D}_{11} - m_1^T \tilde{D}_{12})\, C_{02}\, (k_2^T - 1)/k_2^T}{\tilde{D}_{11}\tilde{D}_{22} - \tilde{D}_{12}\tilde{D}_{21}} \tag{2.5.2}$$

where m_1^T and m_2^T are the partial slopes (including sign) of the ternary liquidus surface at the point defining the liquid composition at the interface; k_1^T and k_2^T, the ternary partition coefficients; C_{01} and C_{02}, the average solute concentrations; $\tilde{D}_{11}$ and $\tilde{D}_{22}$, variable on-diagonal solute diffusivities and $\tilde{D}_{12}$ and $\tilde{D}_{21}$, variable off-diagonal diffusivities. The latter can be calculated with the following first order approximations for dilute ternary solutions (KIRKALDY and PURDY, 1962) :

$$\tilde{D}_{12} \approx \epsilon_{12}\, \tilde{D}_{11}\, C_{L1} \tag{2.5.3}$$

$$\tilde{D}_{21} \approx \epsilon_{12}\, \tilde{D}_{22}\, C_{L2} \tag{2.5.4}$$

where ϵ_{12} is the cross-interaction parameter and C_{L1} and C_{L2}

are the concentrations in the liquid phase expressed in mole fractions.

If diffusional interaction is ignored and the ternary partial slopes and partition coefficients are taken as constant and equal to their binary counterparts, Equation 2.5.2 reduces to:

$$\frac{G}{V} < \frac{m_1 C_{01}}{D_{11}} \left(\frac{k_1 - 1}{k_1}\right) + \frac{m_2 C_{02}}{D_{22}} \left(\frac{k_2 - 1}{k_2}\right) \qquad (2.5.5)$$

which is the simple addition of binary effects suggested by CHALMERS (1964). Generalizing to multicomponent solutions,

$$\frac{G}{V} < {}_i \; \frac{m_i C_{oi}}{D_{ii}} \left(\frac{k_i - 1}{k_i}\right) \qquad (2.5.6)$$

As discussed in Section 4.1.8, COLE and WINEGARD (1963-64) were unsuccessful in interpreting their work on dilute ternary alloys in terms of Equation 2.5.6. It is possible, however, that solidification occurred under convective conditions thereby rendering difficult the interpretation of data in terms of straightforward constitutional supercooling principles.

Statistical and numerical analyses performed by DAVIES (1967) on existing data pertaining to the planar/cellular transition in binary alloys confirmed that the transition was justifiably described by a criterion of the form:

$$G/V \propto C_0 \qquad (2.5.7)$$

The problem of the cellular/cellular-dendritic transition is considerably more complex and has not to date been treated with the same measure of success as has been the planar/cellular transition. WEINBERG and CHALMERS (1952) and WINEGARD and CHALMERS (1954) first suggested that the dendritic structure was a development of the cellular structure and was induced by imposing a greater constitutional supercooling. MORRIS et al. (1955) undertook quantitative experiments on Pb - Sn alloys to determine the conditions of solidification under which the transition from one structure to the other takes place. Their results indicated that the transition occurred at a definite G/V ratio for each composition. The work of TILLER and RUTTER (1956-a) on binary lead-base alloys containing tin, silver and gold indicated that conditions corresponding to the onset of dendritic solidification were dependent as well upon the crystallographic orientation of the solid with respect to the macroscopic growth direction. For a given temperature gradient and solidification rate, higher solute concentrations were required to cause dendritic freezing in crystals growing in an orientation close to the macroscopic growth direction than for crystals growing in an orientation very different from the dendrite direction. For alloys of tin as a solute in lead, the limits of the orientation range were linear when the average solute concentration was plotted as a function of the ratio $G/V^{\frac{1}{2}}$:

$$C_0 = B_H G/V^{\frac{1}{2}} \tag{2.5.8}$$

$$C_0 = B_L G/V^{\frac{1}{2}} \tag{2.5.9}$$

where B_H and B_L are proportionality constants and $B_L > B_H$. If $C_0 > B_H G/V^{\frac{1}{2}}$, cells of high misorientation with respect to the macroscopic growth direction broke down into dendrites; if $C_0 > B_L G/V^{\frac{1}{2}}$, cells of low misorientation broke down into dendrites. TILLER (1956) later proposed a more explicit and general criterion for the transition:

$$G/V^{\frac{1}{2}} = A' d_\theta C_0/k_0 \tag{2.5.10}$$

where A' is a proportionality constant; d_θ, the width of the cells at breakdown for a particular orientation θ; and k_0, the partition coefficient. HOLMES et al. (1957) conducted experiments on alloys of lead containing silver and found that the transitions for their system and the lead-tin system studied by TILLER and RUTTER (1956-a) were roughly coincident when the results were expressed as C_0/k_0 versus $G/V^{\frac{1}{2}}$. However, the experiments of PLASKETT and WINEGARD (1960) on tin-base alloys containing antimony, bismuth and lead did not show the orientation dependence of the transition and plots of $G/V^{\frac{1}{2}}$ versus C_0/k_0 were not linear. The experiments of COULTHARD and ELLIOT (1967-a) on alloys of the lead-tin, lead-indium and tin-lead systems failed to confirm the dependence of cell size on the solidification parameters used by

PLASKETT and WINEGARD (1960). As a result, COULTHARD and ELLIOT concluded that there was reason to doubt the validity of Equation 2.5.10. COULTHARD and ELLIOT (1967-b) reviewed the observations on the dependence of the cellular/cellular/dendritic transition on the solute concentration C_0 and the growth conditions G and V in the lead-tin and tin-lead systems; they also made measurements over a more extensive range of solidification conditions in these systems and found that a transition criterion of the form

$$G/V \propto A_\theta \frac{C_0}{k_0} , \qquad (2.5.11)$$

where A_θ is a proportionality constant, gave a better fit to the data. However, DAVIES (1967) concluded, as a result of statistical and numerical analyses conducted into the data on the cellular/cellular-dendritic transition, that there was a "lamentable" lack of significance in the measurements and that there was no simple criterion for this transition.

In summary, while the experimental work reviewed in the preceding paragraph has failed to yield a quantitative criterion, considerable insight has been gained into the cellular/cellular-dendritic transition: the formation of dendrites is favoured by increasing the constitutional supercooling, that is, by increasing C_0 and decreasing the G/V ratio and k_0; it is also favoured if the size and misorientation of the cells which break down into dendrites are large.

The work of SUBRAMANIAN et al. (1968-a) on the growth morphology of iron alloys revealed that both the planar/cellular and cellular/cellular dendritic transitions occur in the same ingot. The solidification of their alloys proceeded initially by the formation of branching dendrites, followed by thickening of dendrite arms by cellular growth and finally by planar growth into enclosed volumes of liquid. These authors concluded that constitutional supercooling steadily decreased throughout the process, probably as a result of the reduction in growth rate and levelling of solute gradients in the small remaining volumes of liquid.

While the planar/cellular and cellular/cellular-dendritic transitions are the most important and clear-cut transitions, the evolution of the substructure as a function of the degree of constitutional supercooling actually comprises, according to BILONI (1967), a considerable number of identifiable steps:

i) planar interface
ii) ordered nodes
iii) two-dimensional or elongated cells
iv) regular or hexagonal cells
v) distorted cells, or hexagonal cells with branches
vi) dendrites or cellular dendrites

2.6 - DENDRITE ARM SPACING

Once breakdown of the virtual planar or cellular interface has occurred, the question of paramount importance in theoretical and in practical work is the spacing of dendrite arms. ALEXANDER and RHINES (1950) studied the spacing of dendrite arms in a number of aluminium, antimony, cadmium, copper, lead, magnesium, silver, tin and zinc alloys and found that:

i) dendrite arm spacing always increased with increasing solute concentration;

ii) dendrites were generally coarser when the crystal structure of the solvent was less densely packed;

iii) dendrite arm spacing was inversely proportional to the growth rate; and

iv) dendrite arm spacing in a given alloy system varied in the same manner as the ratio of latent heat of fusion to thermal diffusivity.

MICHAEL and BEVER (1954) observed an increase in dendrite arm spacing in aluminium-copper alloys containing up to 5 wt% Cu with decreasing rates of solidification but did not detect an appreciable change in dendrite arm spacing with increasing copper concentration over the composition range investigated.

HORWATH and MONDOLFO (1962) studied the spacing of dendrite arms in aluminium-copper alloys and found that spacing was inversely proportional to cooling rate, but the spacing decreased with increasing solute concentration up to the eutectic composition and then increased again. They proposed a relation of the form

$$d = a_1 \exp a_2 \ln V' + a_3 C_0 \tag{2.6.1}$$

where d is the dendrite arm spacing; V', the cooling rate; C_0, the average mole fraction of solute; and a_1, a_2 and a_3 are constants.

BELL and WINEGARD (1963-64) measured the dendrite arm spacing in tin-lead alloys solidified vertically under steady-state conditions, as a function of the temperature gradient in the liquid, G, the growth velocity V and the solute concentration C_0. They found that dendrite arm spacing decreased as G and V increased, and increased with C_0, and gave the functional dependence as

$$d = (a_1 - a_2 \ln G)\, V^{-n} \tag{2.6.2}$$

where a_1, a_2 and n increased with solute concentration and n was less than unity. No justification was given for this particular form of relationship.

SPEAR and GARDNER (1963) studied the effect of solidification rate and alloy composition upon cell size in aluminium casting alloys and found that the cell size decreased with increasing solute concentration and solidification rate. The relationship between cell size d, in inches, and the cooling rate V', in $^{\circ}$F/sec, was approximately:

$$d = 0.002/\sqrt[3]{V'} \qquad (2.6.3)$$

The dendrite cell size was measured in this work by counting the number of cell intercepts per inch along a straight line and thus yielded an average dendrite arm spacing.

BOWER et al. (1966) measured secondary arm spacing in Al - 4.5 wt% Cu alloys as a function of local solidification time. Combining results of other experimenters and their own, they arrived at the following relation between arm spacing d, in microns, and local solidification time, t_f, in sec

$$d = 7.5 t_f^{0.39} \qquad (2.6.4)$$

ROHATGI and ADAMS (1967) investigated dendrite arm spacing and structure as a function of solute concentration and solidification rate in aluminium-copper alloys. They concluded that dendrite arm spacing was directly proportional to the inverse square root of solidification rate, both in hypo- and hypereutectic alloys and that it increased linearly with increasing solute concentration and proposed a relation of the form:

$$d = (a_1 + a_2 C_0) / (dg/dt)^{\frac{1}{2}} \qquad (2.6.5)$$

where a_1 and a_2 are constants and dg/dt is the change in fraction solid g, with change in time t.

ALBERNY et al. (1969) conducted a series of experiments in an iron alloy containing 0.035 wt%C, 0.009 wt%P and 0.3 wt%Si.

They solidified bars at controlled rates which varied from 2.5 to 97 cm/hr under a controlled temperature gradient in the liquid of approximately 20°C/cm. The relationship between dendrite arm spacing d in microns and growth velocity V in cm/hr can be represented by:

$$d = 646\,V^{-0.217} \tag{2.6.6}$$

ROHATGI et al. (1969) measured dendrite arm spacing as a function of freezing rate, solute concentration and solute diffusivity in dilute solutions of potassium chloride, sodium chloride, lithium chloride and hydrogen chloride in water. They observed that dendrite arm spacings increased linearly with solute concentration, solute diffusivity and decreased linearly with the inverse square root of the freezing rate according to the relation

$$d = a_1/(dg/dt)^{\frac{1}{2}} + a_2C_0 + a_3D_L + a_4 \tag{2.6.7}$$

where a_1, a_2, a_3 and a_4 are constants and D_L is the solute diffusivity in the liquid.

BÄCKERUD and CHALMERS (1969) studied dendritic growth in binary alloys of aluminium-copper system containing up to 4 wt% Cu and found that secondary dendrite arms developed closer to each other with increasing rate of heat extraction and solute concentration.

In summary, the literature indicates that dendrite arm spacing varies:

i) directly as the average concentration, C_0 (although the evidence is somewhat conflicting in this case), the solute diffusivity in the liquid, D_L, and:

ii) inversely as the growth velocity, V, and the temperature gradient, G.

RUTTER and CHALMERS (1953) discussed the nature of the variation of cell size spacing in terms of a thermal and compositional "field of influence" concept. Presumably, dendrite cell size would be affected in the same manner. If the solute content of the alloy is increased, the length of the cell projection increases because the width of the constitutionally supercooled liquid ahead of the interface increases. These larger projections exert an influence over a larger area on the interface and consequently the dendrite cell size increases. If the growth velocity is high, there is little time for diffusion of solute parallel to the interface. The compositional field of influence of a projection is therefore reduced as the growth velocity is increased and the cell size or spacing must decrease accordingly. If the temperature gradients in the liquid and solid are steepened, a higher proportion of the latent heat liberated at each projection is channelled into the solid in a direction parallel rather than normal to the growth direction. The thermal field of influence of each projection is reduced and hence a reduction in cell size occurs. RUTTER and CHALMERS also mentioned that the size of cells would be controlled by parameters related to the properties of the alloy such as solute diffusivity in the liquid phase and thermal diffusivities of the liquid and solid phases. However, they made no attempt to estimate the precise influence of such parameters on the cell size.

TILLER (1959) stated that while the variation of the cell size with equilibrium partition coefficient k_0 was not known experimentally, it was probable that cell size varied inversely as k_0. Presumably the variation of k_0 affects dendrite arm spacing in a similar manner.

It was assumed in the aforementioned studies that all dendrite arms formed during solidification are stable throughout the process. Other studies have shown, however, that coarsening, i.e., the growth of large dendrite arms at the expense of small dendrite arms, occurs at a non-negligible rate. Experiments which directly illustrate this coarsening have been conducted on a number of organic materials and metallic alloys and have indeed shown that coarsening is of overriding importance in determining the final dendrite arm spacing. Isothermal coarsening of dendrites in organic materials was investigated by PAPAPETROU (1935), CHERNOV (1956), KLIA (1956) and JACKSON et al. (1966). The experiments of JACKSON et al. on the growth of dendrites in cyclohexanol with fluorescein provided unequivocal evidence for dendrite coarsening. KATTAMIS, COUGHLIN and FLEMINGS (1967) studied the phenomenon in aluminium-copper alloys and KATTAMIS, HOLMBERG and FLEMINGS (1967) in magnesium-zinc alloys. AHEARN and FLEMINGS (1967) studied the dendrite structure of a unidirectionally solidified Sn - 12 wt% Bi specimen and SUBRAMANIAN et al. (1968-a), the growth morphology of some iron alloys. They observed that interstices between dendrite arms tended to fill in preferentially to form plates parallel or perpendicular to the heat flow direction.

The experiments and conclusions of the study by KATTAMIS, COUGHLIN and FLEMINGS (1967) have considerable bearing on the present work and hence shall be summarized in the following. Specimens of an Al - 4.5 wt% Cu alloy were heated to a temperature between the liquidus and solidus and maintained isothermally for various lengths of time and then water-quenched. Metallographic examination revealed that smaller dendrite arms disappeared with increasing holding time while larger arms grew in diameter. Some figures are presented here in order to convey the magnitude of the effect: for a columnar specimen with an initial solidification time of 9.3×10^3 sec, the dendrite arm spacing increased from an initial value of 300 microns to the value 400 microns in 10.8×10^3 sec. The dendrite arm spacing of equiaxed specimens with an initial solidification time of 400×10^3 sec and an initial spacing of 190 microns more than doubled in 9×10^3 sec. The dendrite arm spacing of fine equiaxed specimens having an initial solidification time of 1.7 sec and an initial spacing of 5 microns grew to 10.5 microns in 1 sec. Several experiments were also conducted to determine if coarsening occurred during solidification as well as during isothermal holding. Specimens of the same alloy were melted, cooled at a constant rate of 18°C/hour and quenched at different time intervals during solidification. Plots of dendrite arm spacing versus coarsening time (defined as the sum of the solidification and isothermal holding times) for both isothermal and solidification experiments, and dendrite arm spacing versus local solidification time were found to be overlapping. As a result of these experiments and observations, KATTAMIS et al. concluded that in specimens of Al - 4.5 wt% Cu with dendrite arm spacings in the range 5 - 1000 microns,

i) the dendrites coarsen rapidly when held isothermally between the solidus and liquidus of the alloy;

ii) solidification coarsening occurs at the same rate as isothermal coarsening;

iii) final dendrite arm spacing in castings is related to coarsening time in roughly the same manner as is final dendrite arm spacing in isothermal interrupted solidification experiments;

iv) the rate of coarsening decreases somewhat with increasing fraction solid.

The investigators also considered two idealized models for isothermal coarsening and showed that

i) the driving force for the observed coarsening was reduction of the solid-liquid interfacial area;

ii) the alloy characteristics influenced the rate of coarsening;

iii) the observed rapid coarsening could be anticipated in a wide variety of alloys.

In the first model, the radius of one dendrite arm is considered smaller than the radius of other dendrite arms. Isothermal holding of the system at the melting point of the larger arms causes transport of solute from the smaller to the larger arms. The dendrite arm spacing increases as a result of the dissolution of the smaller arm.

In the second model, due to CHERNOV (1956), a dendrite arm of radius ρ_a with a root radius of ρ_r, where $\rho_r < \rho_a$, is considered. For the same reason as above, transport of solute occurs from the region of radius ρ_r to that of radius ρ_a. Hence the arm melts off at the root and increases the dendrite arm spacing. The work of JACKSON et al. (1966) indicates that both mechanisms (dendrite dissolution and dendrite separation) operate simultaneously.

2.7 - INFLUENCE OF CARBON ON SEGREGATION OF ALLOYING ELEMENTS

A final area touched upon by this investigation concerns the effect of carbon addition on microsegregation.

De BEAULIEU and KOHN (1957) studied the influence of carbon on the segregation of arsenic, chromium, cobalt, copper, manganese, molybdenum and tungsten by autoradiography and did not detect segregation of these elements in the absence of carbon. In melts containing about 0.4 wt% C, they observed a weak segregation of chromium, cobalt and molybdenum, a marked segregation of copper, manganese and tungsten and an intense segregation of arsenic. Carbon, they reasoned, increases the solidification interval of an alloy, that is, the temperature difference between the liquidus and solidus and hence gives rise to segregation of the second solute. However, it should be pointed out that an increase in the solidification interval does not necessarily lead to an increased segregation of the second solute: there must be a solute interaction between carbon and the second solute for this to occur.

PHILIBERT et al. (1965) demonstrated by electron-probe microanalysis that the addition of carbon to iron-base binary alloys had a marked influence on the segregation of alloying elements in laboratory melts solidified at rates similar to those of industrial ingots. Carbon influenced the segregation of Ni, Mn, Si, Cr, Mo, As, Sn, P, Nb, S, its influence becoming greater in the order listed. The solute partition coefficients, it should be noted, were roughly in the same order, decreasing from approximately 0.8 for nickel to 0.05 for sulphur. The authors also showed that the absolute value rather than the sign of the interaction parameter seemed to be of importance in determining the effect of carbon on various solutes.

In the work of DOHERTY and MELFORD (1966) on Fe - X wt% C - 1.5 wt% Cr alloys the segregation index, I_s, of chromium rose to a maximum around 1.5 wt% C and decreased again as X varied from 0 to 2.2. One possible explanation, they suggested, was that carbon affected k_0, the equilibrium partition coefficient of chromium in the iron. They conducted experiments on melts of Fe - X wt% C - 1.5 wt% Cr to determine the variation of k_0 with wt% C. This involved equilibrating a melt in the solid-liquid region with 3 - 10 wt% liquid, quenching into brine and measuring the composition of the two phases by electron-probe microanalysis. The measurements showed that increasing the carbon concentration to 1.5 wt% decreased the partition coefficient of chromium by approximately 25% and enhanced its segregation; increasing the carbon concentration beyond that value raised the partition coefficient almost to the value for the Fe - Cr binary and attenuated the segregation of chromium. The experiments thus appeared to explain, at least in part, the variation of I_s with the concentration of carbon.

WEINBERG and BUHR (1967) studied the effect of composition on the general casting structure using radioactive tracer techniques. They compared the structure of AISI 4340 castings (0.41 wt% C - 0.95 wt% Cr - 0.66 wt% Mn - 0.28 wt% Mo - 1.88 wt% Ni - 0.010 wt% P - 0.12 wt% S - 0.35 wt% Si) with similar castings of electrolytic Fe - 0.012 wt% P, Fe - 2.08 wt% Ni - 0.18 wt% P, and low-carbon AISI 4300 type steel. The results suggested that the casting structure was controlled by the carbon concentration in the melt. The authors proposed that the growth fronts were planar in low-carbon systems and dendritic in systems containing greater amounts of carbon. Constitutional supercooling calculations effectively indicated that carbon was the overriding contributor to the casting structure.

The work of SUBRAMANIAN et al. (1968-a) on the solidification of iron alloys containing arsenic chromium, nickel and carbon showed that solute elements of low partition coefficient had an important effect on the degree of branching of the dendrites. In iron-chromium alloys, primary, secondary and tertiary arms, and primary and secondary plates were found. The addition of arsenic produced quaternary arms and tertiary plates, and the addition of carbon, arms and plates of even higher order.

TURKDOGAN and GRANGE (1968) evaluated in an approximate manner the isothermal variation of the manganese partition coefficient k_{Mn} as a function of the carbon content at 1490°C in the $\gamma_{Fe}+$ liquid region of the Fe - Mn - C system. Their results showed that k_{Mn} decreased by a factor of two as the carbon concentration increased and thus gave some support for the experimental evidence that carbon enhances the segregation of manganese. They did not extend their calculations to other systems.

2.8 - CONTROLLED SOLIDIFICATION TECHNIQUES

It is perhaps useful at this juncture to review the literature on techniques employed to solidify iron alloys in a controlled manner.

In the context of the present investigation, <u>controlled</u> solidification also implies <u>directional</u> solidification, and it is therefore instructive to review, at first, some examples of directional solidification. The most familiar example of directional solidification is found in ingots cast by conventional methods. Such ingots generally comprise three zones: a chill zone next to the mould wall, consisting of very fine grains; an equiaxed zone in the central part of the ingot, consisting of randomly oriented grains; and a columnar zone located between the chill and equiaxed zones, consisting of directionally solidified columnar grains. The preferred direction of columnar growth in cubic metals is the heat flow direction [100] . WALTON and CHALMERS (1959) have shown that if the angle between the [100] directions of two adjacent columnar grains is divergent, the more favourably oriented grain grows at the expense of the others.

The principle of directional solidification has been applied to steel castings by many workers with different objectives in mind. HEUVERS (1929), CHWORINOW (1940), BRIGGS (1946), CAINE (1948), ADAMS and TAYLOR (1953), WLODAWER (1966) and others, whose interests laid in producing sound steel castings, made systematic studies of the feeding of castings by directional solidification. The attentions of FLEMINGS et al. (1961), AHEARN and QUIGLEY (1964), POLICH and FLEMINGS (1965) and NEREO et al. (1965) were focussed on the mechanical properties of directionally solidified steels. These workers produced fully columnar ingots by extracting heat from a single face of the mould. They maintained a steep temperature gradient throughout solidification by using a chill in combination with refractory moulds, preheated moulds, exothermic mould materials, and other means of maintaining elevated temperatures in certain parts of the mould. This type of directional solidification is a transient state process: indeed, to a first approximation, the rate of advancement of the solidification front varies inversely with the square root of time (RUDDLE, 1957; CHALMERS, 1964). The spacing of the dendrites which make up the grains and the width of the grains vary with distance from the chill (FLEMINGS et al., 1961), which complicates, to a certain extent, the interpretation of results.

Controlled directional solidification, or simply controlled solidification, on the other hand, allows the solidification to proceed at a constant rate and temperature gradient. Numerous workers have employed controlled solidification in studies of segregation and solute rejection in low melting-point alloys (CHALMERS, 1964). However, little such work has been carried out on iron-base alloys.

DIEHL et al. (1965) studied dendritic segregation and arm spacing in iron-carbon-chromium alloy bars solidified in a controlled manner by progressive withdrawal from a resistance furnace. A globar-heated furnace capable of melting specimens at temperatures up to 1650^{o}C was constructed with a heating chamber consisting of a vertical tube 20 in. ($\sim$50 cm) in length. The furnace body was mounted in a vertical framework and connected to a variable-speed drive unit capable of raising or lowering the furnace at a pre-set rate. The specimen consisted of an alloy bar 30 in. ($\sim$75 cm) in length and 1 1/8 in. ($\sim$2.9 cm) in diameter, with the upper 13 in. ($\sim$33 cm) machined to 1 in. ($\sim$2.5 cm) diameter. The upper portion of the specimen was fitted into a 1 in. ($\sim$2.5 cm) mullite tube, 16 in. ($\sim$40 cm) in length, and open at both ends. The mullite tube served as a crucible to contain the molten alloy, while the unmelted portion of the specimen provided a means of supporting the crucible within the furnace and of extracting heat during solidification. The specimens were thus solidified vertically and free from stirring and vibration. DIEHL et al. mentioned neither temperature control of the furnace nor measurement of temperature gradients in the specimen.

SMITH and BEELEY (1968) directed their research towards the determination of structure and segregation in steel bars produced by controlled solidification under turbulent conditions promoting complete mixing in the liquid phase. These conditions were achieved by progressive withdrawal of an alloy specimen from a copper induction coil. The mould assembly consisted of a mullite tube supported in a zircon-base ramming compound for mechanical reinforcement and insulation. The outer container was a laminated asbestos paper tube. The assembly rested on a water-cooled copper base driven by an electric motor. The specimens were 14 in. (∼35 cm) in length and 1.25 in. (∼3.25 cm) in diameter. Precise temperature control could not be maintained in the system because of the impossibility of continuous immersion pyrometry. No measurements of temperature gradient in the specimen were made.

As reported in Section 2.6, ALBERNY et al. (1969) solidified iron alloys under independent conditions of temperature gradient and growth velocity. Although no details of the technique were given, it is presumed that they employed controlled solidification in their experiments.

CHAPTER 3

OBJECT OF PRESENT INVESTIGATION

The main object of this investigation was to obtain information on the solidification of industrially important alloys of the type Fe - low Mn - S and Fe - low Mn - S - C. However, a considerable amount of work was also done on Fe - high Mn - S alloys; the purpose was to obtain the clearest possible information on problems such as the relation between microsegregation patterns and inclusions, between dendrite arm spacing and solidification velocity, and phenomena such as homogenization of the solid phase in the vicinity of the solid-liquid interface. The information obtained on the high manganese alloys was found to be useful in the interpretation of the less transparent results of experiments on the low manganese alloys.

The solidification of the alloys was carried out under controlled conditions using a technique based on the controlled solidification techniques reviewed in Section 2.8. The object of using this approach was again to facilitate the interpretation of results. The technique consisted of cycling each infinitesimal slice of a specimen through the same temperature profile and quenching the specimen at some point during the solidification process, thereby yielding a complete spectrum of solidification phenomena. In order to avoid complications arising from vibration and convection effects, it was decided to solidify the melts in vertical small-bore crucibles using a movable resistance furnace. The solidification apparatus — designed especially for the solidification of high temperature alloys under closely controlled conditions — is described in Sections 5.1 to 5.5.

Upon reviewing the literature, it became apparent that many areas of the science and technology of solidification needed further attention. The topics which appeared to require immediate attention were treated in this investigation. They are outlined in the following paragraphs.

As seen in Section 2.7 of the literature review, carbon has a pronounced effect on the microsegregation behaviour of most solutes. In multicomponent solutions, microsegregation is presumably affected by constitutional interaction of solutes which modifies the interface equilibria and hence the partition coefficients and the amount of microsegregation. A theoretical treatment of constitutional interaction of solutes in ternary systems, the simplest of multicomponent systems, was therefore carried out. This treatment is presented in Section 4.1 along with several illustrative examples.

The microsegregation models reviewed in Section 2.3 are applicable to unidirectional solidification, that is, to the advance of a planar macroscopic or microscopic solid-liquid interface. In dendritic specimens, however, the thickening of dendrites occurs most often by cylindrical (two-dimensional) or spherical (three-dimensional) growth. In this investigation, the planar maximum segregation equation was modified to account for this effect. The modified equation and implications thereof are discussed in Section 4.2.1.

It was seen in Section 2.3.2 of the literature review that the solute concentration of dendrite axes sometimes exceeds the value k_0C_0 and as a result the amount of solute redistribution decreases. An undercooling model based on the maximum segregation model was developed in this study. The model is presented in Section 4.2.2.

The microsegregation models reviewed in Section 2.3 treat very special cases of solidification. An attempt was made to arrive at a more general model taking into account diffusion of two solutes during solidification of a finite system. The model and results of calculations are presented in Section 4.2.3.

The literature review showed that the field of inclusion formation and transport is in a rather confused state. In this study, some basic principles were grouped together in the hope of shedding light on the formation mechanism and transport of inclusions during solidification.

It was seen in Section 2.6 that most of the information on dendrite arm spacing is couched in engineering correlations employing empirical units, for example, cooling rate in degrees per unit time as opposed to solidification rate in units of distance per unit time. During the course of the present investigation it became apparent that it was now desirable to attack the problem in more fundamental terms, i.e., in terms of controllable variables such as temperature gradient, solidification rate, composition, and variables which measure the constitutional and thermal properties of the alloy such as solute diffusivity, partition coefficient, latent head of fusion and thermal conductivity. The "field of influence" concept of RUTTER and CHALMERS (1953) was therefore extended to account for the variation of dendrite arm spacing with variables other than C_0, V and G. Dimensional analysis was also used to obtain a general, dimensionally correct and physically coherent relation between the dendrite arm spacing, alloy parameters and solidification conditions. These treatments are given in Section 4.4.

CHAPTER 4

THEORETICAL CONSIDERATIONS

4.1 - CONSTITUTIONAL INTERACTION OF SOLUTES IN TERNARY SYSTEMS

The purpose of this section is to give an analytical description of terminal two-phase equilibria in ternary systems and discuss constitutional interaction of solutes in terms of this analytical description. (See HONE et al., 1970).

4.1.1 - TANGENT PLANE EQUATIONS

GIBBS (1961) has shown that boundaries of two-phase regions of ternary isotherms may be generated by rolling a doubly tangent plane about two isothermal free enthalpy surfaces corresponding to the participating phases, each set of tangency points defining a tie-line. For clarity, a ternary free enthalpy versus composition diagram is sketched in Figure 4.1.1. The geometrical consequences of this construction have been discussed by MEIJERING (1966) and in the following, the analytical consequences are pursued.

For the case where an increase in both solute concentrations depresses the $\alpha \rightarrow \beta$ transformation temperature, pure solvent (0) in the α state and pure solutes (1 and 2) in the β state are chosen as reference states.

The reactions and free enthalpy changes describing the formation of one mole of β solution are:

$$x_0^{\beta} + x_1^{\beta} + x_2^{\beta} = 1 \text{ mole } \beta \text{ solution}, \quad \Delta g_M^{\beta} \tag{4.1.1}$$

$$x_0^{\alpha} = x_0^{\beta} \quad , \quad x_0^{\beta} \Delta g_0^{\alpha\beta} \tag{4.1.2}$$

which upon summation give:

$$x_0^{\alpha} + x_1^{\beta} + x_2^{\beta} = 1 \text{ mole } \beta \text{ solution}, \quad \Delta g_m^{\beta} \tag{4.1.3}$$

Similarly, for the formation of one mole of α solution:

$$x_0^{\alpha} + x_1^{\alpha} + x_2^{\alpha} = 1 \text{ mole } \alpha \text{ solution}, \quad \Delta g_M^{\alpha} \tag{4.1.4}$$

$$x_1^{\beta} = x_1^{\alpha} \quad , \quad -x_1^{\alpha} \Delta g_1^{\alpha\beta} \tag{4.1.5}$$

$$x_2^{\beta} = x_2^{\alpha} \quad , \quad -x_2^{\alpha} \Delta g_2^{\alpha\beta} \tag{4.1.6}$$

which upon summation give:

$$x_0^{\alpha} + x_1^{\beta} + x_2^{\beta} = 1 \text{ mole } \alpha \text{ solution}, \quad \Delta g_m^{\alpha} \tag{4.1.7}$$

In these equations,

x_i^{ϕ} is the mole fraction of component i in the ϕ phase,

$\Delta g_i^{\alpha\beta}$ is the free enthalpy of formation of one mole of pure component i from the α to β state, and

Δg_M^{ϕ} and Δg_m^{ϕ} are free enthalpies of mixing.

The free enthalpies of mixing in Equations 4.1.1 and 4.1.4 may be expressed as:

$$\Delta g_M^{\phi} = \mu_s^{\phi} - x_0^{\phi} \mu_0^{0\phi} - x_1^{\phi} \mu_1^{0\phi} - x_2^{\phi} \mu_2^{0\phi} \qquad (4.1.8)$$

where μ_s^{ϕ} is the molar free enthalpy of solution ϕ

and $\mu_i^{0\phi}$ is the molar free enthalpy of pure component i.

Substituting into Equation 4.1.8 the general thermodynamic relation

$$\mu_s^{\phi} = x_0^{\phi} \mu_0^{\phi} + x_1^{\phi} \mu_1^{\phi} + x_2^{\phi} \mu_2^{\phi} \quad , \qquad (4.1.9)$$

where μ_i^{ϕ} is the partial molar free enthalpy of component i in phase ϕ, and collecting terms gives:

$$\Delta g_M^{\phi} = x_0^{\phi} (\mu_0^{\phi} - \mu_0^{0\phi}) + x_1^{\phi} (\mu_1^{\phi} - \mu_1^{0\phi}) + x_2^{\phi} (\mu_2^{\phi} - \mu_2^{0\phi}) \qquad (4.1.10)$$

Substituting the defining relation for the activity of component i in the ϕ phase, a_i^{ϕ} ,

$$RT \ln a_i^{\phi} = \mu_i^{\phi} - \mu_i^{0\phi} \qquad (4.1.11)$$

into Equation 4.1.10 gives:

$$\Delta g_M^{\phi} = RT (x_0^{\phi} \ln a_0^{\phi} + x_1 \ln a_1^{\phi} + x_2 \ln a_2^{\phi}) \qquad (4.1.12)$$

The complete expressions for the free enthalpy surfaces are thus:

$$\Delta g_m^{\beta} = x_0^{\beta} \Delta g_0^{\alpha\beta} + RT \left[x_0^{\beta} \ln a_0^{\beta} + x_1^{\beta} \ln a_1^{\beta} + x_2^{\beta} \ln a_2^{\beta} \right] \qquad (4.1.13)$$

$$\Delta g_m^{\alpha} = -x_1^{\alpha} \Delta g_1^{\alpha\beta} - x_2^{\alpha} \Delta g_2^{\alpha\beta} + RT \left[x_0^{\alpha} \ln a_0^{\alpha} + x_1^{\alpha} \ln a_1^{\alpha} + x_2^{\alpha} \ln a_2^{\alpha} \right] \qquad (4.1.14)$$

Thus, as shown in Figure 4.1.1, $\Delta g_m^{\alpha} = 0$ at $x_0 = 1$, and

$\Delta g_m^\beta = 0$ at $x_1 = 1$ and $x_2 = 1$. As usual, the solute mole fractions are chosen as independent variables.

At equilibrium, the chemical potential of each component is uniform throughout the two phase system:

$$\mu_0^\alpha = \mu_0^\beta \tag{4.1.15a}$$

$$\mu_1^\alpha = \mu_1^\beta \tag{4.1.15b}$$

$$\mu_2^\alpha = \mu_2^\beta \tag{4.1.15c}$$

Equivalently,

$$\mu_0^\alpha - \mu_0^{0\alpha} = \mu_0^\beta - \mu_0^{0\alpha} \tag{4.1.16a}$$

$$\mu_1^\alpha - \mu_1^{0\beta} = \mu_1^\beta - \mu_1^{0\beta} \tag{4.1.16b}$$

$$\mu_2^\alpha - \mu_2^{0\beta} = \mu_2^\beta - \mu_2^{0\beta} \tag{4.1.16c}$$

where $\mu_0^{0\alpha}$ is the chemical potential of pure solvent in the α phase and $\mu_1^{0\beta}$ and $\mu_2^{0\beta}$ are the chemical potentials of pure solutes in the β phase. The terms $\mu_0^\alpha - \mu_0^{0\alpha}$, $\mu_1^\alpha - \mu_1^{0\beta}$ and $\mu_2^\alpha - \mu_2^{0\beta}$ are the intercepts on the free energy axes at $x_0 = 1$, $x_1 = 1$ and $x_2 = 1$, respectively, of the plane tangent to the Δg_m^α surface described by Equation 4.1.14. Similarly, the terms on the right hand side of Equations 4.1.16a, 4.1.16b and 4.1.16c describe the intercepts on the free enthalpy axes of the plane tangent to the

Δg_m^{β} surface. Equations 4.1.16a, 4.1.16b and 4.1.17c state that the intercepts of the two tangent planes are equal at equilibrium, i.e., the planes are congruent as shown in Figure 4.1.1. It follows that the equilibrium conditions may be rewritten in terms of one equality of intercepts on the Δg_m axis at $x_0 = 1$ and two equalities of partial slopes:

$$\Delta g_m^{\beta} - \left[\frac{\partial \Delta g_m^{\beta}}{\partial x_1}\right] x_1^{\beta} - \left[\frac{\partial \Delta g_m^{\beta}}{\partial x_2}\right] x_2^{\beta} =$$

$$\Delta g_m^{\alpha} - \left[\frac{\partial \Delta g_m^{\alpha}}{\partial x_1}\right] x_1^{\alpha} - \left[\frac{\partial \Delta g_m^{\alpha}}{\partial x_2}\right] x_2^{\alpha} \qquad (4.1.17)$$

$$\frac{\partial \Delta g_m^{\alpha}}{\partial x_1} = \frac{\partial \Delta g_m^{\beta}}{\partial x_1} \qquad (4.1.18)$$

$$\frac{\partial \Delta g_m^{\alpha}}{\partial x_2} = \frac{\partial \Delta g_m^{\beta}}{\partial x_2} \qquad (4.1.19)$$

Substitution of Equations 4.1.3 and 4.1.4 into the partial slopes yields terms of the form

$$\begin{aligned} \frac{\partial \Delta g_m^{\phi}}{\partial x_i} = - \Delta g_i^{\alpha\beta} + RT \Bigg[& x_0^{\phi} \frac{\partial \ln a_0^{\phi}}{\partial x_i} - \ln a_0^{\phi} \\ & + x_1^{\phi} \frac{\partial \ln a_1^{\phi}}{\partial x_i} + \ln a_i^{\phi} \\ & + x_2^{\phi} \frac{\partial \ln a_2^{\phi}}{\partial x_i} \Bigg] \end{aligned} \qquad (4.1.20)$$

In view of the Gibbs - Duhem relation:

$$\sum_i x_i d\mu_i = 0 \qquad (4.1.21)$$

the sum of the three terms containing differentials are zero. Indeed, the chemical potential μ_i is a function of the independent composition variables x_1 and x_2 :

$$\mu_i = \mu_i (x_1, x_2) \qquad (4.1.22)$$

of which the total differential is:

$$d\mu_i = \frac{\partial \mu_i}{\partial x_1} dx_1 + \frac{\partial \mu_i}{\partial x_2} dx_2 \qquad (4.1.23)$$

Expressing the chemical potential as

$$\mu_i = \mu_i^0 + RT \ln a_i \qquad (4.1.24)$$

the partial derivatives in Equation 4.1.23 are

$$\frac{\partial \mu_i}{\partial x_1} = RT \frac{\partial \ln a_i}{\partial x_1} \qquad (4.1.25)$$

$$\frac{\partial \mu_i}{\partial x_2} = RT \frac{\partial \ln a_i}{\partial x_2} \qquad (4.1.26)$$

Substituting Equations 4.1.26 and 4.1.25 into 4.1.23 and the latter into 4.1.21 and rearranging gives:

$$\left[x_0 \frac{\partial \ln a_0}{\partial x_1} + x_1 \frac{\partial \ln a_1}{\partial x_1} + x_2 \frac{\partial \ln a_2}{\partial x_2}\right] dx_1$$

$$+ \left[x_0 \frac{\partial \ln a_0}{\partial x_2} + x_1 \frac{\partial \ln a_2}{\partial x_2} + x_2 \frac{\partial \ln a_2}{\partial x_2}\right] dx_2 = 0 \qquad (4.1.27)$$

As dx_1 and dx_2 are independent and can possess any value, the bracketed terms must be equal to zero. Then terms of the form given by Equation 4.1.20 become

$$\frac{\partial \Delta g_m^{\phi}}{\partial x_i} = - \Delta g_i^{\alpha\beta} + RT\left[\ln a_i - \ln a_0\right] \qquad (4.1.28)$$

Substituting Equations 4.1.13 and 4.1.14 into 4.1.17, 4.1.18 and 4.1.19, performing the differentiations, applying the Gibbs-Duhem relation and rearranging yields three relations among the composition variables:

$$\frac{1}{RT} \Delta g_0^{\alpha\beta} = \ln k_0^T + \ln \Gamma_0 \qquad (4.1.29)$$

$$\frac{1}{RT} \Delta g_1^{\alpha\beta} = \ln k_1^T + \ln \Gamma_1 \qquad (4.1.30)$$

$$\frac{1}{RT} \Delta g_2^{\alpha\beta} = \ln k_2^T + \ln \Gamma_2 \qquad (4.1.31)$$

where: $k_i^T \equiv \dfrac{x_i^\alpha}{x_i^\beta}$, $\Gamma_i \equiv \dfrac{\gamma_i^\alpha}{\gamma_i^\beta}$ and $\gamma_i^\phi \equiv \dfrac{a_i^\phi}{x_i^\phi}$

Upon specification of the temperature and one composition variable, say x_1^α, the previous equations may be solved for the three remaining compositions, x_2^α, x_1^β and x_2^β, yielding one tie-line. Repetition of this procedure, for a given temperature and different values of x_1^α, generates a set of ternary partition coefficients and the phase boundaries of the isotherm.

Expressions for the activity coefficients are required in Equations 4.1.29, 4.1.30 and 4.1.31. For dilute solutions a low order Taylor series expansion may be used (WAGNER, 1952):

$$\ln \gamma_0^\phi = -\frac{\epsilon_{11}^\phi}{2} x_1^{\phi 2} - \epsilon_{12}^\phi x_1^\phi x_2^\phi - \frac{\epsilon_{22}^\phi}{2} x_2^{\phi 2} \qquad (4.1.32)$$

$$\ln \gamma_1^\phi = \ln \gamma_1^{0\phi} + \epsilon_{11}^\phi x_1^\phi + \epsilon_{12}^\phi x_2^\phi \qquad (4.1.33)$$

$$\ln \gamma_2^\phi = \ln \gamma_2^{0\phi} + \epsilon_{21}^\phi x_1^\phi + \epsilon_{22}^\phi x_2^\phi \qquad (4.1.34)$$

In these expressions, the $\gamma_i^{0\phi}$ are Henry's law coefficients and the ϵ_{ij}^ϕ are interaction parameters.

Richer solutions may be described by a higher order Taylor series expansion or by a quadratic formalism due to DARKEN (1967):

$$\ln \gamma_0^{\phi} = \alpha_{01}^{\phi} x_1^{\phi 2} + \alpha_{02}^{\phi} x_2^{\phi 2} + (\alpha_{01}^{\phi} + \alpha_{02}^{\phi} - \alpha_{12}^{\phi}) x_1^{\phi} x_2^{\phi} \qquad (4.1.35)$$

$$\ln \gamma_1^{\phi} = \gamma_1^{0\phi} - 2 \alpha_{01}^{\phi} x_1^{\phi} + (\alpha_{12}^{\phi} - \alpha_{01}^{\phi} - \alpha_{02}^{\phi}) x_2^{\phi}$$

$$+ \ln \gamma_0^{\phi} \qquad (4.1.36)$$

$$\ln \gamma_2^{\phi} = \ln \gamma_2^{0\phi} - 2 \alpha_{02}^{\phi} x_2^{\phi} + (\alpha_{12}^{\phi} - \alpha_{01}^{\phi} - \alpha_{02}^{\phi}) x_1^{\phi}$$

$$+ \ln \gamma_0^{\phi} \qquad (4.1.37)$$

It should be noted that DARKEN's activity coefficient relations may be obtained formally by adding $\ln \gamma_0^{\phi}$ to $\ln \gamma_1^{\phi}$ equations since the relations between the epsilon and alpha parameters are:

$$\epsilon_{11}^{\phi} = - 2 \alpha_{01}^{\phi} \qquad (4.1.38)$$

$$\epsilon_{22}^{\phi} = - 2 \alpha_{02}^{\phi} \qquad (4.1.39)$$

$$\epsilon_{12}^{\phi} = \alpha_{12}^{\phi} - \alpha_{01}^{\phi} - \alpha_{02}^{\phi} \qquad (4.1.40)$$

In the special cases where the solutions are dilute or where the interaction parameters tend to zero, Equations 4.1.29, 4.1.30 and 4.1.31 reduce to:

$$k_0^{T} = \exp \left[\frac{\Delta g_0^{\alpha\beta}}{RT} \right] \qquad (4.1.41)$$

$$k_1^T = \frac{\gamma_1^{0\beta}}{\gamma_1^{0\alpha}} \exp\left[\frac{\Delta g_1^{\alpha\beta}}{RT}\right] \tag{4.1.42}$$

$$k_2^T = \frac{\gamma_2^{0\beta}}{\gamma_2^{0\alpha}} \exp\left[\frac{\Delta g_2^{\alpha\beta}}{RT}\right] \tag{4.1.43}$$

The ternary partition coefficients are thus constant and equal to the partition coefficients of the limiting binary systems.

In ideal solutions, the Henry's law coefficients, $\gamma_i^{0\phi}$, are equal to unity and Equations 4.1.42 and 4.1.43 reduce to the ideal binary solution relations derived by THURMOND (1953).

If the dependent composition variables x_1^β, x_2^β and x_2^α are expressed in terms of the partition coefficients and the independent composition variable, x_1^α, as

$$x_1^\beta = \frac{x_1^\alpha}{k_1^T} \tag{4.1.44}$$

$$x_2^\beta = \frac{1 - k_0^T}{k_2^T - k_0^T} - \frac{1}{k_1^T}\left[\frac{k_1^T - k_0^T}{k_2^T - k_0^T}\right] x_1^\alpha \tag{4.1.45}$$

$$x_2^\alpha = k_2^T\left[\frac{1 - k_0^T}{k_2^T - k_0^T}\right] - \frac{k_2^T}{k_1^T}\left[\frac{k_1^T - k_0^T}{k_2^T - k_0^T}\right] x_1^\alpha \ , \tag{4.1.46}$$

it is seen that the phase boundaries of an isotherm become linear as the partition coefficients become constant, i.e., as the solute concentrations or interaction parameters tend to zero.

This result implies that limiting dilute ternary two-phase equilibria may be generated via a "binary approximation"; i.e., by constructing linear phase boundaries joining limiting binary equilibrium points and tie-lines consistent with the (constant) binary solute partition coefficients. The concentration range for which this approximation is valid will vary from system to system, and it would seem appropriate whenever possible, to test its applicability through substitution of available data in Equations 4.1.29, 4.1.30 and 4.1.31.

The insensitivity of very dilute systems to solute interaction suggests that successful determinations of true dilute parameters from the curvature of isothermal phase boundaries, or from the isothermal variation of solute partition coefficients, will require the use of extremely precise experimental methods.

In summary, if reliable thermodynamic data are available and the binary phase diagrams are well established, then the methods described here may be employed to compute precise constitutional data, valid in the range where the expressions 4.1.32 to 4.1.34 or 4.1.35 to 4.1.37 adequately describe the variation of activity coefficients with composition.

There appears to be no metallic terminal ternary systems for which complete experimental constitutional and solution data exist. As further information becomes available, the test of internal consistency will be an important application of computations of this kind.

At low solute concentrations (even for fairly strong solute interactions) or at higher solute concentrations in systems exhibiting weak interactions, terminal isotherms are characterized by approximately linear phase boundaries and constant solute partition coefficients. The range of validity of this "binary approximation" may be established for any system using the methods discussed in this section.

4.1.2 - ROOTS OF TANGENT PLANE EQUATIONS

The roots of Equations 4.1.29, 4.1.30 and 4.1.31 may be found by application of the Newton-Raphson algorithm (LAPIDUS, 1962). The composition variables are first expressed as functions of the partition coefficients, as in Equations 4.1.44, 4.1.45 and 4.1.46. The terms in the LHS of the tangent-plane equations are then transferred to the RHS and the resulting functions designated f_0, f_1 and f_2. Expanding the functions

$$f_i\,(k_0^T,\ k_1^T,\ k_2^T) = 0 \qquad i = 0,\ 1,\ 2 \qquad (4.1.47)$$

in Taylor series in terms of estimates $\bar{k}_0$, $\bar{k}_1$ and $\bar{k}_2$ of the roots k_0^T, k_1^T and k_2^T, and truncating second and higher order terms, the following simultaneous linear equations result:

$$f_i\,(\bar{k}_0,\ \bar{k}_1,\ \bar{k}_2) + \sum_{r=0}^{2} \left[\frac{\partial f_i}{\partial k_r} \right] \Delta k_r^T = 0 \qquad i = 0, 1, 2 \qquad (4.1.48)$$

where: $\Delta k_r^T = k_r^T - \bar{k}_r$

These equations are then solved for the Δk_r^T corresponding to the $\bar{k}_r$ and superior estimates of k_r^T equal to $\bar{k}_r + \Delta k_r^T$ are used to restart the procedure.

Using the partition coefficients calculated from the binary equilibria as the initial $\bar{k}_0$, $\bar{k}_1$ and $\bar{k}_2$, the iterative process normally converges to acceptable values of the roots within ten to fifteen steps.

The derivatives of the functions in Equations 4.1.48 may be evaluated by the relation

$$\frac{\partial f_i}{\partial k_r} \approx \frac{f_i\ (k_r + q) - f_i\,(k_r - q)}{2q} \qquad (4.1.49)$$

where q is a small arbitrary constant.

4.1.3 - TERNARY ISOTHERM PROGRAM

A program for calculating ternary isotherms using the Newton-Raphson algorithm was written in Fortran IV machine language for the McMaster CDC 6400 computer. It is listed in Appendix A.1.

4.1.4 - FREE ENTHALPY FUNCTIONS

The free enthalpy functions $\Delta g_i^{\alpha\beta}$ used in Equations 4.1.13 and 4.1.14 are discussed in the present section.

In studies of phase transformations it is generally assumed that the enthalpy and entropy of transformation of pure component i from the α to the β phase are constant in the temperature range of interest (SWALIN, 1962). This leads to expressions for the free enthalpy of transformation $\Delta g_i^{\alpha\beta}$ of the form

$$\Delta g_i^{\alpha\beta} = \Delta h_i^{\alpha\beta} \left[1 - \frac{T}{T_i^{\alpha\beta}} \right] \tag{4.1.50}$$

where T is the isotherm temperature, $T_i^{\alpha\beta}$ is the transformation temperature of pure component i and $\Delta h_i^{\alpha\beta}$ is the enthalpy of transformation. The transformation enthalpy and temperature of pure solvents and solutes stable at the temperature of interest are generally available. However, when these data are unknown, the temperature variation of the free enthalpy must be tailored so that the calculated ternary isotherms are consistent with the limiting binary phase diagrams. In order to obtain a proper fit it is necessary, in some cases, to use an expression slightly more general than Equation 4.1.50. Assuming the entropy $\Delta s_i^{\alpha\beta}$ and the enthalpy $\Delta h_i^{\alpha\beta}$ of transformation are both linear functions of temperature,

$$\Delta h_i^{\alpha\beta} = \zeta_i + b_i T \quad (4.1.51)$$

$$\Delta s_i^{\alpha\beta} = c_i + \eta_i T \quad (4.1.52)$$

Then $$\Delta g_i^{\alpha\beta} = \zeta_i + b_i T - c_i T - \eta_i T^2 \quad (4.1.53)$$

since $$\Delta g_i^{\alpha\beta} = \Delta h_i^{\alpha\beta} - T \Delta s_i^{\alpha\beta} \quad (4.1.54)$$

Isolating the constants c_i and b_i, Equation 4.1.53 becomes:

$$c_i - b_i = \frac{\zeta_i - \eta_i T^2 - \Delta g_i^{\alpha\beta}}{T} \quad (4.1.55)$$

At the transformation temperature $T = T_i^{\alpha\beta}$, $\Delta g_i^{\alpha\beta} = 0$. Therefore

$$c_i - b_i = \frac{\zeta_i - \eta_i (T_i^{\alpha\beta})^2}{T_i^{\alpha\beta}} \quad (4.1.56)$$

Substituting Equation 4.1.56 into 4.1.55 and rearranging gives:

$$\Delta g_i^{\alpha\beta} = \zeta_i \left(1 - \frac{T}{T_i^{\alpha\beta}}\right) + \eta_i T (T_i^{\alpha\beta} - T) \quad (4.1.57)$$

in which the constants ζ_i and η_i may be manipulated to match the calculated binary diagrams to the experimental ones.

If $\eta_i = 0$, Equation 4.1.57 reduces to the linear functional form generally employed to represent $\Delta g_i^{\alpha\beta}(T)$, and in this case, ζ_i is the enthalpy of transformation $\Delta h_i^{\alpha\beta}$.

4.1.5 - SOLUTION PARAMETERS AND STANDARD STATES

In the application of tangent plane equations to the calculation of a given phase field care should be taken to ensure that the solution data refer to the standard states adopted in the derivation of the equations. It will be shown in this section that the Henry's law coefficients change in value with a change in standard state and that the interaction parameters are independent.

As the chemical potentials of elements in solution remain unchanged as the standard states are changed from A to B,

$$(\mu_i)_A = (\mu_i)_B \qquad (4.1.58)$$

and

$$\mu_i^A + RT\ln\ (a_i)_A = \mu_i^B + RT\ln\ (a_i)_B \qquad (4.1.59)$$

or:

$$\ln\ (a_i)_B = \ln\ (a_i)_A - \frac{(\mu_i^B - \mu_i^A)}{RT} \qquad (4.1.60)$$

Since the concentration does not change with a change in standard state,

$$(x_i)_A = (x_i)_B \qquad (4.1.61)$$

and

$$\ln\ (\gamma_i)_A = \ln\ (\gamma_i)_B - \frac{(\mu_i^B - \mu_i^A)}{RT} \qquad (4.1.62)$$

Then

$$\frac{\partial \ln\ (\gamma_i)_B}{\partial x_i} = \frac{\partial \ln\ (\gamma_i)_A}{\partial x_i} \qquad (4.1.63)$$

and $$\frac{\partial \ln (\gamma_i)_B}{\partial x_j} = \frac{\partial \ln (\gamma_i)_A}{\partial x_j} \tag{4.1.64}$$

However, these partial derivatives are the definitions of the self and cross interaction parameters of the Wagner activity coefficient formalism, Equations 4.1.33 and 4.1.34.

Therefore:

$$(\epsilon_{ii})_B = (\epsilon_{ii})_A \tag{4.1.65}$$

$$(\epsilon_{ij})_B = (\epsilon_{ij})_A \tag{4.1.66}$$

and from Equation 4.1.62

$$(\gamma_i^0)_B = (\gamma_i^0)_A \exp\left[-\frac{(\mu_i^B - \mu_i^A)}{RT}\right], \tag{4.1.67}$$

quod erat demonstrandum.

4.1.6 - δ_{Fe} + LIQUID EQUILIBRIA IN THE Fe - Mn - S SYSTEM

The foregoing analytical method was used to calculate tie-lines of the 1500°C isotherm for δ_{Fe} + Liquid equilibria in the Fe - Mn - S constitution diagram, using the Fe - S and Fe - Mn phase diagrams of Figures 4.1.2 and 4.1.3, and the data of Table 4.1.1. In this particular case, the parameters η_{Mn}, η_S, ζ_{Mn}, ζ_S, $T_S^{\alpha\beta}$, ϵ^{δ}_{MnMn} and ϵ^{δ}_{SS} were manipulated until the calculated binary equilibria matched the experimental equilibria shown in Figures 4.1.2 and 4.1.3. This procedure, while clearly less satisfying than direct experimental determination of thermodynamic parameters, provided reasonable estimates for the purpose of checking for variation of partition coefficients.

The activity coefficients were related to concentrations by Equations 4.1.35, 4.1.36 and 4.1.37, and the epsilon formalism parameters of Table 4.1.1 were converted to alpha formalism using Equations 4.1.38, 4.1.39 and 4.1.40.

The results of these iterative calculations are listed in Table 4.1.2 for two cases; in the first, self-and cross-interactions between solutes are taken into account, while in the second, cross-interactions are neglected. The results are given to five digits in order to demonstrate the variation of the partition coefficients. They must on no account be regarded as physically significant to the same precision, in view of the limitations of the experimental data. However, the calculation serves to illustrate the effect of thermodynamic interaction on phase boundary curvature and partition coefficients, and, perhaps more important, supports the "binary approximation" up to these levels of solute concentration and interaction. The results for the full interaction case have been plotted in Figure 4.1.4.

For this particular system, inclusion of negative cross-interaction in the calculations alters the curvature of the liquidus, from slightly concave to slightly convex. This effect is most readily appreciated by examining the variation of k_{Fe}^{T}. The variations in k_{Mn}^{T} and k_{S}^{T} are also appreciably larger if cross-interaction is taken into account. However, the curvature of the phase boundaries and variation of the partition coefficients for this relatively rich solution system typifying fairly strong solute interaction are within limits of typical experimental error.

4.1.7 - γ_{Fe} + LIQUID EQUILIBRIA IN THE Fe - Mn - C SYSTEM

In their study of microsegregation in Fe - Mn - C alloys, TURKDOGAN and GRANGE (1968) calculated the 1490°C ternary isotherm for metastable γ_{Fe} + Liquid equilibrium. As shown in Figure 4.1.5, they plotted the experimental isoactivity curves of carbon in the γ_{Fe} and liquid phases on the composition triangle and generated the tie-lines and partition coefficients of the two-phase field by joining the limiting binary liquidus and solidus points with straight lines. Their results are shown in Figure 4.1.6. The partition coefficients exhibit a surprising variation from one end of the two-phase field to the other. In particular, the manganese partition coefficient varies from 0.75 of the Fe - Mn binary limit to 0.35 of the Fe - C binary. It was thus decided to examine their results in the light of calculations on the same isotherm using the tangent plane equations.

The first step in the calculations was to evaluate the solution parameters for carbon in the austenite and liquid phases, $\gamma_C^{0\gamma}$, ϵ_{CC}^{γ}, ϵ_{CMn}^{γ}, γ_C^{0L}, ϵ_{CC}^{L} and ϵ_{CMn}^{L} from the activity data used by TURKDOGAN and GRANGE (1968). A regression analysis of $\ln \gamma_C$ on x_C and x_{Mn} yielded the intercept on the ordinate $\ln \gamma_C^0$ and the partial slopes ϵ_{CC} and ϵ_{CMn} of the relation proposed by WAGNER (1952):

$$\ln \gamma = \ln \gamma^0 + \epsilon_{11} x_1 + \epsilon_{12} x_2 \qquad (4.1.68)$$

These values are listed in Table 4.1.3.

The Henry's law coefficients were modified using Equation 4.1.67 to take into account the change in standard state from pure solid graphite, used by TURKDOGAN and GRANGE to pure liquid graphite required by the tangent plane equations. Then

$$(\gamma_C^{0\gamma})_{Lgr} = (\gamma_C^{0\gamma})_{Sgr} \exp\left[-\frac{\Delta g_{gr}^f}{RT}\right] \qquad (4.1.69)$$

$$(\gamma_C^{0L})_{Lgr} = (\gamma_C^{0L})_{Sgr} \exp\left[-\frac{\Delta g_{gr}^f}{RT}\right] \qquad (4.1.70)$$

The free enthalpy of fusion of graphite, Δg_{gr}^f, was calculated from the relation

$$\Delta g_{gr}^f = T_{gr}^f \, \Delta s_{gr}^f \left[1 - \frac{T}{T_{gr}^f}\right] \qquad (4.1.71)$$

where T_{gr}^f is the fusion temperature of graphite and Δs_{gr}^f, the entropy of fusion.

The free enthalpy of the γ to liquid transformation in pure iron as a function of the absolute temperature was calculated from the regression equation:

$$\Delta g_{Fe}^{\gamma L} = 2.51830 \times 10^{3} - 6.47724 \times 10^{-1} (T + 3) - 4.13711 \times 10^{-4} (T + 3)^{2} \qquad (4.1.72)$$

fitted to the data compiled by DARKEN and GURRY (1953) by the method of least squares. The transformation (T + 3) was used in Equation 4.1.72 to account for the difference between the fusion temperature adopted for this work, 1802.16°K (1529°C) and that used by DARKEN and GURRY, 1805.16°K (1532°C).

The free enthalpies of fusion of γ manganese and " γ carbon" were calculated from Equation 4.1.57. The parameters ζ_{Mn}, η_{Mn}, ζ_{C}, η_{C} and $T_{C}^{\gamma L}$ were varied until the tangent plane equations generated the limiting binary equilibria shown in Figures 4.1.7 and 4.1.8. The final values of the parameters are listed in Table 4.1.3. As the peritectic reaction on the manganese side of the binary Fe - Mn constitution diagram occurs at 1232°C (HELLAWELL and HUME-ROTHERY, 1957) and the melting point of δ_{Mn} is 1244°C (BASINSKI and CHRISTIAN, 1954), it was assumed that $T_{Mn}^{\gamma L} = 1240^{\circ}C$.

The ϵ formalism interaction parameters of Table 3.1.3 were converted to the more consistent α formalism parameters by means of Equations 4.1.38, 4.1.39 and 4.1.40.

The results obtained by the tangent plane method are given in Tables 4.1.4 and 4.1.5 in terms of atomic and weight percents. The tie - lines of Table 4.1.5 are plotted in Figure 4.1.9. In contrast to the results of TURKDOGAN and GRANGE, the partition coefficients remain relatively constant throughout the range of compositions, and the liquidus and solidus show substantial curvature. The convexity of the phase boundaries is an effect of the negative cross interaction parameters, ϵ^{L}_{MnC} and ϵ^{γ}_{MnC}, as in the case of the δ_{Fe} + Liquid equilibria in the Fe - Mn - S system.

The fact that the partition coefficients are relatively constant leads to significant mathematical economy since the maximum segregation equations of Section 4.4.1 can be integrated exactly rather than numerically as in the investigation of TURKDOGAN and GRANGE (1968).

It is possible that the large partition coefficient variation found by TURKDOGAN and GRANGE is due to the inherent loss of accuracy in graphical measurements in the low solute regions of Figure 4.1.5. For example, $k^{T}_{Mn} = x^{\gamma}_{Mn}/x^{L}_{Mn}$ would be difficult to measure accurately at low manganese concentrations. In effect, it is at low concentrations that k^{T}_{Mn} varies most rapidly as shown in Figure 4.1.6. Similar considerations hold for k^{T}_{C}.

4.1.8 - FURTHER APPLICATIONS OF THE TERNARY TANGENT PLANE THEORY

In addition to enabling the calculation or reasonable estimates of ternary equilibria, the tangent plane theory has several consequences which are of value in the interpretation and use of experimental results. Several examples shall be considered in this section.

As was seen in Section 2.5, the onset of constitutional supercooling in binary alloys is a function of the temperature gradient in the liquid, G, the rate of solidification, V, and the initial composition, C_0. For dilute binary alloys, a planar solid-liquid interface breaks down during solidification to a non-planar or cellular interface if

$$\frac{G}{V} < A C_0 \tag{4.1.73}$$

where:

$$A \equiv \frac{m}{D}\left[\frac{1 - k_0}{k_0}\right] \tag{4.1.74}$$

and m is the slope of the binary liquidus line, D is the diffusion coefficient of the solute in the solvent, and k_0 is the equilibrium distribution coefficient. Since for dilute alloys, m, D and k_0 are constant, a linear relationship exists between G/V and C_0.

COLE and WINEGARD (1963-64) studied the planar to cellular interface transitions in the tin-base alloys, Sn - Sb, Sn - Pb and Sn - Sb - Pb. They reported their binary results as:

$$\left(\frac{G}{V}\right)_{\text{Sb in Sn}} = 2.5 \times 10^4 \, C_0 \tag{4.1.75}$$

and: $$\left(\frac{G}{V}\right)_{\text{Pb in Sn}} = 5.6 \times 10^5 \, C_0 \tag{4.1.76}$$

They stated, quite rightly, that if there were no interaction between the solutes Sb and Pb, then the G/V ratio of the plane to cell transition for the ternary alloy Sn - Sb - Pb should be given by the sum of the binary relations, viz.:

$$\left(\frac{G}{V}\right)_{\text{Sb + Pb in Sn}} = \left(\frac{G}{V}\right)_{\text{Sb in Sn}} + \left(\frac{G}{V}\right)_{\text{Pb in Sn}} \tag{4.1.77}$$

They found, however, that the calculated G/V ratio for a Sn - 0.02 at % Sb - 0.002 at % Pb, $\sim 1600\ ^{\circ}\text{C-sec/cm}^2$, was in poor agreement with the experimental G/V ratio, $\sim 2400\ ^{\circ}\text{C-sec/cm}^2$, and concluded that some form of interaction existed between the two solutes in the ternary system, equivalent to decreasing the equilibrium partition coefficient of the lead, k^T_{Pb}, in the ternary alloy.

It is easily shown that k^T_{Pb} cannot vary at such low concentration levels. Indeed, the WAGNER activity coefficient relations reduce to

$$\ln \gamma^L_{Pb} = \ln \gamma^{0L}_{Pb} \tag{4.1.78}$$

$$\ln \gamma^S_{Pb} = \ln \gamma^{0S}_{Pb} \tag{4.1.79}$$

so that Equation 4.1.42 holds, viz.:

$$k^T_{Pb} = \frac{\gamma^{0L}_{Pb}}{\gamma^{0S}_{Pb}} \quad \exp\left[\frac{\Delta g^{SL}_{Pb}}{RT}\right] \tag{4.1.80}$$

Since the terms in the R.H.S. are constants, k_{Pb}^{T} must be a constant.

COLE and WINEGARD also claim that the relationship between G/V and C_0(Sb) is linear at constant C_0(Pb) indicating that Sb does not interact with Pb. This appears to be true; however, the slopes of the G/V versus C_0(Sb) lines vary as a function of C_0(Pb) indicating that Pb interacts with Sb at constant Sb concentration. These results violate, of course, the WAGNER (1952) relation:

$$\epsilon_{PbSb} = \epsilon_{SbPb} \tag{4.1.81}$$

Therefore the data and/or the interpretation, that is, the positioning of the lines through the points, should be questioned.

Moreover, the work of HUNT et al. (1967) showed that, contrary to the suggestion of COLE and WINEGARD, the effect of increasing the Sb content of a tin-base Sn - Sb - Pb alloy was to increase the partition coefficient of lead, k_{Pb}^{T}. However, HUNT et al., while disproving the conclusions of COLE and WINEGARD, left their work open to criticism when they stated that their own findings could be expected from consideration of the tin-rich isotherm of the Sn - Sb - Pb system. Since the isotherm had apparently not been published, they constructed the isotherm by deducing the common planes of the solidus and liquidus of the Sn - Sb and Sn - Pb binary phase diagrams. They stated, in accordance with the theory developed in the present work, that the construction would closely resemble the true isotherm for very dilute alloys. They inserted in the approximate dilute isotherm their experimental partition coefficient k_{Sb}^{T}, determined for rich solutions and generated the partition coefficient k_{Pb}^{T} which progressively increased as the Sb content of the alloy increased. This is contrary, of course, to one of the principle consequences of the present theory, viz., the variation of the partition coefficient decreases with decreasing solute concentration and interaction, from which it follows that the application of solute partition coefficients determined for rich solutions in studies of very dilute alloy systems is incorrect.

Finally, in ternary alloy systems where the liquidus and solidus have been determined by thermal analysis, the tangent-plane theory shows that tie-lines close to the binary limits may be generated to a fair approximation by employing the relevant binary partition coefficients.

4.2 - MICROSEGREGATION MODELS

The object of this section is to review in detail and extend some existing microsegregation models and develop new models to assist in the interpretation of the experimental results.

4.2.1 - MAXIMUM SEGREGATION MODELS

In calculating microsegregation in alloys, the simplest approach is to relate the concentration of solute at the interface in the solid, C_S^*, to the solidified fraction of the system, g, through the relation

$$C_S^* = k_0 C_0 (1 - g)^{k_0 - 1} \qquad (4.2.1)$$

where k_0 is the equilibrium partition coefficient, and C_0, the average solute concentration of the binary alloy. This equation has been derived by many workers including GULLIVER (1922), SCHEUER (1931), HAYES and CHIPMAN (1939), SCHEIL (1942), McFEE (1947) and PFANN (1952). It is based on the following assumptions:

i) back-diffusion in the solid is negligible;

ii) the solute concentration of the liquid is uniform; and

iii) the equilibrium partition coefficient is constant.

The derivation of Equation 4.2.1 consists of applying a simple mass balance about the liquid phase of the system shown in Figure 4.2.1:

$$v_L \, dC_L^* = (C_L^* - C_S^*)(-dv_L) \qquad (4.2.2)$$

where v_L is the volume of liquid. Since the system has unit cross-section,

$$v_L = \lambda - z \qquad (4.2.3)$$

and hence

$$(\lambda - z)\, dC_L^* = (C_L^* - C_S^*)\, dz \tag{4.2.4}$$

Eliminating z and C_L^* through the relations

$$g = z/\lambda \tag{4.2.5}$$

and

$$C_L^* = C_S^*/k_0 \ , \tag{4.2.6}$$

rearranging and integrating Equation 4.2.4

$$\int_{k_0 C_0}^{C_S^*} \frac{dC_S^*}{C_S^*} = (1 - k_0) \int_0^g \frac{dg}{1 - g} \tag{4.2.7}$$

yields Equation 4.2.1. More detailed derivations have been given by PFANN (1952) and others.

The extension of Equation 4.2.1 to two or three dimensional systems is straightforward. Of particular interest in this work is the maximum segregation equation for a spherical volume of liquid enclosed by a dendritic skeleton, Figure 4.2.2. Solidification causes the radius of the liquid volume to decrease from its initial value of r_0 to $r_0 - z$. Writing, as before, the mass balance:

$$v_L\, dC_L^* = (C_L^* - C_S^*)(-dv_L) \tag{4.2.8}$$

and substituting Equation 4.2.5 and the obvious relations:

$$v_L = \frac{4}{3}\pi (r_0 - z)^3 \tag{4.2.9}$$

and

$$g = z/r_0 \tag{4.2.10}$$

gives:

$$\frac{dC_S^*}{C_S^*} = 3\,(1 - k_0)\frac{dg}{1 - g} \qquad (4.2.11)$$

Integrating as before yields:

$$C_S^* = k_0 C_0\,(1 - g)^{3(k_0 - 1)} \qquad (4.2.12)$$

This result generalizes to:

$$C_S^* = k_0 C_0\,(1 - g)^{n\,(k_0 - 1)} \qquad (4.2.13)$$

where $n = 1$ for a one-dimensional system
$n = 2$ for a two-dimensional system
$n = 3$ for a three-dimensional system

It should be noted that g equals the volume fraction solidified in the one-dimensional system only.

If the partition coefficients are assumed constant, as many equations as there are solutes can be written:

$$C_{Si}^* = k_i C_{0i}\,(1 - g)^{n\,(k_i - 1)} \qquad (4.2.14)$$

Several aspects of Equations 4.2.13 and 4.2.14 are noteworthy:

i) it is valid for systems which solidify slowly enough that the diffusion process levels the solute distribution in the liquid phase but not so slowly that diffusion in the solid becomes important;

ii) it is independent of time;

iii) it defines a maximum limit of segregation in the system.

HELLAWELL (1967) presented essentially the same relation as Equation 4.2.13 and discussed some consequences of this relation. However, his treatment is at variance with the one given in the present study in that the exponent n is a fraction instead of an integer.

The influence of the solidification geometry of the system can be appreciated in Figure 4.2.3 in which Equation 4.2.13 has been plotted for an iron alloy containing 15 wt% Mn and 0.25 wt% S. Assuming the dendrite structure is shaped as in Figure 4.2.2, then Equation 4.2.13 predicts the severest microsegregation will occur in the centre of the enclosed volume ($n = 3$).

The geometry of the system has a profound effect on the location at which nucleation of a second phase should occur as shown in Figure 4.2.4. The solubility product wt% Mn x wt% S of the liquid at the interface have been plotted versus the solidified distance for Fe - 15 wt% Mn - 0.25 wt%S systems with $n = 1$, 2 and 3. The equilibrium solubility product calculated from the data of TURKDOGAN et al. (1955) has been superimposed on the diagram. The intersection of this curve with the interface solubility product curves marks the start of precipitation of MnS. This occurs at ($n = 1$, $g = 9.0$); ($n = 2$, $g = 6.8$) and ($n = 3$, $g = 5.4$).

4.2.2 - UNDERCOOLING MODEL

In some cases of solidification, the initial solid does not have the concentration k_0C_0 but a higher concentration C_u. This phenomenon, known as undercooling, occurs if the melt of average composition C_0 cools below its equilibrium freezing temperature, T_e, to a temperature T_u before nucleation of the solid phase, as shown in the phase diagram of Figure 4.2.5. An obvious relation between the liquidus slope m, the undercooling $\Delta T = T_e - T_u$, C_u and k_0C_0 is:

$$m = \frac{\Delta T}{C_0 - C_u/k_0} \qquad (4.2.15)$$

The simplest method of treating solute redistribution in supercooled liquids is to assume no diffusion in the solid and complete mixing in the liquid except for the layer of rejected solute adjacent to the interface. As shown in Figure 4.2.6 this layer accounts for interface equilibrium, but its extent is normally quite limited (a few microns) in rapidly cooled specimens. Since the quantity of solute in the layer is negligible, the effective partition coefficient k_e must be used in place of the equilibrium coefficient k_0:

$$k_e = \frac{C_S^*}{C_b} = \frac{C_u}{C_0} \qquad (4.2.16)$$

in evaluating the mass balance:

$$(1 - g)\ dC_i^* = (C_L^* - C_S^*)\ dg \ . \qquad (4.2.17)$$

Substituting Equation 4.2.16 and rearranging:

$$\frac{dC_S^*}{C_S^*} = (1 - k_e) \frac{dg}{1 - g} \tag{4.2.18}$$

Integrating from $C_S^* = C_u$ at $g = 0$ to $C_S^* = C_S^*$ at $g = g$ yields

$$C_S^* = C_L^* (1 - g)^{k_e - 1} \tag{4.2.19}$$

or:

$$C_S^* = k_e C_0 (1 - g)^{k_e - 1} \tag{4.2.20}$$

which is effectively the relation derived by PFANN (1958).

Substituting Equation 4.2.15,

$$C_S^* = k_0 \left[C_0 - \frac{T}{m} \right] \left[1 - g \right]^{\left(k_0 - 1 - \frac{k_0 \Delta T}{m C_0} \right)} \tag{4.2.21}$$

When $\Delta T = 0$, this relation reduces to Equation 4.2.1 for maximum segregation; when $\Delta T = \Delta T_{max} = mC_0 \left[1 - \frac{1}{k_0} \right]$, it reduces to

$$C_S^* = C_0 \tag{4.2.22}$$

in which case no segregation of solute occurs during solidification. For a n-dimensional solute redistribution Equation 4.2.21 generalizes as shown in Section 4.2.1 to:

$$C_S^* = k_0 \left[C_0 - \frac{T}{m} \right] \left[1 - g \right]^{n \left(k_0 - 1 - \frac{k_0 \Delta T}{m C_0} \right)} \tag{4.2.23}$$

This relation will be used in the interpretation of solute distributions in Section 7.1.

4.2.3 - TERNARY SOLIDIFICATION MODEL

The mathematical models reviewed in the previous sections have been extremely useful to the understanding of microsegregation. However, these models have limited applicability and attempts to generalize and refine them have involved approximations which leave the validity of the models open to question. One particularly serious weakness is that no allowance is made for diffusive and constitutional interaction of solutes in multicomponent solutions, while in reality interface concentrations are coupled through equilibrium relations and the diffusive fields in both phases must tie in with the interface velocity.

A general, rigorous treatment of diffusional solute redistribution resulting from the solidification of a ternary system does not appear to have been published. However, some work in this direction has been done by KIRKALDY (1970). In the present investigation an approximate analysis predicated on the following assumptions and constraints was made:

i) the solidifying system is unidimensional and finite;

ii) the solid-liquid interface is planar;

iii) local equilibrium obtains at the interface;

iv) the on-diagonal coefficients of the diffusion matrix are finite and constant for both phases;

v) the off-diagonal coefficients are neglected;

vi) the interface temperature is known as a function of time;

vii) the tie-lines of the phase diagram are known.

The system is shown in Figure 4.2.7. As the interface advances in the Z direction, solute diffuses down the concentration gradients in both phases and is reflected at the impermeable boundaries $Z = 0$ and $Z = \lambda$. The interface progresses by ΔZ_0 in a time interval τ and the solid phase incorporates the diffusion sources contained in region BCDE. There remains to dissipate the solute contained in the region ABEF. This amount of solute is approximately the amount contained in region ABEH:

$$\Delta Z_0 \left[C_L^*(t) - C_S^*(t) \right] \tag{4.2.24}$$

where $C_L^*(t)$ and $C_S^*(t)$ are solute concentrations at the interface on the liquid and solid sides, respectively, of the interface, and t is real time. It is now taken that this excess of solute is rejected into the liquid by maintaining the liquid side of the interface at $C_L^*(t+\tau)$ and the solid side at $C_L^*(t+\tau)$ during the time interval τ, thereby allowing an amount of solute M_L to enter the liquid phase and an amount M_S to enter the solid phase. The interfacial mass balance demands that

$$\Delta Z_0 (C_L^* - C_S^*) = M_L + M_S \tag{4.2.25}$$

For a ternary system, two mass balances must hold simultaneously:

$$\Delta Z_0 \, (C^*_{L1} - C^*_{S1}) = M_{L1} + M_{S1} \qquad (4.2.26)$$

$$\Delta Z_0 \, (C^*_{L2} - C^*_{S2}) = M_{L2} + M_{S2} \qquad (4.2.27)$$

The concentration variables are related by a tie-line of the solid + liquid phase field at the appropriate interface temperature. From Phase Rule considerations, the interfacial compositions C^*_{S2}, C^*_{L1}, C^*_{L2} are fixed if C^*_{S1}, the temperature and the pressure are specified.

The problem, therefore, is to find simultaneously the correct tie-line representing the interface equilibrium and the time τ required for a given ΔZ_0.

During the small interval of time τ , the total amount of solute, M_τ , entering a phase is found by integrating the instantaneous interface flux J_t:

$$M_\tau = \int_0^\tau J_t \, d_t \qquad (4.2.28)$$

The interface flux at a given time t is

$$J_t = -D \left. \frac{\partial C}{\partial z} \right|_{z=0} \qquad (4.2.29)$$

where z is the distance from the interface in a given phase.

A physical example of the solidification system under study is given Figure 4.2.8. Two dendrites of solid S, assumed to be sheets of infinite extent in the direction normal to the plane of the figure, grow as indicated into the liquid phase L. The boundaries at $Z = 0$ and $Z = \lambda$ are effectively impermeable as the diffusion fluxes are locally of equal magnitude and opposite sign. The interface is permeable and lets solute in and out.

For mathematical convenience each phase is held to comprise two subsystems. The distance coordinate in each system extends from $z = 0$ to $z = a$. In Subsystem I, one boundary is impermeable, the other is kept at zero concentration and there is an initial distribution of solute $C'(z)$. Subsystem II, one boundary is impermeable, the other is maintained at concentration C_a and the initial concentration is zero.

Solutions of the diffusion equation

$$\frac{\partial C}{\partial t} = D \frac{\partial^2 C}{\partial z^2} \qquad (4.2.30)$$

respecting the initial and boundary conditions of Subsystems I and II have been given by CARSLAW and JAEGER (1947):

SUBSYSTEM I

$$t = 0, \qquad C_I = C'(z)$$

$$t > 0, \quad z = 0, \; \partial C_I/\partial z = 0$$

$$z = a, \qquad C_I = 0$$

$$C_I = \frac{1}{2\sqrt{\pi D\tau}} \int_0^a C'(z') \sum_{n=-\infty}^{\infty} (-1)^n \left\{ \exp\left[- (z - z' - 2na)/4D\tau \right] + \exp\left[- (z + z' - 2na)/4D\tau \right] \right\} dz' \tag{4.2.31}$$

SUBSYSTEM II

$$t = 0, \quad z = 0, \quad C_{II} = 0$$

$$t > 0, \quad z = 0, \partial C_{II}/\partial z = 0$$

$$z = a, \qquad C_{II} = C_a$$

$$C_{II} = C_a \left\{ \sum_{n=0}^{\infty} (-1)^n \operatorname{erfc}\left[\frac{(2n+1)a - z}{2\sqrt{D\tau}} \right] + \sum_{n=0}^{\infty} (-1)^n \operatorname{erfc}\left[\frac{(2n+1)a + z}{2\sqrt{D\tau}} \right] \right\} \tag{4.2.32}$$

As Equation 4.2.30 is a linear differential equation, the sum of Equations 4.2.31 and 4.2.32 is the solution of Equation 4.2.30. Thus the concentration C in a given phase at position z and time τ is:

$$C = C_I + C_{II} \tag{4.2.33}$$

The computation algorithm is as follows:

i) choose ΔZ_0; it remains fixed subsequently;

ii) advance interface by ΔZ_0;

iii) compute initial solute distributions;

iv) choose τ and C^*_{S1} ;

v) compute C^*_{S2}, C^*_{L1} and C^*_{L2} at time t;

vi) compute solute rejected in time τ : M_{L1}, M_{L2}, M_{S1} and M_{S2};

vii) compute closure functions:

$$f_1 = \Delta Z_0 \, (C^*_{L1} - C^*_{S1}) - (M_{L1} + M_{S1})$$

$$f_2 = \Delta Z_0 \, (C^*_{L2} - C^*_{S2}) - (M_{L2} + M_{S2})$$

If the choice of τ and C^*_{S1} is correct,

$$f_1 = f_2 = 0$$

and proceed to step ii). If not, go to step iii). A computer program was written to perform the calculations. It is listed in Appendix A. 2.

For the preliminary computations it was assumed that the initial distribution was uniform rather than arbitrary: the total amount of solute having entered the system during the time interval τ , M_τ , was then calculated from the relation given by CARSLAW and JAEGER (1947):

$$M_\tau = 2M_\infty \left(\frac{D\tau}{a^2}\right)^{\frac{1}{2}} \left[\pi^{-\frac{1}{2}} + 2\sum_{n=1}^{\infty} (-1)^n \, \mathrm{ierfc}\left(\frac{na}{(D\tau)^{\frac{1}{2}}}\right)\right] \quad (4.2.34)$$

where M_∞ is the total amount of solute in the system after infinite time and is given by:

$$M_\infty = aC_a \quad (4.2.35)$$

Equation 4.2.34 can be rewritten:

$$M_\tau = 2C_a (D\tau)^{\frac{1}{2}} \left[\pi^{-\frac{1}{2}} + 2\sum_{n=1}^{\infty} (-1)^n \, \mathrm{ierfc}\left(\frac{na}{(D\tau)^{\frac{1}{2}}}\right)\right] \quad (4.2.36)$$

The integral of the error function complement, ierfc (y), can be evaluated from:

$$\mathrm{ierfc}\,(y) = \pi^{-\frac{1}{2}} \exp(-y^2) - y\,\mathrm{erfc}\,(y) \quad (4.2.37)$$

The following data were used in the computations for the solidification of a pseudo-ternary system, i.e., where both solute had identical properties:

$k_0 = 0.8$

$D_L = 10^{-5}$ cm^2/sec

$D_S = 10^{-8}$ cm^2/sec

$C_0 = 0.15$ wt. fraction

$a = 100$ microns

The interface temperature was lowered at a rate of 10 °C/sec. The results are shown in Figure 4.2.9; the solute distributions in both phases are plotted at a point in time at which one-fifth of the specimen was solid; the loci of the interface concentrations in both phases from the beginning of the solidification event are also plotted. The initial interface velocity, V, was approximately 2.4 microns/sec; the velocity increased as solidification proceeded and levelled off at 32 microns/sec. The D_L/V ratio was approximately:

$$10^{-5}/0.0032 = 3 \times 10^{-3}\text{cm} = 30 \text{ microns}$$

and matched roughly the characteristic distance of the liquid solute distribution.

The amount of solute entering a given phase at each step was computed from Equation 4.2.34 rather than Equation 4.2.28. This was necessary to reduce the computation time. As a result, however, the mass balance was unsatisfactory.

It appears that the present approach to the solution of the general microsegregation problem has reached an impasse: the accuracy of the results can only be increased at the cost of markedly increasing the already inordinately long computing time. Indeed, the computations described above required 10 minutes on a fast computer (CDC 6400); to complete the solution would have required almost 1 hour of computing time and would have been pointless since the mass balance constraint would only have been approximately fulfilled.

However, one observation of considerable import is emphasized by these calculations: the interface concentration rises continuously throughout the solidification process. This means that the criteria proposed by BRODY and FLEMINGS (1966) and reported in Section 2.3.2 of the literature survey,

$$\alpha_S = \frac{D_S t_f}{\lambda^2} \gg 1 \text{ ; complete diffusion in solid}$$

$$\alpha_L = \frac{D_L t_f}{\lambda^2} \gg 1 \text{ ; complete diffusion in liquid}$$

are only rough approximations. Indeed, the criteria are equivalent to the familiar expression for the average distance z, travelled by an atom of diffusivity D, in time t:

$$z = 2\sqrt{Dt}$$

which is also the characteristic value of Equation 6.1.2, a diffusion equation applicable to a problem where the boundary conditions at the interface are fixed, e.g., in a semi-infinite diffusion couple. Therefore the use of BRODY and FLEMINGS' criteria in systems where the boundary conditions vary may be misleading.

4.3 - FORMATION MECHANISM OF SULPHIDE INCLUSIONS

The nature of the solidification products arising from the equilibrium solidification of iron-base Fe - Mn - S alloys was reviewed in Section 2.3. The present section is concerned with the formation mechanism of sulphide inclusions. A qualitative discussion of the two major steps in the inclusion formation process, i.e., the nucleation step and the growth step, is given in the following subsections.

4.3.1 - INCLUSION NUCLEATION

For clarity the discussion is based on a particular section of the Fe - Mn - MnS - FeS constitution diagram, given in Figure 4.3.1, which runs from the Fe - 15 wt% Mn binary to the MnS corner. It is assumed here that the solidification path lies entirely in this section. There are two distinct cases of inclusion formation:

i) if the average composition of the melt is less than the eutectic value E in Figure 4.3.1, "secondary" sulphide inclusions form during solidification when the manganese and sulphur concentrations of the liquid phase exceed the eutectic value;

ii) if the average composition lies to the right of point E, "primary" manganese sulphides precipitate in the liquid.

In the first case, nucleation of β_{MnS} inclusions probably occurs heterogeneously at the solid-liquid interface where the liquid is generally richest in solute and the energetic conditions most favourable. In the second case, nucleation presumably occurs at the surface of adventitious nucleants circulating in the liquid phase. Hence in both cases the principles of heterogeneous nucleation apply.

The stability of an embryo forming on the solid surface of the interface depends on the radius of curvature r_c and the stability of the line of contact AB illustrated in Figure 4.3.2. According to nucleation theory (CHALMERS, 1964) the radius of curvature must be equal or greater than the critical radius for a given degree of supersaturation. As the supersaturation approaches zero, the critical radius tends to infinity and hence there must exist a finite degree of supersaturation. The probability of nucleating an inclusion in the form of a spherical cap on the interface is greater than that of nucleating a sphere in the bulk liquid since fewer atoms are required to form a spherical cap of critical radius. The condition of stability of the line of contact is satisfied if the horizontal components of the surface tension balance. From Figure 4.3.2 it is easily seen that a horizontal force balance yields the equilibrium condition:

$$\frac{\sigma_{SL} - \sigma_{SI}}{\sigma_{LI}} = \cos\theta \qquad (4.3.1)$$

where σ_{SL}, σ_{SI} and σ_{LI} are the surface free enthalpies of the interface between solid and liquid, solid and inclusion, and liquid and inclusion, and θ is the contact angle. Thus the inclusion is stable if the balance of surface tension components is such that $180^{\circ} > \theta > 0^{\circ}$. If the contact angle is less than zero, the inclusion is unstable since the surface free enthalpy decreases continuously as the inclusion spreads over the interface; if the contact angle is greater than 180°, any contact between the inclusion and solid increases the surface free enthalpy.

4.3.2 - INCLUSION GROWTH AND TRANSPORT

Once nucleation has taken place, primary inclusions grow from the liquid phase by a simple diffusion process described by Fick's laws. In the case of secondary inclusions, the growth process is complicated by the presence of a moving solid-liquid interface which is rejecting solute. Presumably the inclusions grow by diffusion parallel to the interface if there are steep solute gradients at the interface and by diffusion of solute from the bulk liquid if the solute gradients are small. Depending on the magnitude and direction of the buoyancy force exerted on the inclusion as a result of the density difference between the inclusion and the melt, the contact angle and the rate of growth of the inclusion relative to that of the interface, one of three things happens:

i) the inclusion grows and is pushed by, moves along or floats away from the interface. This occurrence is favoured by a low inclusion growth rate, a low interface velocity and a high contact angle;

ii) the inclusion grows as a stringer in the same direction as the interface. This mode of growth, not unlike that of an ordinary eutectic, occurs if the contact angle is around 90^{o} and if the inclusion grows at the same rate as the interface;

iii) the inclusion is trapped and overgrown by the interface. This event is favoured by a high inclusion growth rate, a high interface velocity and a low contact angle.

UHLMANN and CHALMERS (1964) conducted a theoretical and experimental investigation into the interaction between particles and an advancing solid-liquid interface which has considerable bearing on the present problem. The matrix materials used were: salol, thymol, orthoterphenyl and water; the foreign particles included the following solid materials: graphite, magnesium oxide, silt, silicon, tin, diamond, nickel, zinc, iron oxide and silver oxide. For a given particle type, they observed a critical velocity below which the particles were repulsed by the interface and above which they were overgrown by the advancing interface. The critical velocity for particles smaller than about 15 microns in diameter was found to be independent of the size of the particles. However, for particles several hundred microns in diameter, the critical velocity was found to be smaller for larger particles. Moreover, the critical velocity was found to be shape dependent, being smaller for particles presenting a flatter face to the solid-liquid interface.

From these observations, UHLMANN and CHALMERS suggested that:

i) repulsion of the particle occurs if the particle-solid interfacial free enthalpy, σ_{SP}, is greater than the sum of the particle-liquid and liquid-solid interfacial free enthalpies, σ_{LP} and σ_{SL}:

$$\text{REPULSION: } \sigma_{SP} > \sigma_{LP} + \sigma_{SL} \qquad (4.3.2)$$

ii) entrapment occurs unless the liquid can diffuse at a sufficiently rapid rate to the growing solid behind the particle.

They also considered the relation between the repulsion problem and nucleation. Comparing the equilibrium condition for nucleation, Equation 4.3.1, and the repulsion condition, Equation 4.3.2, it appears that the conditions are mutually exclusive, i.e., the particles which nucleate cannot be repulsed, since for nucleation the contact angle θ must be less than zero and hence cos θ must be less than unity. They resolved this apparent paradox by pointing out that the nucleating particle and the solid-liquid interface should be in a low σ_{SP} configuration, whereas contact between a stationary particle and an advancing interface should be in a random and presumably higher σ_{SP} configuration.

Little research appears to have been conducted on inclusion pushing by an interface in high temperature metal systems. The experiments of the present investigation were carried in part to fill the need for information in this area. As will be seen in Chapter 6, transport of sulphide inclusions by flotation and interface pushing were observed. Some experiments were also especially designed to reveal the interaction between a solid-liquid interface and particles of inert material such as ZrO_2 (Section 6.4.1).

4.4 - SOME ASPECTS OF DENDRITE ARM SPACING

It is possible to extend the field of influence concept of RUTTER and CHALMERS (1953) to account for the variation of dendrite arm spacing with variables other than the average solute concentration C_0, the growth velocity V, and the temperature gradient in the liquid G, such as the partition coefficient k_0, the solute diffusivity in the liquid phase D_L, the latent heat of fusion h and the thermal conductivity K. As seen from Equation 2.3.11 the solute build-up $C_L - C_0$ at a distance z in front of a solid-liquid interface in a steady-state system is:

$$C_L - C_0 = C_0 \left[\frac{1 - k_0}{k_0} \right] \exp \left[- \frac{V}{D_L} z \right] \qquad (4.4.1)$$

Hence the smaller k_0 and the larger D_L, the greater the solute build-up at a given point, the larger the constitutional field of influence and the larger the dendrite arm spacing. Clearly, the thermal conductivity acts in the same direction as the temperature gradient. The higher K, the greater the amount of heat removed from the region of the projection. This reduces its thermal field of influence and hence the dendrite arm spacing. The magnitude of the latent heat of fusion also affects the thermal field of influence: a high h favours large dendrite arm spacings.

It is possible to advance one step farther and apply dimensional analysis in the hope of obtaining a general, dimensionally correct and physically coherent relation between the dendrite arm spacing and the various intrinsic variables characteristic of an alloy system (solute diffusivity, heat conductivity, heat of fusion, partition coefficient, and liquidus slope) and the extrinsic variables of a controlled solidification experiment (solute concentration, temperature gradient and growth velocity).

The relation between dendrite spacing, d, and the various parameters mentioned above can be expressed as

$$d = d\,(C_0,\ D,\ G,\ h,\ K,\ m,\ V) \tag{4.4.2}$$

where:
C_0 = average solute concentration $[\mathrm{g/cm^3}]$
D = solute diffusivity $[\mathrm{cm^2/sec}]$
G = temperature gradient $[\mathrm{deg/cm}]$
h = heat of fusion $[\mathrm{cal/cm^3}]$
K = thermal conductivity $[\mathrm{cal/cm\text{-}deg\text{-}sec}]$
m = liquidus slope $[\mathrm{deg\text{-}cm^3/g}]$
V = growth velocity $[\mathrm{cm/sec}]$

Equation 4.4.2 may be written

$$d = \phi\, C_0^{\alpha}\, D^{\beta}\, G^{\gamma}\, h^{\delta}\, K^{\epsilon}\, m^{\zeta}\, V^{\eta} \tag{4.4.3}$$

where ϕ is a dimensionless coefficient. The exponents α, β, γ, δ, ϵ, ζ, η are not to be confused with parameters used elsewhere in the text. Equation 4.4.3 must be dimensionally homogeneous. Then

$$M^0 L^1 t^0 T^0 H^0 = (M^{\alpha} L^{-3\alpha})(L^{2\beta} t^{-\beta})(T^{\gamma} L^{-\gamma})(H^{\delta} L^{-3\delta})$$
$$(H^{\epsilon} L^{-\epsilon} T^{-\epsilon} t^{-\epsilon})(T^{\zeta} L^{3\zeta} M^{-\zeta})(L^{\eta} t^{-\eta}) \tag{4.4.4}$$

where:

M = mass [g]
L = length [cm]
t = time [sec]
T = temperature [deg]
H = heat [cal]

Equating exponents of like units and rearranging yields:

$$\beta = 1 - \alpha \tag{4.4.5}$$

$$\delta = -\alpha - \gamma \tag{4.4.6}$$

$$\epsilon = \alpha + \gamma \tag{4.4.7}$$

$$\zeta = \alpha \tag{4.4.8}$$

$$\eta = -1 - \gamma \tag{4.4.9}$$

Substituting Equations 4.4.5 to 4.4.9 into 4.4.3 gives:

$$d = \phi\, C_0^{\alpha}\, D^{1-\alpha}\, G^{\gamma}\, h^{-(\alpha+\gamma)} K^{\alpha+\gamma}\, m^{\alpha}\, V^{-(1+\gamma)} \tag{4.4.10}$$

The constant ϕ can be determined solely by experiment. However, the exponents α and γ can be bracketed by considering the "field of influence" concept which agrees, of course, with experimental findings to date. Indications are that the arm spacing varies directly as C_0, D, h, m and inversely as G, K and V. Therefore:

$$1 > \alpha > 0 \tag{4.4.11}$$

$$0 > \gamma > -1 \tag{4.4.12}$$

and:

$$|\gamma| > |\alpha| \tag{4.4.13}$$

are the constraints of Equation 4.4.10. For example, if the relation between arm spacing and growth velocity appears parabolic,

$$\gamma = -1/2 \tag{4.4.14}$$

Assuming

$$\alpha = +1/3 \tag{4.4.15}$$

Equation 4.4.10 becomes

$$d = \phi \, C_0^{1/3} D^{2/3} G^{-1/2} h^{+1/6} K^{-1/6} m^{1/3} V^{-1/2} \tag{4.4.16}$$

or regrouping terms

$$d = \phi \left[D^4 m^2 \frac{h}{K} \right]^{\frac{1}{6}} \left[\frac{C_0^{2/3}}{GV} \right]^{\frac{1}{2}} \tag{4.4.17}$$

$$d = \phi' \sqrt{\frac{C_0^{2/3}}{GV}} \tag{4.4.18}$$

If the relation between arm spacing and growth velocity appears cubic

$$\gamma = -2/3 \tag{4.4.19}$$

Assuming, as before,

$$\alpha = +1/3 \tag{4.4.20}$$

$$d = \phi \left[\frac{D^2 h\, m}{K} \right]^{\frac{1}{3}} \left[\frac{C_0}{G^2 V} \right]^{\frac{1}{3}} \tag{4.4.21}$$

or:

$$d = \phi'' \left[\frac{C_0}{G^2 V} \right]^{\frac{1}{3}} \tag{4.4.22}$$

For multicomponent solutions, spacing relations such as Equation 4.4.21 could be generalized, in a first approximation, to

$$d = \sum_i \phi_i \left[\frac{D^2_i\, h_i\, m_i}{K_i} \right]^{\frac{1}{3}} \left[\frac{C_{0i}}{G^2 V} \right]^{\frac{1}{3}} \tag{4.4.23}$$

It is clear from this discussion and the review of literature in Section 2.6 that experiments to determine the influence of various parameters on dendrite arm spacing have little value unless all the parameters are taken into consideration simultaneously. The controversy over the effect of solute concentration on dendrite arm spacing can be explained by assuming that the experimenters unknowingly varied parameters other than C_0, which had a greater but contrary influence on the dendrite arm spacing.

The controlled directional solidification apparatus designed for this work is well suited for experiments on dendrite arm spacing since the two most important parameters G and V can be measured with accuracy and varied independently to a certain extent. In Chapter 6 of the present investigation, experiments on the variation of dendrite arm spacing with a most important solidification variable, namely solidification rate, are described. A special effort was made to maintain other variables such as temperature gradient and concentration at a constant value.

CHAPTER 5

EXPERIMENTAL TECHNIQUES

5.1 - SOLIDIFICATION APPARATUS

The construction of an apparatus designed especially for controlled directional solidification of iron-base alloys is described in this section.

The apparatus is similar in principle to that of DIEHL et al. (1965) who solidified steel rods in a controlled and directional manner by progressive withdrawal from a vertical resistance furnace. This work was reviewed in Section 2.8.

The work of NAVIAS (1957) on hydrogen-protected molybdenum-wound furnaces was taken into account in the design of the furnace which is shown in cross-section in Figure 5.1.1. The furnace drum of stainless steel encased alumina powder insulation (Norton 46 grit). The alumina furnace tube (McDanel AP35) was held in place at the top and bottom by O-ring seals. The bellows at the top allowed for extension of the tube during the heating-up period. Three coils of 0.050 in. diameter molybdenum wire were cemented to the tube with a slurry of Alundum powder and water, and star-connected to brass feedthroughs in the bottom and plate of the drum. The temperature in the vicinity of the windings was monitored by a movable Pt/Pt - 13% Rh thermocouple in an alumina sheath. A flowing nitrogen - 20% hydrogen gas mixture protected the molybdenum windings from oxidation. Hydrogen hydroxide was supplied to the top and bottom plates of the drum to cool the O-ring seals and the nylon insulating bushings of the electrical feedthroughs. During an experiment, the furnace travelled up the fixed alumina tube containing the specimen, thereby forcing the solid-liquid interface of the specimen to move upwards. The maximum operating temperature inside the working tube was 1700°C.

Figure 5.1.2 offers an overall view of the solidification apparatus. The furnace was hung from a cable supported by pulleys (visible at the top of the photograph) and attached to the cylindrical counterweight on the left. The furnace was driven by a Zeromax variable-speed motor and lead-screw assembly coupled to the counterweight. The voltage impressed on the motor was stabilized by a Sola constant voltage transformer. The range of furnace velocities was 0 - 1000 mm/hr. The working tube was connected to the gas cylinders on the left and to the vacuum pump in the foreground of Figure 5.1.2 through the chamber on the platform over the furnace. A titanium getter located inside the chamber was used to absorb traces of oxygen and nitrogen in the atmosphere of the working tube after it had been evacuated and backfilled with inert gas. The power cables, water cooling tubing to the feedthroughs, and the working tube appear in detail in Figure 5.1.3. The flow of water was stabilized with a Watts C-5 pressure regulator.

5.2 - FURNACE POWER SUPPLY

The furnace was powered by a 7500 watt supply. As shown in Figure 5.2.1, it comprised three star-connected autotransformers operating off the 3-phase, 208 volt (line to line), 60 hertz main line. Each autotransformer slider was protected by a fuse and connected to a furnace winding through an ammeter. This circuitry ensured an independent regulation of power to each winding.

Due to the good line-voltage stability, the furnace temperature normally fluctuated less than $2^{\circ}C$ during the time required for typical solidification experiments.

5.3 - SPECIMEN, CRUCIBLE AND THERMOCOUPLE ASSEMBLY

A sectional view of the specimen, crucible and thermocouple assembly used in preliminary attempts to measure temperature gradients during solidification is given in Figure 5.3.1. The crucible was a Degussit AL 23 alumina tube, 8 mm O.D., 5 mm I.D. and 400 mm long. The thermocouple protection sheath was a Degussit AL 23 single-bore tube, 1.5 mm O.D. and 1.0 mm I.D. The Pt - 20% Rh leg of the thermocouple ran up along the outside of the crucible and down through the axial sheath to the junction. The Pt - 5%Rh leg extended down to the thermocouple feedthrough in the cap of the working tube. The pieces of the specimen were supported by an alumina tube resting on a copper pedestal.

The results of the temperature measurements were unsatisfactory at first. At the outset of Experiment 2, for example, the thermocouple indicated a temperature 100°C in excess of the alloy melting point. After the solidification run, it was found that the thermocouple junction was 1 cm below the initial solid-liquid interface. The temperature gradient was also inordinately shallow and fairly constant at about 2°C/cm. Thermal conductivity effects were suspected at first but it was found difficult to rationalize the results in these terms.

The possibility of a breakdown in the electrical insulating properties of the alumina thermocouple sheath was investigated by measuring the resistance between two platinum wires 4 mm apart and in contact with an alumina sheath as shown in Figure 5.3.2. The resistance decreased from practically infinity at room temperature to 20 ohms in the working range 1500 - 1600°C. It was then reasoned that the alumina sheath in the high temperature region between the initial solid-liquid interface and the melt surface acted as an intermediate conductor in the thermocouple circuit, thereby smearing the point junction over a distance of several centimeters and giving rise to unexpectedly high temperature readings and shallow gradients.

In later solidification experiments the thermocouples were inserted in a transverse sheath as shown in Figures 5.3.3 and 6.3.2 The holes in the alumina crucible accommodating the alumina thermocouple sheath were pierced with a Raytheon Ultrasonic Impact Grinder. The grinding slurry, consisting of boron carbide powder and hydrogen hydroxide, was applied to the crucible with a mild steel shaft. The grinding operation produced clean holes and took only a few seconds to complete.

The fairly uniform temperature across the alumina sheath and thermocouple junction nullified the intermediate conductor effect of the alumina and the temperature measurements turned out to be much more plausible: the gradients in the solid and liquid adjacent to the interface of a Fe - 0.5 wt% Mn - 0.03 wt% S - 0.4 wt% C alloy solidifying at a rate of 50 mm/hr are shown in Figure 5.3.4. It should be noted that in order to avoid electrical interference effects, the furnace power was cut during the two seconds it took to measure the thermocouple output.

5.4 - THERMOCOUPLE CIRCUITRY

The circuit shown in Figure 5.4.1 was designed for stability, precision and convenience in the measurement of a thermocouple electromotive force. Two such circuits were used in the experimental set-up: one for the winding thermocouple and one for the specimen thermocouple. Both cold junctions of the Pt - 5% Rh/Pt - 20% Rh thermocouple were maintained at 0^oC by immersion in the well of a Joseph Kaye Model 2110 Ice-Point Reference Standard. The negative copper transmission line went to the millivolt recorder, and the positive one to the bucking circuit. A double-throw on-off-on switch gave a choice of bucked signal (B), open circuit (O) or normal signal (N). The bucking potential was set by putting the switch in position O and manipulating variable resistor R_1 until it balanced the preset potential of an external precision potentiometer connected at points X and Y.

5.5 - SOLIDIFICATION TECHNIQUE

The furnace was raised to its topmost position, the axial temperature was set and the system was flushed with Matheson Prepurified Grade (99.998%) Argon. The specimen assembly was inserted in the working tube, the gas flow arrested, the tube sealed and the specimen thermocouple wires connected. The system was pumped down to 0.01 mm Hg and backfilled with argon several times.

The gas pressure of the system was balanced with the atmospheric pressure and the titanium getter was heated to collect impurities of oxygen and nitrogen in the gas. The furnace was lowered to its bottommost position which caused melting of the upper 10-15 cm of the specimen, and the furnace was allowed to come to thermal equilibrium. The furnace drive motor was activated, raising the furnace at a preset rate. The furnace having travelled the required distance, normally 5-10 cm, the thermocouple wires were disconnected, the bottom cap was loosened and the whole assembly was dropped directly into a metal tube filled with water.

For the sake of clarity, a photograph of a typical specimen (without thermocouple wires) is given in Figure 5.5.1.

5.6 - PREPARATION OF SOLIDIFICATION SPECIMENS

The materials used in the preparation of the Fe - Mn - S - C alloys were U.S. Steel Ferrovac - E iron, Union Carbide AUC graphite, iron sulphide and master alloys of Fe - 30 wt% Mn. Typical analyses of the materials are given in Table 5.6.1. The iron-manganese master alloys were prepared from U.S. Steel Ferrovac - E iron and A.D. McKay manganese, and cast into 40 g buttons using an Edwards Argon-Arc Melting Unit. The iron-sulphide was obtained by exposing thermocouple-grade iron wire, 0.015 inch in diameter, to an atmosphere of hydrogen sulphide at 900^{o}C for 24 hours.

When several specimens of the same composition were desired, the facilities of an Arthur D. Little Crystal Growing Furnace were used. The materials for a 120 g melt were placed in an alumina crucible and induction melted under an argon atmosphere of 30 p.s.i. An exploded view of the casting assembly designed to fit in the chamber of the furnace is given in Figure 5.6.1. The melt was bottom-poured by raising the alumina stopper rod and chilled in a split copper mold.

When at most two specimens were desired, the Edwards Argon Arc Melting Unit was used. About 40 g of alloy materials were melted and cast in a trough in the water-cooled copper hearth of the unit.

The resulting ingots were swaged into 0.175 in. dia. rod.

5.7 - METALLOGRAPHIC PREPARATION OF SPECIMENS

The experimental techniques for observing microsegregation commonly encountered in the literature review were autoradiography and metallography. The autoradiographic technique consists of adding a radioactive tracer to the melt or neutron-pile irradiating the cast specimen to induce isotope activity. This is followed by metallographic preparation and exposure of the active specimen on photographic plates to produce autoradiographs where variations in blackening reflect the variations in the solute concentration. The concentrations can then be determined quantitatively by microdensitometry. In the metallographic technique, specimens are metallographically prepared and tinted with reagents sensitive to concentration variations or etched with reagents sensitive to structure variations caused by the inhomogeneous distribution of solute. The solute concentrations can then be determined quantitatively by electron-probe microanalysis.

The metallographic approach was taken in this investigation because of the various complications inherent to the autoradiographic technique. The heat treatments and reagents used to reveal the microsegregation patterns are described in the following paragraphs. Some of the heat treatments and reagents were already available in the literature; others had to be especially devised.

The specimens were sectioned with a jeweller's saw and mounted in lucite. After rough-grinding on a No. 80 emery belt, the specimens were hand-ground on Nos. 220, 320, 400 and 600 metallographic emery papers lubricated with water and on a wax lap charged with 30 micron γ-alumina. Polishing was carried out on 6, 1 and 1/4 micron diamond-impregnated cloths lubricated with kerosene. The specimens were cleansed by swabbing with petroleum ether, washing in a detergent solution and rinsing in distilled water.

The segregation patterns in the iron-high manganese-sulphur alloys (13 wt% Mn, 0.25 wt% S) were revealed by immersing the freshly polished specimens for approximately 10 seconds in a solution of distilled water saturated with hydrogen sulphide. As shown in Figures 5.7.3 and 6.3.23 various regions of the specimen were sulphidized to a degree commensurate with their composition. As the thickness of the sulphide film increased in a given area, its appearance alternated between light and dark. Under white light, manganese sulphide inclusions appeared silvery and the manganese segregation was outlined in brown and white. In many instances, the colouring and contrast were markedly increased by exposing the specimen to the atmosphere for several hours. The contrast between the high and low manganese regions was found to lessen with decreasing average manganese concentration. In spite of considerable experimentation, no contrast was obtained in alloys containing less than 7 wt% Mn. Metallographic etching and tinting solutions commonly found in the literature (KEHL, 1949; HABRAKEN and de BROUWER, 1966) were tried without success on alloys containing less than 7 wt% Mn.

Recourse was made to heat treatment in the case of alloys containing both manganese and carbon. An austenitizing treatment (20 min at 900°C) followed by continuous cooling at a rate of 5°C/min proved effective in revealing the microsegregation of alloys containing 0.4 wt% C and 3 wt% Mn. As shown in Figure 6.3.3, ferrite, pearlite and martensite appeared in the dendrite cores (in dark) and austenite containing some martensite was retained in the enriched regions (in light). An austenite etching solution proposed by SCHUMANN (1962) was employed to confirm the presence of austenite in the enriched regions of the specimen. The composition of the solution is:

2 parts — 15 vol % saturated $(NH_4)_2S_2O_8$ solution in water
2 parts — 50 vol % HCl in ethanol
1 part — saturated orthonitrophenol solution.

Continuous cooling treatments did not reveal the microsegregation patterns of alloys containing 0.5 wt% Mn and 0.4 wt% C. However, the treatments produced ferrite bands at the austenite grain boundaries, Figure 5.7.1 and extensive ferrite regions around inclusions, Figure 5.7.2.

An isothermal-transformation treatment similar to the one used by KATTAMIS and FLEMINGS (1965) in their work on low-alloy steels was applied to the low-manganese (0.5 wt%) - carbon alloys. The treatment consisted of austenitizing the specimen for 20 minutes in a chloride-carbonate salt (Park Chemical, K-2) at 840°C, quenching to 600°C in the same salt, holding isothermally for 3 seconds and quenching to room temperature. The relevant isothermal transformation diagrams have been given by McGANNON (1964). As a result of the delay in the transformation of austenite to ferrite and pearlite brought about by the presence of manganese, the manganese-rich regions of the specimen contained more martensite than the manganese-poor regions. The differences in structure were revealed by suitable etchants such as picral or nital and outlined the dendritic structure as shown in Figure 6.3.1. LEGER and DETREZ (1965) employed BEAUJARD's reagent to reveal the microsegregation patterns in their alloy steels. The reagent (BEAUJARD, 1952; BEAUJARD, 1955) consists of:

15 g	$NaNO_3$
40 g	NaOH
80 cm^3	H_2O

and is heated to 100°C for use. The structure of the specimen must be homogeneous if the reagent is to give satisfactory results and an austenitizing treatment at a temperature of $Ac_3 + 50^{\circ}C$ for several minutes followed by a water quench is recommended to produce a uniform martensitic structure. Experiments with this reagent met with no success; however, the reagent is mentioned here for it could prove useful in future work on slightly different alloys.

5.8 - ELECTRON-PROBE MICROANALYSIS

Electron-probe microanalysis was employed in this study to establish concentration profiles of manganese and sulphur in the specimens, to determine the nature and measure the concentration of elements present in inclusions and to measure the average solute concentrations of the matrix.

In principle, the technique consists of focussing a beam of accelerated electrons to a diameter of approximately 1 micron on the specimen. Characteristic x-ray spectra of the elements are generated in the bombarded volume of matter and the emerging x-rays are analysed according to wave length and intensity. Details of the technique can be found in reviews by CASTAING (1960) and POOLE and MARTIN (1969). Much of the existing information on the subject of inclusion analysis which was previously scattered throughout the literature was collated by YAKOWITZ and HEINRICH (1968). The analytical procedures used in the present investigation were based on their review.

For convenience in the analysis, a standard pellet consisting of pieces of pure iron, manganese, iron sulphide, manganese sulphide, zirconium oxide and an electron cage mounted in Lucite was fabricated. The zirconium oxide served as a fluorescent screen to adjust the beam size and the electron cage to measure the electron beam current. The standard and specimen pellets were prepared for analysis by metallographic polishing and coating with carbon in an evaporator to ensure proper electron drainage from the poorly conducting manganese sulphides and zirconium oxide.

The majority of analyses were performed on an Acton-Cameca Microanalyser with an x-ray emergence angle of 18^{o} at McMaster University and the remainder on a Cambridge Geoscan Microanalyser with an x-ray emergence angle of 75^{o} at Dominion Foundries and Steel Company Ltd.

The lowest operating voltage and beam current compatible with reasonable x-ray output were found to be 15 KV and 150 na respectively. The microsegregated regions of the specimen were analysed by point counting for 20 seconds at intervals of 2 - 30 microns depending on the sharpness of the concentration gradients. The intensities of x-rays were recorded where possible along the normal to the fall line of the concentration gradients. A counting time of 20 seconds was also used in analysing the inclusions. In analysing the average solute concentrations a scan length of 100 microns and a travel rate of 625 microns/min were used.

A correction algorithm proposed by HAWORTH (1968) and FRISKNEY and HAWORTH (1968) for the calculation of the true concentration of an element from the measured intensity ratio was employed in this investigation. A computer program, listed in Appendix A. 3, was written in Fortran IV machine language, utilizing where possible HAWORTH's nomenclature. It applies atomic number, absorption and fluorescence corrections and computes the expected intensity ratios over a given range of concentrations. Calibration curves for alloys comprising up to five elements can be constructed with the program.

CHAPTER 6

EXPERIMENTS AND RESULTS

The experiments carried out for the present investigation are described in this chapter. For convenience, the results and preliminary discussion thereof are synthetically grouped under the headings of convection, macrosegregation, microsegregation and inclusions.

6.1 - CONVECTION

In order to validate the assumption that no convection existed in the liquid phase during the solidification of specimens in the apparatus, a diffusion couple experiment was conducted and the results compared with the predictions of diffusion theory.

A liquid iron/liquid iron - 8 wt% nickel alloy couple was held for two hours at 1550°C in a 5 mm bore alumina tube. The problem of gravity segregation was circumvented by seating the iron half of the couple on top of the iron-nickel half.

Following an air quench, the couple was prepared metallographically and the concentration profile of nickel determined by electron-probe microanalysis. The results are shown in Figure 6.1.1.

The concentration profile was calculated from diffusion theory which is summarized below. After CRANK (1957), the solution to the diffusion equation

$$\frac{\partial C}{\partial t} = D \frac{\partial^2 C}{\partial z^2} \qquad (6.1.1)$$

for the boundary conditions of the experiment

$$C = 0 \text{ for } z < 0, \text{ at } t = 0$$

$$C = C_0 \text{ for } z > 0, \text{ at } t = 0$$

is:

$$C(z,t) = \frac{C_0}{2}\left[1 + \mathrm{erf}\left(\frac{z}{2\sqrt{Dt}}\right)\right] \qquad (6.1.2)$$

In these equations, C is concentration of solute; z, the distance coordinate; t, time; and D, solute diffusivity.

In this particular problem,

$$C_0 = 8 \text{ wt\% Ni}$$

$$D = 3 \times 10^{-5} \text{ cm}^2/\text{sec}$$

$$t = 2 \times 3600 \text{ sec}$$

The function C(z,t) for these data is plotted in Figure 6.1.1 as a continuous curve superimposed on the experimental points.

The agreement between the experimental and theoretical concentration profiles is remarkable despite the following sources of variation:

i) the system was not entirely isothermal and the solute concentration was fairly high, which is not in keeping with the assumptions of the error function solution, namely, the diffusion coefficient is not influenced by temperature and composition.

ii) possibly some stirring took place during melting since the diffusion couple in the pre-melted state did not fill the crucible completely.

It is interesting to note that the value of D which yields the best concordance between theory and experiment, $D = 3 \times 10^{-5} cm^2/sec$, is roughly that found by SUBRAMANIAN and PURDY (1969) in their capillary diffusion experiments on iron-nickel alloys. It is also the value favoured by WAGNER (1954) for the diffusion of alloying elements in liquid steel.

It should be pointed out that the greater part of the scatter observed in the experimental profile is not of a statistical nature but rather is a manifestation of nickel microsegregation.

In conclusion, the diffusion experiment substantiates the assumption that convection in the liquid phase was negligible during the solidification of specimens in the present apparatus.

6.2 - MACROSEGREGATION

The longitudinal distribution of solute in nine unidirectionally solidified specimens of various compositions was determined using an electron-probe microanalyser as explained in Section 5.8. The object was to obtain information on possible longitudinal macrosegregation resulting from solute rejection, inclusion transport and evaporation through the top surface of the specimen exposed to the inert gas phase, and to measure the average solute concentrations in the matrix of the unmelted portion of the solidified specimen.

An attempt was made to determine the average concentration profiles of both manganese and sulphur in the matrix. However, preliminary work demonstrated the futility of analysing the iron matrix for sulphur. This element is difficult to detect because of its low solubility in iron alloys, the high mass absorption coefficients of manganese and iron for sulphur (177 and 217) and the long x-ray path ($\sim$ 8 microns) through the matrix (due to the 18^{o} x-ray emergence angle of the Acton-Cameca Microanalyser used for this work). The manganese concentration was easily measured, however, at an operating voltage of 15 KV and a specimen current of 150 na. The average matrix concentration was obtained by using a line scan of 100 microns travelling at a rate of 625 microns/min and avoiding the inclusions where possible.

Six alloy systems were examined:

Fe - 4 wt% Mn

Fe - 3 wt% Mn - 0.005 wt% S

Fe - 3 wt% Mn - 0.005 wt% S - 0.4 wt% C

Fe - 0.5 wt% Mn - 0.030 wt% S

Fe - 0.5 wt% Mn - 0.030 wt% S - 0.4 wt% C

Fe - 15 wt% Mn - 0.25 wt% S

The compositions of the specimens and conditions under which they were solidified are given in Table 6.2.1, and the results are plotted in Figures 6.2.1 to 6.2.9. For convenience in the interpretation of results, the manganese distributions were plotted alongside full-size sketches of the solidified specimens.

The top portion of specimen 6, an Fe - 3 wt% Mn - 0.005 wt% S - 0.4 wt% C alloy, solidified at 50 mm/hr, exhibited a sharp drop in manganese concentration, as shown in Figure 6.2.4. Specimen 2, an Fe - 0.5 wt% Mn - 0.03 wt% S - 0.4 wt% C alloy, solidified under the same conditions, showed no manganese depletion in the top portion. The variation in average composition was pronounced along all but the lower 15 mm of the specimen. The demarcation point between the regions of variable and uniform compositions corresponds to the position of the solid-liquid interface at the start of the solidification run.

The matrices of specimens 1, 5, 7 and 10 were also considerably depleted in manganese towards the top as shown in Figures

6.2.1, 6.2.3, 6.2.5 and 6.2.7. Specimens 1 and 7 were of the same composition, Fe - 3 wt% Mn - 0.005 wt% S but were solidified at velocities of 5 and 50 mm/hr respectively. Specimen 5 was an Fe - 4 wt% Mn alloy and specimen 10, an Fe - 0.5 wt% Mn - 0.03 wt% S alloy; both were solidified at 50 mm/hr.

Specimens 13 and 14 which nominally contained 13 wt% Mn and 0.25 wt% S were solidified at relatively high rates (280 and 600 mm/hr respectively) and showed little manganese loss as seen in Figures 6.2.8 and 6.2.9. Some loss occurred in the case of specimen 9 which had the same nominal composition as 13 and 14 but was solidified at 50 mm/hr. As seen in Figure 6.2.6, the manganese concentration dropped from 14 wt% to 10 wt% near the initial position of the interface but was fairly constant from there on upwards.

The depletion of manganese in specimens 1, 5, 6, 7, 9 and 10 appeared to be related to the high evaporation rate of manganese at elevated temperatures (SMITH, 1965). A rough estimate of the amount of manganese lost by evaporation in specimen 1 was obtained by assuming that diffusion in the melt was rate limiting and considering the system to be of fixed length during the time of holding and solidification. For the case of a finite region $0 \leqslant z \leqslant a$ in which the surface at $z = 0$ is impermeable and the surface z = a is kept at C_a, the initial concentration being C_0, the solution to the diffusion equation

$$\frac{\partial C}{\partial t} = D \frac{\partial C^2}{\partial z^2} \tag{6.2.1}$$

given by CRANK (1957) is:

$$\frac{C - C_0}{C_a - C_0} = \sum_{n=0}^{\infty} (-1)^n \left\{ \operatorname{erfc}\left[\frac{(2n+1)a - z}{2\sqrt{Dt}}\right] + \operatorname{erfc}\left[\frac{(2n+1)a + z}{2\sqrt{Dt}}\right] \right\} \tag{6.2.2}$$

In the particular case of specimen 1,

$C_0 = 2.1$ wt% Mn

$C_a = 0$

$a = 7.5$ cm

$D = 1 \times 10^{-4}$ cm^2/sec

$t = 14$ hours ≈ 50000 sec

The calculated manganese concentration distribution plotted as a continuous line in Figure 6.2.1 bears a certain resemblance to the experimental distribution. The discrepancy between the two distributions is attributable in part to the approximations made in the evaporation calculations but also to the inclusion distribution. The inclusions were finely distributed throughout the unmelted region of the specimen which was in the cast and swaged condition.

The inclusions in the directionally solidified region of the specimen, however, were precipitated from slowly advancing interfaces and were much larger. The manganese of the inclusions was less likely, therefore, to be lumped with the manganese of the matrix during the electron-probe microanalysis. Apart from this local type of redistribution of inclusions common to all specimens, a long-range type prevailed in specimen 1. Many large inclusions (10 - 60 microns in diameter) containing approximately 60 wt% Mn were found in the topmost 20 mm of the specimen. No inclusions of suitable size for microanalysis were found, however, in the lower part of the solidified region. As will be seen in the discussion of results, calculations based on Stokes' law point to inclusion flotation as one probable cause of the long-range redistribution of manganese.

The sharpness of the cut-off in the manganese distribution observed in specimen 6, Figure 6.2.4, suggests that the specimen was solid below this point and liquid above it for a considerable period of time. Presumably the specimen was inserted too far in the furnace before melt-down, causing the upper 20 mm to melt and allowing manganese to evaporate as the furnace was being readied for the solidification run.

Specimen 9, Figure 6.2.6, was held longer in the melted state prior to solidification and also solidified at a slower rate than specimens 13 and 14 with the result that a greater proportion of manganese evaporated from the melt. The shape of the manganese distribution suggests that evaporation was the rate limiting step in the transfer process. Indeed, the concentration is fairly constant along the length of the originally liquid region of the melt. The lower evaporation rate was likely related to the presence of a slag layer over the melt in the three high-manganese specimens. The slag layer appears to have had its origin in the reaction of manganese with the alumina of the crucible.

In future experiments, short melt-down periods and capped crucibles are recommended to reduce solute losses, especially where manganese is present. As shall be seen below, the depletion of manganese in the low-manganese alloys had drastic effects on the composition of inclusions. This suggested a useful technique for rapid determination of inclusion-matrix equilibria in the Fe - Mn -S system. It is described in Section 7.2 and Chapter 8.

6.3 MICROSEGREGATION

Three important facets of the microsegregation which occurred during controlled directional solidification of various iron-base alloys are presented in this section. They are solidification morphology, dendrite arm spacing and distribution of solute.

6.3.1 - SOLIDIFICATION MORPHOLOGY

The solidification structure was particularly clear in eight specimens:

Specimen	Nominal Composition
21	Fe - 0.5 wt% Mn - 0.03 wt% S - 0.4 wt% C
6	Fe - 3.0 wt% Mn - 0.005 wt% S - 0.4 wt% C
9-13-14-24	Fe - 13 wt% Mn - 0.25 wt% S
25	Fe - 13 wt% Mn - 0.25 wt% ZrO_2
23	Fe - 0.03 wt% S - 0.4 wt% C

The alloys were solidified at velocities ranging from 50 to 600 mm/hr under gradients of the order of 25°C/cm. The compositions and growth conditions of the specimens are summarized in Table 6.3.1. In the following paragraphs, observations on these eight specimens are presented in the order given above.

Figures 6.3.1 and 6.3.2 show sections of specimen 21 normal and parallel, respectively, to the macroscopic growth direction. The alloy contained 0.5 wt% Mn, 0.03 wt% S and 0.4 wt% C and was solidified at 50 mm/hr under a gradient of 23°C/cm in the liquid. After solidification, the specimen was austenitized for 20 min at 925°C, quenched to 840°C, held for 3 sec, quenched in water, polished and etched in Picral. In Figure 6.3.1 the dark cruciform regions containing ferrite and pearlite are the manganese- and sulphur-poor dendrite cores. The light regions are martensitic in nature and are relatively richer in manganese and sulphur. The primary dendrite arms are normal to the plane of the micrograph and located in the centre of the crosses. The secondary dendrite arms form the arms of the crosses. In the parallel section, Figure 6.3.2, there is only faint evidence of secondary dendrite arms. The large object embedded in the matrix is a section of the alumina sheath used to protect the thermocouple.

The solidification structure of specimen 6 is shown in Figures 6.3.3 and 6.3.4. The alloy contained 3 wt% Mn, 0.005 wt% S and 0.4 wt% C and was solidified at 50 mm/hr under a gradient of approximately 25°C/cm in the liquid. The solidified specimen was austenitized at 900°C for 20 min, cooled at a rate of 5°C/min, polished and etched in Picral. The structure of the cruciform dendrite cores consists of a mixture of ferrite, pearlite and martensite. The interdendritic region, on the other hand, contains martensite and austenite. The structure is clearer in this case and it appears that stunted tertiary arms have grown from the end of the secondary arms into the interdendritic liquid. Again the structure is less well defined in the parallel section; the secondary arms are nevertheless more prominent than in the case of specimen 21, Figure 6.3.2.

The effect of growth velocity on structure is shown in Figures 6.3.5 to 6.3.10 which are normal and parallel sections of specimens 9, 13 and 14. The alloys nominally contained 13 wt% Mn and 0.25 wt% S and were solidified at rates of 50, 280 and 600 mm/hr, respectively, under an estimated temperature gradient of 30°C/cm. The specimens were polished and tinted with a solution of water saturated with hydrogen sulphide. In Figures 6.3.5 and 6.3.6, the interdendritic regions rich in manganese and sulphur are outlined in dark. The majority of inclusions (manganese sulphides, light in colour) are located in these dark regions. In Figures 6.3.7 to 6.3.10, however, the interdendritic regions are light and the dendrite cores are dark. The spacing of both primary and secondary arms decreases with increasing velocity. The secondary arms of specimen 9, Figure 6.3.6, appear very faintly: this suggests that the structure is almost plate-like in the direction parallel to the macroscopic growth direction. The secondary arms are much more clearly defined in the more rapidly solidified specimens 13 and 14 as seen in Figures 6.3.8 and 6.3.10.

Figures 6.3.2, 6.3.4, 6.3.6, 6.3.8 and 6.3.10 show that the growth direction of primary dendrite arms was rarely aligned to perfection with the macroscopic growth direction. The deviations ranged from almost 0° in Figure 6.3.4 to approximately 30° in Figure 6.3.8. It appears that the competitive growth mechanism proposed by CHALMERS (1964) to explain the growth of columnar dendrites in the direction of heat flow in ingots did not operate in the present experiments for lack of competing crystals.

During the solidification of specimen 24, of same nominal composition as 9, 13 and 14, the growth rate was doubled at regular intervals of distance. Cross-sections of four regions solidified at rates of 50, 100, 200 and 400 mm/hr are shown in Figures 6.3.11 to 6.3.14. The micrographs are not as clear as the micrographs of specimens 9, 13 and 14; however, a certain amount of dendrite refinement is evident in the structure at higher growth rates. (The reason for the lack of clarity was the low manganese content of the specimen (~10 wt%), as electron-probe microanalysis later revealed.) A large number of sulphide inclusions are located in the dark regions which are rich in manganese and sulphur; on the other hand, some inclusions are located in the light regions.

The growth rate of specimen 25 containing 13 wt% Mn and 0.25 wt% ZrO_2 was increased from 50 to 100 mm/hr during solidification. The object of the experiment was to obtain information on pushing of inclusions by an advancing solid-liquid interface. The solidification structure emerged much more clearly than that of specimen 24, as seen in Figures 6.3.15 to 6.3.18, and revealed an interesting phenomenon: the primary dendrite arms tend to become interlocking at higher growth rates, i.e., there is a transition from the open structure of Figures 6.3.15 and 6.3.16 (growth rate of 50 mm/hr) represented by an array of crosses,

```
+ + +
+ + +
+ + +
```

to the more closely packed structure of Figures 6.3.17 and 6.3.18 (growth rate of 100 mm/hr) represented by

```
+    +
   +    +
+    +
   +    +
+    +
```

as the growth rate increases. Figure 6.3.19 is a parallel section of the portion of the specimen solidified at 100 mm/hr. The secondary arms are barely visible and hence the structure appears to be plate-like or cellular-dendritic. Figure 6.3.20 is a cross-section of the region in which the primary dendrite arm tips were growing just prior to quenching, and Figure 6.3.21 shows the fine dendrites in the quenched liquid. The results on pushing of ZrO_2 particles will be given in Section 6.4.1.

The structure of specimen 9 was examined in detail in the region where the solid-liquid interface was located before quenching, on a section of the specimen parallel to the macroscopic growth direction as shown in Figure 6.3.22. The rapidly cooled region is at the top of the composite photograph and the region solidified under controlled conditions, at the bottom. As would be expected, the structure is finer at the top than at the bottom. Details of regions at various levels of the composite photograph are shown in Figures 6.3.23 to 6.3.30.

Details of the region below the letter G are shown in Figures 6.3.23 and 6.3.24. Two large grains, or sets of dendrites with a common orientation are visible in both normal and parallel directions. The regions rich in manganese and sulphur appear dark and contain silver-coloured manganese sulphide inclusions.

Figures 6.3.25 and 6.3.26 show the region in which the primary arm tips were growing at the time of the quench. This region is denoted by the letter C. The concentration gradients are much steeper in this case as indicated by the more developed colour gradation; the lightest regions are enriched in manganese and sulphur but are not different phases. The tertiary arms perpendicular to secondary arms in Figure 6.3.25 are well developed.

Figures 6.3.27 and 6.3.28 are representative of a region which was completely liquid at the time of quenching. The fine dendrites are outlined in black by the last material to solidify. The heat flow in this region is radial: several large grains have grown from the periphery to the centre of the specimen. In the right-hand corner of the micrograph, two long primary arms have grown inwards; perpendicular secondary arms have competed for space in the liquid, as evidenced by the stunted arms and mutual blocking of the arms; tertiary and even quaternary arms are also visible.

The structure of a region which was completely liquid at the time of the quench but even more remote from the primary dendrite arm tips is shown in Figures 6.3.29 and 6.3.30. The dendrites are finer, and the grains are greater in number and randomly orientated.

Specimen 23 containing 0.03 wt% S and 0.4 wt% C was solidified at a velocity of 50 mm/hr and quenched in water. The object of the experiment was to produce FeS inclusions to check the ferrite nucleation efficiency of iron sulphide. This aspect of the experiment will be discussed in Section 6.4.3. Of special interest here in connection with microsegregation phenomena is the structure of the quenched liquid approximately 2 cm in front of the primary dendrite arm tips just prior to quenching. This structure appeared clearly even at the rough-polishing stages, Figure 6.3.31. A nital etch revealed martensite in the dendrite cores and a mixture of austenite, martensite and iron sulphides in the interdendritic regions.

Three aspects of Figure 6.3.31 are noteworthy:

i) it indicates that primary dendrite arms advanced rapidly quite a distance (over 2 cm) into the liquid at the time of the quench without significantly altering their spacing. Although the structure of the region of the alloy solidified under controlled conditions was not revealed successfully, the dendrites probably had roughly the same spacing as observed in Figure 6.3.31. Hence it appears that the system was not allowed sufficient time to renucleate smaller dendrite arm spacings. This observation has considerable bearing on the interpretation of other phenomena which is discussed further on;

ii) the dendrites are in a close-packed formation probably as a result of the extreme growth velocity. This observation substantiates the observations made on specimen 25;

iii) the variations in the amount of martensite indicate a variation in the carbon concentration. It appears that carbon did not have time to back-diffuse into the dendrite cores during and after solidification, due to the high growth velocity, large dendrite arm spacing and rapid cooling. According to BRICK and PHILIPS (1949) the temperature at which martensite starts to form, T_{MS}, is markedly depressed by the addition of carbon. The temperature can be expressed by the relation

$$T_{MS} = 550 - 361 \times \text{wt\% C} \quad (^{o}\text{C})$$

Therefore martensite began forming around

$$T_{MS} = 550 - 361 \times k_0 C_0$$

$$= 550 - 361 \times 0.25 \times 0.4$$

$$= 514^{o}C$$

in the dendrite cores. In the interdendritic region, the high carbon content probably depressed T_{MS} below room temperature with the result that the austenite did not transform. Figure 6.3.31 perhaps constitutes the first experimental observation of carbon microsegregation during solidification.

6.3.2 - DENDRITE ARM SPACING

Dendrite arm spacing is of practical importance in homogenization treatments of castings since the time t required for solute to diffuse a given distance is proportional to the square of the distance z:

$$t \propto z^2/D \tag{6.3.1}$$

where D is the diffusivity. Thus if the dendrite arm spacing, i.e., the diffusion distance is halved, only one quarter of the original homogenization time is required.

In the present investigation, the clear structure of some specimens offered the opportunity of acquiring pertinent information on the relation between dendrite arm spacing and growth conditions.

Micrographs of selected regions of specimens 6, 9, 13, 14, 21 and 25 are shown in Figures 6.3.1 to 6.3.10 and 6.3.15 to 6.3.19. The composition, growth rate V, temperature gradients in the solid and liquid G' and G, and the primary and secondary arm spacings d_1 and d_2 are listed in Table 6.3.2. The arm spacings were measured only along well-defined rows.

The primary dendrite arm spacings were larger than the secondary arm spacings by a factor of at least two. In the Fe - 13 wt% Mn - 0.25 wt% S specimens the ratio of primary to secondary arm spacings increased from approximately 2:1 at the lower growth rates to 3:1 at the higher rates. The variation of arm spacing with growth rate in specimens 9, 13, 14 and 25 was graphed as log d versus log V as shown in Figure 6.3.32. The least square regression equations for the Fe - 13 wt% Mn - 0.25 wt% S specimens were:

$$\log d_1 = 2.84 - 0.314 \log V \text{ or } d_1 = 704\,V^{-0.314} \qquad (6.3.2)$$

$$\log d_2 = 2.63 - 0.453 \log V \text{ or } d_2 = 425V^{-0.453} \qquad (6.3.3)$$

and for the Fe - 10 wt% Mn - 0.25 wt% ZrO_2 specimen:

$$\log d_1 = 2.73 - 0.249 \log V \text{ or } d_1 = 537V^{-0.249} \qquad (6.3.4)$$

The results of ALBERNY et al. (1969) are plotted in Figure 6.3.32 for the purpose of comparison. Steel bars containing 0.35 wt% C - 0.3 wt% Si - 0.003 wt% P were unidirectionally solidified at controlled rates and in a controlled temperature gradient in the liquid phase of approximately 20°C/cm. The relation between the primary arm spacing and the growth velocity can be represented by

$$\log d_1 = 2.81 - 0.218 \log V \text{ or } d_1 = 646V^{-0.218} \qquad (6.3.5)$$

The results of these experiments are discussed in Section 7.1.

6.3.3 - SOLUTE DISTRIBUTION

The microsegregation of manganese was studied quantitatively by electron-probe microanalysis in specimens where the solidification structure emerged with sufficient clarity. These were specimen 6, an Fe - 3 wt% Mn - 0.005 wt% S alloy; specimens 9, 13, 14 and 24, Fe - 13 wt% Mn - 0.25 wt% S alloys. The conditions under which the alloys were solidified are given in Table 6.3.1.

The object of the study was to determine:

i) the segregation ratio of manganese from the maximum and minimum concentrations in the dendrite arms,

ii) the shape of the manganese distribution curves and therefrom the mechanism of solute redistribution, and

iii) the effect of solidification rate on the distribution of solute.

The operating voltage of the microanalyser was set at 15 KV and the specimen current at 150 na. The x-ray intensities were measured by point-counting for 20 sec. The distance between points varied from 10 - 30 microns according to the concentration gradient in a given region. The analyses were carried out on sections perpendicular to the primary arm growth direction, in specimens 6, 9, 13 and 14, along [x] paths such as A → B and [+] paths such as C → D in Figure 6.3.34a.

The results of microanalyses on cross-sections of specimens 6, 9, 13 and 14 solidified under controlled rates and temperature gradients are shown in Figures 6.3.33 to 6.3.36. The manganese concentrations are plotted as weight percent versus distance between points indicated in the accompanying micrographs. The minimum and maximum of the manganese distributions C_m and C_M are listed in Table 6.3.3. The distributions of Figures 6.3.34 to 6.3.36 were not as well defined as could be expected. However, Figure 6.3.33 clearly shows a continuously increasing manganese concentration along both paths of analysis. Two other aspects of the manganese distributions are clear:

i) the concentration minima were located in the axes of the primary dendrite arms perpendicular to the plane of the micrographs and in the centre of the cruciform components of the structure;

ii) the solute redistribution is more intense along [x] paths, where I_S^x varied in the range 1.4 to 1.8, than along [+]paths where I_S^+ varied from 1.3 to 1.4. The segregation ratios of specimens 9, 13 and 14, of same nominal composition but solidified at rates of 50, 280 and 600 mm/hr, respectively, decreased from 1.54 to 1.35 along [x] paths and from 1.40 to 1.29 along [+] paths as the solidification rate increased. The concentration minima in the dendrite cores also increased with increasing solidification rate.

In order to confirm the effect of velocity on the segregation ratio, successive lengths of specimen 24 were solidified at rates of 50, 100, 200 and 400 mm/hr. The nominal composition of this alloy was Fe - 13 wt% Mn - 0.25 wt% S; however, the alloy effectively contained less manganese, namely, 10 wt%. Micrographs of cross-sections of the specimen at each growth rate are shown in Figures 6.3.11 to 6.3.14. Each cross-section was microanalysed for manganese by traversing along the diameter. The segregation ratios at various growth rates are listed in Table 6.3.3. The segregation ratio at 50 mm/hr, $I_S = 1.18$, was significantly lower than the segregation ratios at higher growth rates which were fairly constant at 1.32.

The segregation of manganese in various regions of specimen 9 was studied in detail by electron-probe microanalysis.

The first region studied was the region into which the primary dendrite arm tips were growing at the time of the quench. The electron-probe trace A → B normal to the planar solidification fronts is indicated in Figure 6.3.37 which is an enlargement of the second micrograph from the top in the composite photograph of Figure 6.3.22. The manganese concentrations are plotted versus distance in Figure 6.3.38. The manganese distribution shows well-defined peaks corresponding to the final interdendritic liquid outlined in white in Figure 6.3.37 and valleys marking the cores of the arms. The average minimum and maximum manganese concentrations were 10 and 14.3 wt%, respectively. Hence, the average concentration difference, ΔC, between peaks and valleys was roughly 4 wt%, and segregation ratio was approximately 1.4.

The study revealed other interesting segregation features of specimen 9:

i) the manganese concentration of the long primary arm C - E in Figure 6.3.22 was uniform at about 10 wt%, which is about the value k_0C_0 (0.77 x 13), and

ii) the blurring of the microsegregation structure towards the bottom of Figure 6.3.22 is due to the smaller concentration differences between various parts of the specimen: between the light grey regions of the primary arms and the dark grey regions such as region F, $\Delta C \approx 1$ wt% Mn; between the light grey regions of the primary arms and the white regions such as region G, $\Delta C \approx 4$ wt% Mn. Effectively, then, the micrograph is a fairly accurate map of the degree of microsegregation.

The results of these experiments are discussed in more detail in Section 7.1.

6.4 - INCLUSIONS

Observations on the distribution, morphology and composition of inclusions found in the alloys solidified in this investigation are presented in this section.

6.4.1 - INCLUSION DISTRIBUTION

It appears that the solidification rate had a considerable influence on the longitudinal distribution of inclusions in specimens 1 and 7. Both specimens were Fe - 3 wt% Mn - 0.005 wt% S alloys; however, specimen 1 was solidified at 5 mm/hr and specimen 7 at 50 mm/hr. As indicated in Figures 6.2.1 and 6.2.5, only a few inclusions were found at the top of specimen 1 while a fairly uniform distribution existed in specimen 7.

Myriads of inclusions smaller than 2 microns were present in specimen 12, an Fe - 0.04 wt% S alloy solidified at 50 mm/hr. These were located mainly in the boundaries of segregation cells as shown in Figure 6.4.1.

Specimen 10, an Fe - 0.5 wt% Mn - 0.03 wt% S alloy solidified at a rate of 50 mm/hr also contained numerous inclusions, as shown in Figures 6.4.2 and 6.4.3. The long inclusion in Figure 6.4.3 was in fact about 2000 microns in length; several such inclusions were visible in the longitudinal plane of cutting of the specimen.

The experiments on specimen 25, an Fe - 13 wt% Mn - 0.25 wt% ZrO_2 alloy solidified at 50 and 100 mm/hr were conducted to obtain information on the pushing of inclusions by a solid-liquid interface. The zirconia added to the melt was in the form of spheres about 20 microns in diameter; this oxide was used because of its known low solubility in liquid iron (ELLIOT et al., 1963). The results are shown in Figures 6.3.15 to 6.3.19. The number of inclusions is considerably greater in the light-coloured interdendritic regions than in the dark-coloured dendrite axes. This is especially evident in Figure 6.3.19. Since the zirconia particles were not dissolved by the melt and hence not precipitated, the mechanism by which they were concentrated in the interdendritic liquid must have been pushing by the solid-liquid interfaces. Some consequences of these observations are discussed in Section 7.2.

6.4.2 - INCLUSION MORPHOLOGY

The morphology of inclusions found in various directionally-solidified specimens is described in this section.

Figure 6.4.4 shows inclusions typical of the few found at the top of specimen 1, an Fe - 3 wt% Mn - 0.005 wt% S alloy solidified at 5 mm/hr. As shown in Table 6.4.1, the inclusions in this specimen were generally round, rather large and medium-grey in colour.

Inclusions of specimen 2, an Fe - 0.5 wt% Mn - 0.03 wt% S - 0.4 wt% C alloy solidified at 50 mm/hr are shown in Figures 6.4.5, 6.4.6 and 6.4.7. The inclusions of Figure 6.4.5 are in bead-like formations and delineate microsegregation cells. The "sinusoidal" inclusions shown in Figures 6.4.6 and 6.4 7 were quite common. "Sinusoidal" inclusions of the type shown in Figure 6.4.6 were usually small, medium grey in colour, and located in cell boundaries throughout the specimen. The "sinusoidal" inclusions of the type shown in Figure 6.4.7 were also medium grey but much larger and found only in the immediate vicinity of the initial location of the solid-liquid interface. The latter inclusions appeared to have a common orientation.

Specimen 5, an Fe - 4 wt% Mn alloy solidified at 50 mm/hr contained few inclusions. Some were angular and translucent, as shown in Figure 6.4.8, and others were rounded and translucent or opaque, as shown in Figure 6.4.9.

The inclusions of specimen 6, an Fe - 3 wt% Mn - 0.005 wt% S - 0.4 wt% C alloy were also few in number, angular, medium grey in colour and isolated as shown in Figure 6.4.10. These inclusions were similar in appearance to the Type III inclusions of Figure 2.3.2. Their angular shape was probably due to the relatively low levels of oxygen ($\sim$ 100 ppm) in the system due to the presence of carbon and a fairly high concentration of manganese ($\sim$ 3 wt%). Indeed, the work of MARICH and PLAYER (1969), reviewed in Section 2.3.3 of the literature survey, showed that sulphides tended to be angular in low-oxygen systems.

As shown in Figure 6.4.11, the inclusions of specimen 7, an Fe - 3 wt% Mn - 0.005 wt% S alloy solidified at 50 mm/hr appeared to be comprised of two phases, one medium-grey and the other, tan in colour, when examined at high magnification. However, the dominant colour was medium grey.

The inclusions of specimens 9, 13 and 14, Fe - 13 wt% Mn - 0.25 wt% S alloys solidified at 50, 280 and 600 mm/hr respectively were generally large, round and medium grey in colour. However, close to the initial position of the solid-liquid interface, the matrix contained only large faceted or "sinusoidal" inclusions, Figures 6.4.12 and 6.4.13. These inclusions appeared to have a common orientation, as had the inclusions of specimen 2, Figure 6.4.7. On the other hand, the unmelted portion of the specimen was characterized by inclusion stringers and clouds of smaller inclusions as shown in Figure 6.4.14. In order to relate the location of the large faceted inclusions to the initial position of the interface, the specimen was given a sulphide tint which revealed the segregation pattern of manganese and sulphur, Figure 6.4.15. The inclusions appear as small white spots in the micrograph and the large white regions at the top indicate a more intense segregation of solute due to solidification. It appears here that the interface ran horizontally across the middle of the micrograph, and that the faceted inclusions were located in the so-called "mushy" zone of the specimen.

Table 6.4.1 shows at a glance that the average size of inclusions was smaller in specimens 13 and 14 ($\sim$10 microns) than in specimen 9 ($\sim$ 20 microns). The former specimens were solidified, it will be recalled, at much higher rates than the latter.

Specimen 10, an Fe - 0.5 wt% Mn - 0.03 wt% S alloy solidified at 50 mm/hr, contained extraordinarily long inclusions. Part of an inclusion 2000 microns in length is shown in Figure 6.4.3.

Specimen 12, an Fe - 0.04 wt% S alloy contained on the whole extremely small, medium-grey inclusions, less than 2 microns in diameter, shown in Figure 6.4.1, and a few larger, round, brownish, glassy inclusions, shown in Figure 6.4.16.

It was also observed that inclusions in specimens or regions of specimens where the matrix contained less than approximately 0.5 wt% Mn were two-phase or duplex in nature. Typical duplex inclusions found in specimens 1, 2, 7 and 10 are shown at high magnification in Figures 6.4.17, 6.4.18, 6.4.19 and 6.4.20. The dark phase was medium grey and the light phase was tan-coloured and optically active in polarized light. Since the inclusions generally contained at least 20 wt% O, the dark phase was probably Mn(S,O) and the light phase, Fe(S,O).

6.4.3 - INCLUSION COMPOSITION

The inclusions in the solidified specimens were analysed for iron, manganese and sulphur using an Acton-Cameca Microanalyser. The low x-ray emergence angle (18^o) of this particular instrument did not permit the analysis of inclusions of apparent diameter less than 8 microns. The oxygen concentrations were calculated by difference. The results are reported in Table 6.4.1 along with information on the size, shape and colour of the inclusions. The inclusions were given numbers to indicate their location in Figures 6.2.1 to 6.2.9.

Unlike other specimens in which the composition of inclusions was studied in detail, specimens 2 and 6 had carbon concentrations of industrial interest. Specifically, specimen 2 was an Fe - 0.5 wt% Mn - 0.03 wt% S - 0.4 wt% C alloy and specimen 6, an Fe - 3 wt% Mn - 0.005 wt% S - 0.4 wt% C alloy. The main feature of inclusions in these two specimens was that they contained very little oxygen with the exception of inclusions 26, 27, 30 and 33 in specimen 2 (Table 6.4.1). These inclusions were located close to the crucible wall which suggests that they were produced by a slagging reaction of iron oxide with the alumina of the crucible. On the whole, their quantity was small so that they are considered to have had a negligible effect on the results of the present investigation. However, for investigations on alloy materials of higher purity, it would be advisable to use less reactive refractories, e.g., boron nitride.

The sulphur concentration of most inclusions in specimens 2 and 6 was in the range 36 - 38 wt% S (stochiometric FeS and MnS contain 36.5 and 36.9 wt% S respectively). The iron and manganese concentrations of inclusions in specimen 2 varied in all proportions from almost pure FeS (inclusion 29) to pure MnS (inclusion 36). The majority of iron concentrations, however, were in the range 5 - 10 wt% Fe. The iron concentrations of inclusions in specimen 6 were lower and restricted to a narrower range, 0.5 - 2 wt% Fe. Finally, the number of elongated inclusions was greater in specimen 2 than in specimen 6.

The greater number of elongated inclusions in specimen 2 relative to specimen 6 can be explained in terms of the wettability of the inclusions. Indeed the wettability of an iron-manganese sulphide is proportional to its iron content (JOSEFSSON et al., 1959).

Specimens 1, 5, 7, 10 and 12 were alloys of iron, manganese and sulphur. The manganese content of these alloys was at most 4 wt%.

The inclusions of specimen 5, an Fe - 4 wt% Mn alloy, contained approximately 45 wt% Mn, some iron and sulphur and a seemingly disproportionate amount of oxygen, 50 wt%. No sulphur was detected in the small inclusions of specimen 12, which was surprising since the alloy nominally contained 0.04 wt% S. The few inclusions large enough for analysis contained, as in the case of specimen 5, large amounts of oxygen. Inclusion 2, 6 and 8 were particularly high in sulphur and elongated. The inclusions shown in Figure 6.4.16 contained an apparent 30 wt% Fe and no manganese, nor sulphur nor any other element detectable by electron probe microanalysis.

Since the oxygen concentration was obtained by difference, it was suspected at first that other elements were included under the heading of oxygen in the case of specimens 5 and 12. However, no common elements were detected by scanning the radiation emitted by the bombarded inclusions with the spectrometer of the electron-probe microanalyser. In future work on inclusions in this type of material, it would be advisable to include FeO, MnO and other oxide standards in the standard pellet of the electron-probe microanalyser.

The inclusions of specimens 1, 7 and 10 also contained considerable amounts of oxygen but little sulphur. Especially interesting, however, is the fact that the inclusions were iron-rich at the top of the specimen and manganese-rich at the bottom while the non-metallic (sulphur plus oxygen) levels remained approximately constant. The inclusions of specimen 7, in particular, showed an abrupt change in composition in the lower part of the specimen where the manganese concentration of the matrix more than doubled. The iron level of the inclusions decreased to approximately 1 wt%, the manganese to 30 wt% while the apparent oxygen level increased to 68 wt%. As would be expected from the lower manganese content of specimen 10, the non-metallics concentration in the inclusions was higher (25 - 35 wt%) than in the inclusions of specimens 1 and 7 (15 - 25 wt%).

Specimens 9, 13 and 14 had the same nominal solute content, 13 wt% Mn and 0.25 wt% S, and were solidified at rates of 50, 280 and 600 mm/hr respectively. The inclusion compositions were remarkably constant in a given specimen and from one specimen to the next as shown in Table 6.4.1, in spite of the large differences in solidification rates and variations in the manganese concentration of the matrix. Although no carbon was present, the inclusions contained little, if any, oxygen, and only an average of 1.5 wt% Fe.

Small amounts of iron — generally in the range 1 - 2 wt% — were found in the inclusions of specimens 5, 6, 9, 13 and 14. The validity of these results was questionned, however, because of the presence of an iron-rich matrix around the inclusions and the penetrating white radiation generated by the electron beam of the microanalyser. Indeed, there is the possibility that the weak iron radiation apparently emitted by the inclusions was in fact iron radiation from the matrix excited by the white radiation. A few attempts to extract the inclusions from the matrix for microanalysis in the isolated condition were made but were unsuccessful. However, the work of KIESSLING et al. (1963) showed that it is possible to extract the inclusions using suitable techniques. A sketch of the inclusions isolated in their work is given in Figure 2.3.2.

In the review of the literature on the influence of inclusions on the nucleation of ferrite (Section 2.4), it was seen that MnS inclusions were very effective in nucleating ferrite in the surrounding matrix. An illustration of this phenomenon is given in two micrographs of specimen 2, Figures 5.7.2 and 6.4.21: large white areas of ferrite surround each MnS inclusion, medium-grey in colour. Specimen 2 was an Fe - 0.5 wt% Mn - 0.03 wt% S - 0.4

wt% C alloy solidified at 50 mm/hr. Most workers, it was seen, believed that the nucleation of ferrite was enhanced by the lower manganese content of the matrix around the inclusion. Others, however, implied that nucleation was favoured by the presence of a phase boundary. Electron-probe microanalyses were carried out in the vicinity of the inclusions but did not conclusively reveal the existence of manganese concentration gradients. It was then decided to examine the effectiveness of FeS inclusions in bringing about the nucleation of ferrite. To this effect, specimen 23 was produced by solidifying, under conditions similar to those which prevailed during the solidification of specimen 2, an alloy containing the same amount of carbon and sulphur but no manganese. The specimen was then heat treated in the same manner, i.e., austenitized and slowly cooled. Figure 6.4.22 shows a typical tan-coloured inclusion and regions of ferrite and pearlite. In contradistinction to Figure 6.4.21, there appears to be no marked correlation between the location of the pearlite and ferrite regions and the inclusion.

CHAPTER 7

DISCUSSION OF RESULTS

As a result of carrying out the experiments under controlled and non-convective conditions, it was possible to make a number of significant observations which were reported and given a preliminary discussion in the previous chapter. The most important observations are discussed in more detail in the present chapter. For the sake of clarity, the observations are grouped and discussed under two general headings: microsegregation and inclusions.

7.1 - MICROSEGREGATION

SOLIDIFICATION STRUCTURE

From a study of Figures 6.3.1 to 6.3.31, it was concluded that the solidification structure was cellular-dendritic. The structure of specimens containing carbon, for example specimen 21, Figure 6.3.1, is similar to the structure reported by KATTAMIS and FLEMINGS (1965). The structures shown in Figures 6.3.2, 6.3.6, 6.3.19 and 6.3.24 are essentially plate-like, while the structures of Figures 6.3.4, 6.3.8, 6.3.10 and 6.3.26 -- in which the secondary arms are distinguishable -- are more aptly termed rod-like. It appears that the two types of structures derive basically from essentially the same dendritic skeleton. A wax model of such a skeleton is shown in Figure 7.1.1-a. The primary and secondary arm spacings, d_1 and d_2, are indicated in the corresponding isometric sketch of Figure 7.1.1-b. In plate-like structures, the interstices between secondary arms fill in at an early stage of solidification, while in rod-like structures, the interstices fill in at a late stage of solidification. As a result, a considerable solute build-up takes place between secondary arms in rod-like structures. It seems that rod-like structures are characteristic of more severe growth conditions.

TRANSITIONS IN STRUCTURE

The transition from the open type of structure shown in Figures 6.3.15 and 6.3.16 to the close-packed type of structure shown in Figures 6.3.17 to 6.3.18 appears to be a real effect. This transition does not seem to have been explicitly reported in the literature although it is evident in the results of some investigations. For example, in the experiments of ALBERNY et al. (1969) on the solidification of steel bars (see Section 2.6), the transition from an open to a close-packed structure seems to have taken place over the range of growth rates of 94 to 188 mm/hr.

Hence, in the presence of more severe growth conditions, the solidifying system can choose between at least two alternate modes of creating new solid-liquid area for increased solute rejection: one mode is to decrease primary and secondary arm spacings and the other is to rearrange the configuration of primary dendrite arms.

Some simple models of segregation in the open type of structure shown in Figure 7.1.2-a were derived in Section 4.2. It appears that no modification of these models is necessary for describing the segregation patterns of close-packed structures. Indeed, as shown in Figure 7.1.2-b, the area of a two-dimensional segregation cell in a close-packed structure is ideally one-quarter the area of a cell in an open type of structure but the basic shape of the cell remains unaltered.

INFLUENCE OF CARBON ON MICROSTRUCTURE

It was seen in Section 2.7 of the literature survey that carbon had considerable influence on the solidification behaviour of iron-base melts. The effects of carbon encountered in this investigation are discussed in the following paragraphs.

It is of interest to note that specimens in which the solidification structure was successfully revealed contained either carbon or a considerable amount of manganese, as seen in Table 6.3.1. No trace of segregation was observed in low manganese specimens lacking carbon, such as 1, 5, 7 and 10, even after having submitted the specimens to a variety of metallographic treatments. Two possible explanations are:

i) the sulphide tinting technique was not sufficiently sensitive to the concentration differences produced by segregation. After some experimentation, it was found that the sulphide tinting technique did not outline the structure of an Fe - Mn alloy unless it contained at least 7 wt% Mn. The nominal manganese concentrations of the four specimens mentioned above were all less than 7 wt% Mn. Moreover, Figures 6.2.1, 6.2.3, 6.2.5 and 6.2.7 show that the effective concentrations were considerably less than nominal as a result of evaporation during the solidification experiments:

	Wt% Manganese	
Specimen	Nominal	Effective
1	3	2 → 0
5	4	1.5
7	3	0.75
10	0.5	0.2 → 0

ii) there was little or no microsegregation of manganese. The work of de BEAULIEU and KOHN (1957) cited in Section 2.7 of the literature review lends considerable support to this second explanation. Indeed, autoradiographs of an as-cast Fe - 0.5 wt% Mn alloy were of uniform density while autoradiographs of an Fe - 0.5 wt% Mn - 0.4 wt% C alloy clearly showed segregation patterns.

In the present investigation, electron-probe microanalysis of specimens 1, 5 and 7 showed no significant concentration differences of manganese and hence confirmed the observations of de BEAULIEU and KOHN.

Two plausible explanations are proposed for the effect of carbon on the intensity of microsegregation:

i) the addition of carbon to an iron alloy increases the stability of the γ Fe phase. This effect is quite evident in the Fe - C phase diagram where the temperature range in which austenite is stable expands with increasing carbon content. It is also well known that solute diffusivities are generally lower in γ_{Fe} (FCC) than in δ_{Fe} (BCC) by an order of magnitude or two. Indeed, as seen in Figure 2.1.1, the diffusion coefficient of manganese is roughly one and one half orders of magnitude larger in δ_{Fe} than in γ_{Fe}. Hence the amount of solute back-diffusion in the solid phase during the solidification process will be greater, and the intensity of microsegregation, lower, if the system crystallizes to δ_{Fe} rather than γ_{Fe} in the presence of carbon;

ii) the cross-interaction between carbon and a second solute is large enough to influence the partition coefficient of the second solute and hence modify the intensity of microsegregation. The results of calculations on the Fe - Mn - C system at 1490°C, based on the theory of Section 4.1, are shown in Figure 7.1.3: the equilibrium partition coefficients of carbon and manganese are plotted as a function of the carbon content of the liquid phase. In reality, the cross-interactions in both phases are weak, and ϵ^{L}_{MnC} and ϵ^{S}_{MnC} are small, namely -1.3 and -0.4, so that in the case of the Fe - Mn - C system, carbon has little effect on the partition coefficient of manganese. However, it is interesting to note that had the interaction been larger, with ϵ^{L}_{MnC} and ϵ^{S}_{MnC} around $\pm$ 10, the partition coefficients would have varied significantly as seen in the diagram. In the case of positive interaction parameters, k_{Mn} would have increased from 0.75 at 0 wt% C to 0.9 at 0.6 wt% C, and hence microsegregation would have been attenuated. For negative interaction parameters of the same magnitude, k_{Mn} would have decreased correspondingly from 0.75 to 0.6, and microsegregation would have been enhanced. It should be noted that interaction parameters of $\pm$ 10 are commonly encountered in steelmaking systems so that the effect of carbon on the partition coefficient of a solute must be reckoned with in microsegregation studies of such systems.

By applying a number of approximations to the rigourous tangent plane equations derived in Section 4.1, PURDY (1970) arrived at an explicit relation between the cross-interaction parameter in the liquid phase ϵ^L_{12}, the mole fraction of solute 1, x^L_1, and the partition coefficient of solute 2, k^T_2:

$$k^T_2 = k_2 + \epsilon^L_{12} x^L_1 \qquad (7.1.1)$$

where k_2 is the partition coefficient measured in the binary solvent-solute 2 phase diagram. It is quite obvious from this relation that the partition coefficient k^T_2 decreases with a negative ϵ^L_{12} and increases with a positive ϵ^L_{12}, as shown in Figure 7.1.3.

For the present case, it appears that the austenite stabilizing properties of carbon best explain the large difference between manganese segregation in carbon-containing alloys and that in carbon-free alloys.

One interesting aspect of Figure 7.1.3 and Equation 7.1.1 is that it points to the possibility of attenuating the degree of segregation in castings. Indeed the value of k^T_2 may even be made equal to unity by a judicious choice of species 1 and mole fraction thereof. This species should not only interact strongly and positively with species 2 but also be a fast diffuser in the solid state in order that it not be, in itself, a source of microsegregation.

DENDRITE ARM SPACING

In the present investigation the dendrite arm spacing measurements were obtained in specimens solidified under non-convective conditions (as demonstrated by the experiments described in Section 6.1) and at constant temperature gradient and growth velocity (as demanded by the theory presented in Section 4.4). The measurements of dendrite arm spacing were made only in well-defined areas. Hence they could serve eventually to check the predictions of a theoretical dendrite arm spacing model, which of necessity would comprise a regular solidification structure.

The primary dendrite arms were more clearly resolved than secondary arms in all the specimens listed in Table 6.3.2. Indeed, in specimens 21 and 25, the secondary arms were not revealed with sufficient clarity for spacing measurements. However, no difficulty was encountered in measuring primary arm spacings. This is because the variation in concentration between the secondary arms of a given primary arm was smaller than the variation between primary arms. This supports the proposal put forth by WEINBERG and BUHR (1967) to the effect that properties of a casting should be related to primary rather than secondary arm spacing.

In previous investigations, reviewed in Section 2.6 of the literature survey, it was reported that dendrite arm spacing varied with the inverse of the growth rate with an exponent in the range 1/2 to 1/3. The results of the present investigation suggest that the lower end of this range should be extended to 1/4, as seen in Equations 6.3.2 to 6.3.5.

The present results also indicate that primary arm spacing is less sensitive than secondary arm spacing to variations in the growth rate, at least for the Fe - 13 wt% Mn - 0.25 wt%S specimens. Indeed, as shown in Equations 6.3.2 and 6.3.3, the exponents of the growth rate are close to -1/3 for the primary arm spacings and to -1/2 for the secondary arm spacings. It is of interest to compare these results with those of WEINBERG and BUHR (1967) whose work was briefly reviewed in Section 2.7. Indeed, they observed that primary dendrite arm spacing changed more rapidly than the secondary arm spacing with distance from the chill surface of a mould and concluded that primary arm spacing was more sensitive to growth conditions. In the work of WEINBERG and BUHR, however, two growth parameters, namely growth rate and temperature gradient, varied continuously throughout the period of solidification: in effect, both parameters decreased as the solid-liquid front moved away from the chill surface. While both parameters affect the dendrite arm spacing in the same manner, as seen in Section 2.6, the results of the present experiments, in which the temperature gradient across the growing solid-liquid region was not changed, show indirectly that the temperature gradient has a more pronounced influence on the primary arm spacing than on secondary arm spacing. More direct experiments which would involve varying the temperature gradient at constant composition and velocity are required to confirm this point.

Since BÄCKERUD and CHALMERS (1969) showed that solute concentration has considerably less influence on dendrite arm spacing than growth rate, it follows from the discussion above that caution must be exercised to avoid variations in temperature gradient in experiments designed to determine the effect of concentration on dendrite arm spacing. This is possibly the reason for conflicting evidence in the literature on the influence of solute concentration on dendrite arm spacing.

The decrease in secondary arm spacing in relation to primary arm spacing in the Fe - 13 Wt% Mn - 0.25 wt% S specimens as growth rate increased is possibly related to dendrite arm coarsening (growth of large dendrite arms at the expense of small ones). The work of KATTAMIS, COUGHLIN and FLEMINGS (1967), JACKSON et al. (1966) and others discussed in Section 2.6 of the literature review showed that coarsening occurs rapidly when dendrite arms are in contact with the interdendritic liquid. In the present experiments, the secondary arms were in contact with the liquid phase a shorter period of time at the higher growth rate; hence less time was available for coarsening and the secondary arm spacings remained smaller. Coarsening did not affect primary arm spacing to the same extent because of the much larger diffusion distances between primary arms.

MICROSEGREGATION IN IRON-HIGH MANGANESE-SULPHUR ALLOYS

The results of experiments on specimen 9 were particularly clear and merit a detailed discussion.

There has been a tendency in the literature to confuse inter-dendrite arm regions with primary grain boundaries and associate the location of sulphide inclusions and solute enrichment with austenite grain boundaries in as-cast steel structures. TURKDOGAN and GRANGE (1968) pointed out the difference in Fe - 1.5 wt% Mn - 0.05 wt% S - 0.25 wt% C alloys that were heat-treated and chemically etched. Autoradiographs in the work of WEINBERG and BUHR (1967) on AISI 4340 castings (0.41 wt% C, 0.66 wt% Mn, 0.35 wt% Si, 0.12 wt% S, 0.01 wt% P, 1.88 wt% Ni, 0.95 wt% Cr and 0.28 wt% Mo) also indicated that many of the dendrites were coupled together in regular arrays and hence were part of the same grain. The distinction is particularly clear in Figure 6.3.24 of the present investigation, which shows the steady-state growth region of specimen 9, an Fe - 13 wt% Mn - 0.25 wt% S alloy. Two large grains are visible and each one contains segregation cells or dendrite arms of common orientation delineated by manganese sulphide inclusions and dark interdendritic regions enriched in manganese and sulphur. There is no enhancement of solute segregation or inclusion density in the boundary region between the two grains.

There are other important points about the structure of specimen 9. In Figure 6.3.22, the solidification structure is essentially invariant in the bottom micrograph of the composite; the micrograph at the top contains horizontal dendrites which grew from the alumina crucible wall, an indication that this region was liquid at the time of the quench. At first glance, it seems that the only statement possible as to the location of the tips of primary dendrite arms just prior to quenching is that they were in the region covered by the three middle micrographs. Upon closer inspection, however, it is seen that the secondary arm spacing changes very rapidly in the region indicated by the letter D. It is also evident from the necking down of the primary arm at point D that a change in growth conditions has taken place. There are two types of spacing changes: the first is due to the acceleration of dendritic growth on quenching and the second is due to the fact that the secondary arms do not have time to coarsen. It is important to know the location of the primary arm tips at the moment of quenching because it then becomes possible to observe the succession of solidification-related events in time.

A notable phenomenon evident in Figure 6.3.22 is the variation in segregation degree between secondary arms. Indeed, in the bottom micrograph near point G there is only faint evidence of composition differences, while in the micrographs above, white areas with a $\Delta C_{Mn} \approx 4$ wt% are quite numerous. The distance between points C and G is approximately 1 cm; the corresponding time differential is about 12 min and the temperature differential about 30°C.

As was seen in Section 2.3.2, one mode of homogenization is back-diffusion of solute during solidification. In order to verify the possibility of this mechanism, it is instructive to apply FLEMINGS' criterion for back-diffusion:

$$\alpha_S = D_S t_f / \lambda^2 , \qquad \alpha_S \gg 1 \text{ for back-diffusion}$$

Assuming the solid phase is γ_{Fe}, the diffusivity of Mn is around 10^{-8} cm^2/sec, as shown in Figure 2.1.1. Substituting $t_f = 12$ min and $\lambda = 50$ microns,

$$\alpha_S = \frac{10^{-8} \times 60 \times 12}{(50 \times 10^{-4})^2} \approx 0.3$$

This value indicates that back-diffusion in the solid phase during solidification is not a large effect. Even if it is assumed that the system crystallizes to δ_{Fe} (unlikely), in which case the diffusivity of Mn is around 10^{-7} cm^2/sec (Figure 2.1.1) and $\alpha_S \approx 3$, the amount of manganese diffusion does not appear to be large enough to explain the effectively uniform-solute distribution between secondary arms.

It appears that the homogenization phenomenon can be better explained in terms of continuous variations in the solidification structure, as shown in Figure 7.1.4-a. The top portion of this figure corresponds to the top portion of Figure 6.3.22, which is an arrested growth picture revealing roughly what the structure was like during the initial stages of solidification. The secondary arms around the primary arm tips have a spacing dictated by the local growth conditions. As the secondary arms grow away from the primary arm, they reject solute laterally, i.e., in a direction parallel to the primary arms in Figure 7.1.4-a. The depth of the grooves between the secondary arms attached to a given primary arm varies in proportion to the severity of growth conditions; at higher growth rates, the grooves are deeper, and the secondary arms are more rod-like in appearance. The spacing of the secondary arms at some distance from the primary arm tips is different and is likely controlled by local growth conditions quite different from those prevailing at the primary arm tips. In particular, the temperature gradient in the direction normal to the primary arms is undoubtedly very shallow. As growth continues, solute flows outwards from the roots of the secondary arms of a given primary arm into the interprimary arm liquid, as shown in Figure 7.1.4-a, and from regions where the solute fields of secondary arms of different primary arms impinge, as shown in Figure 7.1.4-b. Capillarity effects also raise the liquid interfacial concentration and hence assist in the process of driving solute out. Hence the solute is driven to the interprimary arm liquid from all directions, as is apparent in the bottom portion of Figure 6.3.22.

This explanation appears reasonable because it involves solute transport by diffusion in the liquid phase, which is a relatively fast process. The fact that it was manganese that was rapidly redistributed during solidification of specimen 9 gives added support to this mechanism.

As reported in Section 6.3.3, the large light-grey areas of the structure of Figure 6.3.22 had a uniform composition close to k_0C_0 and were delineated by small areas comprising sharp concentration gradients (in white). This is an indication that the primary dendrite arm tips were rather blunt during growth and rejected a considerable amount of solute into small interdendritic volumes.

This mode of solidification brings to mind the "duplex" solidification model used by DOHERTY and MELFORD (1966), whose work was reviewed in Section 2.3.2. They interpreted their results on microsegregation experiments by combining the steady-state model of BOLLING and TILLER (1961) for primary dendritic growth and the maximum segregation model represented by Equation 4.2.13 for solidification of the final interdendritic liquid. It should be noted here that in view of the work done on the variation of k_0 with concentration (Section 4.1), and the large solute accumulation in the final interdendritic liquid and the cellular structure in the last stage of solidification, it is doubtful that the multicomponent maximum segregation model, Equation 4.2.14, would hold in this alloy.

As reported in Section 6.3.3, some manganese distributions were measured in the area where the primary dendrite tips were located just prior to quenching. These distributions are shown in Figure 6.3.38. It is interesting to note that they have the shape of horizontal braces, not unlike those reported in a paper by KOHN and PHILIBERT (1960) for a Fe - 1.1 wt% P alloy solidified by aspirating the melt into a cold refractory tube. The fact that the distributions have the shape of horizontal braces is good evidence that the solidification mechanism involved a decaying solute profile ahead of the solid-liquid interface. It is possible, however, that the distributions in this area were in fact transient state distributions produced by rapid growth on quenching. Indeed, as seen in Figures 6.3.22 and 6.3.37, the microanalysed area was possibly slightly ahead of the primary dendrite arm tips at the time of the quenching operation.

EFFECT OF SOLIDIFICATION GEOMETRY ON MICROSEGREGATION

In the following, some interesting effects of solidification geometry encountered in Figures 6.3.33 to 6.3.36 are discussed in terms of the theory outlined in Section 4.2.1. The electron probe traces across primary dendrite arms in specimens 6, 9, 13 and 14 revealed that the degree of microsegregation along [x] paths was greater than along [+] paths. This effect appears to be accounted for in terms of the generalized maximum segregation model which led to Equation 4.2.13. The index n in this equation would be around 1 for the [+] path, approximately 2 for the [x] path in the quasi-cellular structure of specimens 6 and 9 shown in Figures 6.3.33 and 6.3.34, and possibly 3 for the [x] path in specimens 13 and 14 as shown in Figures 6.3.35 and 6.3.36. In this respect, the results are qualitatively similar to those of KATTAMIS and FLEMINGS (1965) who studied the segregation of Ni and Mn in AISI 4340 steels. However, these workers did not propose an explanation for the difference in the degree of microsegregation between [x] and [+] paths.

The segregation ratios of specimens 6, 9, 13 and 14 were determined from the electron-probe traces. However, before discussing these results, a few words of caution à propos the segregation ratio are in order.

While the segregation ratio has been extensively used in the literature to characterize microsegregation, it is important to keep in mind that it is a rather incomplete measure of microsegregation. Indeed, it takes into consideration only two points on the solute distribution curve. It is thus conceivable for two entirely different segregation patterns to yield the same segregation ratio. In theory, maximum segregation occurs at low cooling rates (provided there is no back-diffusion of solute into the solid), when the effective partition coefficient k_e equals the equilibrium partition coefficient k_0. At relatively higher cooling rates, solute build-up in front of the interface increases the value of k_e and reduces the amount of segregation. The two cases are shown in Figure 7.1.5. Clearly the segregation ratios are similar while the severities of segregation are very different. The values of C_M are also subject to considerable error as the peaks of the solute distributions are generally quite sharp and difficult to determine accurately; also, values of C_m may be so low as to be immeasurable: in such cases, the segregation ratio is meaningless.

The manganese segregation ratios of specimens 9, 13 and 14 (alloys of Fe - 13 wt% Mn - 0.25 wt% S) were found to decrease slightly with increasing solidification rate. However, these results were questioned on the basis that the manganese distributions of Figures 6.3.34 to 6.3.36 would be expected to change somewhat with the location of the cross-sections normal to the macroscopic growth direction of the specimens. Indeed, the experiments conducted on specimen 24 (an iron alloy which effectively contained 10 wt% Mn and 0.25 wt% S) solidified at growth rates of 100 to 400 mm/hr did not confirm the former results: no variation of segregation ratio with growth rate was observed. The latter results are in accord with the views of BRODY and FLEMINGS (1966) and the experiments of KATTAMIS and FLEMINGS (1965) who found no marked effect of cooling rate on microsegregation. More confidence should be placed on the results obtained on specimen 24 since

i) the solute distributions between a greater number of dendrite arms were examined;

ii) the average composition was the same at all levels of specimen 24 and hence at all growth rates;

iii) the temperature gradient was the same at all levels of the specimen.

The segregation ratio at 50 mm/hr is slightly but significantly lower: it is probable that the solidification structure was somewhat different in this region, e.g., tending more towards a cellular rather than a cellular-dendritic morphology. It is interesting to note that the lower segregation ratio in the region of specimen 24 solidified at 50 mm/hr is reflected in the appearance of Figure 6.3.11 where the contrast is definitely not as sharp as in Figures 6.3.12 to 6.3.14 which are typical of regions solidified at higher rates.

The reason for the constancy in the degree of microsegregation is that the dendrite arm spacing — growth rate relationship admits of a rough dimensional similarity. FLEMINGS (1964) touched on this effect of dimensional similarity in his analysis of diffusion in the solid phase during solidification. He stated that the important parameter determining the extent of diffusion was:

$$\alpha_L = D_S t_f / \lambda^2 \qquad (7.1.2)$$

Recognizing that the dendrite arm spacing, d, and hence one-half the dendrite arm spacing, λ, was proportional to the local solidification time, t_f, to the power n, and the diffusivity in the solid D_S,

$$\lambda \propto D_S t_f^n \qquad (7.1.3)$$

and substituting this relation into the previous equation, FLEMINGS obtained:

$$\alpha_S \propto D_S / t_f^{2n-1} \qquad (7.1.4)$$

He then pointed out that when $n \approx \frac{1}{2}$, (this is often true as seen in Sections 2.6, 4.4 and 6.3.2) then:

$$\alpha_S \propto D_S \qquad (7.1.5)$$

and hence α_S was independent of the solidification time.

FLEMINGS' analysis can be extended to the case of diffusion in the liquid phase. This yields

$$\alpha_L \propto D_L / t_f^{2n-1} \qquad (7.1.6)$$

and for $n = \frac{1}{2}$

$$\alpha_L \propto D_L \qquad (7.1.7)$$

Therefore the homogenization parameter α_L is also independent of solidification time or velocity.

In view of Equations 7.1.4 and 7.1.6, it is clear that the microsegregation should be at most a weak function of growth rate or solidification time.

In cases where $n < \frac{1}{2}$, Equation 7.1.4 shows that α_S is proportional to t_f and hence homogenization of the solid phase can be expected to occur and reduce the degree of microsegregation. However, this means that the degree of homogenization in the liquid phase is also greater, as seen from Equation 7.1.6, and hence, by virtue of the theory given in Section 4.2, the degree of microsegregation tends to be more severe. Therefore, the net effect is that the degree of microsegregation tends to remain at a constant value, even when $n < \frac{1}{2}$. As was seen in the results of the present investigation (Section 6.3.2), the value of n is in some cases as low as approximately 1/4.

7.2 - INCLUSIONS

OXIDE INCLUSIONS

Some unusual and interesting results on inclusions obtained in this experimental investigation are discussed at the beginning of this section.

While it had been planned originally to study solidification Fe - low Mn - S alloys, oxygen had to be taken into account since the oxygen reached as high as 400 ppm during the solidification process. As a result, the inclusions of specimens 1, 5, 7, 10 and 12 precipitated as Fe - Mn - S - O inclusions containing small amounts of sulphur (typically 5 wt%) and large amounts of oxygen (typically 20 wt%) as shown in Table 6.4.1. In the case of specimens 1, 7 and 10, the evaporation of manganese through the free surface at the top of the specimens became an added complication, setting up concentration gradients as shown in Figures 6.2.1, 6.2.5 and 6.2.7. This in turn caused a variation in the Fe/Mn ratio of the inclusion as seen in Table 6.4.1 and reported in Section 6.4.3: as the manganese concentration increased from almost 0 wt% at the top of the specimen to its constant value in the unmelted matrix, the inclusions became progressively richer in manganese and correspondingly poorer in iron.

The relevance of this phenomenon is that it suggests an interesting technique for the rapid determination of isotherms in the Fe - Mn - S system and higher under systems of industrial interest, e.g., Fe - Mn - S - X - Y. Indeed, specimens such as 1, 7 and 10 could be homogenized for a short period of time at a given temperature to allow the inclusions to attain local equilibrium with the surrounding matrix. After quenching the specimen, the inclusion and matrix compositions could be measured by electron-probe microanalysis. A large portion of the isotherm could thus be determined using one specimen. Details of the technique are given in the summary under suggestions for future work.

INCLUSION FLOTATION

Another interesting phenomenon was inclusion flotation which, it appears, was responsible in part for the differences between the inclusion distributions of specimens 1 and 7. As reported in Section 6.4.1, inclusions were found only in a region 2 cm long at the top of specimen 1, while inclusions were evenly distributed in specimen 7.

The terminal velocity of an inclusion of a given diameter rising in a melt can be estimated from Stokes' law:

$$V_I = \frac{\omega \Phi^2 (\psi_M - \psi_I)}{18\nu} \qquad (7.2.1)$$

where: V_I = terminal flotation velocity of inclusion [cm/sec]

ω = gravity constant [$\mathrm{cm/sec^2}$]

Φ = diameter of inclusion [cm]

ψ_I = density of inclusion [$\mathrm{g/cm^3}$]

ψ_M = density of metal [$\mathrm{g/cm^3}$]

ν = viscosity [poise]

Hence, the diameter Φ of inclusions which avoid entrapment by the solid-liquid front advancing at a rate V_I can be calculated by rearranging the previous relation:

$$\Phi = \left[\frac{18\ V_I\ \nu}{\omega(\psi_M - \psi_I)} \right]^{\frac{1}{2}} \tag{7.2.2}$$

Substituting into this relation the data of Table 7.2.1 and the solidification velocity of specimen 1, $V_I = 1.4 \times 10^{-4}$ cm/sec, gives:

$$\Phi = \left[\frac{18 \times 1.4 \times 10^{-4} \times 0.07}{981\ (7.3-4)} \right]^{\frac{1}{2}} \approx 2 \times 10^{-4}\ \text{cm}$$

or: $\Phi \approx$ 2 microns

The calculation indicates that, in the case of specimen 1, inclusions of diameter equal or greater than 2 microns should escape to the surface of the melt. Repeating the calculation for specimen 7, solidified at a velocity greater by an order of magnitude ($V_I = 1.4 \times 10^{-3}$ cm/sec), it is found that only inclusions of somewhat larger diameter (~ 7 microns) should be capable of floating away from the interface. Hence the macrosegregation of inclusion material should be more intense in specimen 1.

The analysis assumes, of course, that the inclusions have an open channel to the surface. The structure of specimen 1 was probably less tortuous than that of specimen 7 since the growth conditions were less severe, and hence less likely to retain inclusions. However, this is somewhat speculative since efforts to reveal the solidification structure of specimens 1 and 7 were unsuccessful.

INCLUSION-INTERDENDRITIC LIQUID CORRELATIONS

A strong correlation between the position of inclusions and last-solidified regions was observed in all specimens where the microsegregation was revealed with sufficient clarity. Good examples of this correlation are found in Figures 6.3.5, 6.3.6, 6.3.23, and 6.3.24 which are micrographs of specimen 9, an Fe - 13 wt% Mn - 0.25 wt%S alloy solidified at 50 mm/hr. This correlation is also evident, upon closer inspection in other micrographs. Even in regions of specimens quenched from the liquid state, such as those shown for example in Figures 6.3.27 to 6.3.30, the sulphides were generally in the last-solidified region. In the light of the results on specimen 25 in which zirconia particles were pushed into the interdendritic regions by the solid-liquid interfaces, it can be concluded that even if sulphides are nucleated near the core of dendrites they will eventually wind up in the interdendritic regions. There is some uncertainty here as to whether or not the sulphide inclusions behave as zirconia particles. However, in the light of the work of UHLMANN and CHALMERS (1964) reviewed in Section 4.3.2, it is probable that the aforementioned conclusions are valid. These observations have some bearing on the validity of experiments, reported in Section 2.3.3 of the literature, which attempted to establish correlations between the position and type of inclusion, e.g., type II inclusions in cell boundaries and type III inclusions in dendrite cores.

The mechanism of inclusion-pushing probably contributed to the long-range inclusion transport observed in specimen 1: it is possible that inclusions too small to float upwards were pushed by the advancing solid-liquid interface.

There is an interesting correlation between the inclusion patterns of Figures 6.4.2 and 6.4.3 and the columnar dendrite model of Figure 7.1.1. With respect to this model, the long inclusion of Figure 6.4.3 would be located in the interdendritic space in the centre of the four dendrite units; the inclusions of Figure 6.4.2 disposed in circles would appear to have precipitated around the secondary arms of the dendritic skeleton. It is possible that the inclusion material, which was most likely liquid because of the high oxygen content of the melt ($\sim$ 400 ppm), was pushed to the centre of the dendrite units by the advancing solid fronts and coalesced to form the lengthy stringers.

INCLUSIONS IN HIGH MANGANESE ALLOYS

The experiments on specimens 9, 13 and 14 yielded a considerable amount of information on inclusions which merits further discussion. These specimens, it will be recalled, were Fe - 13 wt%

Mn - 0.25 wt% S alloys solidified at growth rates of 50, 280 and 600 mm/hr respectively.

The formation of these inclusions can be interpreted in terms of the divorced eutectic concept — see CHALMERS (1964). It appears from Figure 2.3.4 that with 0.25 wt% S, the composition of the specimens was close to the eutectic trough which runs parallel to the Fe - Mn binary of the Fe - Mn - S system. Also, it is clear from this diagram that sulphur is the controlling species in the precipitation of MnS sulphides. Thus sulphur was rejected with the result that the concentration at the solid-liquid interface eventually exceeded the eutectic composition and entered the Fe + β MnS region, as shown in Figure 2.3.3 -b. At a given supersaturation degree the manganese sulphides nucleated. Since the amount of second phase was small, the growth was non-cooperative, with the result that the MnS inclusions grew as isolated entities.

The large faceted MnS inclusions found in the vicinity of the original interface and shown in Figures 6.4.12 and 6.4.13 are strong evidence that inclusions undergo a ripening process in solid-liquid systems. Indeed, comparisons of Figures 6.4.12 and 6.4.14 which are micrographs of adjacent regions in the specimen strongly suggest that the larger inclusions grew at the expense of the smaller ones which dissolved into the matrix. This phenomenon is generally referred to as "OSTWALD ripening" and occurs because the surface free enthalpy per unit volume is greater for the smaller inclusions than it is for the larger ones. The ripening process in the solid system at the same temperature, Figure 6.4.14, is clearly much slower.

The reason why these large inclusions were found only in the vicinity of the initial location of the solid-liquid interface is that the specimens were usually held in the fixed temperature gradient for approximately an hour before the start of solidification to allow the solidification apparatus to attain thermal equilibrium. The inclusions which precipitated from the melt during solidification did not remain in solid-liquid regions long enough for ripening to occur to the same extent. As mentioned, however, in Section 6.4.2, the inclusions of specimen 9 were significantly larger than the inclusions of specimens 13 and 14, the reason being, of course, that more time was available for inclusion growth in specimen 9.

INCLUSIONS IN Fe - Mn - S - C ALLOYS

There remains to be discussed the observations on specimens 2 and 6 which are iron-base alloys with manganese, sulphur and carbon concentrations approaching those of commercial steels.

While specimens 2 and 6 were Fe - Mn - S - C alloys, their solidification behaviour can be interpreted in terms of the more tractable Fe - Mn - S system, which was reviewed in Section 2.2. Indeed, it was seen that carbon distorts the Fe - Mn - S phase space but does not qualitatively alter it, at least in the iron-rich portion of the diagram: the principal effect of carbon is to pull the eutectic trough into the iron corner. It was also seen in Section 2.3.2 of the literature survey and indeed in this investigation that alloys seldom solidify under true equilibrium conditions. The composition changes accompanying solidification may be followed in relation to the phase diagram: as manganese and sulphur are rejected to the liquid, the maximum instantaneous solute concentration at the solid-liquid interface must increase to a level given by some point on the liquidus isotherm at the interface temperature. As the local temperature drops, the interface composition trajectory (equivalent to the composition of the liquid phase if it is uniform) approaches the eutectic trough EDC shown in Figure 2.2.3. In general, a finite undercooling is necessary for the nucleation of a new phase, in this case, sulphide, which depends on the ease with which nucleation of the new solid can take place. This undercooling is expected to be important in the present case where the equilibrium volume fraction of the sulphide phase is very small, and the cooperative eutectic reaction is easily suppressed. This leads to the ternary analogue of the divorced eutectic reaction discussed by CHALMERS (1964). It is then necessary to consider the metastable regions of the solid-liquid iron and FeS - MnS equilibria. These are shown schematically in Figure 7.2.1. For high manganese alloys, e.g., specimen 6 which contained 3 wt% Mn, the segregation trajectory given by a calculation similar to that of Figure 4.2.3 will cause a supersaturation with respect to MnS only, as shown by path AB on Figure 7.2.1. This case is similar to that of inclusion formation in the high manganese alloys of specimens 9, 13 and 14 which was discussed before in less detail. On the other hand, for low manganese alloy, e.g., specimen 2 which contained 0.5 wt% Mn, the segregation trajectory CD may cause a supersaturation with respect to β MnS or both β MnS and L_2 (liquid FeS) depending on the precise location of the phase fields. This gives a plausible explanation for the presence of duplex FeS - MnS inclusions in specimen 2, Figure 6.4.18, and the variation in the Fe/Mn ratio of the inclusions (Table 6.4.1). Indeed, as can be appreciated in Figure 4.2.4, variations in the solidification geometry in a given specimen can alter the solidification trajectory of an alloy and cause a variation in the type and Fe/Mn ratios of the products. KIESSLING and LANGE (1963) also reported quite a variation in the Fe/Mn ratio of inclusions in a given carbon steel sample, but did not propose an explanation for this effect.

Some interesting features of inclusions in specimen 2 also warrant further discussion. Indeed, these inclusions often had a sinusoidal interface, as shown in Figure 6.4.6. These inclusions were identical to the bead-like inclusions of Figure 6.4.5 but were positioned differently with respect to the plane of metallographic polishing. Generally, the beads were sections normal to the arms of "sinusoidal" inclusions. From the discussion of Section 2.3.3, these inclusions could be classified as Type II inclusions. Indeed, they bear some resemblance to the Type II inclusions in the work of KIESSLING et al. (1963), shown in Figure 2.3.10. The inclusions would be more correctly described as film-like inclusions.

The presence of a sinusoidal interface is good evidence that these inclusions undergo transformations after precipitation from the melt. Moreover, a trend to increasing manganese concentration with time and temperature can be seen in Table 6.4.1 and may further reflect these transformations.

The transformations can be discussed in terms of Figure 7.2.2, a schematic version of the Fe - Mn - S isotherm at 1300°C presented in Figure 2.2.5 of the literature survey. A liquid FeS inclusion surrounded by solid γ_{Fe} effectively constitutes a diffusion couple which for conceptual purposes can be thought of as semi-infinite. It is then possible to follow the evolution of the diffusion process by superposing various diffusion paths leading from point A, liquid FeS, to point D, solid γ_{Fe} containing manganese. Diffusion paths in this system have been studied by NAKAO (1967) and SMITH (1970). One possible path is ABCD, in which case the sulphur concentration in the liquid FeS decreases gradually up to the diffusion couple interface (AB) then drops sharply (BC) and decreases again as sulphur diffuses into the γ_{Fe} phase (CD). However, if a segment of the diffusion path such as AB' cuts into the two-phase region γ_{Fe} + liquid FeS, the sulphide becomes supersaturated in iron, the interface becomes unstable and γ_{Fe} grows into the liquid FeS, giving rise to the shape of inclusion shown in Figure 6.4.6.

The diffusion path does not remain stationary in time but shifts across the diagram until it reaches the MnS side, path ABEFGHD. This effect is perhaps responsible for the duplex inclusions of Figure 6.4.18. Indeed, it is possible that the MnS phase was sweeping across the FeS at the time of the quench, as would be expected from the diffusion path ABEFGHD.

FERRITE NUCLEATION

Finally, a word about the ferrite nucleation experiments on specimens 2 and 23 described in Section 6.4.3. These experiments indicate that ferrite nucleates preferentially around MnS inclusions and that there is no marked correlation between the location of ferrite and FeS inclusions. On the sole basis of these experiments, it is difficult to decide which of the two following ferrite nucleation mechanisms is operating: nucleation in a manganese-poor region or nucleation at a phase boundary. Indeed, the two sulphides may have different nucleating efficiencies. However, the present experiments do lend support to the mechanism of ferrite nucleation in a manganese-poor region.

CHAPTER 8

SUMMARY

This chapter contains the sum and substance of the work carried out and the results obtained in the course of this investigation on high-temperature solidification phenomena in some Fe - Mn base alloys.

FURNACE AND SPECIAL TECHNIQUES

1) An apparatus was designed, constructed and utilized in the controlled solidification of iron-base alloys. A vertical furnace design was chosen so as to minimize natural convective stirring of the melt and was successful in this regard as demonstrated by a diffusion couple experiment involving liquid iron on one side and a liquid iron - 8 wt% nickel alloy on the other side. The penetration curve of nickel in iron was closely approximated by an error function solution of the diffusion equation, and hence mixing was considered to have taken place by diffusion only. The diffusivity of nickel in iron at 1550°C was found to be 3×10^{-5} cm^2/sec.

2) The practical operating limits of the apparatus are 0.5 - 100 cm/hr for solidification velocity and 0 - 50°C/cm for tempera-

ture gradients. The furnace temperature at any given point normally fluctuates less than 2°C during the solidification runs.

3) A technique for measuring temperature gradients in the specimens during solidification runs was developed and improved until accurate results were obtained. In the final solution, a 0.010" dia. Pt/Pt - 13% Rh thermocouple protected by a small (1.5 mm dia.) alumina sheath was run horizontally through the vertical melt.

4) The segregation patterns in iron-high manganese-sulphur alloys can be revealed using the sulphide tinting technique developed in this investigation. The technique consists essentially of immersing a freshly-polished surface containing at least 7 wt% Mn in a solution of H_2S-saturated water.

CONSTITUTIONAL INTERACTION OF SOLUTES

1) A mathematical analysis of terminal two-phase equilibria in ternary systems was carried out in the course of this investigation. The isotherms determined, using the results of this analysis, are possibly more accurate and certainly more economically obtained than isotherms determined by experimental methods, provided that the limiting binary phase diagrams and the relevant thermodynamic parameters are accurately known.

2) The analysis also gives a justification for straight-line construction of phase boundaries and generation of tie-lines by constant

partition coefficients used for approximating dilute ternary isotherms.

3) Moreover, the analysis predicts the effect of interaction between solutes on the value of the equilibrium partition coefficients in ternary systems. In the Fe - Mn - C system where the interaction between manganese and carbon in the solid and liquid phases is weak, both solute partition coefficients decrease slightly with increasing carbon concentration. However, had the interaction been large and negative, e.g., $\epsilon_{12}^{L} = \epsilon_{12}^{S} = -10$, the partition coefficient of carbon would have increased and that of manganese would have decreased, both in significant amounts; conversely had the interaction been large and positive, e.g., $\epsilon_{12}^{L} = \epsilon_{12}^{S} = +10$, the partition coefficient of carbon would have decreased and that of manganese would have increased. Since carbon interacts in a strong and negative manner with most solutes in steel melts, it is proposed that this constitutional-type of interaction is one mechanism whereby carbon enhances the segregation of other elements, especially in the final stage of solidification when the interdendritic liquid is highly enriched.

4) Finally, the analysis shows that it is possible, at least in theory, to reduce microsegregation in castings by a judicious choice of solute elements, e.g., by using a fast-solid-state diffusing ele-

ment to increase to unity the partition coefficient of another slowly diffusing element.

DENDRITE ARM SPACING

1) The review of literature and the theoretical considerations on the relationship between dendrite arm spacing and important solidification parameters and growth conditions showed that spacing measurements had to be carried out under well-defined experimental conditions in order to be meaningful. A number of measurements of primary and secondary arm spacings as a function of growth velocity at fixed concentration and thermal gradient were carried out using the controlled-solidification apparatus constructed for this investigation.

2) Dendrite arm spacing varies with the inverse of the growth rate with an exponent in the range 1/2 to 1/4.

3) Primary arm spacing is less sensitive than secondary arm spacing to variations in the growth rate.

4) The secondary arm spacing decreases in relation to primary arm spacing as growth rate increases. This effect is possibly related to the phenomenon of dendrite arm coarsening. Indeed, the secondary arms remain in contact with the liquid phase a shorter period of time at higher growth rates, and hence less time is available for coarsening.

MICROSEGREGATION

1) There is no enhancement of solute segregation or inclusion density in boundary regions between primary grains on dendrites of different orientation.

2) The solidification structure in the steady-state regions of specimens was cellular-dendritic and generally more plate-like than rod-like. In the quenched regions of the specimens, the structure was truly dendritic. The concentration variation across the primary arms was much weaker in cellular-dendritic structures than in purely dendritic structures. This is considered to be due to the large volume fraction occupied on initial growth by the rather blunt cellular dendrites.

3) Secondary arms develop at an early stage of solidification with a spacing dictated by growth conditions (especially solidification rate and temperature gradient). Coarsening takes place continually. The geometry of the solid-liquid closure requires that solute diffusion take place parallel to the solid-liquid interfaces resulting in intense segregation channels parallel to primary dendrite arms.

4) A transition from an open type of cellular-dendritic structure to a close-packed type of structure as growth rate increased was observed in the present study. It appears that this transition takes place because the system can no longer create enough new solid-

liquid area for solute rejection by a simple change in dendrite arm spacing.

5) It was found that, for a given solidification structure, there was a considerable variation in the degree of microsegregation along different paths in the structure. This effect is attributable to differences in the geometry of various solidifying portions of the structure and is predicted by the generalized maximum segregation model developed in this study.

6) Solute distributions between secondary arms in the quenched liquid immediately ahead of the primary dendrite arms were found to have the shape of horizontal braces. This was taken as evidence for solute inhomogeneity in the liquid phase.

7) Stepped velocity experiments showed that the degree of microsegregation was independent of solidification rate provided only that the solidification structure remained similar. This is to be expected since the dendrite arm spacing-growth rate and the characteristic diffusion distance-growth rate relationships are roughly similar. Indeed, both dendrite spacing and characteristic distance are approximately proportional to the inverse square root of the growth rate.

8) As a result of calculations on a ternary coupled-diffusion model developed in this study, it appears that the application of

diffusion criteria to solidification problems, as proposed by BRODY and FLEMINGS (1966), can be misleading. These criteria are unquestionably valid when applied to systems in which boundary conditions are fixed, e.g., in semi-infinite diffusion couples. However, the boundary conditions at a solid-liquid interface vary continuously as solidification proceeds.

INCLUSIONS

1) Ferrite nucleation experiments on iron-manganese-sulphur-carbon alloys indicated that ferrite nucleates preferentially around MnS inclusions and that there is no marked correlation between the location of ferrite and FeS inclusions.

2) Inclusions are chiefly found in interdendritic regions regardless of their origin. This is to be expected on two counts: firstly, in the case of sulphide inclusions a microsegregation mechanism must operate to increase the sulphur concentration to a point where it exceeds the solubility limit; secondly, the physical pushing of inclusions by a solid-liquid interface is fairly well established. In the present investigation the phenomenon of inclusion pushing was verified by solidifying iron-manganese alloys containing zirconia powder. After solidification, the zirconia was found in the interdendritic channels.

3) The development of inclusions in steels (iron-manganese-

sulphur-carbon alloys) was followed in this investigation. In alloys containing 3 wt% Mn, there are indications that solid β MnS inclusions form directly from the melt. On the other hand, in alloys containing 0.5 wt% Mn, the results suggest that the initial sulphide formed is liquid FeS which subsequently transforms to MnS with an attendant rejection of iron.

4) The formation of sulphide inclusions was interpreted in terms of multicomponent divorced eutectic solidification. As the melt cools, the interfacial liquid concentration rises and eventually becomes supersaturated. The initial manganese and sulphur concentrations then determine whether the microsegregation trajectory first enters the metastable FeS + Liquid or MnS + Liquid regions of the constitution diagram.

SUGGESTIONS FOR FUTURE RESEARCH

1) It is suggested that the feasibility of the following technique for the determination of isotherms in the Fe - Mn - S system and higher order systems of industrial interest be explored:

i) allow the melt to remain stationary for several hours to establish a manganese concentration gradient;

ii) solidify the specimen at a rate of roughly 50 mm/hr to produce inclusions sufficiently large for electron-probe microanalysis;

iii) quench the specimen;

iv) homogenize the specimen at the isotherm temperature of interest (local equilibrium between the inclusions and the matrix should obtain after a short homogenization period);

v) quench the specimen;

vi) use electron-probe microanalysis to determine the composition of inclusions and adjacent matrix at various locations in the specimen.

Clearly, the specimen could be rehomogenized at different temperatures and other isotherms determined in this manner.

2) It would be interesting to carry out a critical experiment to ascertain by which mechanism ferrite nucleates around manganese-rich inclusions. It is proposed that a specimen containing (Fe, Mn) S inclusions be prepared, then given a first heat treatment to promote rejection of manganese rather than iron, and a second treatment to cause nucleation of ferrite. The presence of pearlite rather than ferrite next to the inclusions would support the mechanism of ferrite nucleation in a manganese-poor region rather than the mechanism of nucleation at a phase boundary.

REFERENCES

ADAMS, C.M. and TAYLOR, H.F., Trans. Am. Found. Soc., 61, 686 (1953).

ADCOCK, F., J. Iron Steel Inst., 135, 281 (1937).

AHEARN, P.J. and QUIGLEY, F.C., Trans. Am. Found. Soc., 72, 435 (1964).

AHEARN, P.J. and FLEMINGS, M.C., Trans. Met. Soc. AIME, 239, 1590 (1967).

ALBERNY, R., SERRA, J. and TURPIN, M., Trans. Met. Soc., AIME, 245, 55 (1969).

ALEXANDER, B.H. and RHINES, F.N., Trans. AIME, 188, 1267 (1950).

BÄCKERUD, L. and CHALMERS, B., Trans. Met. Soc. AIME, 245, 309 (1969).

BARLOGA, A.M., BOCK, K.R. and PARLEE, N., Trans. Met. Soc. AIME, 221, 173 (1961).

BASINSKI, Z.S. and CHRISTIAN, J.W., Proc. Roy. Soc. A-223, 544 (1954).

BEAUJARD, L., Rev. Mét., 49, 531 (1952).

BEAUJARD, L., Rev. Mét., 52, 750 (1955).

BEERWALD, A.H., Z. Elektrochem., 49, 238 (1943).

BELL, J.A.E. and WINEGARD, W.C., J. Inst. Met., 92, 357 (1963-64).

BILONI, H., in The Solidification of Metals, ISI Publ. 110, London, 74 (1967).

BOLLING, G.F. and TILLER, W.A., J. Appl. Phys., 32, 2587 (1961).

BOOTH, A.R. and CHARLES, J.A., Iron and Steel, 42, 298 (1969).

BOWER, T.F., BRODY, H.D. and FLEMINGS, M.C., Trans. Met. Soc. AIME, 236, 624 (1966).

BRICK, R.M. and PHILLIPS, A., Structure and Properties of Alloys, McGraw-Hill, New York (1949).

BRIGGS, C.W., The Metallurgy of Steel Castings, McGraw-Hill, New York (1946).

BRODY, H.D. and FLEMINGS, M.C., Trans. Met. Soc. AIME, 236, 615 (1966).

BROWER, T.E., LARSEN, B.M. and SHENK, W.E., Trans. AIME, 113, 61 (1934).

BURTON, J.A., PRIM, R.C. and SLICHTER, W.P., J. Chem. Phys., 21, 1987 (1953).

CAINE, J.B., Trans. Am. Found. Soc., 56, 492 (1948).

CARSLAW, H.S. and JAEGER, J.C., Conduction of Heat in Solids, Oxford University Press, London (1947).

CASTAING, R., Adv. Electronics Electron Phys., 13, 317 (1960).

CATTIER, P., DUBOIS, C., BLETON, J. and BASTIEN, P., Rev. Mét., 50, 275 (1953).

CHALMERS, B., Principles of Solidification, John Wiley and Sons, New York (1964).

CHAO, H.C., VAN VLACK, L.H., OBERIN, F. and THOMASSEN, L., Trans. ASM, 57, 885 (1964).

CHERNOV, A.A., Kristallographiia, 1, 583 (1956).

CHWORINOV, N., Giesserei, 27, 177 (1940).

CLARK, I.S.R., Master's Thesis, McMaster University (1964).

CLAYTON, D.B., SMITH, T.B. and BROWN, J.R., J. Inst. Met., 90, 224 (1961).

COATES, D.E., SUBRAMANIAN, S.V. and PURDY, G.R., Trans. Met. Soc. AIME, 242, 800 (1968).

COLE, G.S. and WINEGARD, W.C., J. Inst. Met., 92, 322 (1963-64).

COLE, G.S. and WINEGARD, W.C., J. Inst. Met., 93, 193 (1964-65).

COLE, G.S., Can. Met. Quart., 8, 189 (1969).

COULTHARD, J.O. and ELLIOT, R., J. Inst. Met., 95, 21 (1967-A).

COULTHARD, J.O. and Elliot, R., in The Solidification of Metals, ISI Publ. 110, London, 61 (1967-B).

CRANK, J., The Mathematics of Diffusion, Oxford University Press, London (1956).

CRUSSARD, C., KOHN, A., de BEAULIEU, C. and PHILIBERT, J., Rev. Mét., 56, 395 (1959).

DAHL, W., HENGSTENBERG, H. and DUREN, C., Stahl Eisen, 86, 782 (1966).

DARKEN, L.S. and GURRY, R.W., Physical Chemistry of Metals, McGraw-Hill, New York (1953).

DARKEN, L.S., Trans. Met. Soc. AIME, 239, 90 (1967).

DAVIES, G.J., in The Solidification of Metals, ISI Publ. 110, London, 66 (1967).

de BEAULIEU, C. and KOHN, A., C.R. Acad. Sci. France, 245, 1244 (1957).

de BEAULIEU, C. and PHILIBERT, J., C.R. Acad. Sci. France, 246, 3615 (1958).

DELORME, J., MARTIN, P., ROQUES, C. and BASTIEN, P., Mém. Sci. Rev. Mét., 58, 423 (1961).

DIEHL, R.W., McCAULEY, J.K. and LANGENBERG, F.C., J. Aust. Inst. Met., 10, 17 (1965).

DOHERTY, R.D. and FEEST, A., in The Solidification of Metals, ISI Publ. 110, London, 102 (1967).

DOHERTY, R.D. and MELFORD, D.A., J. Iron Steel Inst., 204, 1131 (1966).

ELLIOT, J.F., GLEISER, M. and RAMAKRISHNA, V., Thermochemistry for Steelmaking, Vol. 2, Addison-Wesley, Reading, Mass. (1963).

ELLIOT, R.P., Constitution of Binary Alloys, 1st Suppl., McGraw-Hill, New York (1965).

FINNISTON, H.M. and FEARNEHOUGH, T.D., J. Iron Steel Inst., 169, 5 (1951).

FLEMINGS, M.C., Trans. Am. Found. Soc., 72, 353 (1964).

FLEMINGS, M.C., in The Solidification of Metals, ISI Publ. 110, London, 277 (1967).

FLEMINGS, M.C., BARONE, R.V., URAM, S.Z. and TAYLOR, H.F., Trans. Am. Found. Soc., 69, 422 (1961).

FLEMINGS, M.C., URAM, S.Z. and TAYLOR, H.F., Trans. Am. Found. Soc., 68, 670 (1960).

FRIEDRICH, K., Metallurgie, 7, 257 (1910).

FRISKNEY, C.A. and HAWORTH, C.W., J. Sci. Instr. 1 (Ser. 2), 753 (1968).

GIBBS, J.W., Scientific Papers, Vol. 1, Dover, New York (1961).

GULLIVER, G.H., Metallic Alloys, Chas. Griffin, London (1922).

HABRAKEN, L. and DE BROUWER, J.L., De Ferri Metallographia, Vol. 1, Presses Académiques Européenes, Bruxelles (1966).

HANSEN, M., Constitution of Binary Alloys, 2nd Ed., McGraw-Hill, New York (1958).

HAWORTH, C.W., Summer School in Electron Microscopy and Microprobe Analysis, McMaster University (1968).

HAYES, A. and CHIPMAN, J., Trans. AIME, 135, 85 (1939).

HELLAWELL, A. and HUME-ROTHERY, W., Phil. Trans. Roy. Soc. Lon., A249, 417 (1957).

HELLAWELL, A., in The Solidification of Metals, ISI Publ., London, 110, 83 (1967).

HEUVERS, A., Stahl Eisen, 49, 1249 (1929).

HILTY, D.C. and CRAFTS, W., Trans. AIME, 194, 1307 (1952).

HILTY, D.C. and CRAFTS, W., Trans. AIME, 200, 959 (1954).

HOLMES, E.L., RUTTER, J.W. and WINEGARD, W.C., Can. J. Phys., 35, 1223 (1957).

HONE, M., SUBRAMANIAN, S.V. and PURDY, G.R., Can. Met. Quart., 8, 251 (1970).

HORWATH, J.A. and MONDOLFO, L.F., Acta Met., 10, 1037 (1962).

HUNT, M.D., SPITTLE, J.A. and SMITH, R.W., J. Inst. Met., 95, 123 (1967).

JACKSON, K.A., Acta Met., 7, 148 (1959).

JACKSON, K.A., HUNT, J.D., UHLMANN, D.R. and SEWARD, T.P., Trans. Met. Soc. AIME, 236, 149 (1966).

JOSEFSSON, A., KOENEMAN, J. and LAGERBERG, G., J. Iron Steel Inst., 191, 240 (1959).

KATTAMIS, T.Z. and FLEMINGS, M.C., Trans. Met. Soc. AIME, 233, 992 (1965).

KATTAMIS, T.Z., COUGHLIN, J.C. and FLEMINGS, M.C., Trans. Met. Soc. AIME, 239, 1504 (1967).

KATTAMIS, T.Z., HOLMBERG, U.T. and FLEMINGS, M.C., J. Inst. Met., 95, 343 (1967).

KEHL, G.L., The Principles of Metallographic Laboratory Practice, 3rd Ed., McGraw-Hill, New York (1949).

KIESSLING, R. and LANGE, N., J. Iron Steel Inst., 201, 761 (1963).

KIESSLING, R., BERGH, S. and LANGE, N., J. Iron Steel Inst., 201, 965 (1963).

KIESSLING, R. and WESTMAN, C., J. Iron Steel Inst., 204, 377 (1966).

KIESSLING, R. and LANGE, N., Non-Metallic Inclusions in Steel, Part II, ISI Publ. 100, London, (1968).

KIESSLING, R., Non-Metallic Inclusions in Steel, Part III, ISI Publ. 100, London (1968).

KIRKALDY, J.S. and PURDY, G.R., Can. J. Phys., 40, 208 (1962).

KIRKALDY, J.S., BRIGHAM, R.J., DOMIAN, H.A. and WARD, R.G., Can. Met. Quart., 2, 233 (1963).

KIRKALDY, J.S., McMaster University, private communication (1970).

KIRKWOOD, D.H. and EVANS, D.J., in The Solidification of Metals, ISI Publ. 110, London, 108 (1967).

KLIA, M.O., Kristallographiia, 1, 576 (1956).

KOHN, A., Rev. Mét., 51, 503 (1954).

KOHN, A., and PHILIBERT, J., Mém. Sci. Rev. Mét., 57, 291 (1960).

KOHN, A., in The Solidification of Metals, ISI Publ. 110, London, 130 (1967).

KONONYUK, I.F., Phys. Met. Metallog., 19, 159 (1965).

KUBASCHEWSKI, O. and EVANS, E. LL., Metallurgical Thermochemistry, Pergamon Press (1956).

LAPIDUS, L., Digital Computation For Chemical Engineers, McGraw-Hill, New York (1962).

LEGER, M.T. and DETREZ, P., Rev. Mét., 62, 767 (1965).

LICHY, E.J., DUDERSTADT, G.C. and SAMWAYS, N.L., J. Metals, 17, 769 (1965).

LYMAN, T., Ed., Metals Handbook, ASM, Metals Park, Novelty, Ohio (1948).

MARICH, S. and PLAYER, R., Paper Submitted for Publication in J. Iron Steel Inst. (1969).

McCARRON, R.L. and BELTON, G.R., Trans. Met. Soc. AIME, 245, 1161 (1969).

McFEE, R.H., J. Chem. Phys., 15, 856 (1947).

McGANNON, H.E., Ed., The Making, Shaping and Treating of Steel, United States Steel Corp., Pittsburg, Pa., 8th ed. (1964).

MEIJERING, J.L., Philips Tech. Rev., 27, 213 (1966).

MELFORD, D.A. and GRANGER, D.A., in The Solidification of Metals, ISI Publ. 110, London, 289 (1967).

MEYER, V.O. and SCHULTE, F., Archiv Eisen, 8, 187 (1934).

MICHAEL, A.B. and BEVER, M.B., Trans. AIME, 200, 47 (1954).

MIYAZAKI, K., Science Reports, Tohoku University, 17, 877 (1928).

MOOHLA, P.P. and BEECH, J., J. Iron Steel Inst., 207, 177 (1969).

MORGAN, D.W. and KITCHNER, J.A., Trans. Far. Soc., 51, 51 (1955).

MORRIS, W., TILLER, W.A., RUTTER, J.W. and WINEGARD, W.C., Trans. ASM, 47, 463 (1955).

MURPHY, J.B., Acta Met., 9, 563 (1961).

NAKAO, H., Master's Thesis, McMaster University (1967).

NAVIAS, L., Bul. Amer. Cer. Soc., 36, 262 (1957).

NEREO, G.E., POLICH, R.F. and FLEMINGS, M.C., Mod. Cast., 47, No. 2, 57 (1965).

OL'SHANSKII, Y.I., Dokaldy Akademii Nauk S.S.S.R., 80, 893 (1951).

PAPAPETROU, A., Z. Krist., A92, 89 (1935).

PASCHE, M. and HAUTTMANN, A., Archiv Eisen, 6, 305 (1935).

PFANN, W.G., Trans. AIME, 194, 747 (1952).

PFANN, W.G., Zone Melting, John Wiley and Sons, New York (1958).

PHILIBERT, J., and BIZOUARD, H., Mém. Sci. Rev. Mét., 56, 187 (1959).

PHILIBERT, J. and de BEAULIEU, C., Mém. Sci. Rev. Mét., 56, 171 (1959).

PHILIBERT, J., WEINRYB, E. and ANCEY, M., Metallurgia, 72, 203 (1965).

PLASKETT, T.S. and WINEGARD, W.C., Can. J. Phys., 38, 1077 (1960).

POLICH, R.F. and FLEMINGS, M.C., Trans. Am. Found. Soc., 73, 28 (1965).

POOLE, D.M. and MARTIN, P.M., Met. Rev., 3, 61 (1969).

PURDY, G.R., McMaster University, to be published (1970).

REYNIK, R.J., Trans. Met. Soc. AIME, 245, 75 (1969).

ROHATGI, P.K. and ADAMS, C.M., Trans. Met. Soc. AIME, 239, 1737 (1967).

ROHATGI, P.K., JAIN, S.M., FRENCH, D.N. and ADAMS, C.M., Trans. Met. Soc. AIME, 245, 267 (1969).

ROSENQVIST, T. and DUNICZ, B.L., Trans. AIME, 194, 604 (1952).

ROY, P. and HULTGREN, R., Trans. AIME, 233, 1811 (1965).

RUDDLE, R.W., The Solidification of Castings, Institute of Metals, London (1957)

RUER, R. and GOERENS, F., Ferrum, 14, 161 (1916-17).

RUTTER, J.W. and CHALMERS, B., Can. J. Phys., 31, 15 (1953).

SAITO, T., KAWAI, Y., MRUYA, K. and MAKI, M., Physical Chemistry of Process Metallurgy, Part 1, Interscience Publishers, New York (1961).

SALMON COX, P.H. and CHARLES, J.A., J. Iron Steel Inst., 203, 493 (1965).

SCHEIL, E., Z. Metallkunde, 34, 70 (1942).

SCHEUER, E., Z. Metallkunde, 23, 237 (1931).

SCHUMANN, H., Metallographie, Veb. Deutscher Verlag für Grundstoffindustrie, Leipzig (1962).

SEIBEL, G., Mém. Sci. Rev. Mét., 61, 413 (1964).

SHARP, R.M., cited by A. HELLAWELL in The Solidification of Metals, ISI Publ. 110, London, 83 (1967).

SIMS, C.E. and DAHLE, F.B., Trans. Am. Found. Soc., 46, 65 (1938).

SIMS, C.E., Trans. Met. Soc. AIME, 215, 367 (1959).

SIMS, C.E., Electric Furnace Steelmaking, Vol. 2, Iron and Steel Division, AIME, Interscience Publishers, New York (1963).

SMITH, L. and BEELEY, P.R., in The Solidification of Metals, ISI Publ. 110, London, 330 (1967).

SMITH, P.N., Master's Thesis, McMaster University (1965).

SMITH, P.N., Doctoral Thesis, McMaster University (1970).

SMITH, V.G., TILLER, W.A. and RUTTER, J.W., Can. J. Phys., 33, 723 (1955).

SPEAR, R.E. and GARDNER, G.R., Mod. Cast., 43, No. 5, 209 (1963).

SUBRAMANIAN, S.V., HAWORTH, C.W. and KIRKWOOD, D.H., J. Iron Steel Inst., 206, 1027 (1968-A).

SUBRAMANIAN, S.V., HAWORTH, C.W. and KIRKWOOD, D.H., J. Iron Steel Inst., 206, 1124 (1968-B).

SUBRAMANIAN, S.V. and PURDY, G.R., McMaster University, Unpublished Research (1969).

SWALIN, R.A., Thermodynamics of Solids, John Wiley and Sons, New York (1962).

SWISHER, J.H., Trans. Met. Soc. AIME, 239, 110 (1967)

THURMOND, C.D., J. Phys. Chem., 57, 827 (1953).

TILLER, W.A., JACKSON, K.A., RUTTER, J.W. and CHALMERS, B., Acta Met., 1, 428 (1953).

TILLER, W.A., Can. J. Phys., 34, 729 (1956).

TILLER, W.A. and RUTTER, J.W., Can. J. Phys., 34, 96 (1956-A).

TILLER, W.A., J. Iron Steel Inst., 192, 338 (1959).

TURKDOGAN, E.T., IGNATOWICZ, S. and PEARSON, J., J. Iron Steel Inst., 180, 349 (1955).

TURKDOGAN, E.T. and GRANGE, R.A., Paper Intended for Publication in Trans. Met. Soc. AIME (1968).

UHLMANN, D.R. and CHALMERS, B., J. Appl. Phys., 35, 2986 (1964).

VOGEL, V.R. and HOTOP, W., Archiv Eisen, 11, 41 (1937).

WAGNER, C., Thermodynamics of Alloys, Addison Wesley, Reading, Mass. (1952).

WAGNER, C., Trans. AIME, 200, 154 (1954).

WALTON, D. and CHALMERS, B., Trans. Met. Soc. AIME, 215, 447 (1959).

WARD, R.G., J. Iron Steel Inst., 188, 337 (1958).

WEAST, R.C., Ed., *Handbook of Chemistry and Physics*, 45th Edition, Chemical Rubber Co., Cleveland (1964).

WEINBERG, F. and CHALMERS, B., Can. J. Phys., 30, 488 (1952).

WEINBERG, F., Trans. Met. Soc. AIME, 227, 231 (1963).

WEINBERG, F. and BUHR, R.K., in *The Solidification of Metals*, ISI Publ. 110, London, 295 (1967).

WELLS, C. and MEHL, R.F., Trans. AIME, 145, 315 (1941).

WELLS, C., BATZ, W. and MEHL, R.F., Trans. AIME, 188, 553 (1950).

WHITELEY, J.H., *7th Report on The Heterogeneity of Steel Ingots*, ISI Publ. 16, London (1937).

WINEGARD, W.C. and CHALMERS, B., Trans. ASM., 46, 1214 (1954).

WLODAWER, N., *Directional Solidification of Steel Castings*, Pergamon Press, London (1966).

YAKOWITZ, H. and HEINRICH, K.F.J., Metallography, 1, 55 (1968).

YEO, R.B.G., J. Metals, 19, No. 7, 23 (1967).

ZAITSEVA, I.P., Works of The Leningrad Polytechnic Institute, 180, 13 (1955).

ZHURENKOV, P.M. and GOLIKOV, I.N., Metalloved. Term. Obrab. Met., 293 (1964).

APPENDICES

A.1 - TERNARY ISOTHERM

LIST OF SYMBOLS

AI - STORAGE VARIABLES FOR FI.
ASIJ ALPHA FORMALISM INTERACTION PARAMETER A INVOLVING COMPONENTS I AND J IN SOLUTION S.
BI - STORAGE VARIABLES FOR FI.
DGELG - DOUBLE PRECISION SUBROUTINE FOR SOLUTION OF SYSTEM OF LINEAR EQUATIONS BY GAUSSIAN ELIMINATION.
DJLGSI - DERIVATIVE D WITH RESPECT TO COMPONENT J OF THE LOGARITHM L OF THE ACTIVITY COEFFICIENT GAMMA OF COMPONENT I IN SOLUTION S.
DT - TEMPERATURE DIFFERENCE BETWEEN SUCCESSIVE ISOTHERMS.
DXS1 - INCREMENT IN XS1.
FI - ERROR IN TANGENT-PLANE EQUATION I.
H - SMALL ARBITRARY CONSTANT USED IN THE NUMERICAL EVALUATION OF FUNCTION DERIVATIVES.
HH - CONSTANT RELATED TO H.
INDEX - INDEX OF TIE-LINE.
INDFOR - FORMALISM INDICATOR. IF INDFOR = 1, ALPHA FORMALISM IS EMPLOYED. IF INDFOR = 1, EPSILON FORMALISM IS EMPLOYED.
INDSOL - INDICATOR REPORTING OUTCOME OF THE SOLUTION OF THE LINEAR EQUATIONS BY DGELG.
KI - PARTITION COEFFICIENTS.
KS(I) - STORAGE VECTOR FOR KI.
LBIN - INDICATOR. IF LBIN = 1, COMPUTE BINARY TIE-LINE FOR COMPONENT 1. IF LBIN = 1, COMPUTE TERNARY TIE-LINE.
LGSI LOGARITHM L OF THE ACTIVITY COEFFICIENT GAMMA OF COMPONENT I IN SOLUTION S.
LG0SI LOGARITHM L OF THE ACTIVITY COEFFICIENT GAMMA OF COMPONENT I IN SOLUTION S AT INFINITE DILUTION.
P(I) - SOLUTION VECTOR RETURNED BY DGELG.
Q(I) - STORAGE VECTOR FOR PARTIAL SLOPES OF FUNCTIONS FI.
TC - ISOTHERM TEMPERATURE IN DEGREES CELCIUS.
TFI - FUSION TEMPERATURE OF COMPONENT I.
TK - ISOTHERM TEMPERATURE IN DEGREES KELVIN.
UI - INTERACTION FUNCTIONS.
VI - FREE ENTHALPY FUNCTIONS.
XBSI - BINARY PHASE DIAGRAM ATOM FRACTION XB OF COMPONENT I IN SOLUTION S.
XKI - SINGLE PRECISION FORM OF KI.
XSI - ATOM FRACTION X OF COMPONENT I IN SOLUTION S.
XXSI - ATOMIC PERCENT OF COMPONENT I IN SOLUTION S.
Z(I) - STORAGE VECTOR FOR KS(I) INCREMENTED OR DECREMENTED BY H.

PROGRAM

```
- TIE-LINES OF LIQUID + DELTA FIELD IN FE-MN-S
      COMMON/C1/XL0,XL1,XL2,XS0,XS1,XS2
      COMMON/C2/G0L1,G0L2,G0S1,G0S2
      COMMON/C3/EL11,EL12,EL21,EL22,ES11,ES12,ES21,ES22
      COMMON/C4/U0,U1,U2,K0,K1,K2
      COMMON/C5/V0,V1,V2
      COMMON/C6/F0,F1,F2
      COMMON/C7/Z(3)
      COMMON/C10/LGL0,LGL1,LGL2,LGS0,LGS1,LGS2
      COMMON/C11/LG0L1,LG0L2,LG0S1,LG0S2
      COMMON/C12/AL01,AL02,AL12,AS01,AS02,AS12
      DIMENSION KS(3),P(3),Q(9)
  100 FORMAT(8F10.2)
  101 FORMAT(8F10.5)
  102 FORMAT(8E10.3)
  103 FORMAT(I1)
  200 FORMAT(//45X,5HTC = ,1P1E15.4/43X,7HDGF0 = ,1P1E15.4/43X,7HDGF1 =
     *1P1E15.4/43X,7HDGF2 = ,1P1E15.4)
  201 FORMAT(//3X,5HINDEX,8X,3HXL0,9X,3HXL1,9X,3HXL2,9X,3HXS0,9X,3HXS1,9
     *X,3HXS2,10X,2HK0,10X,2HK1,10X,2HK2/)
  202 FORMAT(2X,I4,4X,9E12.5)
  203 FORMAT(/43X,7HDHF0 = ,1P1E15.4/43X,7HDHF1 = ,1P1E15.4/43X,7HDHF2 =
     * ,1P1E15.4)
  204 FORMAT(/43X,7HEL11 = ,1P1E15.4/43X,7HEL12 = ,1P1E15.4/43X,7HEL21 =
     * ,1P1E15.4/43X,7HEL22 = ,1P1E15.4/43X,7HES11 = ,1P1E15.4/43X,7HES1
     *2 = ,1P1E15.4/43X,7HES21 = ,1P1E15.4/43X,7HES22 = ,1P1E15.4)
  205 FORMAT(/43X,7HG0L1 = ,1P1E15.4/43X,7HG0L2 = ,1P1E15.4/43X,7HG0S1 =
     * ,1P1E15.4/43X,7HG0S2 = ,1P1E15.4)
  206 FORMAT(/44X,6HTF0 = ,1P1E15.4/44X,6HTF1 = ,1P1E15.4/44X,6HTF2 = ,1
     *P1E15.4)
  207 FORMAT(/45X,5HDT = ,1P1E15.4/44X,6HTLO = ,1P1E15.4/44X,6HTHI = ,1P
     *1E15.4)
  208 FORMAT(/45X,5HDZ = ,1P1E15.4/44X,6HZLO = ,1P1E15.4/44X,6HZHI = ,1P
     *1E15.4)
  209 FORMAT(/50X,17HEPSILON FORMALISM//)
  210 FORMAT(/50X,17HPIVOT ELEMENT = 0//)
  211 FORMAT(/50X,29HPOSSIBLE LOSS OF SIGNIFICANCE//)
  212 FORMAT(//3X,5HINDEX,8X,2HF0,10X,2HF1,10X,2HF2/)
  215 FORMAT(/43X,7HXBL1 = ,1P1E15.4/43X,7HXBS1 = ,1P1E15.4/43X,7HXBL2 =
     * ,1P1E15.4/43X,7HXBS2 = ,1P1E15.4/43X,7HDXS1 = ,1P1E15.4)
  216 FORMAT(/45X,5HW0 = ,1P1E15.4/45X,5HW1 = ,1P1E15.4/45X,5HW2 = ,1P1E
     *15.4)
  217 FORMAT(/50X,15HALPHA FORMALISM//)
      REAL K0,K1,K2
      REAL KB1,KB2,KS
      REAL LGL0,LGL1,LGL2,LGS0,LGS1,LGS2
      REAL LG0L1,LG0L2,LG0S1,LG0S2
      DATA DEL,H,NIT,R/1.0E-10,1.0E-10,20,1.98725/
      HH=2.0*H
      READ(5,103)INDFOR
      READ(5,100)DHF0,DHF1,DHF2
```

```
      READ(5,102)W0,W1,W2
      READ(5,101)EL11,EL12,EL21,EL22,ES11,ES12,ES21,ES22
      READ(5,101)G0L1,G0L2,G0S1,G0S2
      READ(5,100)TF0,TF1,TF2
      READ(5,100)DT,TLO,THI
      IF(INDFOR.EQ.1)GO TO 403
      WRITE(6,209)
      GO TO 404
  403 WRITE(6,217)
  404 WRITE(6,203)DHF0,DHF1,DHF2
      WRITE(6,216)W0,W1,W2
      WRITE(6,204)EL11,EL12,EL21,EL22,ES11,ES12,ES21,ES22
      WRITE(6,205)G0L1,G0L2,G0S1,G0S2
      WRITE(6,206)TF0,TF1,TF2
      WRITE(6,207)DT,TLO,THI
C- COMPUTE ALPHA PARAMETERS
      AL01=-EL11/2.0
      AL02=-EL22/2.0
      AL12=EL12+AL01+AL02
      AL21=EL21+AL01+AL02
      AS01=-ES11/2.0
      AS02=-ES22/2.0
      AS12=ES12+AS01+AS02
      AS21=ES21+AS01+AS02
C- COMPUTE LOGARITHMS OF HENRYS LAW COEFFICIENT
      LG0L1=ALOG(G0L1)
      LG0L2=ALOG(G0L2)
      LG0S1=ALOG(G0S1)
      LG0S2=ALOG(G0S2)
C- COMPUTE SOME CONSTANTS
      TF0=TF0+273.16
      TF1=TF1+273.16
      TF2=TF2+273.16
C- COMPUTE HIGHEST ISOTHERM TEMPERATURE
      TK=THI+273.16
C- INPUT LIMITING BINARY COMPOSITION VALUES AND XS1 INCREMENT
  400 READ(5,102)XBL1,XBS1,XBL2,XBS2,DXS1
      WRITE(6,215)XBL1,XBS1,XBL2,XBS2,DXS1
      XS1=0.0
C- COMPUTE BINARY PARTITION COEFFICIENTS
      Z(1)=(1.0-XBS2)/(1.0-XBL2)
      Z(2)=XBS1/XBL1
      Z(3)=XBS2/XBL2
C- COMPUTE FREE ENTHALPIES OF FUSION
      DGF0=DHF0*(1.0-TK/TF0)+W0*TK*(TF0-TK)
      DGF1=DHF1*(1.0-TK/TF1)+W1*TK*(TF1-TK)
      DGF2=DHF2*(1.0-TK/TF2)+W2*TK*(TF2-TK)
C- COMPUTE FREE ENERGY FUNCTIONS
      V0=DGF0/R/TK
      V1=(DGF1-DGF0)/R/TK
      V2=(DGF2-DGF0)/R/TK
```

```
      TC=TK-273.16
      WRITE(6,200)TC,DGF0,DGF1,DGF2
      INDEX=0
      LBIN=0
      CALL FMIN(INDFOR,LBIN)
C- COMPUTE TERNARY TIE-LINES AND PARTITION COEFFICIENTS
C- NEWTON-RAPHSON TECHNIQUE
  408 DO 301 L=1,NIT
C- STORE FUNCTIONS FOR SOLUTION OF LINEAR EQUATIONS
      P(1)=-F0
      P(2)=-F1
      P(3)=-F2
C- STORE ARGUMENTS FOR SOLUTION OF LINEAR EQUATIONS
      KS(1)=K0
      KS(2)=K1
      KS(3)=K2
C- COMPUTE NUMERICALLY PARTIAL SLOPES OF FUNCTIONS
      DO 300 I=1,3
      J=3*I-2
      Z(I)=KS(I)+H
      CALL FMIN(INDFOR,LBIN)
      A0=F0
      A1=F1
      A2=F2
      Z(I)=KS(I)-H
      CALL FMIN(INDFOR,LBIN)
      B0=F0
      B1=F1
      B2=F2
C- STORE PARTIAL SLOPES OF FUNCTIONS IN Q
      Q(J)=(A0-B0)/HH
      Q(J+1)=(A1-B1)/HH
      Q(J+2)=(A2-B2)/HH
C- RESET ELEMENT Z(I) OF ARGUMENT Z
  300 Z(I)=KS(I)
C- SOLVE SET OF LINEAR EQUATIONS
      CALL GELG(P,Q,3,1,DEL,INDSOL)
      IF(INDSOL.EQ.0)GO TO 405
      IF(INDSOL.EQ.(-1))GO TO 406
  407 WRITE(6,211)
      GO TO 1000
  406 WRITE(6,210)
      GO TO 1000
C- SOLUTION VECTOR IS CONTAINED IN P
C- COMPUTE NEW ARGUMENTS
  405 DO 302 I=1,3
  302 Z(I)=Z(I)+P(I)
C- COMPUTE NEW FUNCTIONS CORRESPONDING TO NEW ARGUMENTS
  301 CALL FMIN(INDFOR,LBIN)
      WRITE(6,201)
      WRITE(6,202)INDEX,XL0,XL1,XL2,XS0,XS1,XS2,K0,K1,K2
```

```
      WRITE(6,212)
      WRITE(6,202)INDEX,F0,F1,F2
C- COMPUTE NEXT TIE-LINE
      INDEX=INDEX+1
      XS1=XS1+DXS1
      IF(LBIN.EQ.1)GO TO 409
      IF(XS1.LT.XBS1)GO TO 408
      XS2=0.0
      XL2=0.0
      LBIN=1
      GO TO 408
  409 TK=TK-DT
      IF((TK-273.15).GE.TLO)GO TO 400
 1000 STOP
      END
      SUBROUTINE FMIN(INDFOR,LBIN)
      COMMON/C1/XL0,XL1,XL2,XS0,XS1,XS2
      COMMON/C2/G0L1,G0L2,G0S1,G0S2
      COMMON/C3/EL11,EL12,EL21,EL22,ES11,ES12,ES21,ES22
      COMMON/C4/U0,U1,U2,K0,K1,K2
      COMMON/C5/V0,V1,V2
      COMMON/C6/F0,F1,F2
      COMMON/C7/Z(3)
      COMMON/C10/LGL0,LGL1,LGL2,LGS0,LGS1,LGS2
      COMMON/C11/LG0L1,LG0L2,LG0S1,LG0S2
      COMMON/C12/AL01,AL02,AL12,AS01,AS02,AS12
      REAL K0,K1,K2
      REAL LGL0,LGL1,LGL2,LGS0,LGS1,LGS2
      REAL LG0L1,LG0L2,LG0S1,LG0S2

      K0=Z(1)
      K1=Z(2)
      K2=Z(3)
      IF(LBIN.EQ.0)GO TO 400
      XL1=(K0-1.0)/(K0-K1)
      XL0=1.0-XL1
      XS1=K1*XL1
      XS0=1.0-XS1
      GO TO 401
  400 XL1=XS1/K1
      XL2=(K0*(1.0-XL1)+XS1-1.0)/(K0-K2)
      XL0=1.0-XL1-XL2
      XS2=K2*XL2
      XS0=1.0-XS1-XS2
  401 IF(INDFOR.EQ.1)GO TO 402
      CALL EPSIL
      GO TO 403
  402 CALL ALPHA
  403 F0=ALOG(K0)+U0-V0
      F1=ALOG(K1/K0)+U1-V1
      F2=ALOG(K2/K0)+U2-V2
      RETURN
      END
```

```
      SUBROUTINE ALPHA
C- COMPUTE ALPHA FORMALISM ACTIVITY COEFFICIENT RELATIONS
      COMMON/C1/XL0,XL1,XL2,XS0,XS1,XS2
      COMMON/C2/G0L1,G0L2,G0S1,G0S2
      COMMON/C3/EL11,EL12,EL21,EL22,ES11,ES12,ES21,ES22
      COMMON/C4/U0,U1,U2,K0,K1,K2
      COMMON/C10/LGL0,LGL1,LGL2,LGS0,LGS1,LGS2
      COMMON/C11/LG0L1,LG0L2,LG0S1,LG0S2
      COMMON/C12/AL01,AL02,AL12,AS01,AS02,AS12
      REAL LG0L1,LG0L2,LG0S1,LG0S2
      REAL LGL0,LGL1,LGL2,LGS0,LGS1,LGS2
C- COMPUTE LOGARITHM OF ACTIVITY COEFFICIENTS
      LGL0=AL01*XL1*XL1-EL12*XL1*XL2+AL02*XL2*XL2
      LGL1=LG0L1-2.0*AL01*XL1+EL12*XL2+AL01*XL1*XL1+AL02*XL2*XL2-
     *1*XL2
      LGL2=LG0L2-2.0*AL02*XL2+EL21*XL1+AL02*XL2*XL2+AL01*XL1*XL1-
     *1*XL2
      LGS0=AS01*XS1*XS1-ES12*XS1*XS2+AS02*XS2*XS2
      LGS1=LG0S1-2.0*AS01*XS1+ES12*XS2+AS01*XS1*XS1+AS02*XS2*XS2-
     *1*XS2
      LGS2=LG0S2-2.0*AS02*XS2+ES21*XS1+AS02*XS2*XS2+AS01*XS1*XS1-
     *1*XS2
C- COMPUTE INTERACTION FUNCTIONS
      U0=LGS0-LGL0
      U1=LGS1-LGL1-LGS0+LGL0
      U2=LGS2-LGL2-LGS0+LGL0
      RETURN
      END
      SUBROUTINE EPSIL
C- COMPUTE EPSILON FORMALISM ACTIVITY COEFFICIENT RELATIONS
      COMMON/C1/XL0,XL1,XL2,XS0,XS1,XS2
      COMMON/C3/EL11,EL12,EL21,EL22,ES11,ES12,ES21,ES22
      COMMON/C4/U0,U1,U2,K0,K1,K2
      COMMON/C10/LGL0,LGL1,LGL2,LGS0,LGS1,LGS2
      COMMON/C11/LG0L1,LG0L2,LG0S1,LG0S2
      REAL LG0L1,LG0L2,LG0S1,LG0S2
      REAL LGL0,LGL1,LGL2,LGS0,LGS1,LGS2
C- COMPUTE LOGARITHM OF ACTIVITY COEFFICIENTS
      LGL0=-EL11/2.0*XL1*XL1-EL12*XL1*XL2-EL22/2.0*XL2*XL2
      LGL1=LG0L1+EL11*XL1+EL12*XL2
      LGL2=LG0L2+EL21*XL1+EL22*XL2
      LGS0=-ES11/2.0*XS1*XS1-ES12*XS1*XS2-ES22/2.0*XS2*XS2
      LGS1=LG0S1+ES11*XS1+ES12*XS2
      LGS2=LG0S2+ES21*XS1+ES22*XS2
C- COMPUTE INTERACTION FUNCTIONS
      U0=LGS0-LGL0
      U1=LGS1-LGL1-LGS0+LGL0
      U2=LGS2-LGL2-LGS0+LGL0
      RETURN
      END
```

```
1
3360.0      1720.0      13000.0
-1.220E-04 0.000E+00-1.340E-02
-0.6        0.0         0.0        -3.7        -0.80       0.0         0.0         -67
1.38        0.18        1.41        0.095
1536.0      900.0       119.0
10.0        1510.0      1510.0
 5.300E-02 3.900E-02 1.300E-02 6.300E-04 5.000E-03
 7.300E-02 5.400E-02 1.800E-02 8.700E-04 1.000E-02
 9.300E-02 6.900E-02 2.300E-02 1.060E-03 1.000E-02
 1.140E-01 8.400E-02 2.800E-02 1.250E-03 1.000E-02
 1.200E-02 8.000E-03 3.000E-03 1.500E-04 2.000E-03
 3.200E-02 2.400E-02 8.000E-03 4.000E-04 3.000E-03
```

A.2 - TERNARY MICROSEGREGATION MODEL

LIST OF SYMBOLS

```
NOTE      - BASIC UNITS ARE CM,SEC,MOLES, CELCIUS DEGREES
          - NOMENCLATURE OF VARIABLES IN SUBPROGRAMS CAN BE TRACED
            THROUGH COMMON STATEMENTS OR SUBPROGRAM ARGUMENTS
          - ALL VARIABLES BEGINNING WITH W OR V ARE WORKING VARIABLES
            DEFINED IN THE PROGRAM
A(I)      - STORAGE FOR ARGUMENTS IN NEWTON-RAPHSON ALGORITHM
AS(I)     - ARGUMENTS USED IN THE NEWTON-RAPHSON ALGORITHM
A1        - VARIABLE CONTAINING FUNCTION F1
A2        - VARIABLE CONTAINING FUNCTION F2
B1        - VARIABLE CONTAINING FUNCTION F1
B2        - VARIABLE CONTAINING FUNCTION F2
CA1       - AVERAGE CONCENTRATION OF SOLUTE 1
CA2       - AVERAGE CONCENTRATION OF SOLUTE 2
CCOL1     - STORAGE VARIABLE FOR COL1(I)
CCOL2     - STORAGE VARIABLE FOR COL2(I)
CCOS1     - STORAGE VARIABLE FOR COS1(I)
CCOS2     - STORAGE VARIABLE FOR COS2(I)
CL1(I)    - CONCENTRATION OF SOLUTE 1 IN LIQUID
CL2(I)    - CONCENTRATION OF SOLUTE 2 IN LIQUID
CS1(I)    - CONCENTRATION OF SOLUTE 1 IN SOLID
CS2(I)    - CONCENTRATION OF SOLUTE 2 IN SOLID
COL1(I)   - INTERFACE CONCENTRATION OF SOLUTE 1 IN LIQUID PHASE
COL2(I)   - INTERFACE CONCENTRATION OF SOLUTE 2 IN LIQUID PHASE
COS1(I)   - INTERFACE CONCENTRATION OF SOLUTE 1 IN SOLID PHASE
COS2(I)   - INTERFACE CONCENTRATION OF SOLUTE 2 IN SOLID PHASE
CNL1(I)   - CONCENTRATION OF SOLUTE 1 IN THE VIRTUAL LIQUID ON THE
            NEGATIVE SIDE OF THE INTERFACE
```

CNL2(I) - CONCENTRATION OF SOLUTE 2 IN THE VIRTUAL LIQUID ON THE NEGATIVE SIDE OF THE INTERFACE
CNS1(I) - CONCENTRATION OF SOLUTE 1 IN THE PHYSICAL SOLID ON THE NEGATIVE SIDE OF THE INTERFACE
CNS2(I) CONCENTRATION OF SOLUTE 2 IN THE PHYSICAL SOLID ON THE NEGATIVE SIDE OF THE INTERFACE
CPL1(I) - CONCENTRATION OF SOLUTE 1 IN THE PHYSICAL LIQUID ON THE POSITIVE SIDE OF THE INTERFACE
CPL2(I) - CONCENTRATION OF SOLUTE 2 IN THE PHYSICAL LIQUID ON THE POSITIVE SIDE OF THE INTERFACE
CPS1(I) - CONCENTRATION OF SOLUTE 1 IN THE VIRTUAL SOLID ON THE POSITIVE SIDE OF THE INTERFACE
CPS2(I) - CONCENTRATION OF SOLUTE 2 IN THE VIRTUAL SOLID ON THE POSITIVE SIDE OF THE INTERFACE
DL1 - DIFFUSION COEFFICIENT OF SOLUTE 1 IN LIQUID
DL2 - DIFFUSION COEFFICIENT OF SOLUTE 2 IN LIQUID
DS1 - DIFFUSION COEFFICIENT OF SOLUTE 1 IN SOLID
DS2 - DIFFUSION COEFFICIENT OF SOLUTE 2 IN SOLID
DT - INCREMENT OF TIME
DZ0 - INCREMENT OF INTERFACE POSITION
FLAM - FRACTIONAL LENGTH OF SYSTEM
GT - TEMPERATURE GRADIENT WITH RESPECT TO TIME
H - INCREMENT IN ARGUMENT VALUES IN NEWTON-RAPHSON ALGORITHM
HZ - TABULATION INCREMENT IN SOLUTE DISTRIBUTION FUNCTIONS
IBL - INDEX OF VECTOR ELEMENT AT OR NEXT TO LIQUID BOUNDARY
IBS - INDEX OF VECTOR ELEMENT AT OR NEXT TO SOLID BOUNDARY
INDSOL - INDICATOR WHICH REPORTS ON THE OUTCOME OF SOLUTION. IF INDSOL = 0, SOLUTION IS SATISFACTORY
IS - INDEX FOR THE I≠TH STEP
INXP - INTEGRAL FOR NEGATIVE X PRIMES
IPXP - INTEGRAL FOR POSITIVE X PRIMES
JL01 - APPROXIMATE FLUX OF SOLUTE 1 ENTERING LIQUID AT T=0
JL02 - APPROXIMATE FLUX OF SOLUTE 2 ENTERING LIQUID AT T=0
JS01 - APPROXIMATE FLUX OF SOLUTE 1 ENTERING SOLID AT T=0
JS02 - APPROXIMATE FLUX OF SOLUTE 2 ENTERING SOLID AT T=0
JL1 - FLUX OF SOLUTE 1 ENTERING LIQUID AT TEPS OR MULTIPLE
JL2 - FLUX OF SOLUTE 2 ENTERING LIQUID AT TEPS OR MULTIPLE
JS1 - FLUX OF SOLUTE 1 ENTERING SOLID AT TEPS OR MULTIPLE
JS2 - FLUX OF SOLUTE 2 ENTERING SOLID AT TEPS OR MULTIPLE
K1 - PARTITION COEFFICIENT OF SOLUTE 1
K2 - PARTITION COEFFICIENT OF SOLUTE 2
LAM - LENGTH OF SYSTEM UNDER CONSIDERATION
L1 - LIQUIDUS SLOPE ON SOLVENT-SOLUTE 1 CONSTITUTION DIAGRAM
L2 - LIQUIDUS SLOPE ON SOLVENT-SOLUTE 2 CONSTITUTION DIAGRAM
ML1 - AMOUNT OF SOLUTE 1 REJECTED INTO LIQUID BY SOURCE
ML2 - AMOUNT OF SOLUTE 2 REJECTED INTO LIQUID BY SOURCE
MS1 - AMOUNT OF SOLUTE 1 REJECTED INTO SOLID BY SOURCE
MS2 - AMOUNT OF SOLUTE 2 REJECTED INTO SOLID BY SOURCE
NDR - NUMBER OF DOUBLE REFLECTIONS
NSR - NUMBER OF SINGLE REFLECTIONS
NIT - NUMBER OF ITERATIONS IN NEWTON-RAPHSON ALGORITHM

NTP - NUMBER OF TABULATED POINTS IN A SOLUTE DISTRIBUTION FUNCTION
OI - INDICATOR USED IN OUTPUT OF RESULTS.
P(I) - VECTOR CONTAINING FUNCTIONS F1 AND F2
Q(I) - VECTOR CONTAINING PARTIAL SLOPES OF FUNCTIONS F1 AND F2
S1 - SOLIDUS SLOPE ON SOLVENT-SOLUTE 1 CONSTITUTION DIAGRAM
S2 - SOLIDUS SLOPE ON SOLVENT-SOLUTE 2 CONSTITUTION DIAGRAM
T - SOLIDIFICATION TIME
TAU - DIFFUSION TIME AT EACH STEP
TEPS - FRACTION OF TAU
T0 - LIQUIDUS TEMPERATURE FOR AVERAGE SOLUTE CONCENTRATIONS
TF - TEMPERATURE OF FUSION FOR PURE SOLVENT
TI - INTERFACE TEMPERATURE
XBL - DISTANCE FROM INTERFACE TO LIQUID BOUNDARY
XBS - DISTANCE FROM INTERFACE TO SOLID BOUNDARY
XDEL - RUN OF SOLUTE GRADIENT AT INTERFACE
Z0 - INTERFACE DISTANCE FROM SOLID BOUNDARY
ZL(I) - DISTANCE IN THE LIQUID PHASE FROM SOLID BOUNDARY
ZS(I) - DISTANCE IN THE SOLID PHASE FROM SOLID BOUNDARY

PROGRAM

```
- MAIN PROGRAM
      COMMON/K01/COL1( 501),COL2( 501),COS1( 501),COS2( 501)
      COMMON/K02/E1,E2,F1,F2,MTL1,MTL2,MTS1,MTS2
      COMMON/K04/W0L1,W0L2,W0S1,W0S2
      COMMON/K05/W1L1,W1L2,W1S1,W1S2
      COMMON/K06/W2L1,W2L2,W2S1,W2S2
      COMMON/K07/W3L1,W3L2,W3S1,W3S2
      COMMON/K08/K1,K2,L1,L2,S1,S2
      COMMON/K09/GT,T,T0,TF,TI
      COMMON/K10/IS
      COMMON/K11/TAU
      COMMON/K12/XBL,XBS
      COMMON/K14/CCL1( 501),CCL2( 501),CCS1( 501),CCS2( 501)
      COMMON/K16/CL1( 501),CL2( 501),CS1( 501),CS2( 501)
      COMMON/K17/SQRIPI
      COMMON/K19/A(2),AS(2),P(2),Q(4)
      COMMON/K21/DL1,DL2,DS1,DS2
      COMMON/K22/ITER,DZ0
      DIMENSION RI( 501),ZL( 501),ZS( 501)
      DIMENSION XL(501),XS(501),XLS(501),XSS(501)
  100 FORMAT(8F10.5)
  101 FORMAT(8E10.3)
  200 FORMAT(10X,1I10,3F20.14)
  201 FORMAT(1X,I5,5E25.13)
  205 FORMAT(/40X,22HSOLUTION DIFFICULTY = ,I2)
```

```
 209 FORMAT(/55X,5HK1 = ,E10.3/55X,5HK2 = ,E10.3)
 210 FORMAT(/54X,6HDZ0 = ,E10.3/54X,6HTAU = ,E10.3)
 211 FORMAT(/55X,5HGT = ,E10.3/55X,5HTF = ,E10.3)
 212 FORMAT(/55X,5HL1 = ,E10.3/55X,5HL2 = ,E10.3/55X,5HS1 = ,E10.3/55X,
     *5HS2 = ,E10.3)
 213 FORMAT(/54X,6HDL1 = ,E10.3/54X,6HDL2 = ,E10.3/54X,6HDS1 = ,E10.3/5
     *4X,6HDS2 = ,E10.3)
 214 FORMAT(/54X,6HCA1 = ,E10.3/54X,6HCA2 = ,E10.3)
 215 FORMAT(/53X,7HFLAM = ,E10.3/54X,6HLAM = ,E10.3)
 216 FORMAT(/55X,5HT0 = ,E10.3)
      REAL JL01,JL02,JL1,JL2,JS01,JS02,JS1,JS2
      REAL K1,K2,LAM,L1,L2
      REAL MTL1,MTL2,MTS1,MTS2
C- INPUT DATA
      DATA DEL,H,NIT/1.0E-10,1.0E-10,12/
      DATA NTP/201/
      DATA OI/0.0/
      DATA PI/3.1415926536/
      READ(5,101)TAU,DCOS1
      READ(5,101)GT,TF
      READ(5,101)L1,L2,S1,S2
      READ(5,101)DL1,DL2,DS1,DS2
      READ(5,100)CA1,CA2
      READ(5,100)FLAM,LAM
C- COMPUTE CONSTANTS
      SQRIPI=SQRT(1.0/PI)
      HH=2.0*H
      DZ0=LAM/FLOAT(NTP-1)
      EDZ0=DZ0/2.0
      K1=L1/S1
      K2=L2/S2
      W0L1=2.0*SQRT(PI*DL1)
      W0L2=2.0*SQRT(PI*DL2)
      W0S1=2.0*SQRT(PI*DS1)
      W0S2=2.0*SQRT(PI*DS2)
      W1L1=4.0*DL1
      W1L2=4.0*DL2
      W1S1=4.0*DS1
      W1S2=4.0*DS2
      W2L1=2.0*SQRT(DL1)
      W2L2=2.0*SQRT(DL2)
      W2S1=2.0*SQRT(DS1)
      W2S2=2.0*SQRT(DS2)
      W3L1=2.0*SQRT(DL1/PI)
      W3L2=2.0*SQRT(DL2/PI)
      W3S1=2.0*SQRT(DS1/PI)
      W3S2=2.0*SQRT(DS2/PI)
C- CHECK INPUT DATA AND SOME CONSTANTS
      WRITE(6,210)DZ0,TAU
      WRITE(6,211)GT,TF
      WRITE(6,212)L1,L2,S1,S2
```

```
      WRITE(6,209)K1,K2
      WRITE(6,213)DL1,DL2,DS1,DS2
      WRITE(6,214)CA1,CA2
      WRITE(6,215)FLAM,LAM
C-PERFORM COMPUTATIONS FOR INITIAL STEP
      Z0=0.0
      T=0.0
      IS=1
C- COMPUTE INTERFACE TEMPERATURE AT T=0 CORRESPONDING TO AVERAGE SOLUTE
C- CONCENTRATIONS CA1 AND CA2
      TI=TF+L1*CA1+L2*CA2
      T0=TI
      WRITE(6,216)T0
C- COMPUTE EQUILIBRIUM INTERFACE CONCENTRATIONS FOR T0

      C0L1(1)=CA1
      C0L2(1)=CA2
      C0S1(1)=K1*CA1
      C0S2(1)=K2*CA2
C- COMPUTE INITIAL SOLUTE DISTRIBUTIONS IN LIQUID
      I=0
  430 I=I+1
      XLS(I)=LAM-DZ0*FLOAT((I-1)*(I-1))
      IF(XLS(I).LT.0.0)XLS(I)=0.0
      CL1(I)=C0L1(1)
      CL2(I)=C0L2(1)
      IF(XLS(I).GT.0.0)GO TO 430
      ILL=I
C- COMPUTE INITIAL DISTRIBUTIONS IN SOLID
      XSS(1)=0.0
      CS1(1)=C0S1(1)
      CS2(1)=C0S2(1)
      ILS=1
C- PERFORM COMPUTATIONS FOR THE ITH STEP
C- STORE EQUILIBRIUM VALUES
  400 CC0L1=C0L1(IS)
      CC0L2=C0L2(IS)
      CC0S1=C0S1(IS)
      CC0S2=C0S2(IS)
C- COMPUTE EXCESS SOLUTE
      E1=DZ0*(CC0L1-CC0S1)
      E2=DZ0*(CC0L2-CC0S2)
C- COMPUTE NEW STEP INDEX, INTERFACE POSITION IN Z SPACE AND BOUNDARY
C- LIMITS IN X SPACE
      IS=IS+1
      Z0=Z0+DZ0
      XBL=LAM-Z0
      XBS=Z0
C- STORE INITIAL SOLUTE DISTRIBUTIONS IN LIQUID PHASE
      ILL=ILL-1
      DO 300 I=1,ILL
      XL(I)=XLS(I+1)
      CCL1(I)=CL1(I+1)
```

```
  300 CCL2(I)=CL2(I+1)
C- STORE INITIAL SOLUTE DISTRIBUTIONS IN SOLID PHASE
      XS(1)=XBS
      CCS1(1)=CS1(1)
      CCS2(1)=CS2(1)
      ILS=ILS+1
      DO 301 I=2,ILS
      XS(I)=XSS(I-1)
      CCS1(I)=CS1(I-1)
  301 CCS2(I)=CS2(I-1)
C- COMPUTE INITIAL FUNCTIONS F1 AND F2
C- INITIAL CHOICE OF DT EQUALS FINAL CHOICE FOR PREVIOUS STEP
C- INITIAL CHOICE OF COS1 EQUALS FINAL CHOICE FOR PREVIOUS STEP PLUS
C- SMALL INCREMENT
      A(1)=TAU
      A(2)=CCOS1+DCOS1
      ITER=1
      CALL FMIN(ILL,ILS)
C- NEWTON-RAPHSON METHOD
      DO 310 L=1,NIT
C- STORE FUNCTIONS FOR SOLUTION OF LINEAR EQUATIONS
      P(1)=-F1
      P(2)=-F2
C- STORE ARGUMENTS FOR SOLUTIONS OF LINEAR EQUATIONS
      AS(1)=A(1)
      AS(2)=A(2)
C- COMPUTE NUMERICALLY PARTIAL SLOPES OF FUNCTIONS
      DO 307 I=1,2
      J=2*I-1
      A(I)=AS(I)+H
      CALL FMIN(ILL,ILS)
      A1=F1
      A2=F2
      A(I)=AS(I)-H
      CALL FMIN(ILL,ILS)
      B1=F1
      B2=F2
C- STORE PARTIAL SLOPES OF FUNCTIONS IN Q
      Q(J)=(A1-B1)/HH
      Q(J+1)=(A2-B2)/HH
C- RESET ELEMENT A(I) OF ARGUMENT VECTOR A
  307 A(I)=AS(I)
C- SOLVE SET OF LINEAR EQUATIONS
      CALL GELG(P,Q,2,1,DEL,INDSOL)
      IF(INDSOL.EQ.0)GO TO 405
      WRITE(6,205)INDSOL
      GO TO 999
C- SOLUTION VECTOR IS CONTAINED IN P
C- COMPUTE NEW ARGUMENTS
```

```
  405 DO 308 I=1,2
  308 A(I)=A(I)+P(I)
C- NEGATIVE OR ZERO TIME PROTECTION
      IF(A(1).LE.0.0)A(1)=AS(1)/2.0
C- COMPUTE NEW FUNCTIONS CORRESPONDING TO NEW ARGUMENTS
      CALL FMIN(ILL,ILS)
      IF(ABS(F1).LT.1.0E-18.AND.ABS(F2).LT.1.0E-18)GO TO 406
  310 CONTINUE
  406 CONTINUE
C- THE NEW TIME INTERVAL TAU AND TIE-LINE HAVE BEEN FOUND
C- ALLOW DIFFUSION TO PROCEED DURING TIME TAU
C- COMPUTE CONCENTRATIONS OF SOLUTES 1 AND 2 IN LIQUID AS A FUNCTION
C- OF THE Z COORDINATE
C- UPDATE TOTAL SOLIDIFICATION TIME
      T=T+TAU
C- COMPUTE INSTANTANEOUS INTERFACE VELOCITY
      RI(IS)=DZ0/TAU
      WRITE(6,201)IS,F1,F2,TI,RI(IS),TAU
      ITER=0
C- COMPUTE DISTRIBUTION OF SOLUTE 1 IN LIQUID AT NEW REAL TIME T
      I=1
      CL1(I)=COL1(IS)
      ZL(I)=Z0
  402 X=XBL-DZ0*FLOAT(I*I)
      IF(X.LT.0.0)X=0.0
      I=I+1
      XLS(I)=X
      ZL(I)=Z0+XBL-X
      CL1(I)=CXT(COL1,CCL1,XL,W0L1,W1L1,W2L1,X,XBL,TAU,IS,ILL)
      IF(X.GT.0.0)GO TO 402
      ILL=I
C- COMPUTE DISTRIBUTION OF SOLUTE 2 IN LIQUID AT NEW REAL TIME T
      I=1
      CL2(I)=COL2(IS)
  410 X=XBL-DZ0*FLOAT(I*I)
      IF(X.LT.0.0)X=0.0
      I=I+1
      CL2(I)=CXT(COL2,CCL2,XL,W0L2,W1L2,W2L2,X,XBL,TAU,IS,ILL)
      IF(X.GT.0.0)GO TO 410
C- COMPUTE DISTRIBUTION OF SOLUTE 1 IN SOLID AT NEW REAL TIME T
      I=1
      CS1(I)=COS1(IS)
      DCOS1=COS1(IS)-CCOS1
      XSS(1)=XBS
      ZS(I)=Z0
  413 X=XBS-DZ0*FLOAT(I*I)
      IF(X.LT.0.0)X=0.0
      I=I+1
      XSS(I)=X
      ZS(I)=X
      CS1(I)=CXT(COS1,CCS1,XS,W0S1,W1S1,W2S1,X,XBS,TAU,IS,ILS)
```

```
      IF(X.GT.0.0)GO TO 413
C- COMPUTE DISTRIBUTION OF SOLUTE 2 IN SOLID AT NEW REAL TIME T
      ILS=I
      I=1
      CS2(I)=COS1(IS)
  416 X=XBS-DZ0*FLOAT(I*I)
      IF(X.LT.0.0)X=0.0
      I=I+1
      CS2(I)=CXT(COS2,CCS2,XS,WOS2,W1S2,W2S2,X,XBS,TAU,IS,ILS)
      IF(X.GT.0.0)GO TO 416
      WRITE(6,200)(I,ZL(I),CL1(I),CL2(I),I=1,ILL)
      WRITE(6,200)(I,ZS(I),CS1(I),CS2(I),I=1,ILS)
  401 CONTINUE
      IF((Z0+DZ0).LT.LAM)GO TO 400
  999 STOP
      END
      SUBROUTINE EQUIL
C- PHASE EQUILIBRIUM MODEL FOR PLANAR SOLIDUS AND LIQUIDUS
      COMMON/K01/COL1( 501),COL2( 501),COS1( 501),COS2( 501)
      COMMON/K08/K1,K2,L1,L2,S1,S2
      COMMON/K09/GT,T,T0,TF,TI
      COMMON/K10/IS
      REAL K1,K2,L1,L2
C- COMPUTE EQUILIBRIUM INTERFACE COMPOSITIONS
      COL1(IS)=COS1(IS)/K1
      COS2(IS)=(TI-TF-S1*COS1(IS))/S2
      COL2(IS)=COS2(IS)/K2
      RETURN
      END
      FUNCTION CXT(C0,CC,XC,W0,W1,W2,X,XB,T,IS,IL)
C- COMPUTE CONCENTRATION AS A FUNCTION OF DISTANCE AND TIME
      COMMON/K22/ITER,DZ0
      DIMENSION CC(501),C0(501),XC(501)
      EXTERNAL FCT
      REAL N
C- COMPUTE SOME CONSTANTS
      V0=2.0*XB
      V1=W0*SQRT(T)
      V3=W2*SQRT(T)
      V4=W1*T
C- COMPUTE SOURCE TERMS
      NN=0
      JJ=0
C- COMPUTE TERM FOR N=0
      C2=2.0-ERF((XB-X)/V3)-ERF((XB+X)/V3)
      SC2=C2*1.0E-10
C- COMPUTE TERMS FOR N GT 0
  400 NN=NN+1
      N=NN
      V2=V0*N+XB
      CC2=(-1.0)**NN*(2.0-ERF((V2-X)/V3)-ERF((V2+X)/V3))
```

```
      C2=C2+CC2
      IF(ABS(CC2).GT.SC2)GO TO 403
      JJ=JJ+1
      IF(JJ.GT.3)GO TO 404
      GO TO 400
  403 JJ=0
      GO TO 400
  404 C2=C0(IS)*C2
C- COMPUTE INITIAL SOLUTE DISTRIBUTION TERM
      IF(ITER.EQ.0)GO TO 401
      C1=0.0
      GO TO 402
  401 EPS=C0(IS)*1.0E-40
      XPU=X
  411 XPU=XPU+DZ0
      IF(XPU.GT.XB)GO TO 410
      IF(FCT(XPU,X,CC,XC,V0,V4,IL).LT.EPS)GO TO 412
      GO TO 411
  410 XPU=XB
  412 XPL=X
  415 XPL=XPL-DZ0
      IF(XPL.LT.0.0)GO TO 413
      IF(FCT(XPL,X,CC,XC,V0,V4,IL).LT.EPS)GO TO 414
      GO TO 415
  413 XPL=0.0
  414 DXP=(XPU-XPL)/50.0
      FINTS=0.0
      XPLL=XPL
      XPUU=XPLL+DXP
      DO 300 I=1,50
      CALL QG4(XPLL,XPUU,FCT,FINT,X,CC,XC,V0,V4,IL)
      FINTS=FINTS+FINT
      XPLL=XPUU
  300 XPUU=XPUU+DXP
      C1=FINTS/V1
  402 CXT=C1+C2
      RETURN
      END
      FUNCTION FCT(XP,X,CC,XC,V0,V4,IL)
      DIMENSION ARG(2),VAL(2),CC(501),XC(501)
      REAL N
      CALL ATSM(XP,XC,CC,IL,1,ARG,VAL,2)
      CALL ALI(XP,ARG,VAL,CCC,2,1.0E-10,IER)
      JJ=0
      NN=0
C- COMPUTE TERM FOR N=0
      V5=EXP(-(X-XP)**2/V4)+EXP(-(X+XP)**2/V4)
      SV5=V5*1.0E-20
C- COMPUTE TERMS FOR N GT OR LT 0
  402 IF(NN.GE.0)NN=NN+1
      NN=-NN
      N=NN
```

```
      V6=X-V0*N
      VV5=(-1.0)**NN*(EXP(-(V6-XP)**2/V4)+EXP(-(V6+XP)**2/V4))
      V5=V5+VV5
      IF(ABS(VV5).GT.SV5)GO TO 400
      JJ=JJ+1
      IF(JJ.GT.3)GO TO 401
      GO TO 402
  400 JJ=0
      GO TO 402
  401 FCT=CCC*V5
      RETURN
      END
      SUBROUTINE QG4(XL,XU,FCT,Y,XX,CC,XC,V0,V4,IL)
      DIMENSION CC(501),XC(501)
      A=0.5000000000000000*(XU+XL)
      B=XU-XL
      C=0.4305681557970262*B
      Y=0.1739274225687269*(FCT(A+C,XX,CC,XC,V0,V4,IL)+FCT(A-C,XX,CC,X
     *,V0,V4,IL))
      C=0.1699905217924281*B
      Y=B*(Y+0.3260725774312730*(FCT(A+C,XX,CC,XC,V0,V4,IL)+FCT(A-C,XX
     *CC,XC,V0,V4,IL)))
      RETURN
      END
      SUBROUTINE FMIN(ILL,ILS)
      COMMON/K01/COL1( 501),COL2( 501),COS1( 501),COS2( 501)
      COMMON/K02/E1,E2,F1,F2,MTL1,MTL2,MTS1,MTS2
      COMMON/K04/W0L1,W0L2,W0S1,W0S2
      COMMON/K05/W1L1,W1L2,W1S1,W1S2
      COMMON/K06/W2L1,W2L2,W2S1,W2S2
      COMMON/K07/W3L1,W3L2,W3S1,W3S2
      COMMON/K09/GT,T,T0,TF,TI
      COMMON/K10/IS
      COMMON/K11/TAU
      COMMON/K12/XBL,XBS

      COMMON/K14/CCL1( 501),CCL2( 501),CCS1( 501),CCS2( 501)
      COMMON/K17/SQRIPI
      COMMON/K19/A(2),AS(2),P(2),Q(4)
      COMMON/K21/DL1,DL2,DS1,DS2
      REAL MTL1,MTL2,MTS1,MTS2
      REAL MIL1,MIL2,MIS1,MIS2
C- SET NEW TRIAL ARGUMENTS
      TAU=A(1)
      COS1(IS)=A(2)
      SQRTAU=SQRT(TAU)
C- COMPUTE NEW INTERFACE TEMPERATURE
      TI=T0+GT*(T+TAU)
C- COMPUTE OTHER INTERFACIAL CONCENTRATIONS
      CALL EQUIL
C- COMPUTE TOTAL AMOUNT OF REJECTED SOLUTE DURING TIME INTERVAL TAU
      MIL1=COL1(IS)-CCL1(ILL)
      MIL2=COL2(IS)-CCL2(ILL)
```

```
      MIS1=COS1(IS)-CCS1(ILS)
      MIS2=COS2(IS)-CCS2(ILS)
      MIL1=MIL1*0.5
      MIL2=MIL2*0.5
      MIS1=MIS1*0.5
      MIS2=MIS2*0.5
      MTL1=MIL1*W2L1*SQRTAU*(SQRIPI+2.0*SIERFC(XBL/SQRT(DL1*TAU)))
      MTL2=MIL2*W2L2*SQRTAU*(SQRIPI+2.0*SIERFC(XBL/SQRT(DL2*TAU)))
      MTS1=MIS1*W2S1*SQRTAU*(SQRIPI+2.0*SIERFC(XBS/SQRT(DS1*TAU)))
      MTS2=MIS2*W2S2*SQRTAU*(SQRIPI+2.0*SIERFC(XBS/SQRT(DS2*TAU)))
C- COMPUTE CLOSURE FUNCTIONS
      F1=E1-MTL1-MTS1
      F2=E2-MTL2-MTS2
      RETURN
      END
      FUNCTION SIERFC(QQ)
      COMMON/K17/SQRIPI
      REAL N
      V7=0.0
      NN=0
      DO 300 I=1,20
      NN=NN+1
      N=NN
      V8=N*QQ
      VV7=(-1.0)**NN*(SQRIPI*EXP(-V8**2)-V8*(1.0-ERF(V8)))
  300 V7=V7+VV7
      SIERFC=V7
      RETURN
      END
 1.629E+00 8.000E-04
-1.000E+01 1.529E+03
 1.629E+00 8.000E-04
-8.000E+02-8.000E+02-1.000E+03-1.000E+03
 1.629E+00 8.000E-04
 1.000E-05 1.000E-05 1.000E-08 1.000E-08
 1.629E+00 8.000E-04
0.15      0.15
0.5       0.01
```

A-3 - MICROANALYSIS CORRECTIONS

LIST OF SYMBOLS

A(I) - ATOMIC WEIGHT OF ELEMENT I
AB - ABSORPTION CORRECTION INDICATOR.
IF AB = 0, NO CORRECTION
IF AB = 1, CORRECTION
ABSC - ABSORPTION CORRECTION FACTOR
AT - ATOMIC NUMBER CORRECTION INDICATOR
IF AT = 0, NO CORRECTION
IF AT = 1, CORRECTION
ATOC - ATOMIC NUMBER CORRECTION FACTOR
AWA - ATOMIC WEIGHT OF ELEMENT A BEING FLUORESCED
AWB(I) - ATOMIC WEIGHT OF ELEMENT B FLUORESCING A, IN THE I≠TH FLUORESCENCE CORRECTION
C(I) - WEIGHT FRACTION OF ELEMENT I. ELEMENT 1 IS BEING ANALYSED
CA - WEIGHT FRACTION OF ELEMENT A BEING FLUORESCED
CB(I) - WEIGHT FRACTION OF ELEMENT B FLUORESCING A IN THE I≠TH CORRECTION
CSCT - COSEC OF TAKE-OFF ANGLE FOR X-RAYS
E - MEAN VALUE OF ELECTRON ENERGY, KEV
EC - EXCITATION ENERGY FOR RADIATION USED IN ANALYSIS, KEV
E0 - ACCELERATION VOLTAGE, KEV
ECA(I) - ABSORPTION EDGE OF FLUORESCED ELEMENT A FOR RADIATION OF THE TYPE CONSIDERED IN THE I≠TH CORRECTION, KEV
ECB(I) - ABSORPTION EDGE OF FLUORESCING ELEMENT B FOR RADIATION OF THE TYPE CONSIDERED IN THE I≠TH CORRECTION, KEV
F(I) - FLUORESCENCE CONTRIBUTION OF THE I≠TH CORRECTION
FL - FLUORESCENCE CORRECTION INDICATOR
FLUC - SUM OF THE I FLUORESCENCE CORRECTIONS
FXA(1) - LAPLACE TRANSFORM RATIO OF ELEMENT 1 IN STANDARD
FXAB - LAPLACE TRANSFORM OF ELEMENT 1 IN ALLOY
HA(I) - ATOMIC NUMBER PARAMETER FOR ELEMENT I
HAB - ATOMIC NUMBER PARAMETER FOR ALLOY
J(I) - MEAN IONIZATION POTENTIAL OF ELEMENT I, KEV
KAA - INTENSITY RATIO CORRECTED FOR ABSORPTION
KAF - INTENSITY RATIO CORRECTED FOR FLUORESCENCE
KAG - INTENSITY RATIO CORRECTED FOR ATOMIC NUMBER EFFECTS
M - NUMBER OF ELEMENTS IN ALLOY
MA(I) - MASS ABSORPTION COEFFICIENT OF ELEMENT I ABSORBING ELEMENT 1 RADIATION
MAAB - MASS ABSORPTION COEFFICIENT OF ALLOY
MAA(I) - MASS ABSORPTION COEFFICIENT OF ELEMENT A FOR A RADIATION IN THE I≠TH FLUORESCENCE CORRECTION
MAB(I) - MASS ABSORPTION COEFFICIENT OF ELEMENT A FOR B RADIATION IN THE I≠TH FLUORESCENCE CORRECTION

MBB(I) - MASS ABSORPTION COEFFICIENT OF ELEMENT B FOR B RADIATION IN THE I≠TH FLUORESCENCE CORRECTION

MBA(I) - MASS ABSORPTION COEFFICIENT OF ELEMENT B FOR A RADIATION IN THE I≠TH FLUORESCENCE CORRECTION

N(I) - ATOMIC FRACTION OF I≠TH ELEMENT

NFC - NUMBER OF FLUORESCENCE CORRECTIONS

OMEG(I) - WEIGHT OF LINE ASSOCIATED WITH LEVEL AND ELEMENT FOR THE I≠TH FLUORESCENCE CORRECTION

RA(I) - FRACTION OF POTENTIAL RETAINED IN STANDARD FOR ELEMENT I

RAB - FRACTION OF POTENTIAL RETAINED IN ALLOY

RMAC(I) - RATIO OF MASS ABSORPTION COEFFICIENTS FOR ELEMENTS UNDER CONSIDERATION IN THE I≠TH FLUORESCENCE CORRECTION

SA(I) - ELECTRON STOPPING POWER OF STANDARD FOR ELEMENT I

SAB - ELECTRON STOPPING POWER OF ALLOY

SIG(I) - ELECTRON RETARDATION PARAMETER FOR I≠TH FLUORESCENCE CORRECTION AND FOR ABSORPTION CORRECTION

THETA - TAKE-OFF ANGLE IN DEGREES

THETR - TAKE-OFF ANGLE IN RADIANS

UA(I) - OVERVOLTAGE RATIO FOR ELEMENT A IN THE I≠TH FLUORESCENCE CORRECTION

UB(I) - OVERVOLTAGE RATIO FOR ELEMENT B IN THE I≠TH FLUORESCENCE CORRECTION

WB(I) - FLUORESCENCE YIELD OF ELEMENT B IN THE I≠TH FLUORESCENCE CORRECTION

XA(1) - ABSORPTION PARAMETER FOR ELEMENT 1 IN STANDARD

XAB - ABSORPTION PARAMETER FOR ALLOY

Z(I) - ATOMIC NUMBER OF ELEMENT I

PROGRAM

```
C- 0-0.63 WT FRACTION FE IN MN - 0.3686 S INCLUSION
      DIMENSION A(5),AWB(5),C(5),CB(5),ECA(5),ECB(5),F(5),FXA(5),HA(5)
      DIMENSION J(5),MA(5),MAA(5),MAB(5),MBA(5),MBB(5),N(5)
      DIMENSION OMEG(5),RA(5),RMAC(5),SA(5),SIG(5),UA(5),UB(5)
      DIMENSION WB(5),XA(5),Z(5)
      EQUIVALENCE (CA,C(1)),(AWA,A(1))
  100 FORMAT(3I1)
  101 FORMAT(8F10.4)
  102 FORMAT(2F10.4)
  200 FORMAT(1X,11F10.5)
  210 FORMAT(/52X,8HTHETA = ,F5.1)
  211 FORMAT(/55X,5HEO = ,F5.1,/55X,5HEC = ,F6.3)
  213 FORMAT(/56X,4HM = ,I1)
  214 FORMAT(/54X,6HNFC = ,I1)
  212 FORMAT(/55X,5HAT = ,I1/55X,5HAB = ,I1/55X,5HFL = ,I1)
  215 FORMAT(/9X,1HA,10X,5(5X,F7.2,8X))
  216 FORMAT(/9X,1HZ,10X,5(6X,F5.1,9X))
  217 FORMAT(/9X,1HJ,10X,5(7X,F7.4,6X))
```

```
  218 FORMAT(/8X,2HRA,10X,5(7X,F7.4,6X))
  219 FORMAT(/8X,2HMA,10X,5(3X,F8.1,9X))
  220 FORMAT(/8X,2HCB,10X,5(7X,F5.2,8X))
  221 FORMAT(/7X,3HECA,10X,5(7X,F6.3,7X))
  222 FORMAT(/7X,3HECB,10X,5(7X,F6.3,7X))
  223 FORMAT(/7X,3HMAA,10X,5(3X,F8.1,9X))
  224 FORMAT(/7X,3HMBA,10X,5(3X,F8.1,9X))
  225 FORMAT(/7X,3HMBB,10X,5(3X,F8.1,9X))
  226 FORMAT(/7X,3HMAB,10X,5(3X,F8.1,9X))
  227 FORMAT(/6X,4HRMAC,10X,5(6X,F5.1,9X))
  228 FORMAT(/7X,3HAWB,10X,5(5X,F7.2,8X))
  229 FORMAT(//5X,9HPARAMETER,11X,9HELEMENT 1,11X,9HELEMENT 2,11X,9HELEM
     *ENT 3,11X,9HELEMENT 4,11X,9HELEMENT 5)
  230 FORMAT(//5X,9HPARAMETER,11X,9HFLUOCOR 1,11X,9HFLUOCOR 2,11X,9HFLUO
     *COR 3,11X,9HFLUOCOR 4,11X,9HFLUOCOR 5)
  231 FORMAT(//7X,3HKAF,6X,4HFLUC,7X,3HKAA,6X,4HABSC,7X,3HKAG,6X,4HATOC,
     *6X,4HC(1),6X,4HC(2),6X,4HC(3),6X,4HC(4),6X,4HC(5)//)
  232 FORMAT(/6X,4HOMEG,10X,5(5X,F7.2,8X))
  233 FORMAT(/8X,2HWB,10X,5(5X,F7.2,8X))
  250 FORMAT(I10,4F10.6)
      INTEGER AT,AB,FL
      REAL J,KAA,KAF,KAG,MA,MAA,MAAB,MAB,MBA,MBB,N,NA,NUM,NZ
C- INITIALIZE SOME OUTPUT VARIABLES
      KAG=0.0
      KAA=0.0

      KAF=0.0
      ATOC=0.0
      ABSC=0.0
      FLUC=0.0
C- INPUT DATA
      DATA THETA/18.0/
      READ(5,101)EO,EC
      READ(5,100)M
      READ(5,101)(A(I),I=1,M)
      READ(5,101)(Z(I),I=1,M)
C- READ TYPE OF CORRECTIONS TO BE APPLIED
      READ(5,100)AT,AB,FL
C- ECHO CHECK
      WRITE(6,210)THETA
      WRITE(6,211)EO,EC
      WRITE(6,213)M
      WRITE(6,212)AT,AB,FL
      WRITE(6,229)
      WRITE(6,215)(A(I),I=1,M)
      WRITE(6,216)(Z(I),I=1,M)
      IF(AT.EQ.0)GO TO 400
C- INPUT ATOMIC NUMBER CORRECTION DATA
      READ(5,101)(J(I),I=1,M)
      READ(5,101)(RA(I),I=1,M)
C- ECHO CHECK
      WRITE(6,217)(J(I),I=1,M)
```

```
      WRITE(6,218)(RA(I),I=1,M)
  400 IF(AB.EQ.0)GO TO 401
C- INPUT ABSORPTION CORRECTION DATA
      READ(5,101)(MA(I),I=1,M)
C- ECHO CHECK
      WRITE(6,219)(MA(I),I=1,M)
  401 IF(FL.EQ.0)GO TO 402
C- INPUT FLUORESCENCE CORRECTION DATA
      READ(5,100)NFC
      READ(5,101)(AWB(I),I=1,NFC)
      READ(5,101)(CB(I),I=1,NFC)
      READ(5,102)(ECA(I),ECB(I),I=1,NFC)
      READ(5,102)(MAA(I),MBA(I),I=1,NFC)
      READ(5,102)(MBB(I),MAB(I),I=1,NFC)
      READ(5,101)(OMEG(I),I=1,NFC)
      READ(5,101)(RMAC(I),I=1,NFC)
      READ(5,101)(WB(I),I=1,NFC)
C- ECHO CHECK
      WRITE(6,214)NFC
      WRITE(6,230)
      WRITE(6,228)(AWB(I),I=1,NFC)
      WRITE(6,220)(CB(I),I=1,NFC)
      WRITE(6,221)(ECA(I),I=1,NFC)
      WRITE(6,222)(ECB(I),I=1,NFC)
      WRITE(6,223)(MAA(I),I=1,NFC)
      WRITE(6,224)(MBA(I),I=1,NFC)
      WRITE(6,225)(MBB(I),I=1,NFC)
      WRITE(6,226)(MAB(I),I=1,NFC)
      WRITE(6,232)(OMEG(I),I=1,NFC)
      WRITE(6,227)(RMAC(I),I=1,NFC)
      WRITE(6,233)(WB(I),I=1,NFC)
  402 CONTINUE
C- PRELIMINARY COMPUTATIONS
      WRITE(6,231)
C- CONVERT THETA FROM DEGREES TO RADIANS
      THETR=THETA*6.28318/360.0
C- COMPUTE COSEC(THETR)
      CSCT=1.0/SIN(THETR)
C-----------------------------------------------------------------------
  406 CONTINUE
C- INPUT CONCENTRATIONS
      DO 350 IC=1,64
      C(1)=FLOAT(IC-1)/100.0
      C(3)=0.3686
      C(2)=1.0-C(3)-C(1)
C-----------------------------------------------------------------------
C- COMPUTE ATOMIC FRACTIONS
      DEN=0.0
      DO 301 L=1,M
  301 DEN=DEN+C(L)/A(L)
      DO 300 I=1,M
```

```
      NUM=C(I)/A(I)
  300 N(I)=NUM/DEN
C- MAKE KAG AND KAA EQUAL TO C(1) IN CASE ATOMIC NUMBER AND/OR
C- ABSORPTION CORRECTIONS ARE BYPASSED
      KAG=C(1)
      KAA=C(1)
      IF(AT.EQ.0)GO TO 403
C- APPLY ATOMIC NUMBER CORRECTIONS
C- COMPUTE MEAN ELECTRON ENERGY
      E=(EO+EC)/2.0
C- COMPUTE ELECTRON STOPPING POWER OF STANDARD
      DO 311 I=1,M
  311 SA(I)=Z(I)/A(I)*ALOG(1.166*E/J(I))
C- COMPUTE ELECTRON STOPPING POWER AND FRACTION OF POTENTIAL RETAINED
C- IN ALLOY

      RAB=0.0
      SAB=0.0
      DO 310 I=1,M
      RAB=RAB+C(I)*RA(I)
  310 SAB=SAB+C(I)*SA(I)
C- COMPUTE GENERATED INTENSITY RATIO
      ATOC=RAB/RA(1)*SA(1)/SAB
      KAG=C(1)*ATOC
  403 IF(AB.EQ.0)GO TO 404
C- APPLY ABSORPTION CORRECTIONS
C- COMPUTE MASS ABSORPTION COEFFICIENT OF ALLOY
      MAAB=0.0
      DO 320 I=1,M
  320 MAAB=MAAB+C(I)*MA(I)
C- COMPUTE ABSORPTION PARAMETER FOR STANDARD
      XA(1)=MA(1)*CSCT
C- COMPUTE ABSORPTION PARAMETER FOR ALLOY
      XAB=MAAB*CSCT
C- COMPUTE ELECTRON RETARDATION PARAMETER
      SIG(1)=2.39E05/(EO**1.5-EC**1.5)
C- COMPUTE ATOMIC NUMBER PARAMETER FOR STANDARD
      HA(1)=1.2*A(1)/Z(1)**2
C- COMPUTE ATOMIC NUMBER PARAMETER FOR ALLOY
      NA=0.0
      NZ=0.0
      DO 321 I=1,M
      NA=NA+N(I)*A(I)
  321 NZ=NZ+N(I)*Z(I)
      HAB=1.2*NA/NZ**2
C- COMPUTE LAPLACE TRANSFORM RATIOS FOR STANDARD AND ALLOY
      FXA(1)=1.0/(1.0+XA(1)/SIG(1))/(1.0+HA(1)/(1.0+HA(1))*XA(1)/SIG(1))
      FXAB=1.0/(1.0+XAB/SIG(1))/(1.0+HAB/(1.0+HAB)*XAB/SIG(1))
      ABSC=FXAB/FXA(1)
C- COMPUTE INTENSITY RATIO CORRECTED FOR ABSORPTION
C- COMPUTE ABSORPTION CORRECTION
```

```
      KAA=KAG*ABSC
  404 IF(FL.EQ.0)GO TO 405
C- APPLY FLUORESCENCE CORRECTIONS
      FLUC=0.0
      DO 330 I=1,NFC
      UA(I)=E0/ECA(I)
      UB(I)=E0/ECB(I)
      SIG(I)=2.39E05/(E0**1.5-ECA(I)**1.5)
      F1=OMEG(I)*WB(I)/2.0*(RMAC(I)-1.0)/RMAC(I)*((UB(I)-1.0)/(UA(I)-1.0
     *))**(5.0/3.0)*AWA/AWB(I)*MAB(I)*CB(I)
      F2=(ALOG(1.0+(MAA(I)*CA+MBA(I)*CB(I))/(MAB(I)*CA+MBB(I)*CB(I))*CSC
     *T))/(MAA(I)*CA+MBA(I)*CB(I))/CSCT
      F3=(ALOG(1.0+SIG(I)/(MAB(I)*CA+MBB(I)*CB(I))))/SIG(I)
      F(I)=F1*(F2+F3)
  330 FLUC=FLUC+F(I)
  405 KAF=KAA*(1.0+FLUC)
      WRITE(6,200)KAF,FLUC,KAA,ABSC,KAG,ATOC,(C(I),I=1,M)
      WRITE(7,250)IC,KAF,KAA,KAG,C(1)
  350 CONTINUE
  999 STOP
      END
```

```
15.0      7.111
3
55.85     54.94     32.066
26.0      25.0      16.0
110
0.332     0.316     0.180
0.901     0.906     0.947
71.4      63.5      167.4
```

TABLE 2.1.1 Summary of Diffusion Data.

Phase	Species	D cm^2/sec	D_0 cm^2/sec	E cal/mole	T °C	Source
L-Fe	Mn		2.055×10^3	60656	1530-1600	PASCHE and HAUTMANN(1935)
"	S	1.7×10^{-4}			1560	McCARRON and BELTON(1969)
"	S		4.9×10^{-4}	4350	1500-1650	SAITO et al.(1961)
"	C		2.447×10^{-3}	13052	1350-1500	MORGAN and KITCHNER(1955)
"	O	2.3×10^{-5}			1560	McCARRON and BELTON(1969)
γFe	Mn		0.486 + 0.011 x wt%Mn	66000	950-1450	WELLS and MEHL (1941)
"	Mn		106.7	79318	1150-1350	NAKAO (1967)
"	S		0.018	38600	1150-1250	KONONYUK (1965)
"	S		2.42	53400	>1200	SEIBEL (1964)
"	C		0.27	34500	1000-1400	WELLS et al. (1950)
"	O	10^{-9}			1100	BROWER et al. (1934)
α,δFe	S		1.35	48400	$907<T>1400$	SEIBEL (1964)
"	Mn		0.264	59500	1446-1494	SMITH (1970)
(Fe,Mn)S	Fe	2×10^{-7}			1300	NAKAO (1967)
"	Mn	2×10^{-7}			1300	NAKAO (1967)

TABLE 4.1.1 Thermodynamic Data Required for Calculation of δ_{Fe} + Liquid Equilibria in the Fe-Mn-S System.

Parameter	Units	Value	Source
ϵ^{L}_{MnMn}	-	-0.6	b)
ϵ^{L}_{SS}	-	-3.7	a)
ϵ^{L}_{MnS}	-	-5.7	a)
ϵ^{δ}_{MnMn}	-	-0.8	c)
ϵ^{δ}_{SS}	-	-67	c)
ϵ^{δ}_{MnS}	-	-5.7	Set equal to ϵ^{L}_{MnS}
γ^{oL}_{Mn}	-	1.38	b)
γ^{oL}_{S}	-	0.18	b)
$\gamma^{o\delta}_{Mn}$	-	1.41	c)
$\gamma^{o\delta}_{S}$	-	0.095	c)
ζ_{Fe}	cal/mole	3360	a)
η_{Fe}	cal/mole/$(^{o}C)^{2}$	-1.2×10^{-4}	c)
$T^{\delta L}_{Fe}$	^{o}C	1536	a)
ζ_{Mn}	cal/mole	1720	c)
η_{Mn}	cal/mole/$(^{o}C)^{2}$	0	c)
$T^{\delta L}_{Mn}$	^{o}C	900	c)
ζ_{S}	cal/mole	13000	c)
η_{S}	cal/mole/$(^{o}C)^{2}$	-1.3×10^{-2}	c)
$T^{\delta L}_{S}$	^{o}C	1190	c)

a) ELLIOT et al. (1963)
b) Calculated from data of ELLIOT et al. (1963)
c) Calculated by fitting tangent-plane equations to binary constitutional data.

TABLE 4.1.2 Tie-lines and Partition Coefficients of 1510°C Isotherm for δ + Liquid Equilibrium in the Fe-Mn-S System.

		Equilibrium Concentrations at %				Partition Coefficients		
		x_{Mn}^{δ}	x_{S}^{δ}	x_{Mn}^{L}	x_{S}^{L}	k_{Fe}^{T}	k_{Mn}^{T}	k_{S}^{T}
Full Interaction	0	0.0000	0.0642	0.0000	1.2883	1.01240	0.70938	0.04987
	1	0.5000	0.0547	0.6980	1.1097	1.01276	0.71637	0.04934
	2	1.0000	0.0456	1.3829	0.9324	1.01299	0.72335	0.04885
	3	1.5000	0.0366	2.0540	0.7567	1.01311	0.73032	0.04841
	4	2.0000	0.0280	2.7127	0.5827	1.01311	0.73728	0.04800
	5	2.5000	0.0195	3.3593	0.4103	1.01299	0.74420	0.04763
	6	3.0000	0.0113	3.9942	0.2998	1.01277	0.75100	0.04730
	7	3.5000	0.0033	4.6177	0.0712	1.01244	0.75795	0.04669
	8	3.7145	0.0000	4.8799	0.0000	1.01227	0.76086	0.04687
No Cross Interaction	0	0.0000	0.0642	0.0000	1.2883	1.01240	0.76064	0.04987
	1	0.5000	0.0553	0.6574	1.1088	1.01233	0.76063	0.04990
	2	1.0000	0.0465	1.3147	0.9313	1.01227	0.76063	0.04993
	3	1.5000	0.0377	1.9720	0.7556	1.01223	0.76064	0.04996
	4	2.0000	0.0291	2.6293	0.5818	1.01221	0.76067	0.04999
	5	2.5000	0.0205	3.2864	0.4098	1.01221	0.76071	0.05002
	6	3.0000	0.0120	3.9434	0.2396	1.01222	0.76076	0.05005
	7	3.5000	0.0036	4.6002	0.0712	1.01225	0.76083	0.05008
	8	3.7145	0.0000	4.8799	0.0000	1.01227	0.76086	0.05009

TABLE 4.1.3 Thermodynamic Data Required for Calculation of Metastable γ_{Fe} + Liquid Equilibria in the Fe-Mn-C System.

Parameter	Units	Value	Source
ϵ^{L}_{MnMn}	-	-0.6	ELLIOT et al.(1963)
ϵ^{L}_{CC}	-	6.0	a)
ϵ^{L}_{MnC}	-	-1.3	a)
ϵ^{γ}_{MnMn}	-	-0.64	ROY and HULTGREN (1965)
ϵ^{γ}_{CC}	-	14	a)
ϵ^{γ}_{MnC}	-	-4.2	a)
γ^{oL}_{Mn}	-	1.38	b)
$\gamma^{oL}_{C})_{Sgr}$	-	0.66	a)
$\gamma^{o\gamma}_{Mn}$	-	1.52	ROY and HULTGREN (1965)
$\gamma^{o\gamma}_{C})_{Sgr}$	-	1.82	a)
ζ_{Fe}	cal/mole	3360	ELLIOT et al. (1963)
η_{Fe}	cal/mole/$(^{o}C)^{2}$	-	c)
$T^{\gamma L}_{Fe}$	^{o}C	1529	DARKEN and GURRY (1953)
ζ_{Mn}	cal/mole	4100	c)
η_{Mn}	cal/mole/$(^{o}C)^{2}$	$-1.1x10^{-3}$	c)
$T^{\gamma L}_{Mn}$	^{o}C	1240	estimated
ζ_{C}	cal/mole	2500	c)
η_{C}	cal/mole/$(^{o}C)^{2}$	$-1x10^{-3}$	c)
$T^{\gamma L}_{C}$	^{o}C	500	c)
T^{f}_{gr}	^{o}C	3700 ± 100	LYMAN (1948)
Δs^{f}_{gr}	cal/mole/^{o}K	6.8	KUBASCHEWSKI and EVANS (1955)

a) Calculated from data of TURKDOGAN and GRANGE (1968)
b) Calculated from data of ELLIOT et al. (1963)
c) Calculated by fitting tangent-plane equations to binary constitutional data.

TABLE 4.1.4 Tie-lines and Partition Coefficients of 1490°C Isotherm for Metastable γ + Liquid Equilibria in Fe-Mn-C System. Atomic % Basis.

	x^{γ}_{Mn}	x^{γ}_{C}	x^{L}_{Mn}	x^{L}_{C}	k^{T}_{Fe}	k^{T}_{Mn}	k^{T}_{C}
0	0.000	0.737	0.000	2.879	1.0220	0.7503	0.2561
1	1.000	0.652	1.332	2.509	1.0228	0.7506	0.2600
2	2.000	0.561	2.664	2.126	1.0234	0.7507	0.2640
3	3.000	0.462	3.996	1.726	1.0240	0.7507	0.2680
4	4.000	0.356	5.329	1.309	1.0244	0.7506	0.2721
5	5.000	0.241	6.664	0.871	1.0248	0.7503	0.2761
6	6.000	0.115	8.002	0.412	1.0251	0.7500	0.2802
7	6.852	0.000	9.146	0.000	1.0252	0.7492	0.2837

TABLE 4.1.5 Tie-lines and Partition Coefficients of 1490°C Isotherm for Metastable γ + Liquid Equilibria in Fe-Mn-C System. Weight % Basis.

	x^{γ}_{Mn}	x^{γ}_{C}	x^{L}_{Mn}	x^{L}_{C}	k^{T}_{Fe}	k^{T}_{Mn}	k^{T}_{C}
0	0.0000	0.159	0.0000	0.634	1.0048	0.7375	0.2517
1	0.989	0.141	1.337	0.551	1.0077	0.7395	0.2562
2	1.977	0.121	2.666	0.465	1.0107	0.7414	0.2607
3	2.963	0.100	3.988	0.376	1.0136	0.7431	0.2653
4	3.948	0.077	5.301	0.285	1.0165	0.7448	0.2700
5	4.932	0.052	6.608	0.189	1.0194	0.7464	0.2747
6	5.913	0.025	7.908	0.089	1.0224	0.7480	0.2795
7	6.748	0.000	9.010	0.000	1.0249	0.7490	0.2829

TABLE 5.6.1 Typical Analyses of Materials Used in the Preparation of Alloys

Ferrovac E (U.S. Steel)

Impurities	wt%
C	0.003
Mn	0.001
P	0.003
S	0.005
Si	0.006
Cu	0.001
Ni	0.014
Cr	0.01
V	0.004
Mo	0.001
O_2	0.00046
Co	0.01
W	0.01
H_2	0.00005
N_2	0.0002
Ti	-
Al	-

AUC Graphite (Union Carbide)

Impurities	wt%
S	0.004
Ca	0.0043
Fe	0.005
Si	0.0014
Ash as Oxide	0.03

Manganese (A.D. McKay)

Impurities	wt%
Mainly Oxygen	0.1

TABLE 6.2.1 Nominal Compositions of Fe-Mn Base Alloys and Growth Conditions of Specimens Examined for Macrosegregation.

	Solute Concentration wt %			Velocity mm/hr	Temp. Grad $^{o}C/cm$
Specimen	Mn	S	C		
1	3.0	0.005	-	5	25
2	0.5	0.03	0.4	50	23
5	4.0	-	-	50	25
6	3.0	0.005	0.4	50	25
7	3.0	0.005	-	50	25
9	13.0	0.25	-	50	30
10	0.5	0.03	-	50	20
13	13.0	0.25	-	280	30
14	13.0	0.25	-	600	30

TABLE 6.3.1 Nominal Compositions and Growth Conditions of Specimens in Which the Solidification Structure was Studied.

	Solute Concentration wt %			Growth Rate mm/hr	Temp. Gradient* °C/cm
Specimen	Mn	S	C		
6	3.0	0.005	0.4	50	25
9	13.0	0.25	-	50	30
13	13.0	0.25	-	280	30
14	13.0	0.25	-	600	30
21	0.5	0.03	0.4	50	23
23	-	0.03	0.4	50	20
24	13.0	0.25	-	50 100 200 400	30
25**	13.0	-	-	50 100	30

* The temperature gradient of specimen 21 was measured; other gradients were estimated.

** Specimen 25 also contained 0.25 wt% ZrO_2.

TABLE 6.3.2 Composition, Growth Conditions and Dendrite Arm Spacings of Specimens Used in Arm Spacing Study

Specimen	Composition wt %			Velocity cm/hr	Temperature Gradient** $^{o}C/cm$		Arm Spacing microns		-
	Mn	S	C	V	G	G'	d_1	d_2	d_1/d_2
9	13	0.25	-	5	30	40	430	207	2.08
13	13	0.25	-	28	30	40	239	91	2.63
14	13	0.25	-	60	30	40	200	68	2.94
6	3	0.005	0.4	5	20	27	825	370	2.23
21	0.5	0.03	0.4	5	23.3	31.4	420		
25*	13	-	-	5	29	39	360		
				10	29	39	303		

* Specimen 25 also contained 0.25 wt % ZrO_2.

** The temperature gradients of specimen 21 were measured. Other gradients were estimated.

TABLE 6.3.3 Electron-probe Measurements of Manganese Microsegregation.

Specimen	Path	C_M wt%	C_m wt%	I_S
6	[x]	4.2	2.3	1.83
	[+]	2.9	2.2	1.32
9	[x]	16.2	10.5	1.54
	[+]	12.7	9.1	1.40
13	[x]	17.0	11.0	1.55
	[+]	13.4	9.7	1.38
14	[x]	15.5	11.5	1.35
	[+]	15.7	12.2	1.29
9	Across Group of Secondary Arms	10.0	14.3	1.43
24	Specimen Diameter			
50 mm/hr		19.5	11.2	1.18
100 "		9.6	12.7	1.32
200 "		9.5	12.4	1.31
400 "		9.4	12.4	1.32

TABLE 6.4.1 Results of Electron-Probe Microanalysis and Optical Examination of Inclusions in Specimens 1, 2, 5, 6, 7, 9, 10, 12, 13 and 14. The Oxygen Contents Were Calculated by Difference.

LEGEND

Shape

A : Angular

E : Elongated

I : Irregular

R : Round

S : Sinusoidal

Colour

DG : Dark Grey

MG : Medium Grey

TA : Tan

TR : Translucent

SPECIMEN 1

No	Concentration wt %				Size microns	Shape	Colour
	Fe	Mn	S	0			
1	62.3	12.2	4.6	20.9	8	R	MG
2	57.6	15.3	4.0	23.1	10	R	MG
3	42.1	36.3	.5	21.1	10	R	MG
4	40.1	39.4	.8	19.7	16x60	R	MG
5	36.7	41.2	.0	22.1	12	R	MG
6	36.5	41.1	0.0	22.4	16	R	MG
7	21.6	57.5	1.0	19.9	18	R	MG
8	19.9	60.3	0.0	19.8	20	R	MG
9	21.3	58.2	.5	20.0	20	R	MG
10	19.6	61.3	0.0	19.1	16	R	MG
11	20.9	57.2	4.1	17.8	32	R	MG
12	20.9	59.2	.0	19.9	16	R	MG
13	20.1	58.9	6.7	14.3	12	R	MG
14	19.4	53.3	14.1	13.2	60	R	MG
15	20.0	59.8	1.6	18.6	10	R	MG
16	21.4	57.6	1.4	19.6	18	R	MG
17	21.4	58.0	1.3	19.3	16	R	MG
18	20.3	59.8	.2	19.7	20	R	MG
19	20.6	56.6	4.6	18.2	12	R	MG
20	21.1	55.9	4.8	18.2	22	R	MG
21	20.0	61.7	.1	18.2	22	R	MG
22	22.3	58.3	.8	18.6	28	R	MG

SPECIMEN 2

No	Concentration wt %				Size microns	Shape	Colour
	Fe	Mn	S	0			
1	9.2	54.1	36.7		20	R	MG
2	6.9	56.8	36.4		18	R	MG
3	9.0	54.6	36.4		20	R	MG
4	11.4	52.3	36.3		18	R	MG
5	6.5	56.6	36.8		10	R	MG
6	5.7	57.9	36.4		10	R	MG
7	6.4	56.5	37.1		15	R	MG
8	7.3	56.3	36.5		15	R	MG
9	8.1	55.5	36.5		10	R	MG
10	9.6	53.2	37.2		15	R	MG

11	7.7	55.7	36.7		35	R	MG
12	6.6	56.5	36.8		20	R	MG
13	8.9	54.6	36.6		14	R	MG
14	23.5	40.1	36.5		15	R	MG
15	17.1	46.1	36.8		30	R	MG
16	11.5	51.7	36.8		12	R	MG
17	16.7	46.9	36.4		10	R	MG
18	4.3	59.2	36.5		10	R	MG
19	4.9	58.8	36.3		10	R	MG
20	5.5	58.1	36.3		15	R	MG
21	14.3	49.0	36.7		10	R	MG
22	19.4	43.1	37.5		10	R	MG
23	22.1	41.1	36.8		18	R	MG
24	14.8	49.3	36.0		26	R	MG
25	14.7	43.3	37.0		25	R	MG
26	68.4	0.1	1.5	30.0	20	R	MG
27	67.1	0.2	1.5	31.2	16	R	MG
28	7.8	55.4	36.8		20	R	MG
29	61.8	3.3	34.9		10x40	E	TA
30	67.9	0.1	0.3	31.7	30	I	MG
31	8.1	55.2	36.7		12	S	MG
32	6.7	56.5	36.7		10	R	MG
33	74.9	0.2	1.2	23.7	14	I	MG
34	7.4	55.6	37.0		18	R	MG
35	2.4	60.8	36.7		14	A	MG
36	1.8	61.1	37.1		8x20	E	MG
37	35.6	26.7	37.7		20	R	MG
38	5.0	58.2	36.8		10	R	MG
39	7.0	56.1	36.9		10	R	MG
40	8.6	54.1	37.3		20	R	MG
41	2.7	60.5	36.8		10x15	E	MG
42	9.0	51.7	39.3		12	R	MG
43	10.4	50.7	38.9		12	R	MG
44	8.5	52.7	38.8		15	R	MG
45	5.8	55.9	38.2		6x10	E	MG
46	6.1	55.2	38.7		20	A	MG
47	3.2	59.5	37.3		15	R	MG
48	7.4	54.2	38.4		10	R	MG
49	7.0	56.1	36.8		15	S	MG
50	8.8	54.4	36.7		10	R	MG
51	20.0	43.2	36.8		20	I	MG
52	11.7	51.3	37.1		15x100	R	MG
53	7.6	55.6	36.7		15x100	E	MG
54	7.8	56.5	35.7		20x100	E	MG
55	9.8	53.0	37.1		20	I	MG
56	10.5	53.0	36.5		10x30	E	MG

SPECIMEN 5

	Concentration wt %				Size microns	Shape	Colour
No	Fe	Mn	S	O			
1	0.8	49.9	3.3	46.0	10	R	TR
2	1.2	40.7	2.7	55.4	14	R	TR
3	0.5	39.6	3.5	56.4	16	R	TR
4	1.4	58.3	4.6	35.7	14	R	TR
5	1.0	49.9	3.9	45.2	20	R	TR
6	1.0	44.6	3.7	50.7	12	R	TR
7	1.3	44.9	0.8	53.0	12	R	TR

SPECIMEN 6

	Concentration wt %				Size microns	Shape	Colour
No	Fe	Mn	S	O			
1	1.4	62.6	36.0		12	R	MG
2	1.8	60.6	37.6		18	R	MG
3	1.5	61.9	36.6		10	A	MG
4	1.0	62.9	36.0		8	A	MG
5	1.1	62.6	36.3		10	A	MG
6	1.2	62.3	36.4		14	A	MG
7	1.0	62.5	36.6		10	S	MG
8	.8	62.2	37.0		12	A	MG
9	1.1	61.8	37.0		10	A	MG
10	1.5	62.0	36.5		20	R	MG
11	.6	61.6	37.8		20	I	MG
12	1.3	60.8	37.9		20	S	MG
13	1.2	61.3	37.5		20	S	MG
14	1.0	61.5	37.5		10x20	I	MG
15	1.2	62.6	36.2		8x20	I	MG
16	1.1	62.4	36.5		16	A	MG
17	.9	62.0	37.1		22	A	MG

SPECIMEN 7

	Concentration wt %				Size microns	Shape	Colour
No	Fe	Mn	S	O			
1	27.4	54.4	0.0	18.2	20	R	MG
2	24.8	51.9	4.2	19.1	10	R	MG
3	64.5	.1	0.0	35.4	8	A	MG

4	66.4	.0	0.0	33.6	8	A	MG
5	22.1	52.4	1.0	24.5	20	R	MG
6	28.5	50.0	.3	21.2	18	R	MG
7	22.3	55.0	.5	22.2	16	R	MG
8	19.6	59.2	1.2	20.0	16	R	MG
9	58.8	.1	0.0	41.1	40	I	MG
10	19.1	64.1	.0	16.8	10	R	MG
11	18.9	64.5	.1	16.5	12	R	MG
12	19.6	61.1	.3	19.0	10	R	MG
13	17.3	66.6	.6	15.5	12	R	MG
14	16.4	66.2	2.1	15.3	16	R	MG
15	16.4	64.5	3.3	15.8	16	R	MG
16	15.3	67.1	3.2	14.4	20	R	MG
17	15.7	67.9	0.0	16.4	10	R	MG
18	20.8	61.1	1.5	16.6	8	R	MG
19	63.4	.4	0.0	36.2	10	I	MG
20	69.0	.2	0.0	30.8	20	I	MG
21	15.9	60.9	5.3	17.9	14	R	MG
22	13.1	65.1	.3	21.5	10	R	MG
23	12.5	67.9	1.8	17.8	10	R	MG
24	11.6	66.6	7.7	14.1	10	R	MG
25	11.6	69.0	5.4	14.0	10	R	MG
26	18.3	63.2	3.5	15.0	10	R	MG
27	10.7	72.5	1.3	15.5	14	R	MG
28	12.0	67.1	6.1	14.8	10	R	MG
29	9.9	70.7	2.2	17.2	14	R	MG
30	9.2	71.5	1.3	18.0	14	R	MG
31	3.7	50.3	.1	45.9	20	R	MG
32	2.7	53.3	1.0	43.0	22	R	MG
33	2.4	59.0	3.3	35.3	28	R	MG
34	2.2	49.4	3.8	44.6	10	R	MG
35	1.3	47.4	3.2	48.1	18	R	MG
36	1.1	39.7	.9	58.3	14	R	MG
37	1.1	30.6	0.0	68.3	64	A	MG

SPECIMEN 9

	Concentration wt %				Size microns	Shape	Colour
No	Fe	Mn	S	0			
1	1.3	62.4	36.4		10	R	MG
2	2.1	62.0	35.8		10	I	MG
3.	2.0	69.0	29.0		20	R	MG
4	3.2	65.5	31.3		14	R	MG
5	1.1	62.5	36.4		20	R	MG
6	1.3	63.1	35.6		32	E	MG
7	1.2	62.8	36.0		30	R	MG
8	1.4	62.3	36.4		14	R	MG
9	1.4	62.3	36.4		16	R	MG

10	.9	63.2	35.9	18	R	MG
11	1.2	62.8	36.0	20	R	MG
12	1.2	62.5	36.2	28	R	MG
13	1.2	62.7	36.1	20	R	MG
14	1.9	62.5	35.5	10x20	R	MG
15	1.4	62.5	36.1	10	R	MG
16	1.0	62.6	36.3	34	R	MG
17	1.0	62.5	36.4	18	R	MG
18	.7	62.6	36.6	20	R	MG
19	1.2	63.0	35.7	20	R	MG
20	.9	63.5	35.6	18	R	MG
21	1.0	63.6	35.3	20	R	MG
22	.7	62.4	36.8	18	R	MG
23	1.1	61.6	37.3	20	I	MG
24	.6	62.4	37.0	20	R	MG
25	1.1	62.6	36.3	18	R	MG
26	.9	62.0	37.0	14	R	MG
27	1.4	61.4	37.1	16	I	MG
28	.7	62.2	37.0	16	I	MG
29	1.1	61.9	37.0	22	R	MG
30	.8	62.5	36.6	12	A	MG
31	1.2	61.9	37.0	12	I	MG
32	1.4	64.0	34.6	15	R	MG
33	1.3	61.7	37.0	16	A	MG
34	1.1	62.0	36.9	20	A	MG
35	.6	62.1	37.3	20	A	MG
36	.5	62.6	36.9	20x50	I	MG
37	.6	62.8	36.5	15x50	S	MG
38	1.5	61.7	36.8	14	A	MG
39	1.4	61.9	36.8	10x50	S	MG
40	1.3	61.7	37.0	10x50	S	MG
41	1.5	62.0	36.5	10	S	MG
42	1.1	62.1	36.8	10x40	S	MG

SPECIMEN 10

	Concentration wt %				Size microns	Shape	Colour
No	Fe	Mn	S	0			
1	72.2	2.3	.1	25.4	30	R	MG
2	72.5	2.2	.9	24.4	28	R	MG
3	71.7	1.8	4.5	22.0	20	R	MG
4	73.9	1.9	.7	23.5	20	R	MG
5	71.8	3.3	2.0	22.9	12	R	MG
6	71.8	3.0	.1	25.1	14	R	MG
7	70.5	2.4	.6	26.5	24	R	MG
8	68.0	0.0	23.3	8.7	4x25	E	TA
9	69.6	2.7	5.4	22.3	20	R	MG
10	69.8	2.8	.4	27.0	30	R	MG

11	70.0	1.9	4.3	23.8	20	R	MG
12	70.2	2.5	.1	27.2	10	R	MG
13	59.9	3.0	.1	37.0	16	R	MG
14	71.2	3.7	.8	24.3	14	R	MG
15	71.5	4.0	1.1	23.4	12	R	MG
16	69.4	3.6	2.4	24.6	28	R	MG
17	71.1	3.4	2.8	22.7	20	R	MG
18	67.3	8.0	.3	24.4	24	R	TA
19	65.9	8.8	1.5	23.8	16	R	MG
20	68.6	4.7	.8	25.9	26	R	MG
21	66.1	10.4	.0	23.5	16	R	MG
22	67.0	8.0	.4	24.6	16	R	MG
23	66.9	7.9	1.5	23.7	22	R	MG
24	68.1	7.9	.0	24.0	14	R	MG
25	69.4	7.5	.1	23.0	20	R	MG
26	65.4	11.4	.1	23.1	20	R	MG
27	62.4	12.8	.2	24.6	16	R	MG
28	63.6	13.3	.3	22.8	18	R	MG
29	61.8	12.0	6.8	19.4	22	R	MG
30	62.0	13.9	.6	23.5	18	R	MG
31	65.8	11.8	0.0	22.4	20	R	MG
32	55.5	16.7	0.2	27.6	12	R	MG
33	50.9	22.1	2.2	24.8	18	R	MG
34	53.0	21.1	.4	25.5	30	R	MG
35	51.8	24.2	.1	23.9	24	R	MG
36	49.7	26.2	.6	23.5	18	R	MG
37	46.0	25.7	.5	27.8	85	R	MG
38	45.2	26.7	.3	27.8	30	R	MG
39	44.4	29.6	2.5	23.5	30	R	MG
40	44.6	30.0	.5	24.9	26	R	MG
41	47.7	25.1	2.0	25.2	30	R	MG
42	49.0	29.5	.1	21.4	36	R	MG
43	45.8	30.7	.3	23.2	14	R	MG
44	45.1	29.4	1.6	23.9	20	R	MG
45	34.2	23.1	.4	42.3	20	R	MG
46	37.2	26.2	4.0	32.6	20	R	MG
47	43.6	29.5	5.0	21.9	36	R	MG
48	43.1	29.6	4.6	22.7	18	R	MG
49	41.3	26.5	.4	31.8	50x100	E	MG
50	41.2	26.3	1.3	31.2	50x100	E	MG
51	41.5	26.8	2.0	29.7	50x100	E	MG
52	42.4	26.7	.1	30.8	50x100	E	MG
53	41.7	26.6	1.9	29.8	50x100	E	MG
54	40.1	26.5	2.2	31.2	50x100	E	MG
55	39.4	27.7	2.7	30.2	50x100	E	MG
56	39.7	27.7	2.1	30.5	50x100.	E	MG
57	37.1	26.4	2.4	34.1	40	R	MG
58	37.9	37.0	5.1	20.0	12	R	MG
59	28.9	35.9	2.8	32.4	50x80	E	MG
60	28.4	35.9	2.6	33.1	50x80	E	MG
61	26.9	36.3	2.6	34.2	50x80	E	MG

SPECIMEN 12

	Concentration wt %				Size microns	Shape	Colour
No	Fe	Mn	S	O			
1	53.2	0.0	1.0	45.9	12	R	TR
2	64.4	0.0	26.0	9.6	12	E	MG
3	29.6	0.0	.1	70.3	15	A	MG
4	24.3	0.0	0.0	75.7	20	A	MG
5	25.4	0.0	.0	74.6	20	A	MG
6	66.1	0.0	26.1	7.8	10x100	E	MG
7	34.4	0.0	.1	65.5	20	R	MG
8	64.2	0.0	30.5	5.3	10x300	E	TA

SPECIMEN 13

	Concentration wt %				Size microns	Shape	Colour
No	Fe	Mn	S	O			
1	1.5	63.9	34.6		10	R	MG
2	1.1	63.5	35.4		10	R	MG
3	1.4	63.6	35.0		10	R	MG
4	1.2	65.9	32.9		8	R	MG
5	4.7	62.3	33.0		8	R	MG
6	2.1	65.9	32.0		8	R	MG
7	1.4	65.9	32.6		12	R	MG
8	3.0	62.8	34.2		8	R	MG
9	1.7	62.5	35.8		8	A	MG
10	2.4	60.9	36.7		10	A	MG
11	1.2	61.5	37.3		10	R	MG
12	1.8	61.5	36.7		10	R	MG
13	1.4	61.7	36.9		10	A	MG
14	1.2	61.9	36.9		16	A	MG
15	1.2	61.7	37.0		10	A	MG
16	1.7	60.5	37.9		12	R	MG
17	1.2	61.7	37.1		10	S	MG
18	1.3	61.5	37.2		10	S	MG
19	1.6	63.4	35.1		12	A	MG
20	1.4	62.4	36.2		10	R	MG
21	1.5	62.2	36.3		10	R	MG
22	1.6	62.6	35.8		10	R	MG
23	1.4	62.1	36.5		10	S	MG
24	1.3	62.3	36.4		10	I	MG
25	1.3	62.0	36.7		10	A	MG
26	1.2	62.5	36.3		12	A	MG
27	1.0	62.3	36.6		20	A	MG
28	1.3	62.4	36.3		12	A	MG

29	1.3	62.7	36.0		10	S	MG
30	1.3	62.5	36.2		12	S	MG
31	1.4	62.1	36.5		14	R	MG
32	1.2	62.4	36.4		18	R	MG
33	1.3	62.4	36.2		14	R	MG
34	1.4	62.0	36.6		12	R	MG
35	1.4	61.8	36.8		10x20	S	MG
36	1.7	62.1	36.3		6x90	S	MG

SPECIMEN 14

	Concentration wt %				Size microns	Shape	Colour
No	Fe	Mn	S	O			
1	3.8	65.4	30.8		8	R	MG
2	2.5	59.9	37.7		8	R	MG
3	11.5	55.4	33.2		8	R	MG
4	1.6	61.2	37.2		10	R	MG
5	1.6	60.7	37.6		10	R	MG
6	1.3	61.7	37.1		10	R	MG
7	1.9	61.0	37.1		10	R	MG
8	1.5	61.6	36.9		8	R	MG
9	3.2	59.4	37.4		8	R	MG
10	1.4	62.0	36.5		10	R	MG
11	12.1	55.1	32.9		8	S	MG
12	7.1	58.0	34.9		10	S	MG
13	3.2	61.0	35.8		8	R	MG
14	1.7	61.9	36.4		12	R	MG
15	3.1	59.3	37.6		10	S	MG
16	.8	60.5	38.7		30x20	S	MG
17	.5	60.6	38.9		12x20	S	MG
18	3.4	57.9	38.7		4x20	E	MG
19	1.7	60.2	38.1		6x10	A	MG
20	4.2	59.8	36.0		8	R	MG
21	1.4	59.7	38.9		8	R	MG
22	1.5	60.0	38.5		8	A	MG
23	1.7	60.0	38.3		8	A	MG
24	1.4	60.5	38.1		10	R	MG
25	.8	60.6	38.6		20x120	S	MG
26	.7	60.8	38.5		100	S	MG
27	1.2	59.5	39.3		10x20	S	MG
28	3.4	61.8	34.8		8	R	MG
29	.6	63.1	36.3		30	S	MG
30	1.5	62.5	36.1		10	R	MG
31	1.2	62.5	36.3		10	I	MG
32	1.5	62.3	36.2		8	R	MG
33	1.5	62.8	35.7		12	R	MG
34	1.4	63.0	35.5		10	R	MG

35	1.5	62.7	35.7	8	A	MG
36	1.3	62.5	36.2	8	R	MG
37	1.5	62.2	36.2	8	R	MG
38	1.6	62.7	35.7	8	A	MG
39	1.5	62.5	36.0	10	R	MG
40	1.4	61.8	36.8	10	R	MG
41	1.5	62.1	36.4	10	R	MG
42	1.4	61.5	37.1	10	E	MG
43	1.4	62.7	35.9	10	E	MG
44	1.0	62.0	37.0	10	R	MG
45	1.1	62.8	36.2	12	R	MG
46	12.7	56.2	31.1	8	R	MG
47	1.5	61.9	36.7	8	R	MG
48	1.1	62.0	36.9	10	R	MG
49	.5	71.2	28.3	20	A	MG
50	1.0	62.5	36.6	16	S	MG
51	1.6	61.6	36.8	4x20	E	MG
52	1.6	61.5	37.0	4x30	E	MG
53	2.4	61.3	36.3	8x50	I	MG
54	1.7	61.4	36.9	6x50	E	MG

TABLE 7.4.1 Data for the Application of Stokes' Law to Inclusion Flotation.

Parameter	Symbol	Value	Units	Source
Gravity Constant	ω	981	cm/sec^2	WEAST (1964)
Viscosity	ν	0.07	poise	ELLIOT et al.(1963)
Inclusion Density	ψ_I	4	g/cm^3	FLEMINGS et al.(1961)
Melt Density	ψ_M	7.3	g/cm^3	ELLIOT et al.(1963)

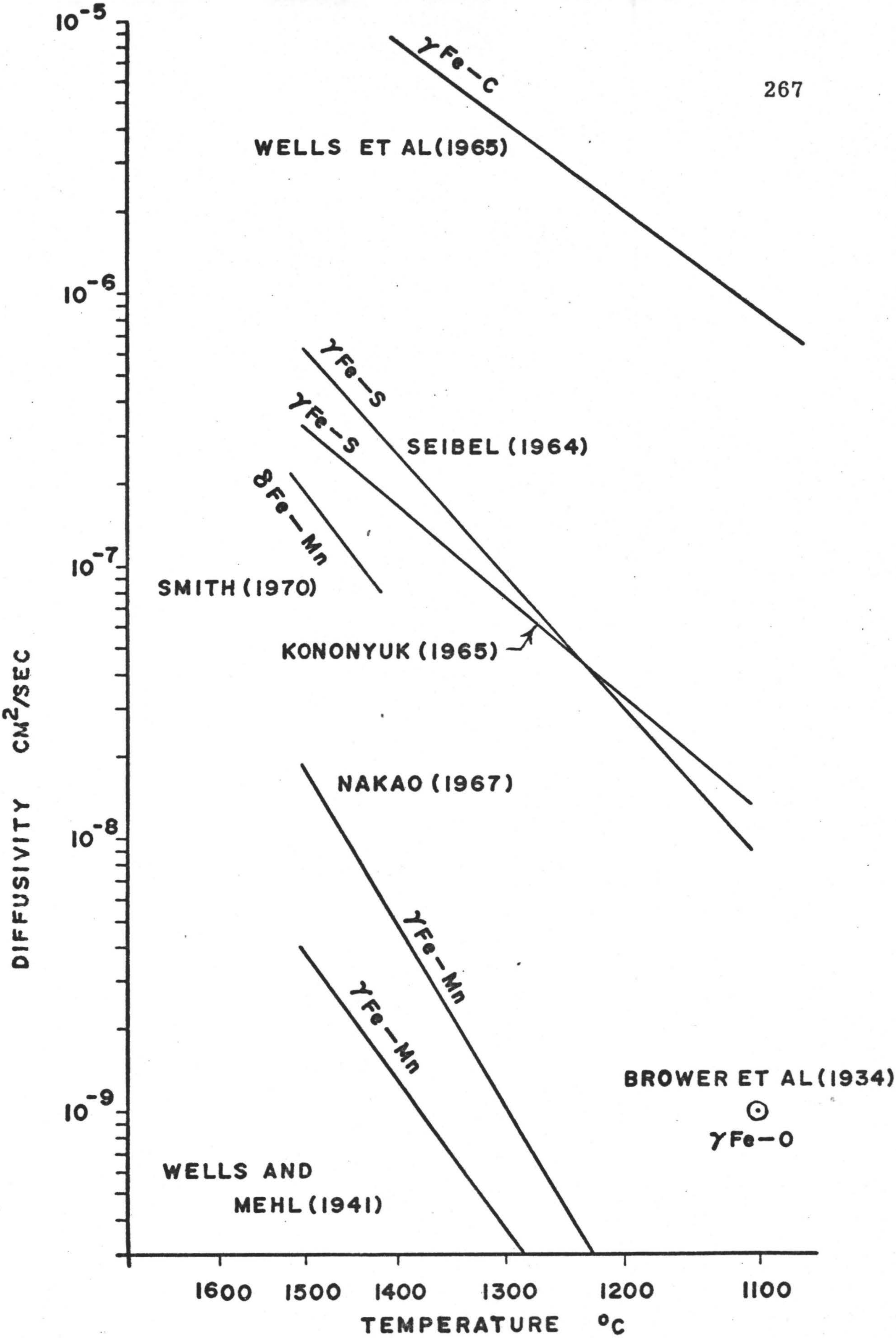

FIGURE 2.1.1 Temperature Dependence of the Diffusion Coefficients of Mn, S, C and O in γ_{Fe} and δ_{Fe}.

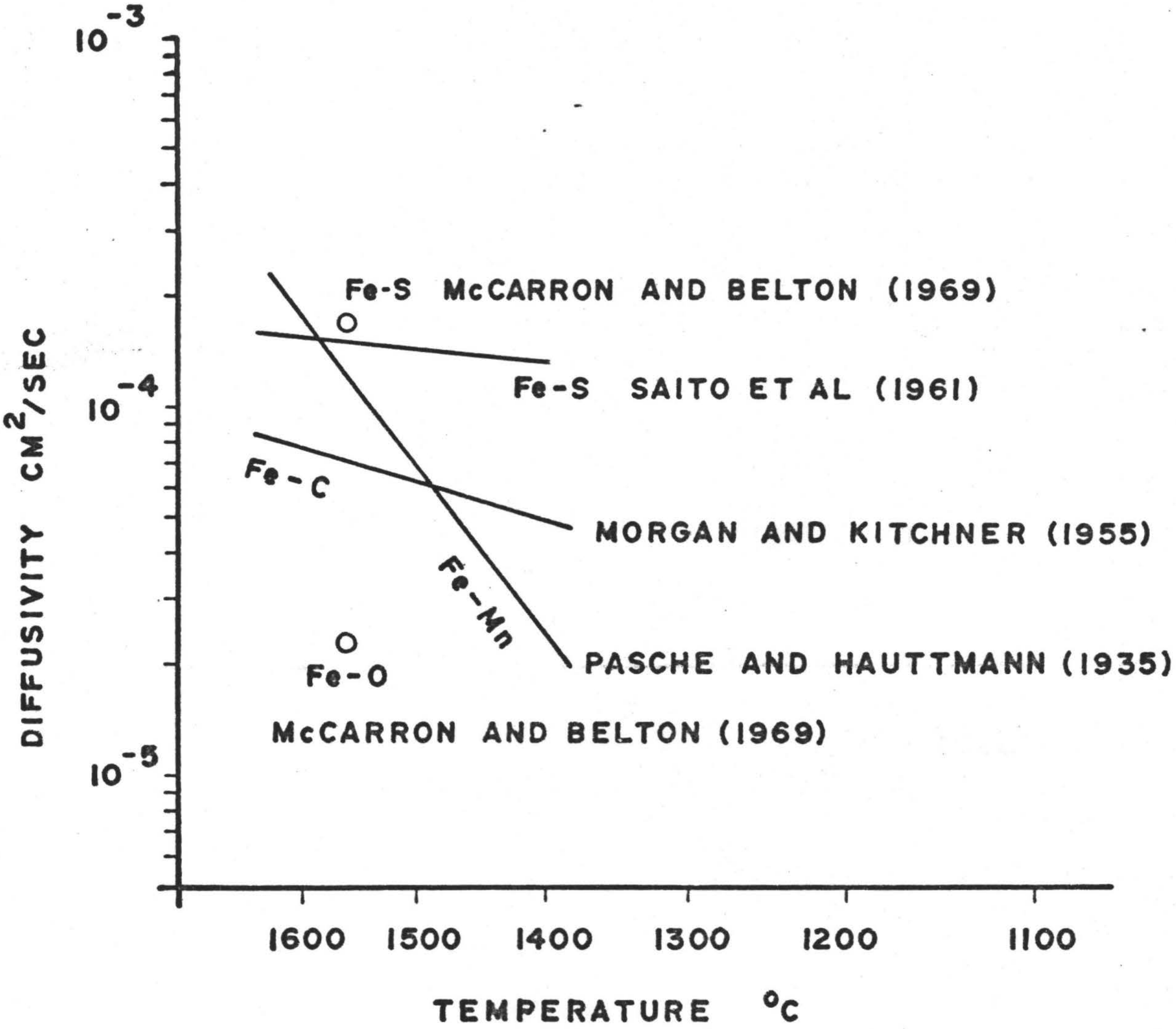

FIGURE 2.1.2 Temperature Dependence of the Diffusion Coefficients of Mn, S, C and O in Liquid Iron.

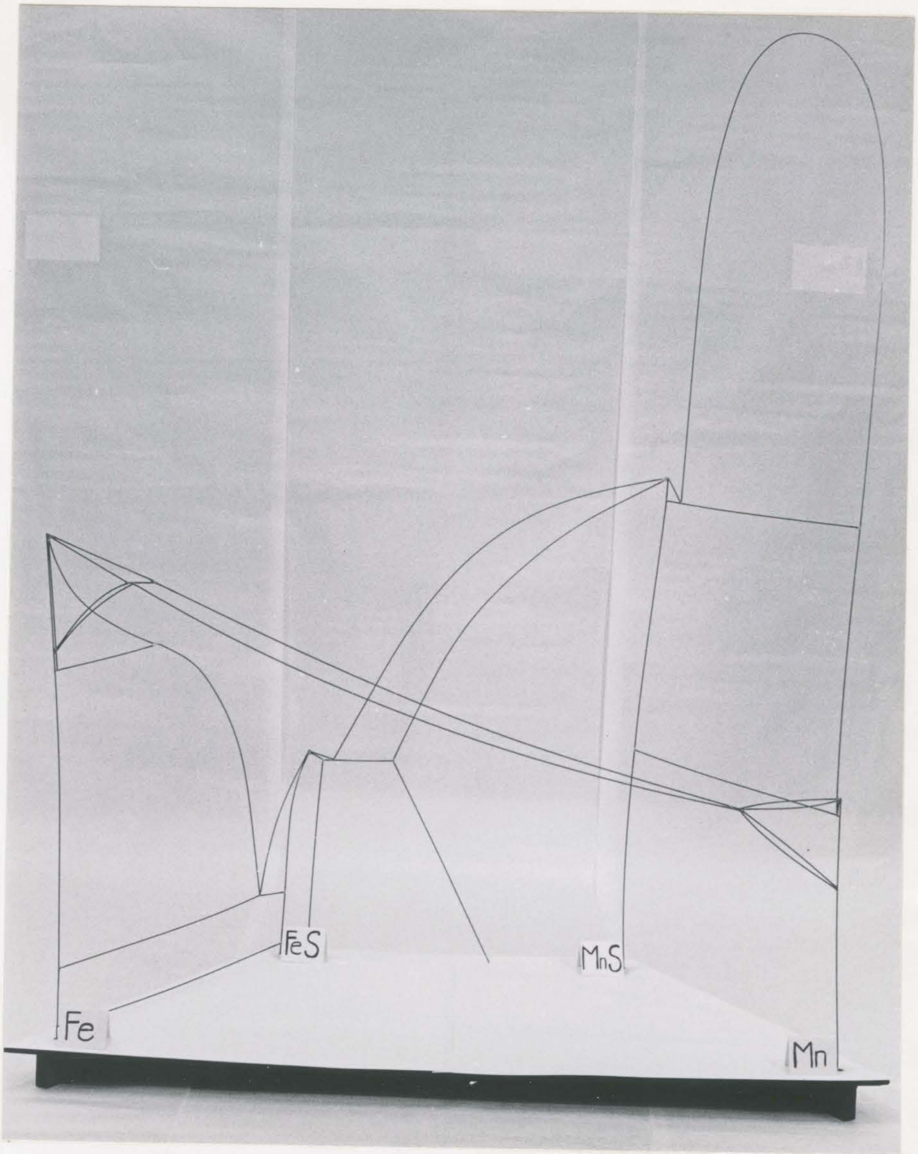

FIGURE 2.2.1 Wire Diagram of the Fe-Mn-MnS-FeS System. The Binary Reactions, Listed in Counter-Clockwise Order Starting from the Fe Corner, are :

$\delta_{Fe} + L_1 = \gamma_{Fe}$	Peritectic	1472°C
$\delta_{Mn} + L'_1 = \gamma_{Mn}$	Peritectic	$\sim$1240°C
$L'_1 = \beta_{MnS} + \delta_{Mn}$	Eutectic	1230°C
$L_2 = \beta_{MnS} + L'_1$	Monotectic	1580°C
$L_2 = \gamma_{FeS} + \beta_{MnS}$	Eutectic	1180°C
$L_2 = \gamma_{FeS} + \gamma_{Fe}$	Eutectic	988°C
$\delta_{Fe} = \gamma_{Fe} + L_2$	Metatectic	1365°C

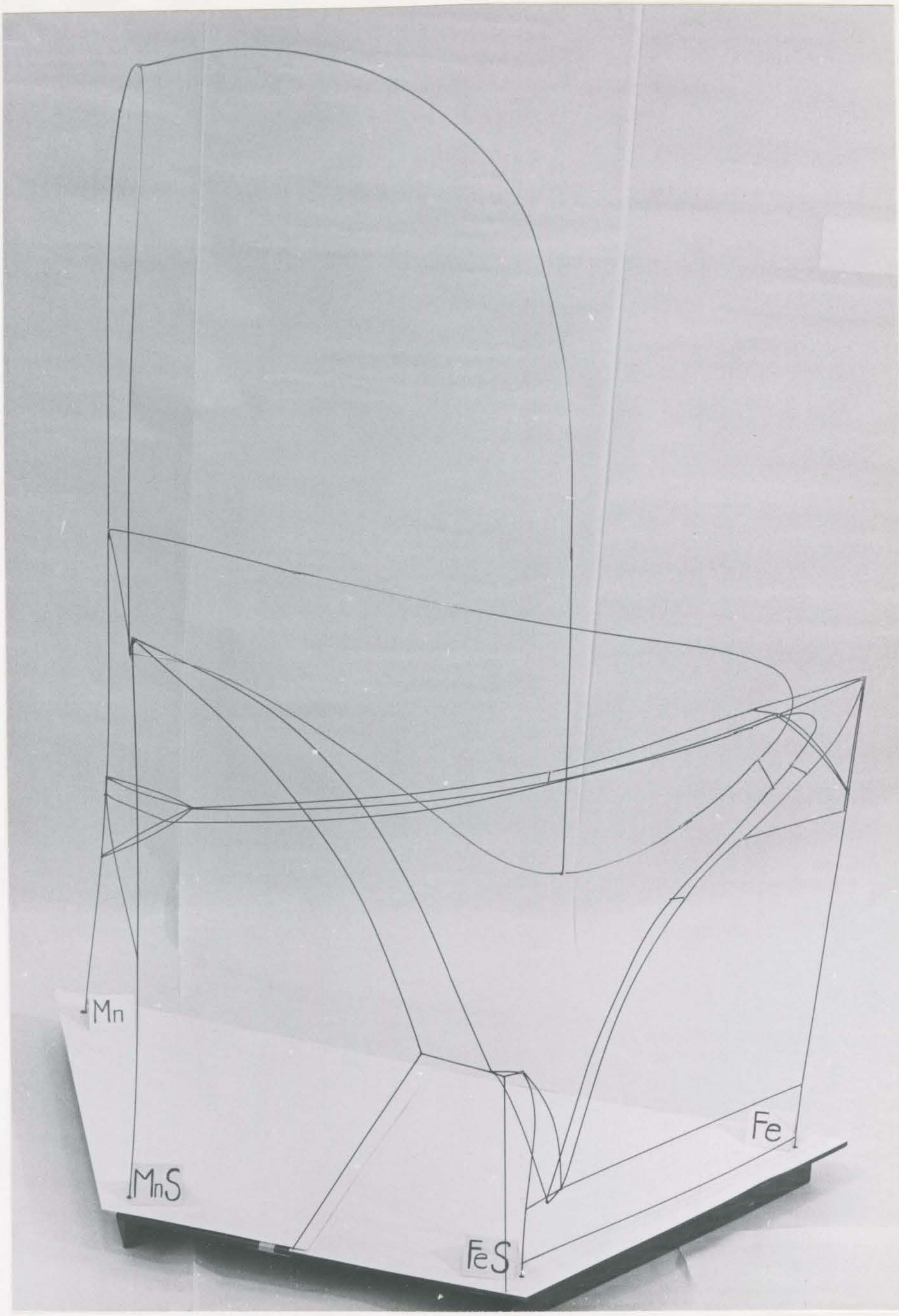

FIGURE 2.2.2 Wire Diagram of the Fe-Mn-MnS-FeS System, Showing Liquidus Surfaces. A Liquid-Liquid Miscibility Gap Is Delimited by the Horizontal Loop Originating at the Mn-MnS Monotectic, and by the Vertical Loop which Is the Locus of the Critical Points. One Eutectic Trough Originates near the Mn-MnS Eutectic, Runs Close to the Fe-Mn Binary Plane, up to a Temperature Maximum in the Fe Corner and Joins the Two other Troughs at a Ternary Eutectic Point in the FeS Corner.

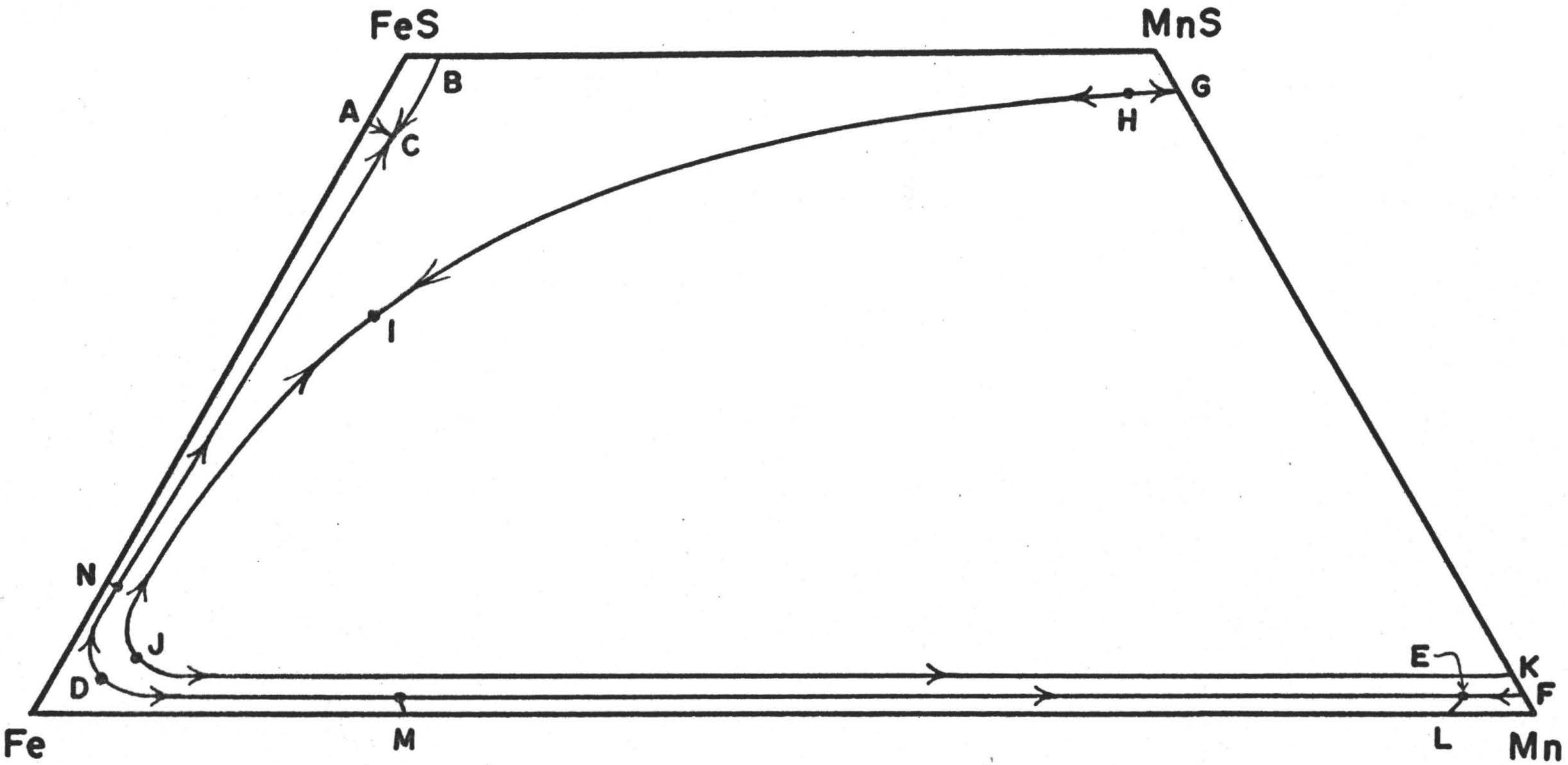

FIGURE 2.2.3 Schematic Projection of Liquidus Surface Intersections of Figure 2.2.2 on the Composition Plane Showing the Miscibility Gap Limits GHIJK and the Principal Eutectic Troughs AC, BC and EDC. The Arrows on the Projection Indicate the Direction of Decreasing Temperature. Hence Points D, J and H Are Temperature Maxima and Points C, G, I and E are Temperature Minima.

FIGURE 2.2.4 Typical Isotherms of the Fe-Mn-MnS-FeS System in the Temperature Range 1620-980°C. The Temperatures and Phase Compositions Are Approximate. The Diagram Is Based on Atomic Fractions.

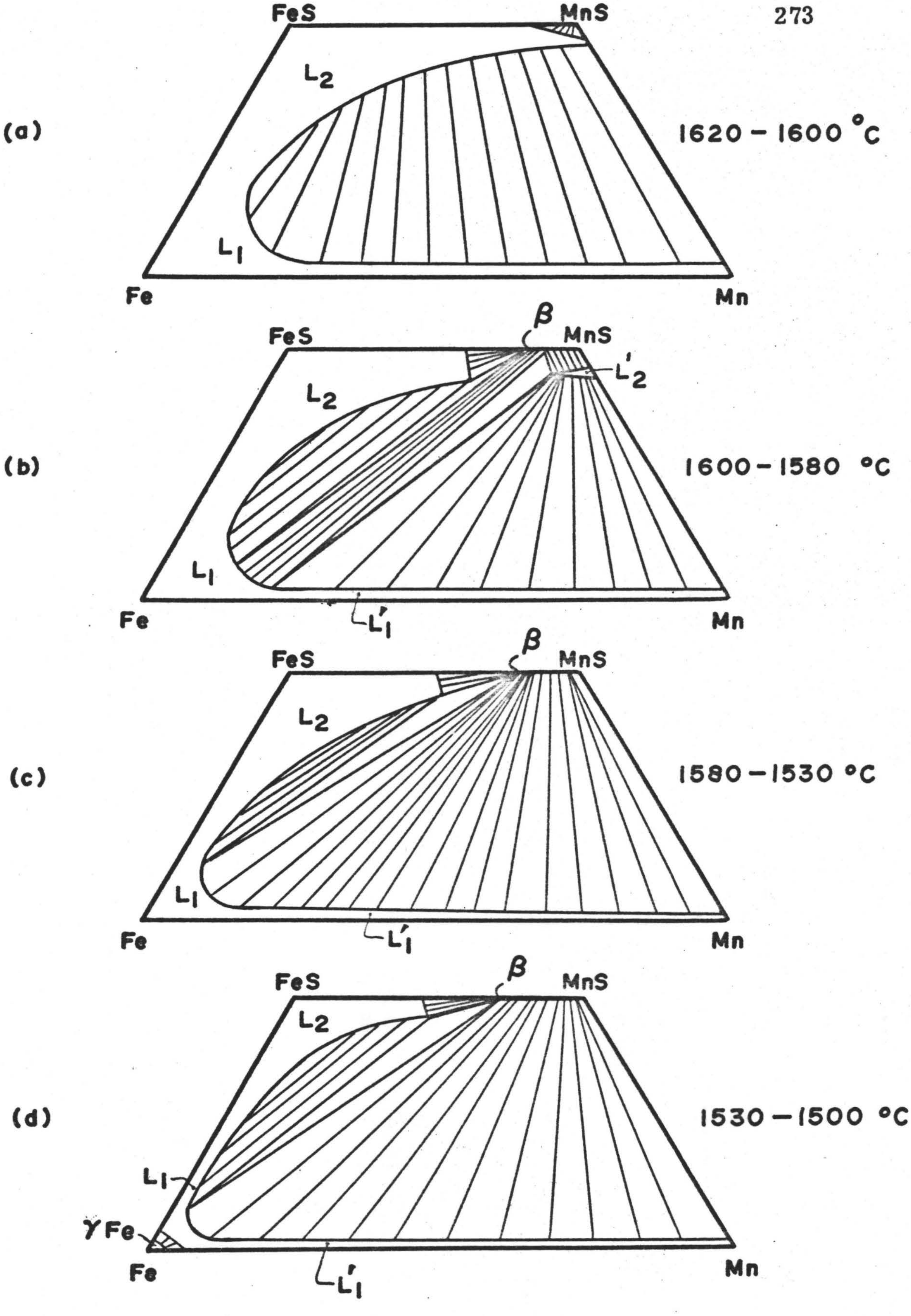
(a)
FeS
MnS
L2
L1
Fe
Mn
1620 – 1600 °C
(b)
FeS
β
MnS
L'2
L2
L1
L'1
Fe
Mn
1600 – 1580 °C
(c)
FeS
β
MnS
L2
L1
L'1
Fe
Mn
1580 – 1530 °C
(d)
FeS
β
MnS
L2
L1
γ Fe
L'1
Fe
Mn
1530 – 1500 °C

(e)

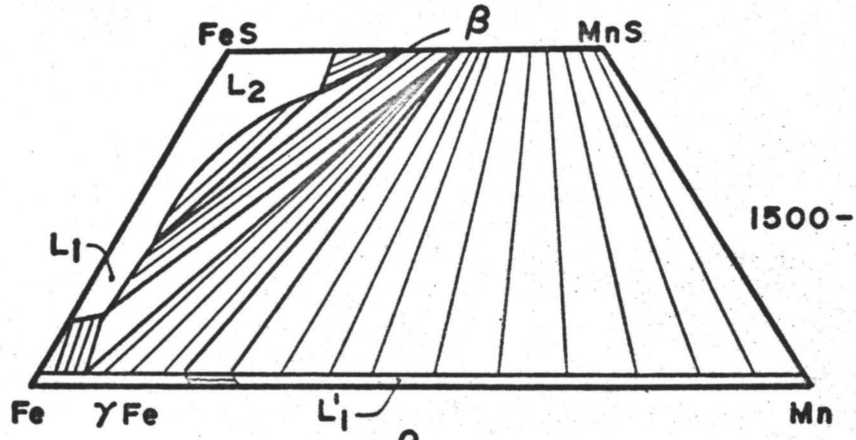

1500 - 1350 °C

(f)

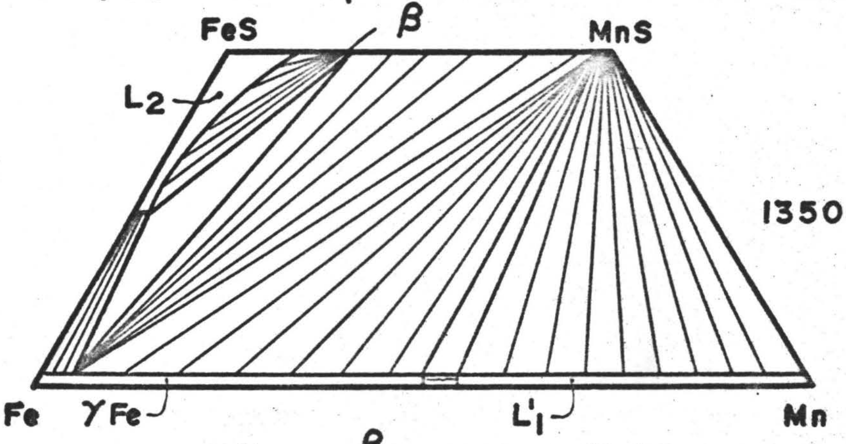

1350 - 1245 °C

(g)

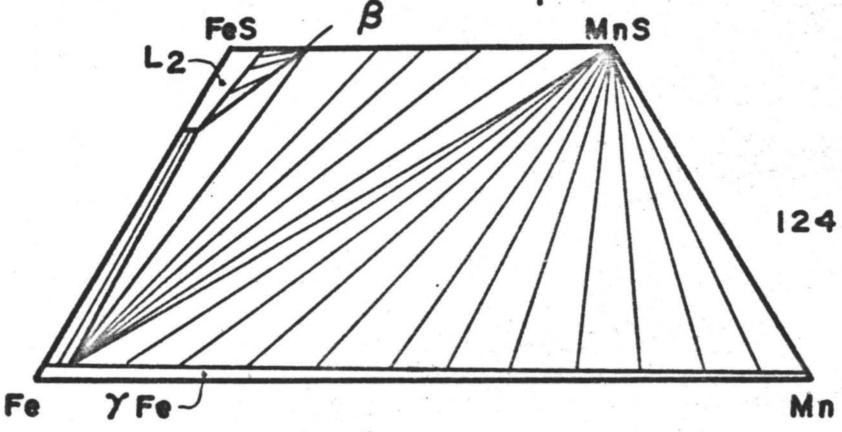

1245 - 1190 °C

(h)

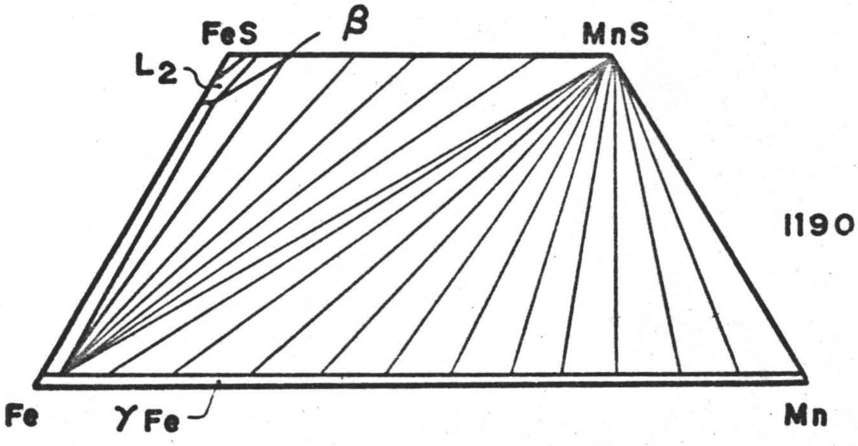

1190 — 1180 °C

(i)

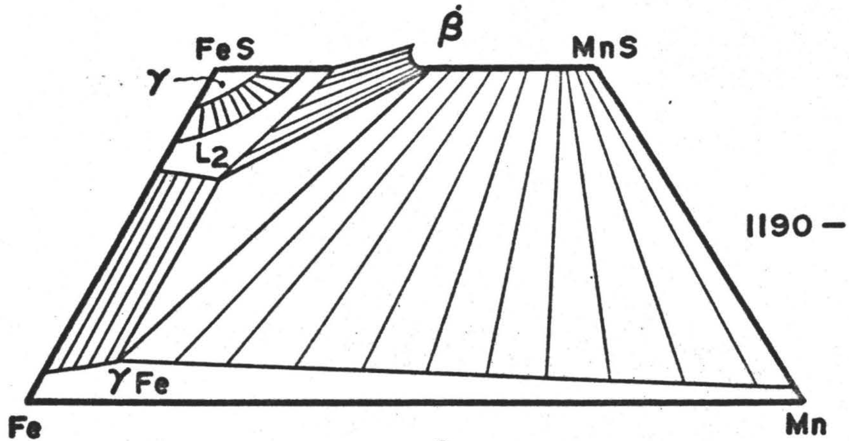

1190 – 1180 °C

(j)

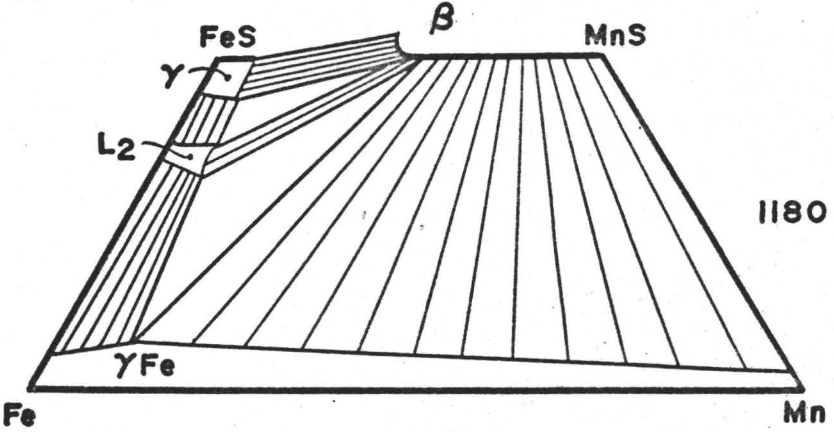

1180 – 988 °C

(k)

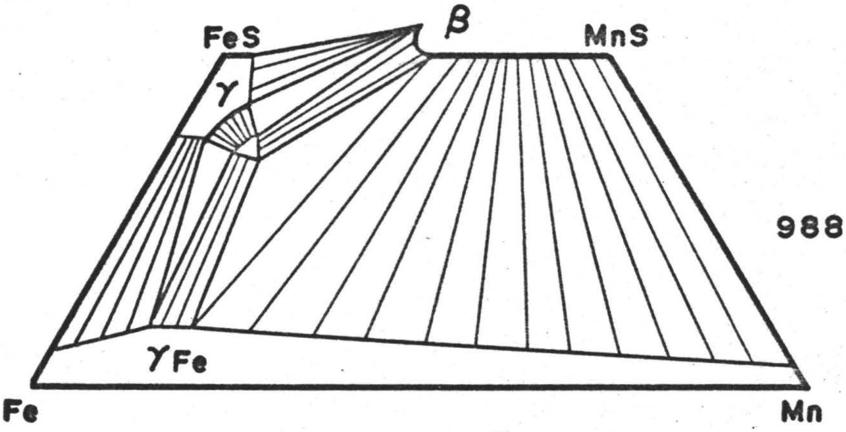

988 – 980 °C

(l)

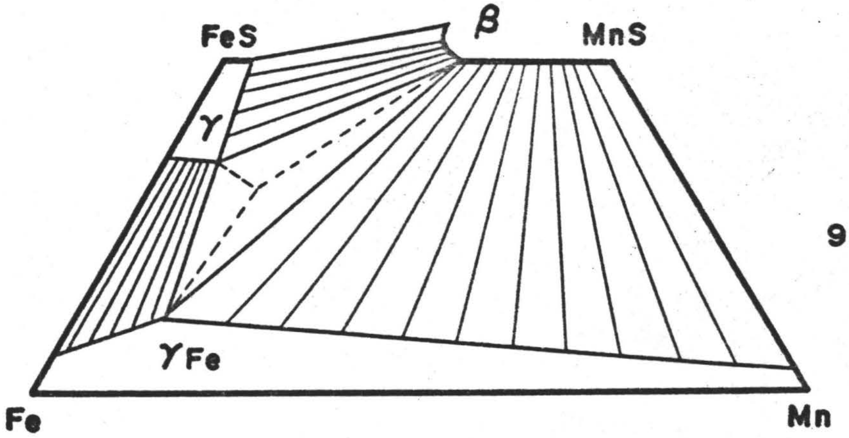

980 °C

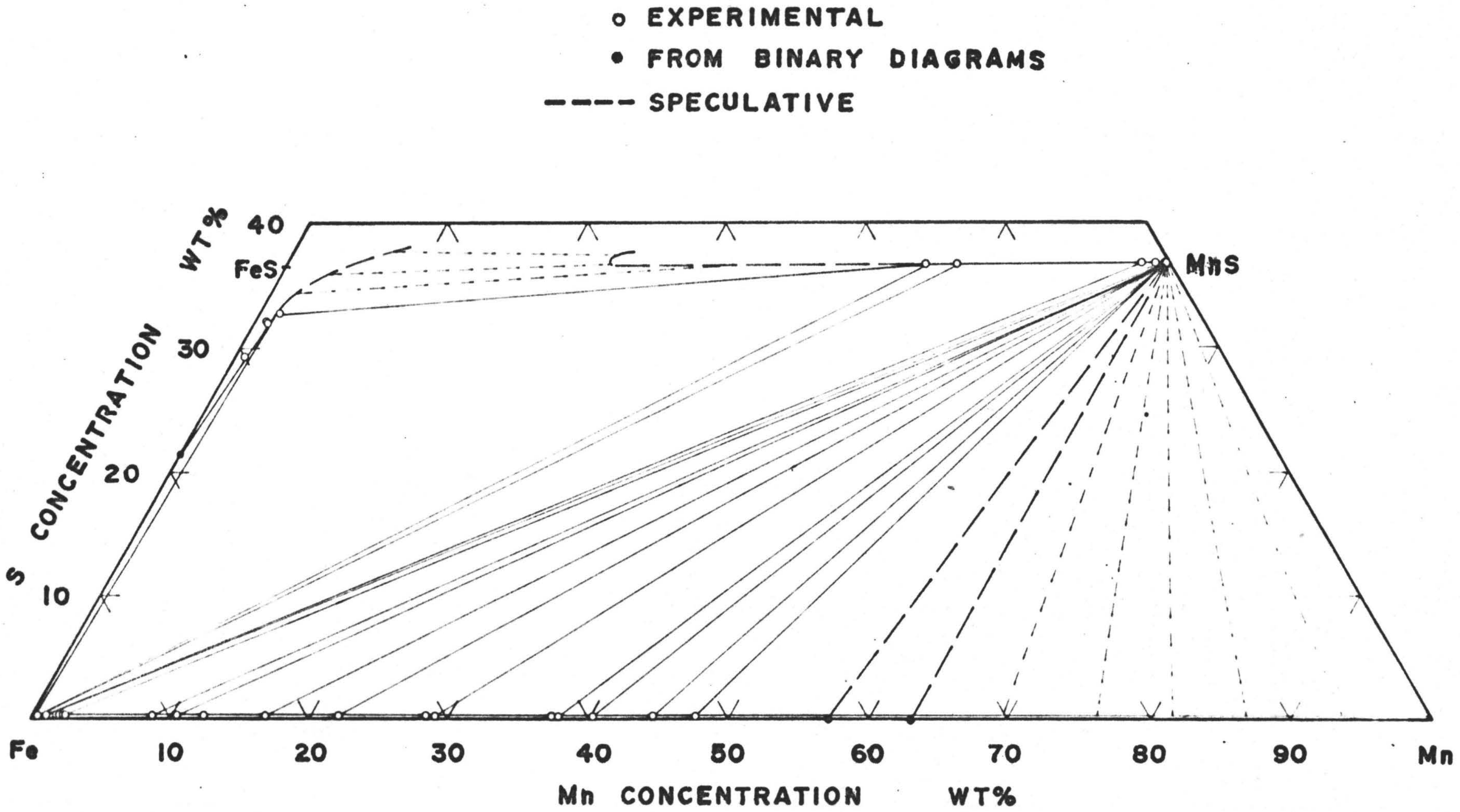

FIGURE 2.2.5 The 1300°C Isotherm of the Fe-Mn-MnS-FeS System (after SMITH, 1970).

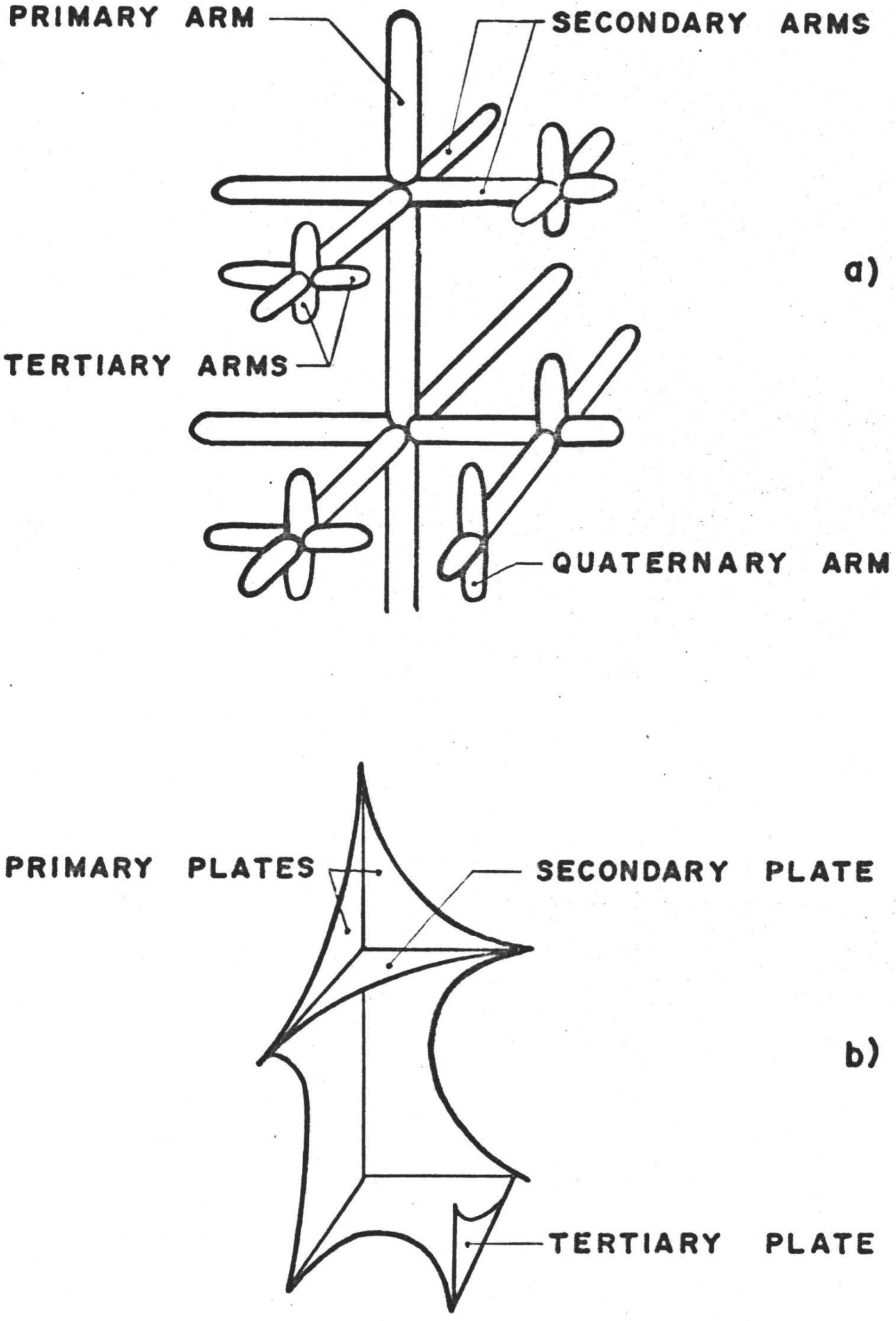

FIGURE 2.3.1. Schematic Diagrams Showing Dendritic Rod and Plate Forms. (After BOWER et al., 1966).

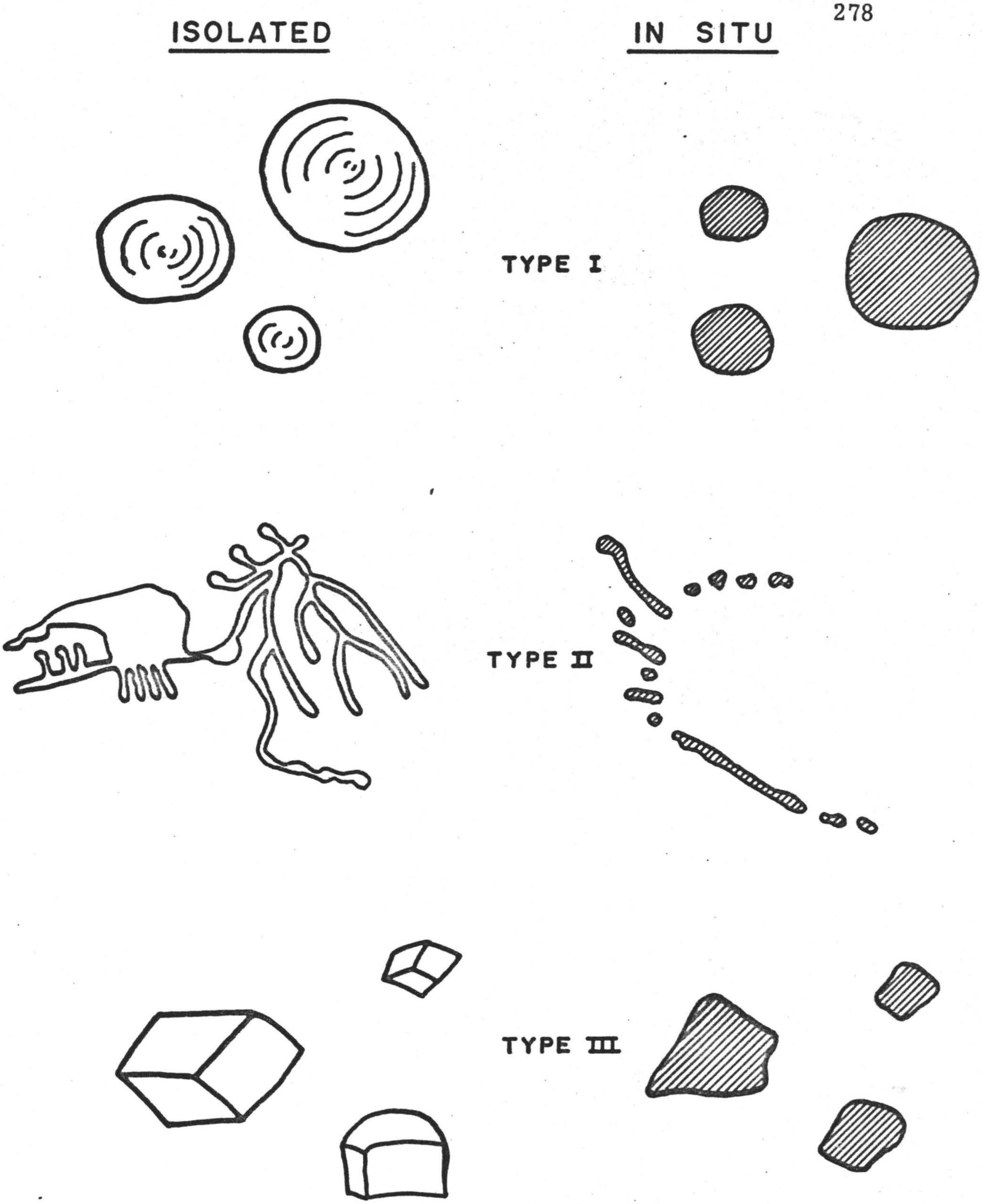

FIGURE 2.3.2 Sketch of the Three Inclusion Types after the Work of KIESSLING et al. (1963).

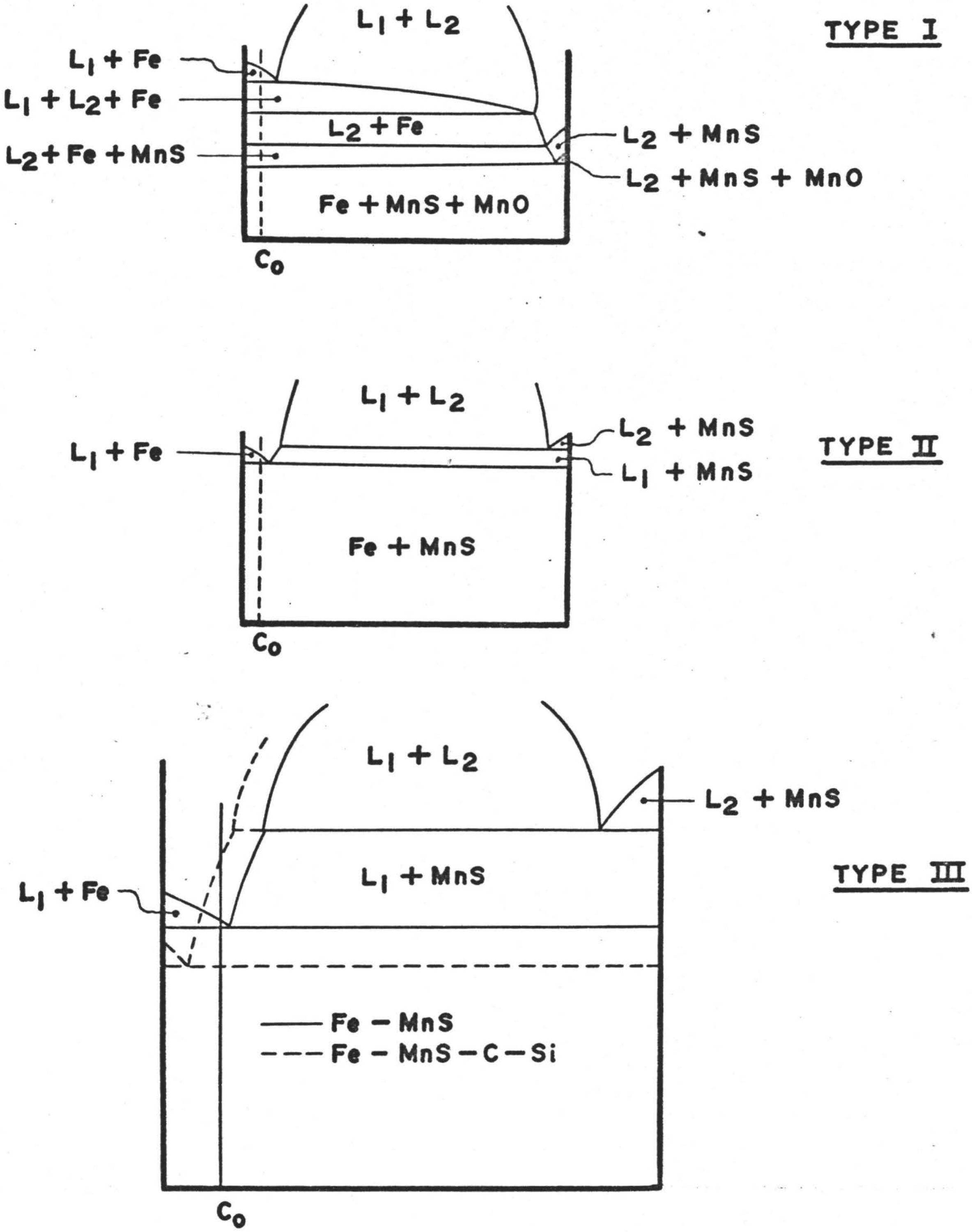

FIGURE 2.3.3 Constitution Diagrams Relating to the Formation of Type I, Type II and Type III Inclusions. After DAHL et al. (1966).

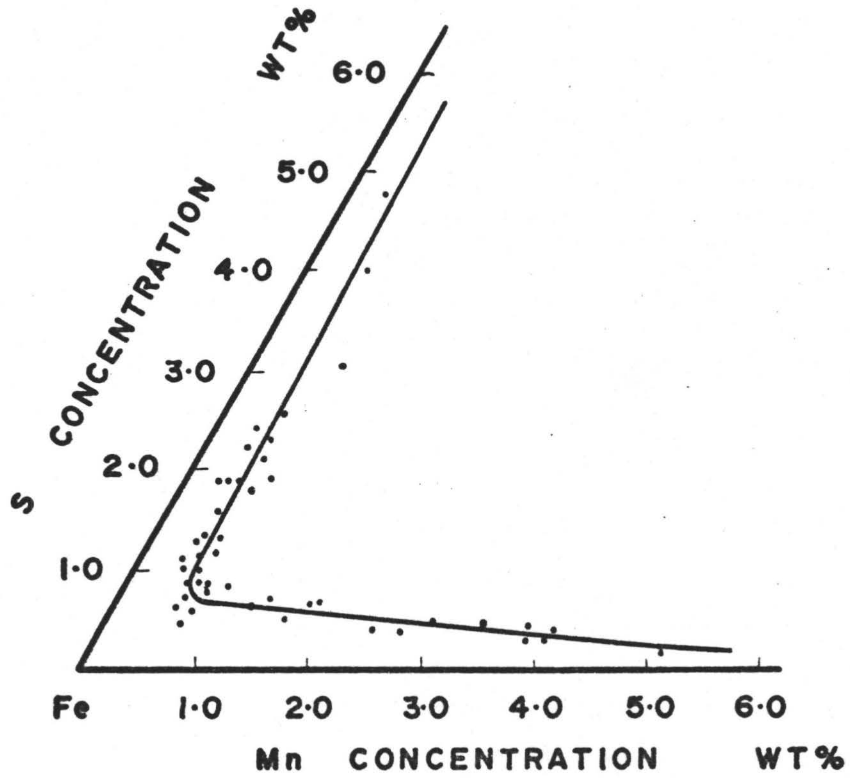

FIGURE 2.3.4 Metal-Rich Boundary of the Miscibility Gap in Fe-Mn-S-O Alloys Around 1520°C, According to BOOTH and CHARLES (1969). The Metal Phase Contained Approximately 0.1 wt% O.

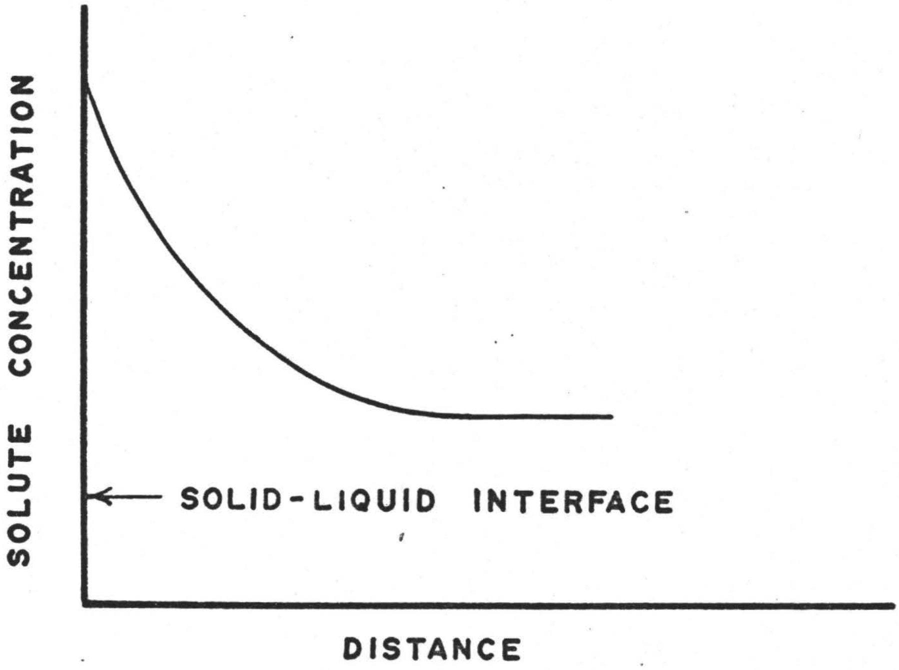

FIGURE 2.5.1 Solute Distribution in the Liquid Ahead of an Advancing Solid-Liquid Interface.

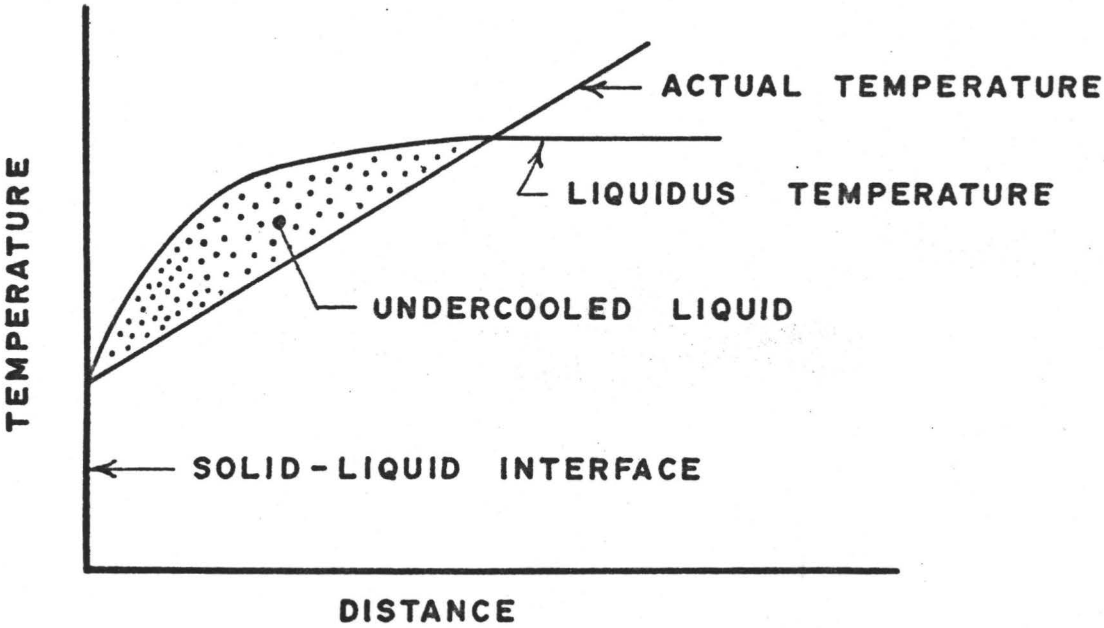

FIGURE 2.5.2 Actual and Liquidus Temperatures in the Liquid Ahead of an Advancing Solid-Liquid Interface.

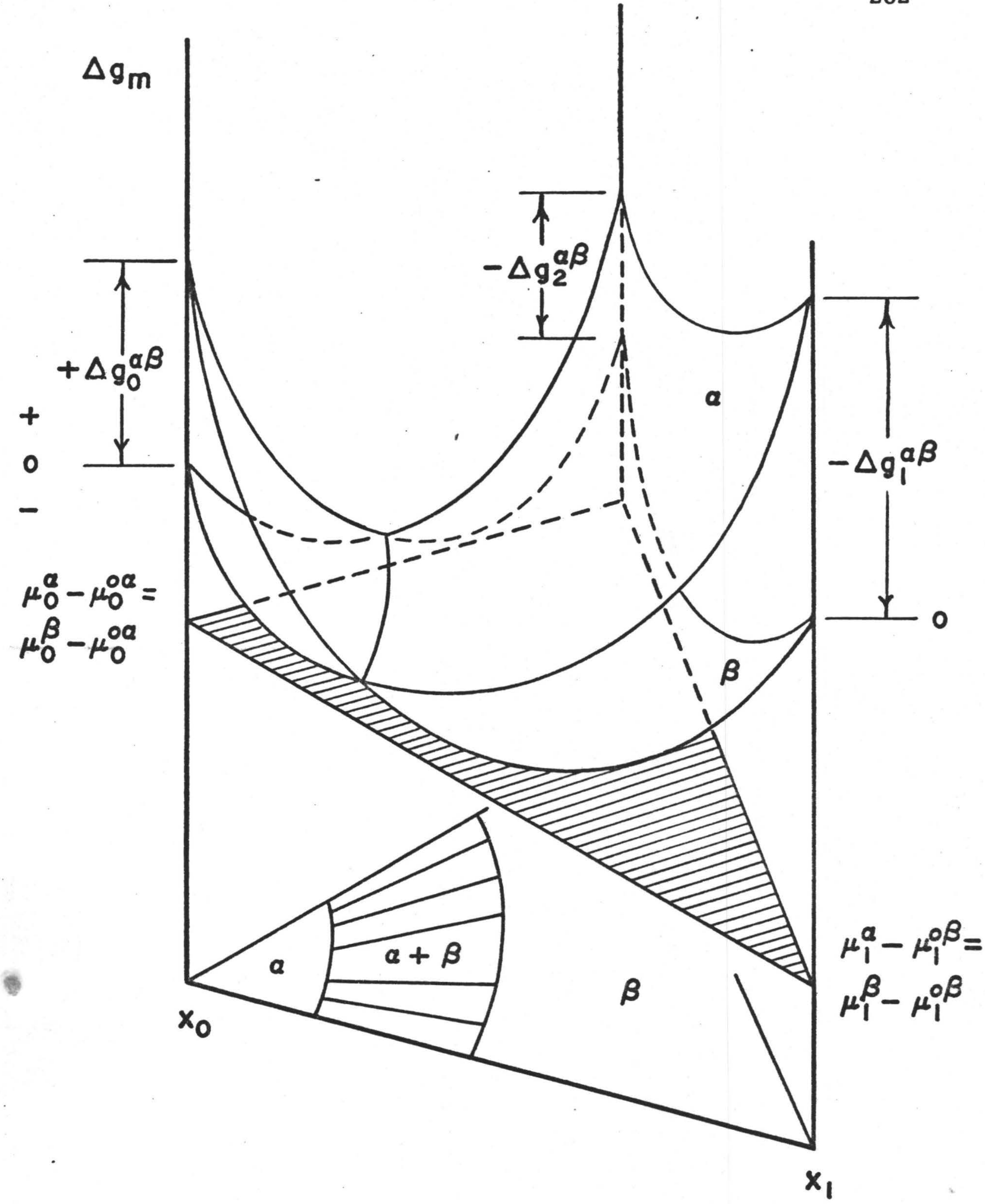

FIGURE 4.1.1 Free Enthalpy versus Composition Diagram Showing a Doubly Tangent Plane Rolling about Two Isothermal Free Enthalpy Surfaces α and β, and Generating the Boundaries and Tie-lines of the Two-Phase Field in the Composition Plane.

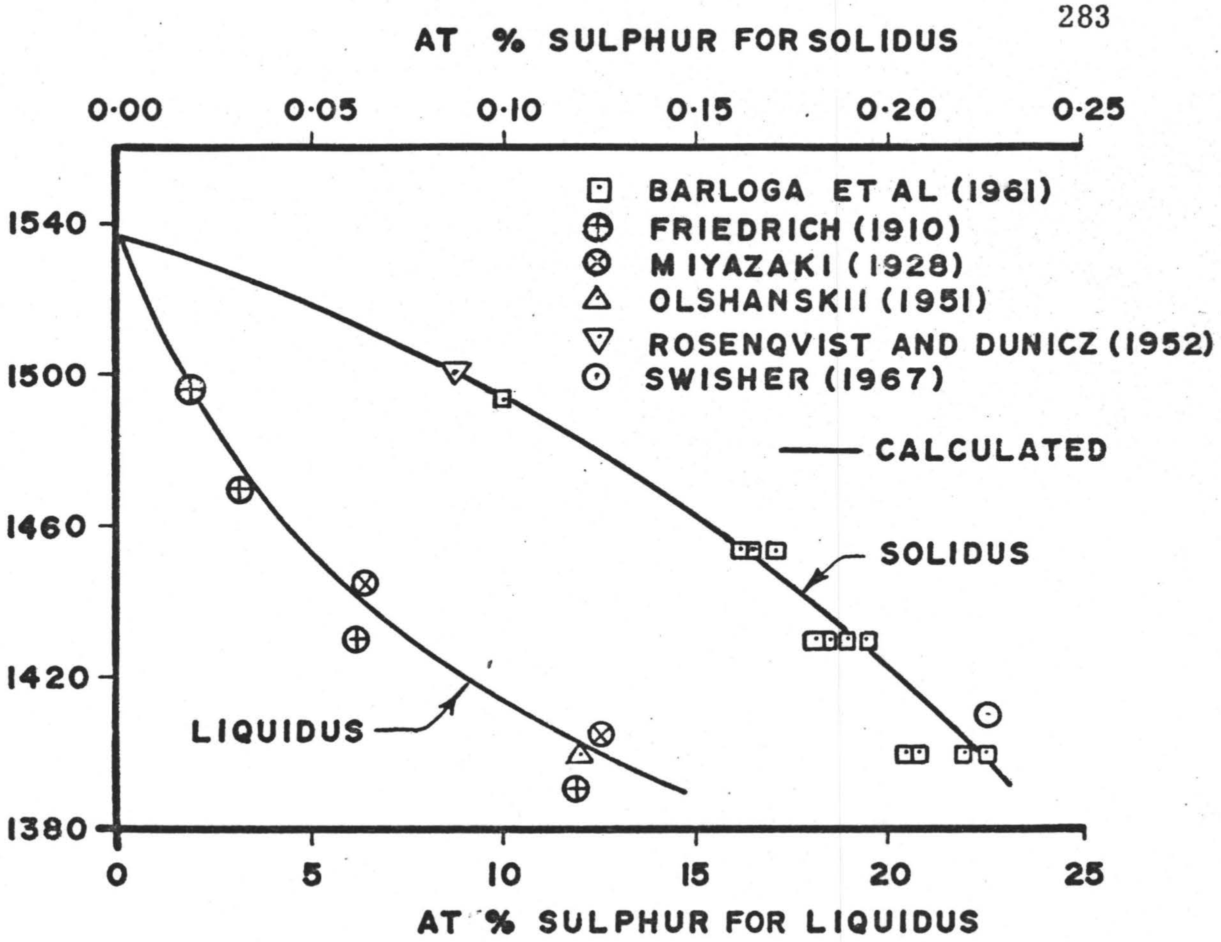

FIGURE 4.1.2 δ_{Fe} + Liquid Equilibria of Fe-S System.

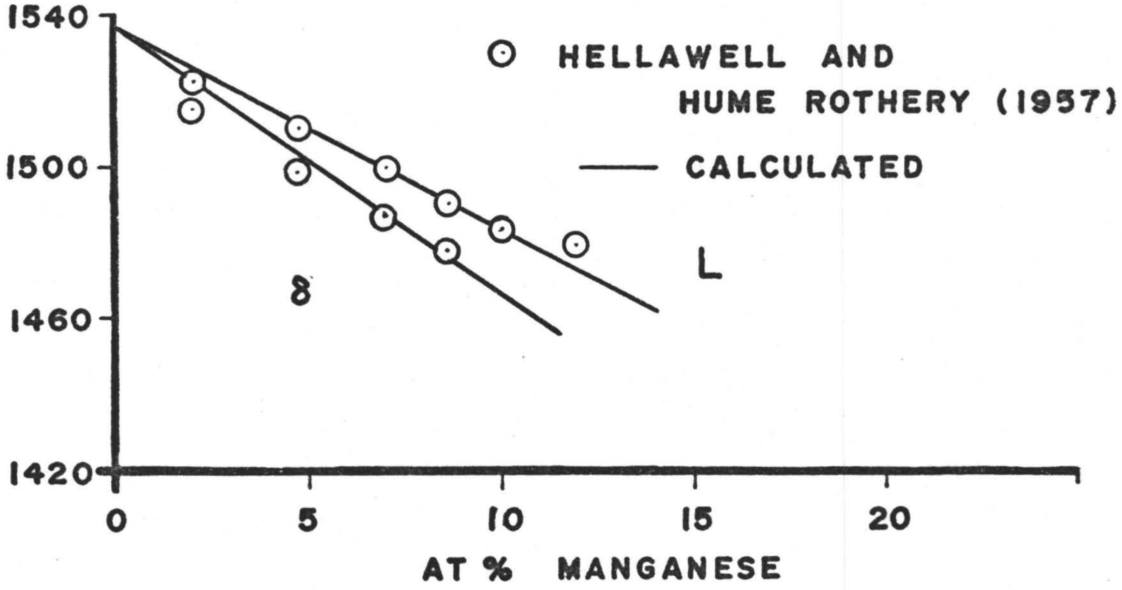

FIGURE 4.1.3 δ_{Fe} + Liquid Equilibria of Fe-Mn System.

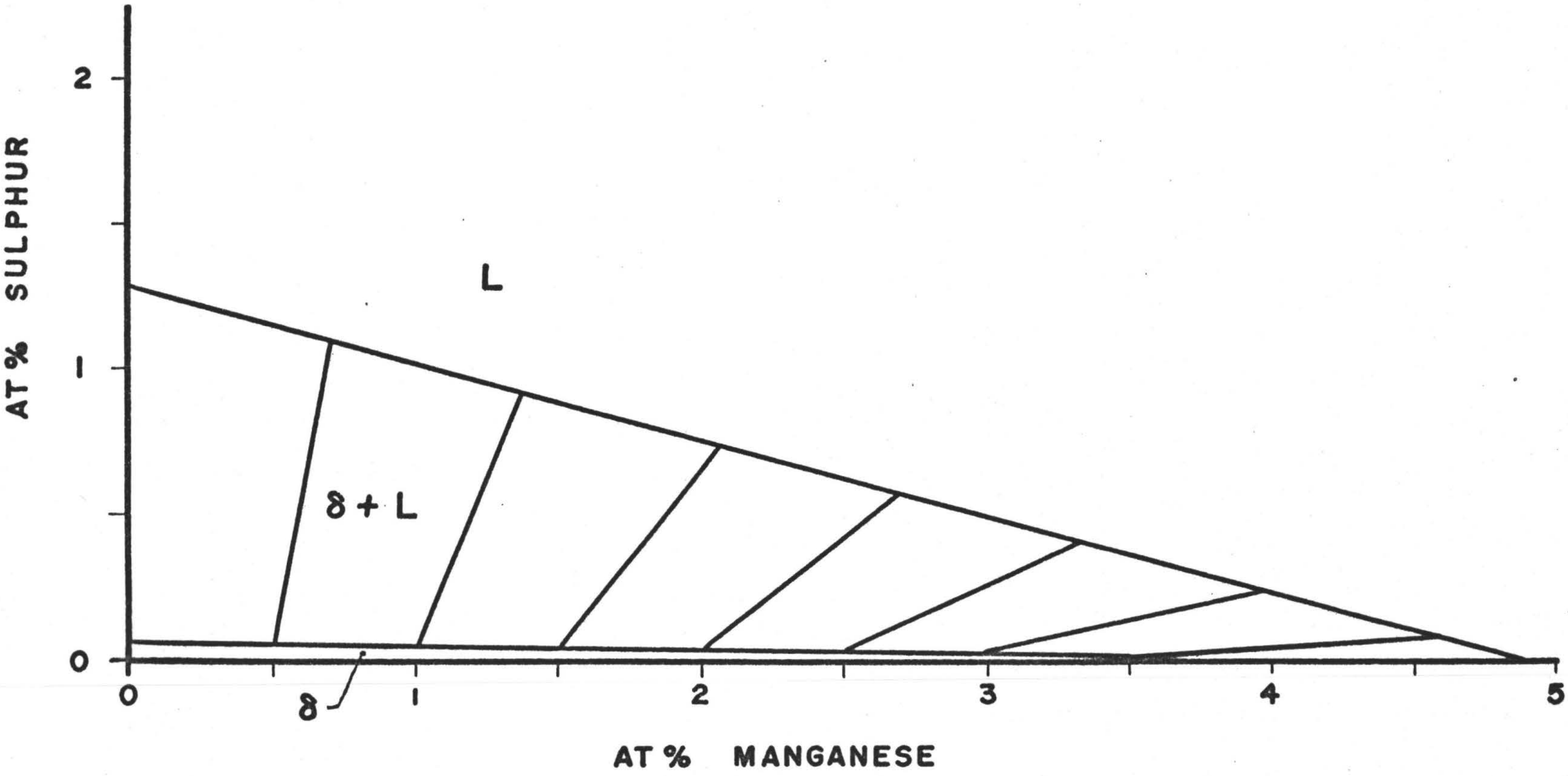

FIGURE 4.1.4 1510°C Isotherm for δ + Liquid Equilibrium in Fe-Mn-S System Calculated by Tangent Plane Method.

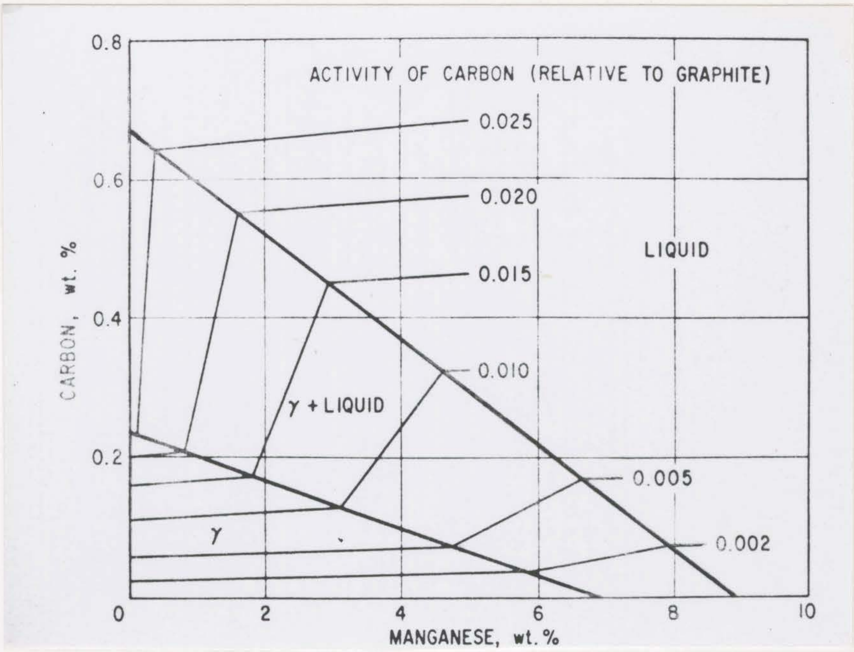

FIGURE 4.1.5 1490 °C Isotherm for Metastable γ + Liquid Equilibrium in Fe-Mn-C. (From TURKDOGAN and GRANGE, 1968).

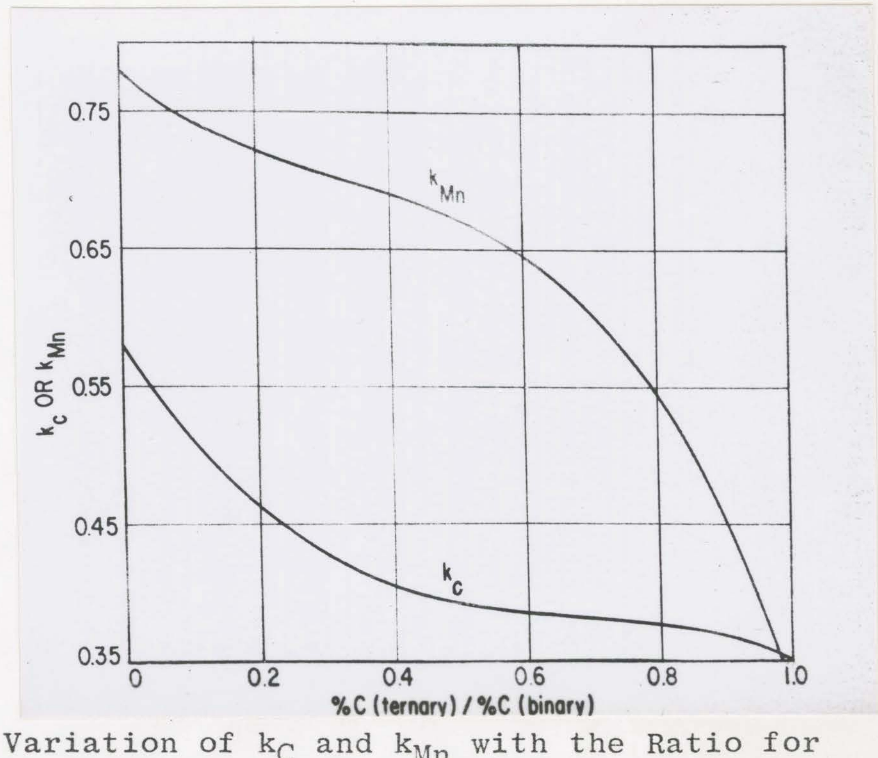

FIGURE 4.1.6 Variation of k_C and k_{Mn} with the Ratio for Liquidus Compositions, %C (Ternary)/%C (Binary) at the Same Temperature, for the Temperature Range 1470 to 1530 °C. (From TURKDOGAN and GRANGE, 1968).

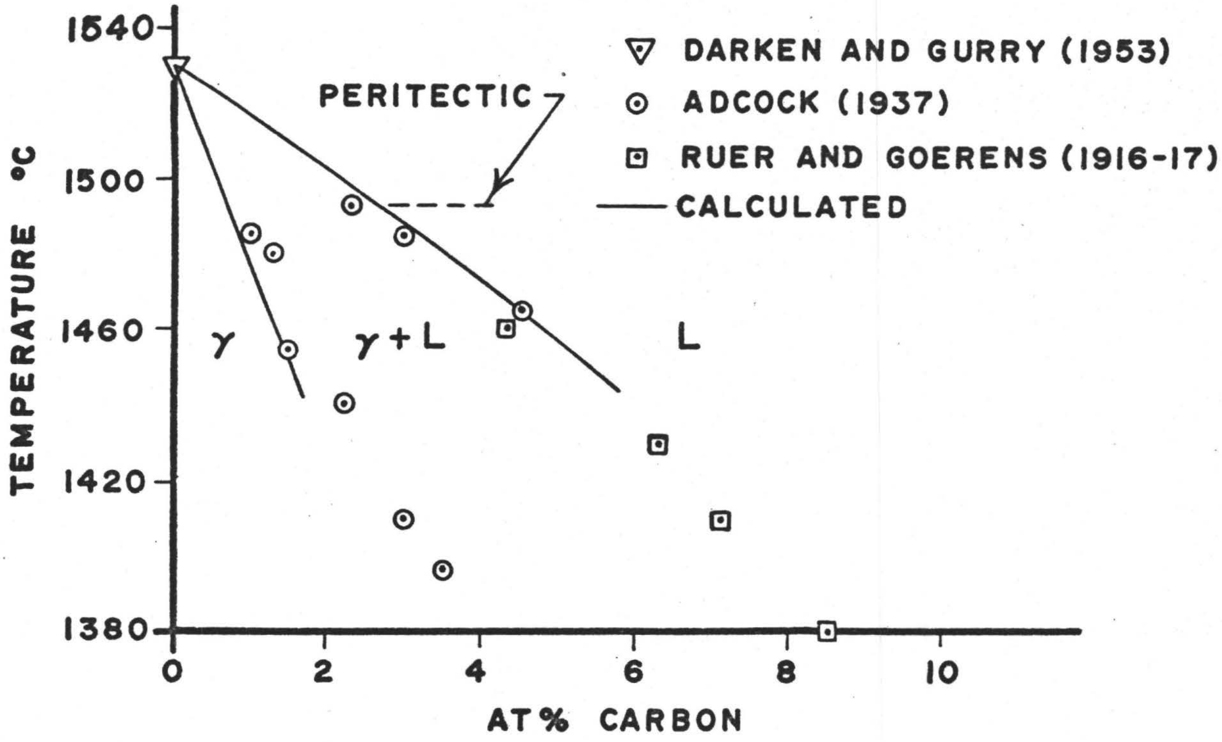

FIGURE 4.1.7 γ_{Fe} + Liquid Equilibria of Fe-C System.

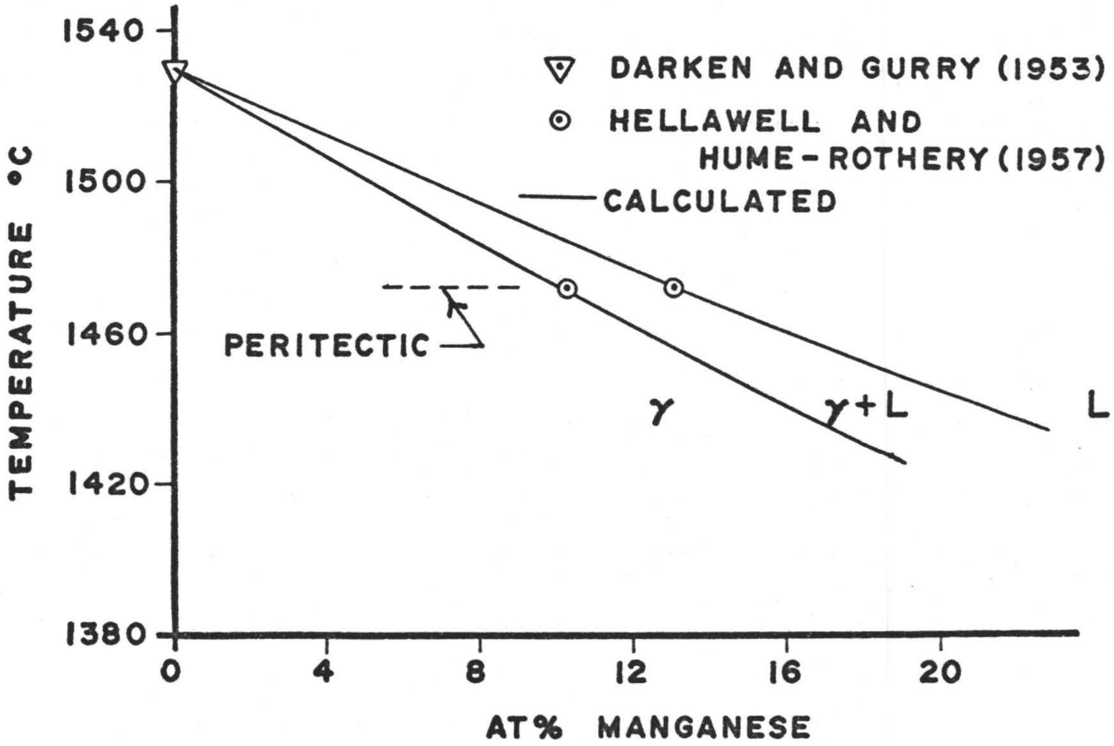

FIGURE 4.1.8 γ_{Fe} + Liquid Equilibria of Fe-Mn System.

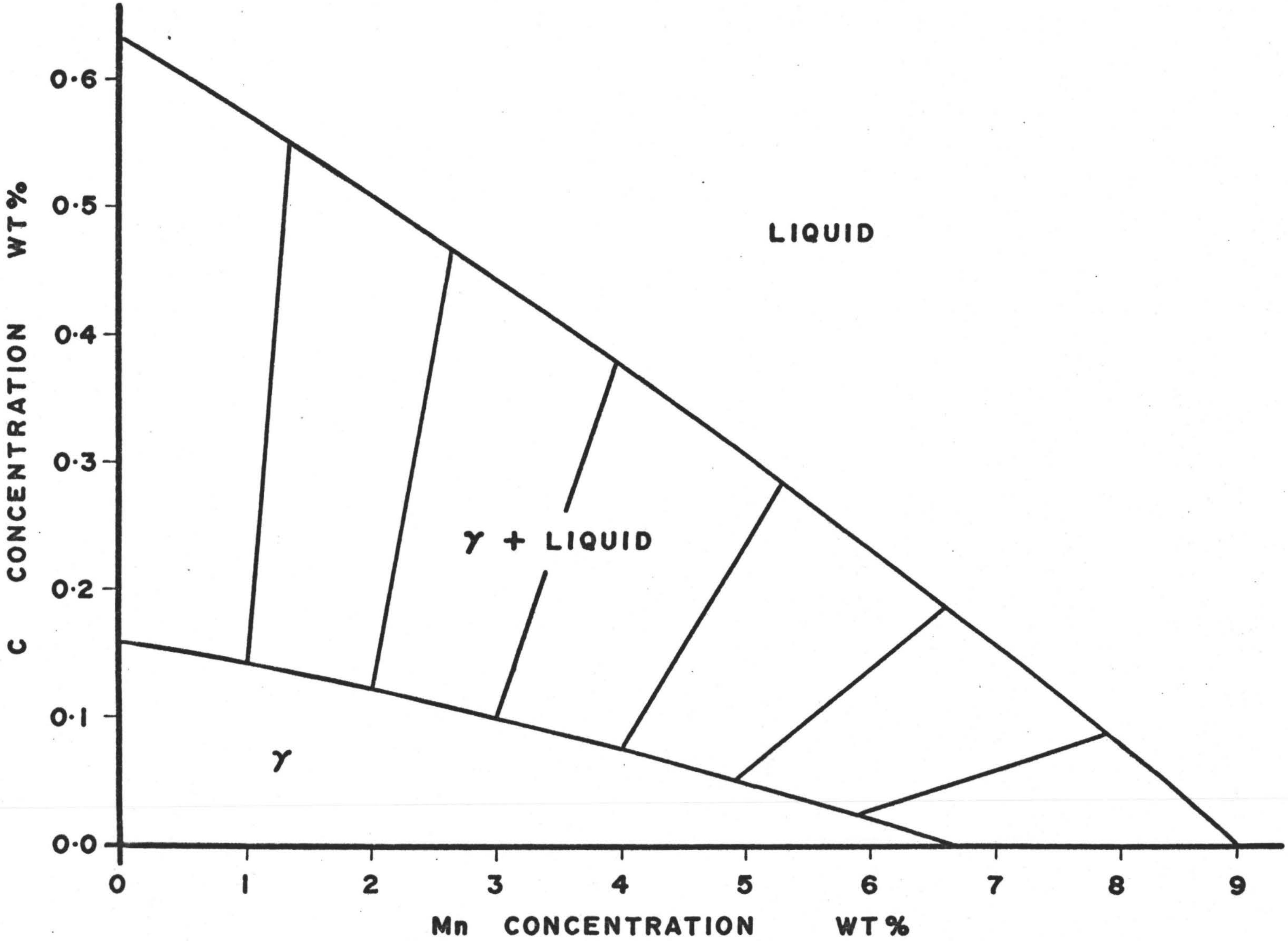

FIGURE 4.1.9 1490°C Isotherm for Metastable γ + Liquid Equilibrium in Fe-Mn-C System Calculated by Tangent Plane Method.

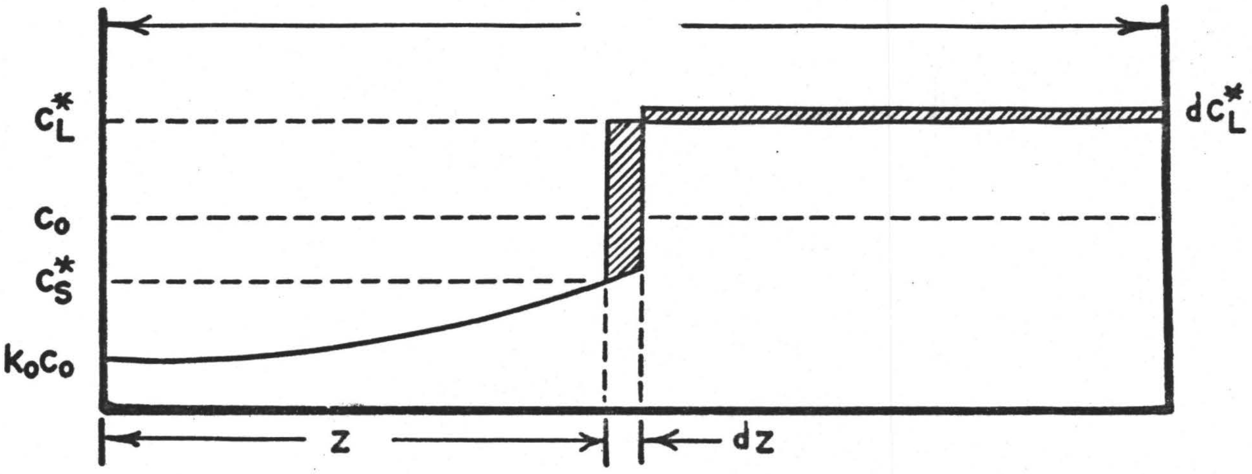

FIGURE 4.2.1 Solute Distribution during Unidirectional Solidification with Complete Mixing in the Liquid Phase.

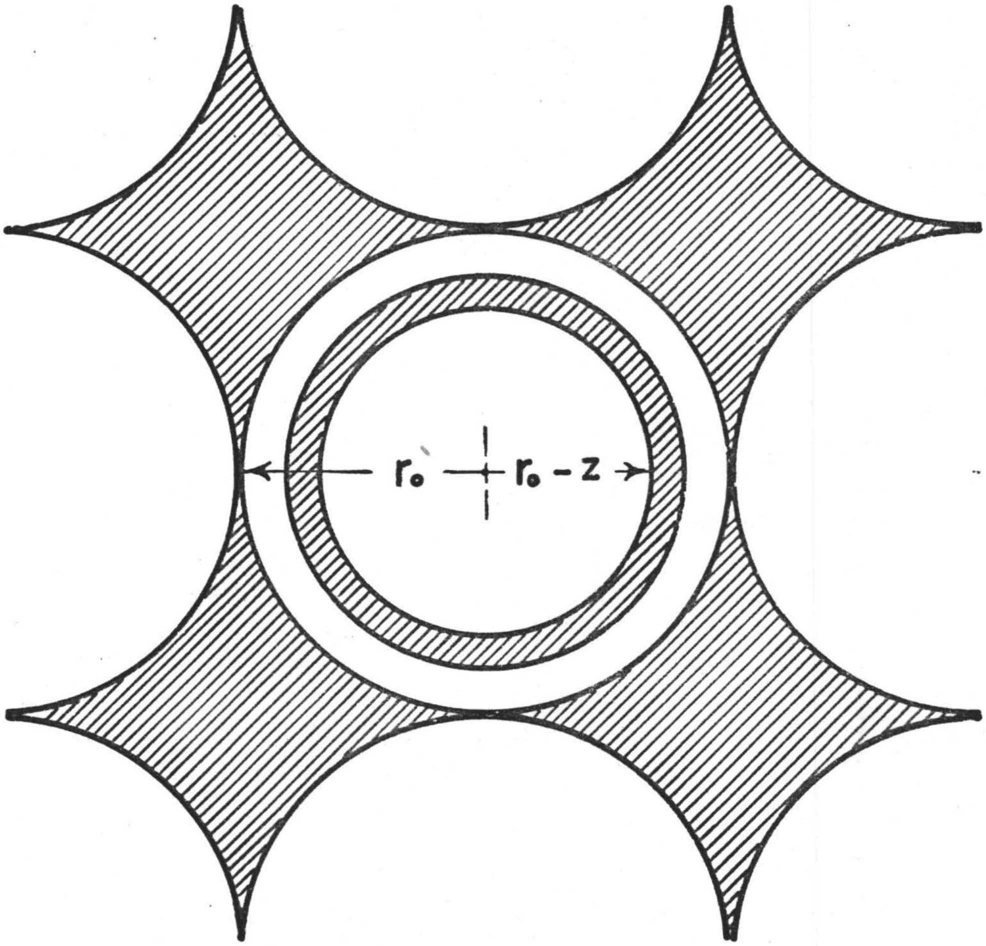

FIGURE 4.2.2 Spherical Volume of Liquid Enclosed by an Idealized Dendritic Structure.

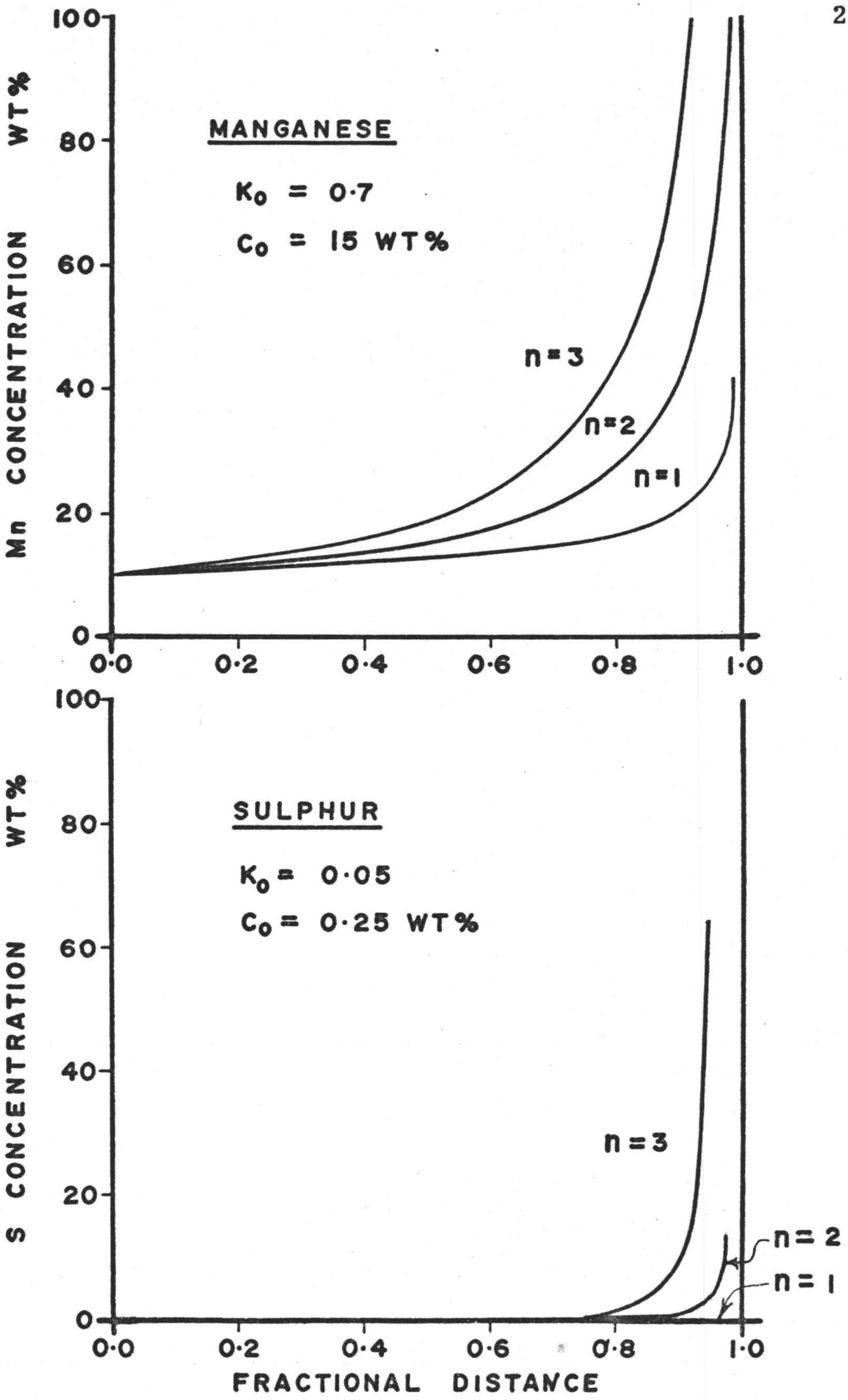

FIGURE 4.2.3 Plots of Maximum Segregation Equation with n = 1, 2 and 3.

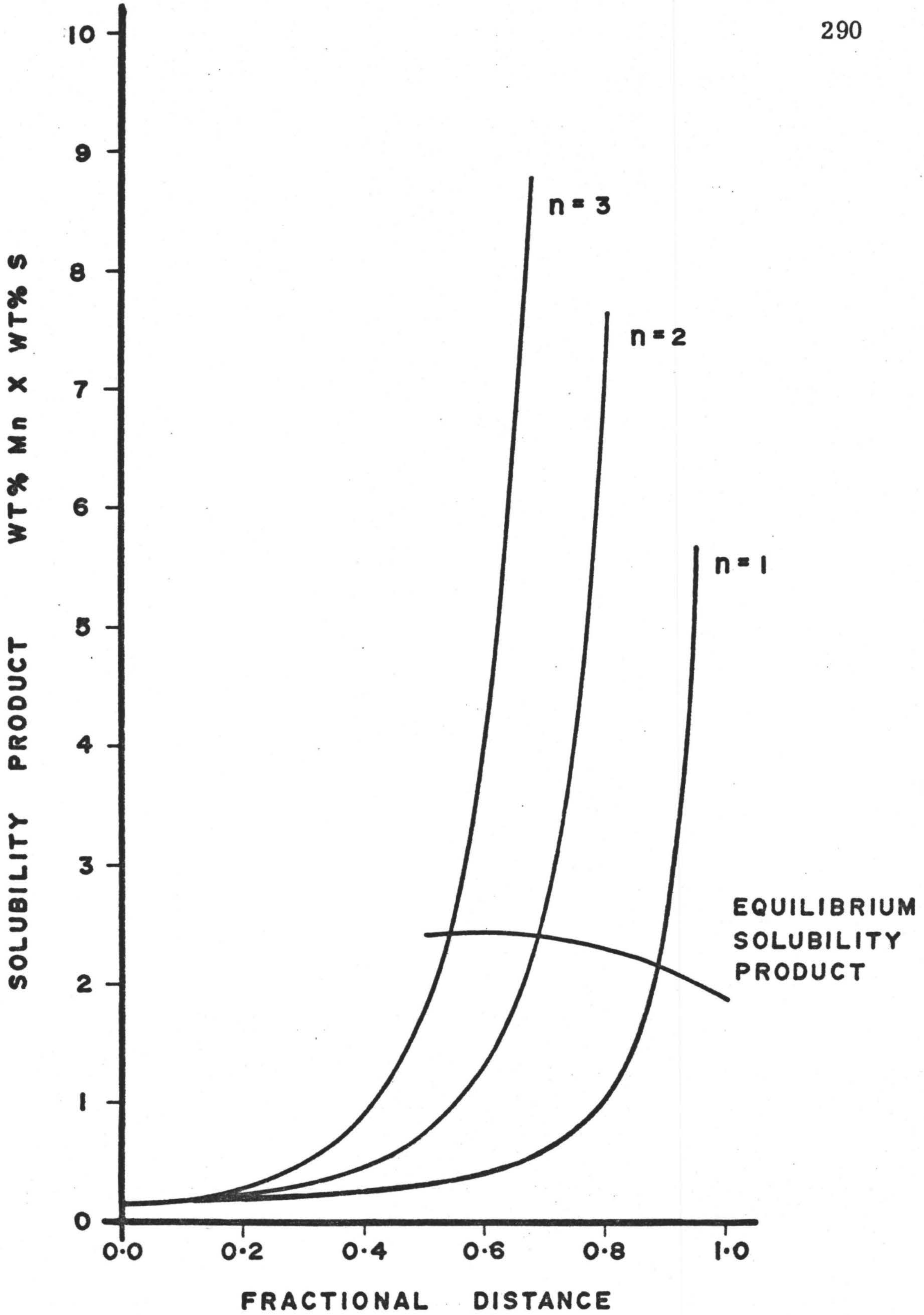

FIGURE 4.2.4 Formation of MnS During Freezing of Fe-15wt% Mn - 0.25wt% S in One-, Two- and Three-Dimensional Systems.

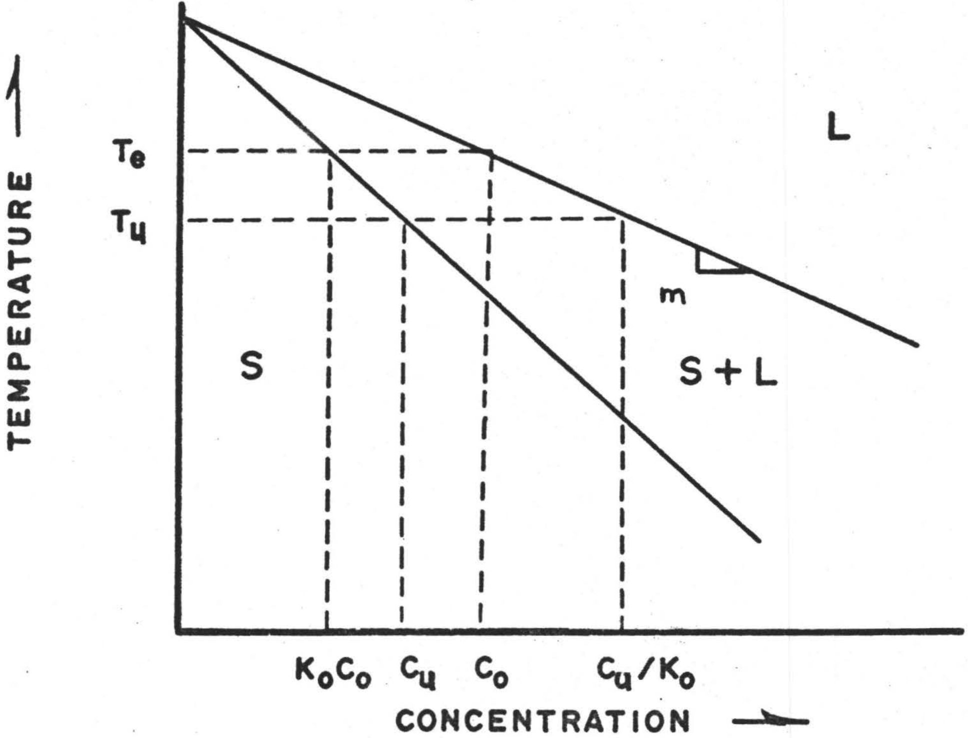

FIGURE 4.2.5 Phase Diagram Illustrating the Phenomenon of Undercooling.

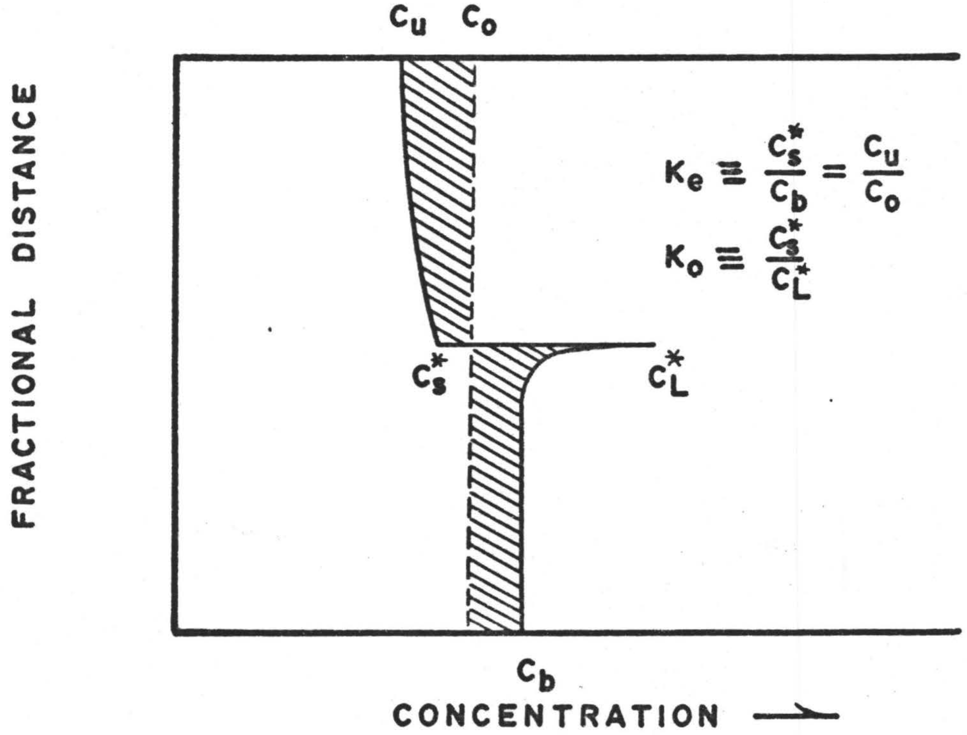

FIGURE 4.2.6 Solute Profiles in Solid and Liquid Phases for Solidification of an Undercooled Specimen.

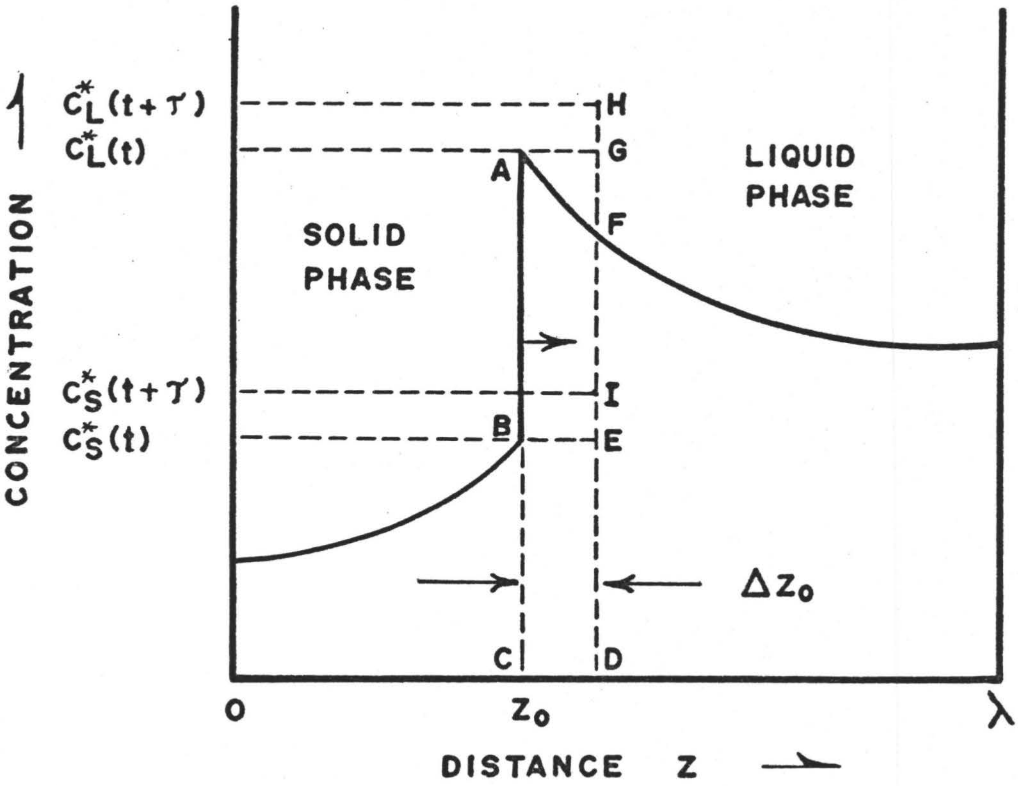

FIGURE 4.2.7 Solid Phase Growing from Liquid Phase. The Interfacial Concentrations C_L^* and C_S^* Increase from A to H and B to I, Respectively, as the Interface Advances by ΔZ_0 in Small Increment of Time τ.

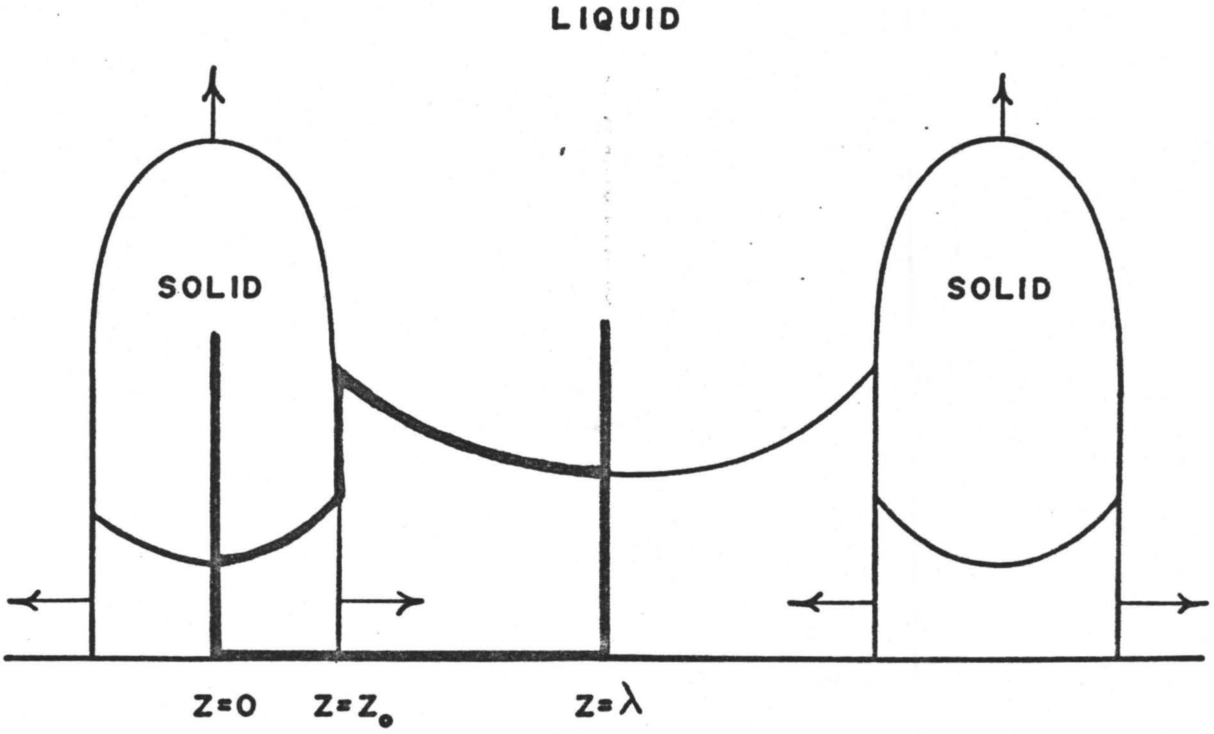

FIGURE 4.2.8 Two-Dimensional Dendrite Arms of Solid Phase Growing in Liquid Phase. The One-Dimensional System under Consideration Is Drawn in Heavy Lines. It Extends from $Z = 0$ to $Z = \lambda$. The Concentration Profiles in Both Phases Are Superimposed on the Outline of the Dendrite Arms.

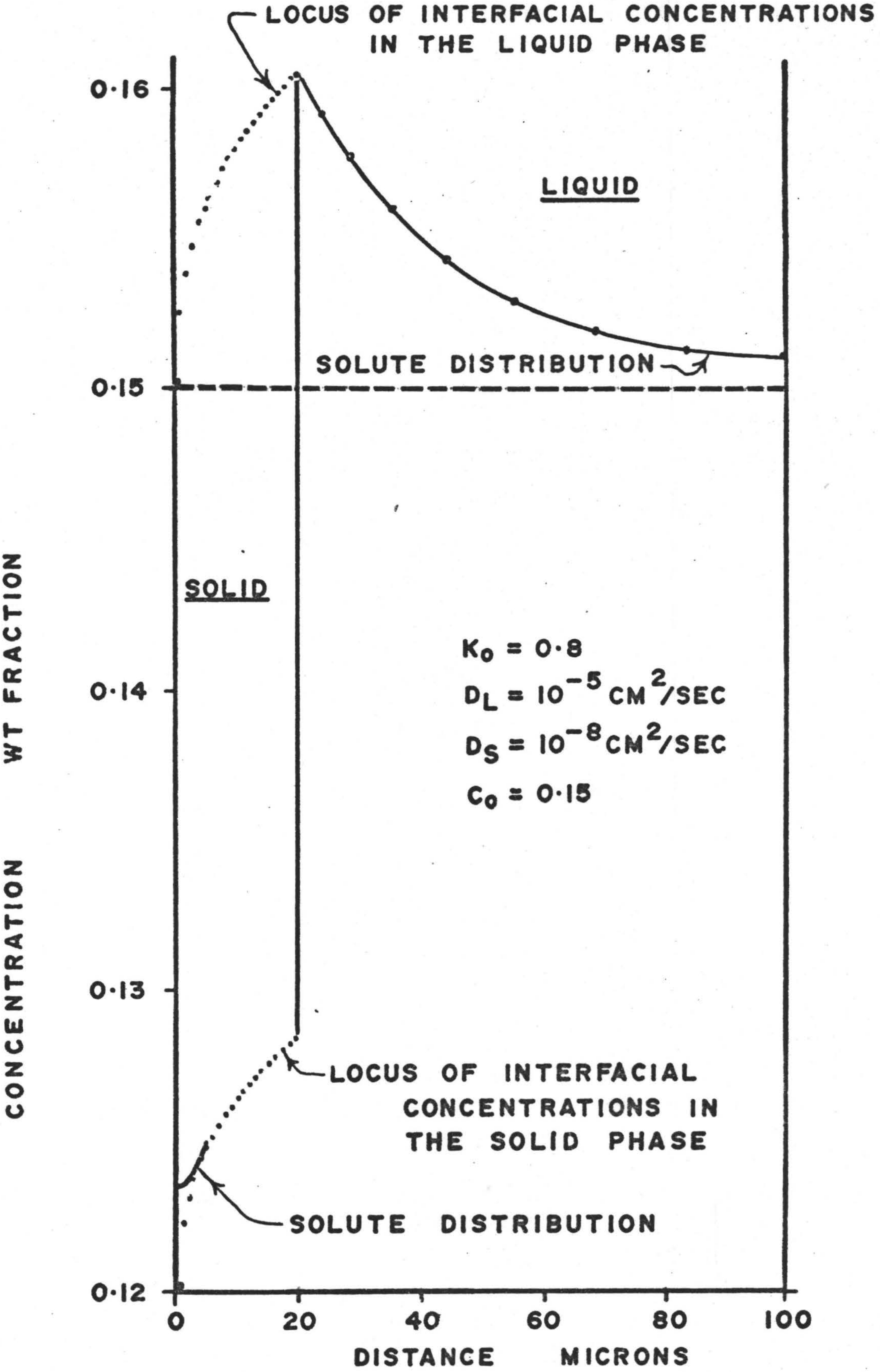

FIGURE 4.2.9 Locus of Interfacial Concentrations and Solute Distributions in Solid and Liquid Phases Computed from Ternary Microsegregation Model.

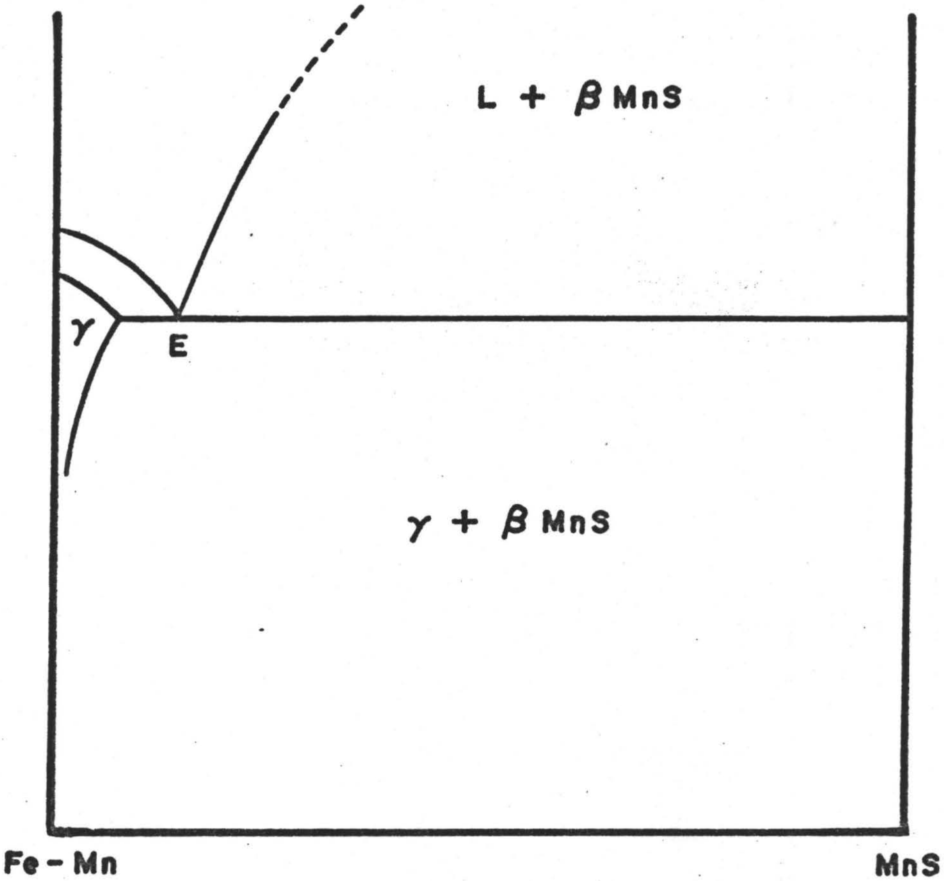

FIGURE 4.3.1 Schematic Vertical Section of the Fe-Mn-MnS-FeS System Used in Illustrating the Formation Mechanism of Sulphide Inclusions.

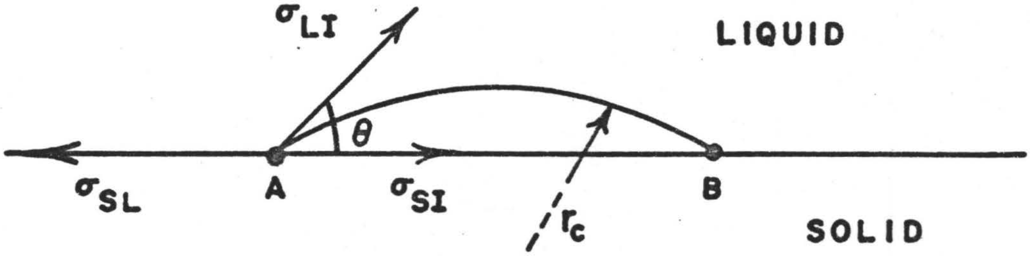

FIGURE 4.3.2 Schematic Drawing of an Inclusion of Curvature Radius r_c on a Solid-Liquid Interface Showing the Horizontal Balance of Surface Tensions and Contact Angle θ.

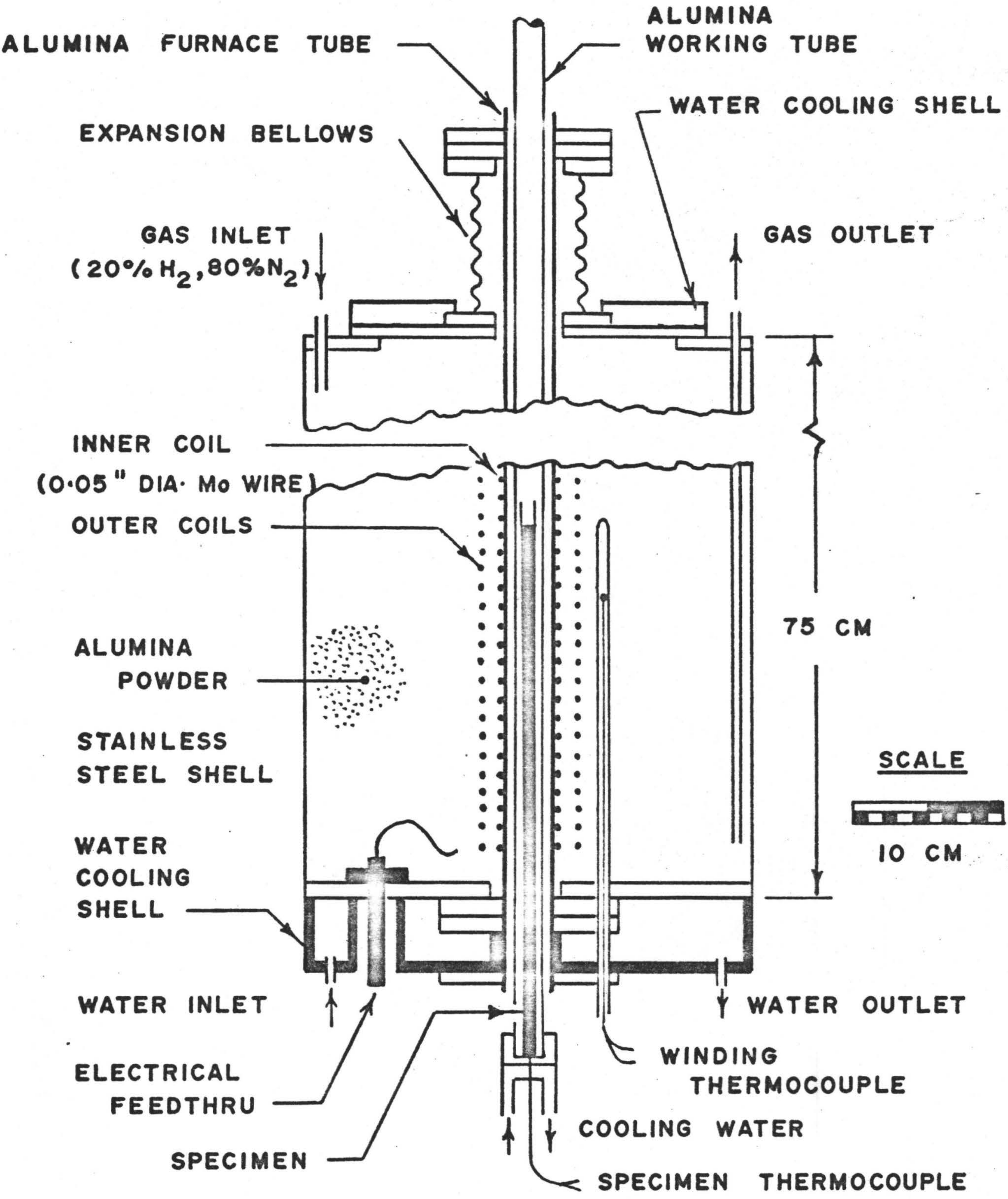

FIGURE 5.1.1 Sectional View of Resistance Furnace

FIGURE 5.1.2 Overall View of Solidification Apparatus.

FIGURE 5.1.3 View of Travelling Furnace and Working Tube.

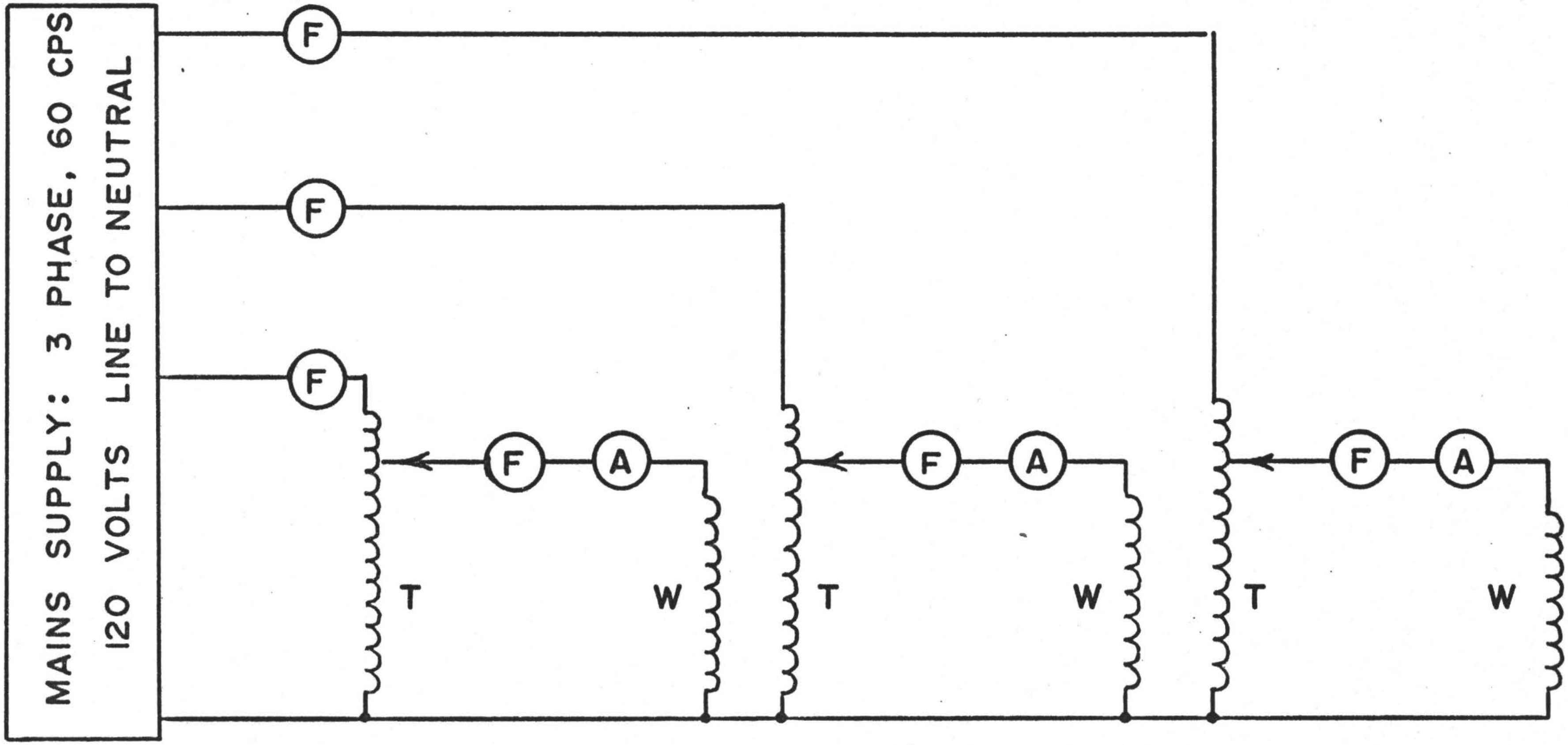

A : AMMETER

T : AUTOTRANSFORMER

F : FUSE 20 AMP

W : FURNACE WINDING

FIGURE 5.2.1 Wiring Diagram of Furnace Power Supply.

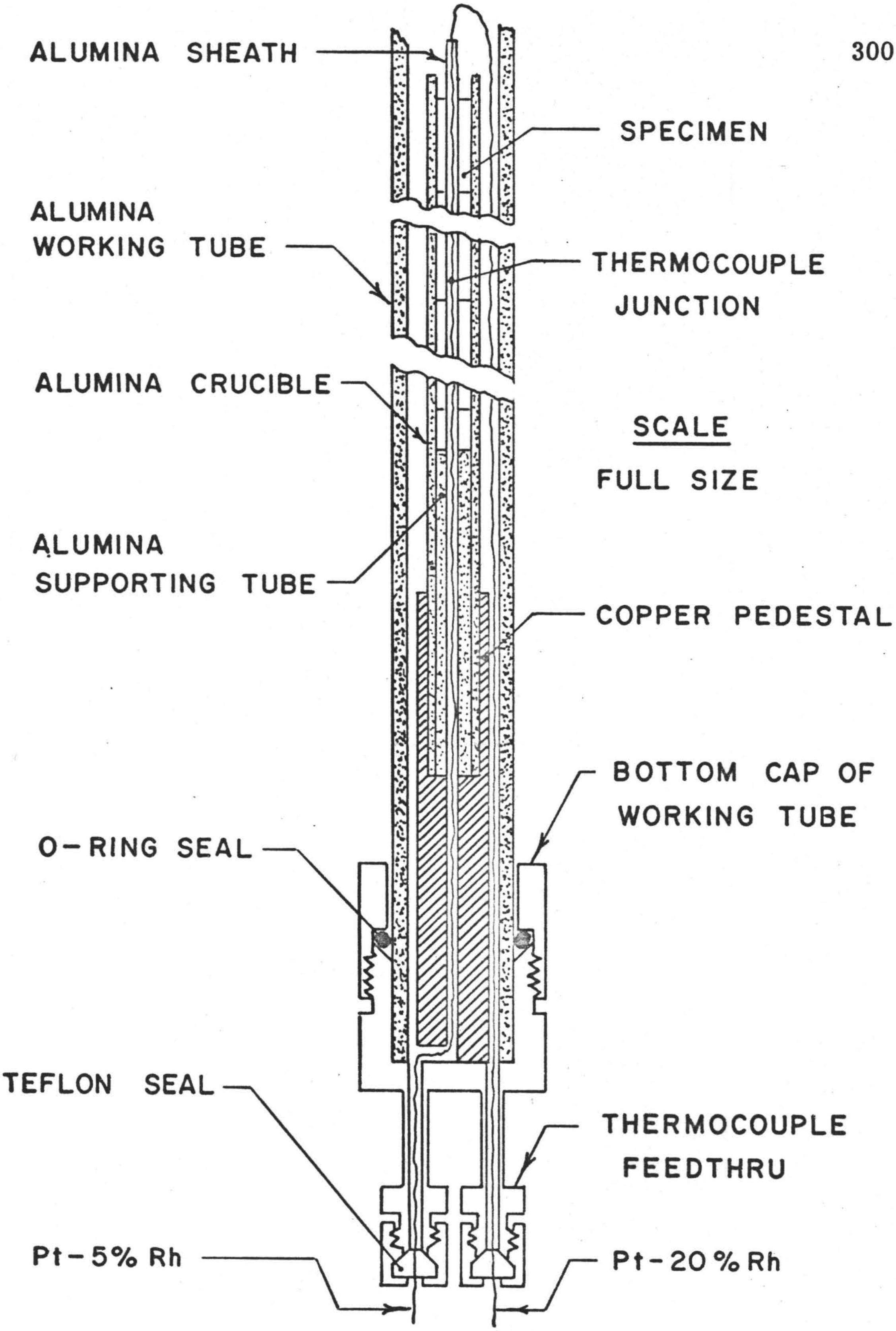

FIGURE 5.3.1 Sectional View of Specimen, Crucible and Thermocouple in Working Tube.

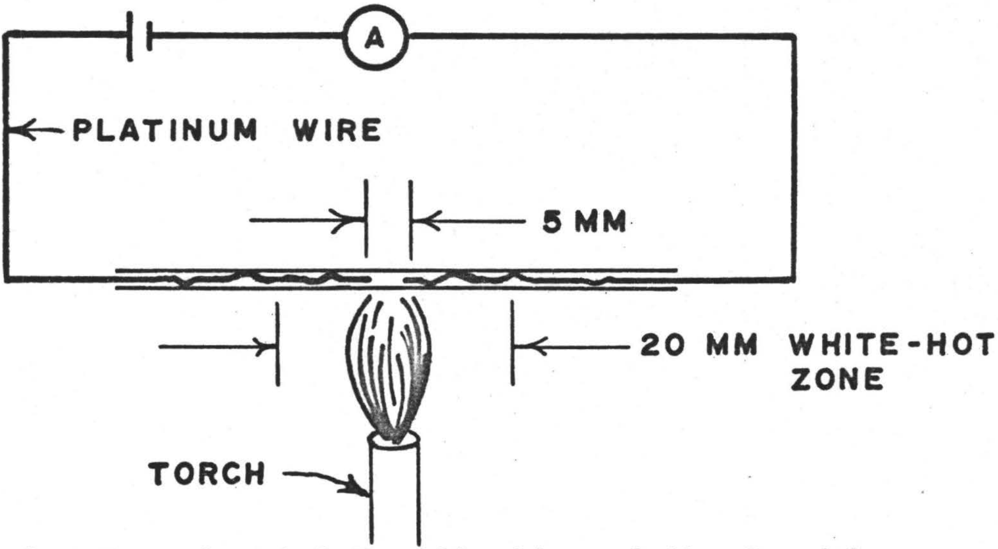

FIGURE 5.3.2 Experimental Verification of the Breakdown in Electrical Insulating Properties of an Alumina Thermocouple Sheath at Working Temperatures.

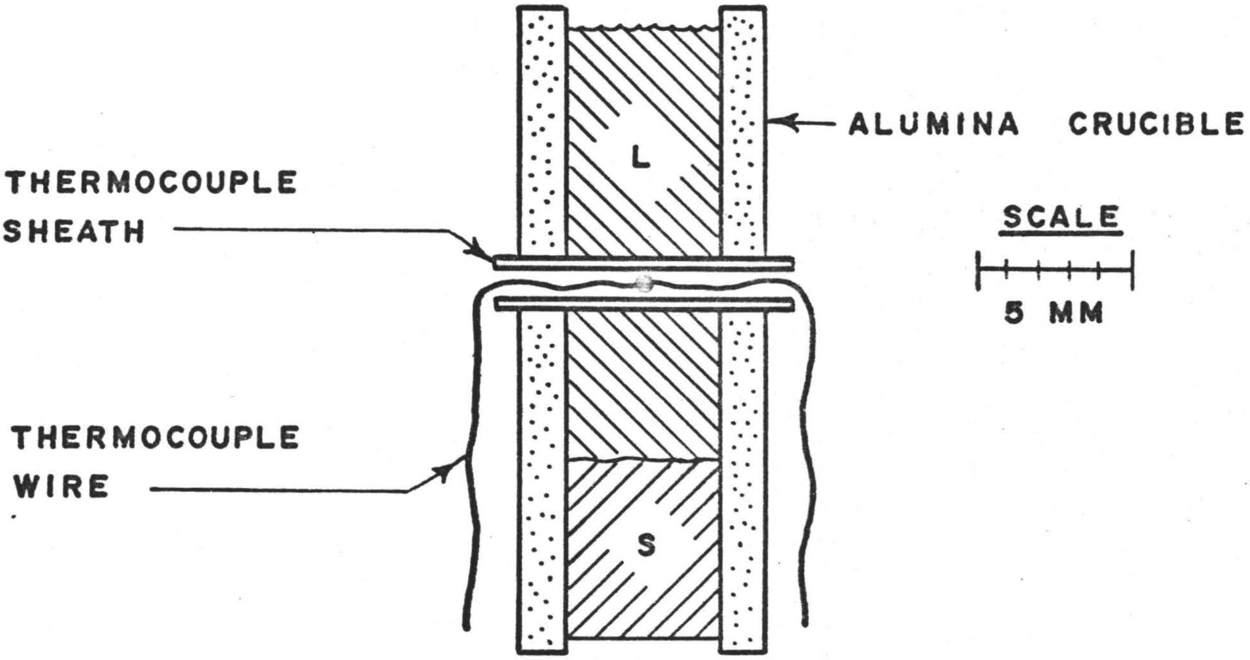

FIGURE 5.3.3 Modified Specimen, Crucible and Thermocouple Assembly.

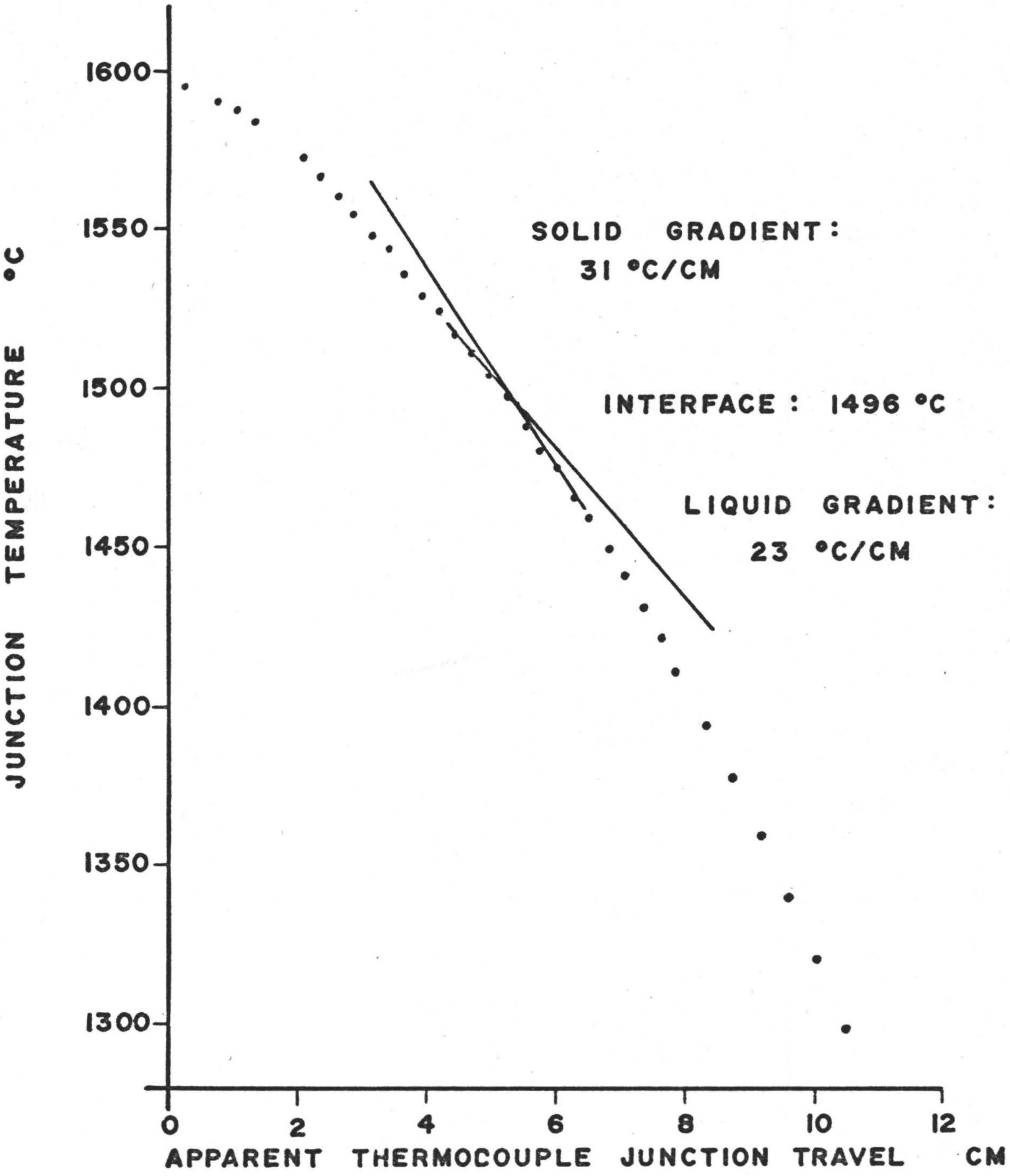

FIGURE 5.3.4 Temperature Profile Described by Thermocouple Junction During Solidification Run (Specimen 21).

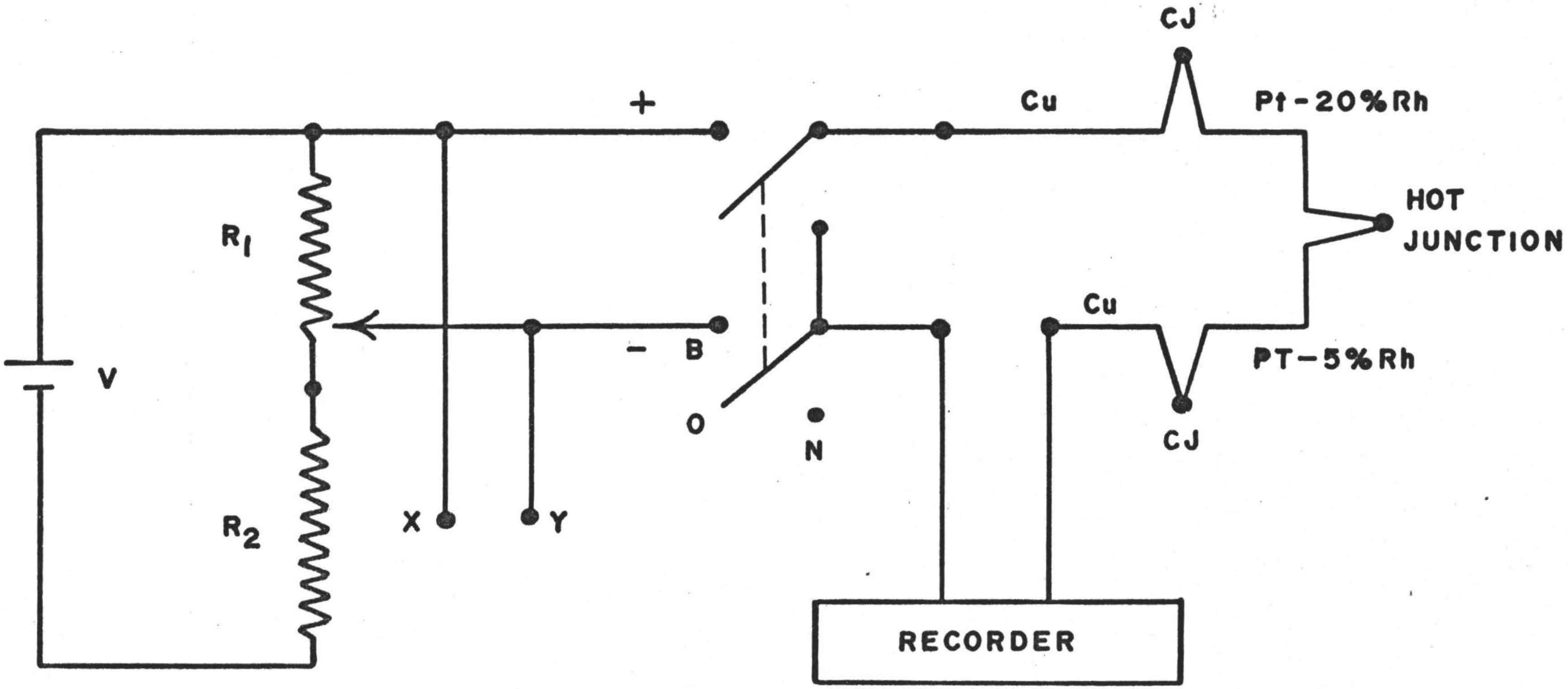

R1 : 0·5K 10-TURN POT
R2 : 50K 1 WATT
V : 2 VOLT ELECTROLYTIC CELL 200 AMP-HR

B : BUCKING POSITION
O : OPEN POSITION
N : NORMAL POSITION
CJ : JOSEPH KAYE ICE-POINT STANDARD

FIGURE 5.4.1 Thermocouple Circuitry.

QUENCHED LIQUID

FINAL POSITION OF SOLID-LIQUID INTERFACE

NOTE LARGE CRYSTALS

SCALE

FULL SIZE

INITIAL POSITION OF SOLID-LIQUID INTERFACE

UNMELTED PORTION OF SPECIMEN

FIGURE 5.5.1 Photograph of Typical Unidirectionally-Solidified Specimen.

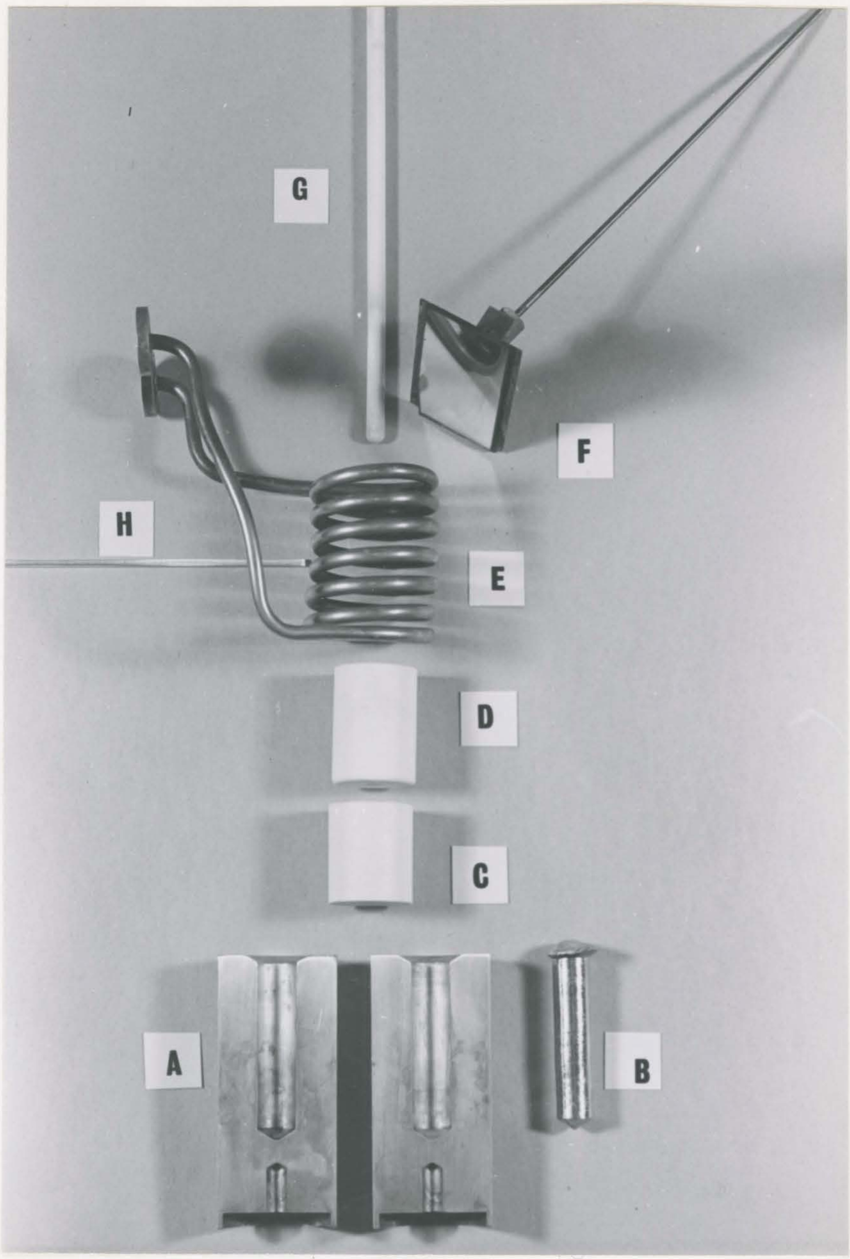

A : MOLD

B : ALLOY CASTING

C : ALUMINA SPACER

D : ALUMINA CRUCIBLE

E : INDUCTION COIL

F : OBSERVATION MIRROR

G : ALUMINA STOPPER ROD

H : SAPPHIRE RADIATION ROD

FIGURE 5.6.1 Exploded View of Alloy Casting Assembly.

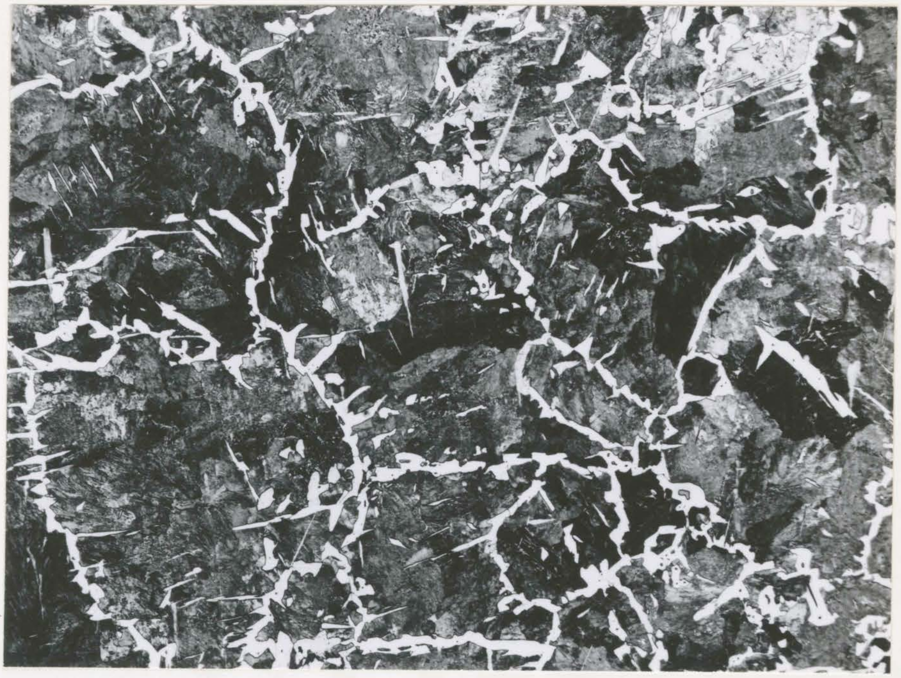

FIGURE 5.7.1 Specimen 2, Austenitized and Slowly Cooled. Ferrite Has Nucleated on Austenite Boundaries. Section Parallel to Growth Direction. Picral Etch. X50.

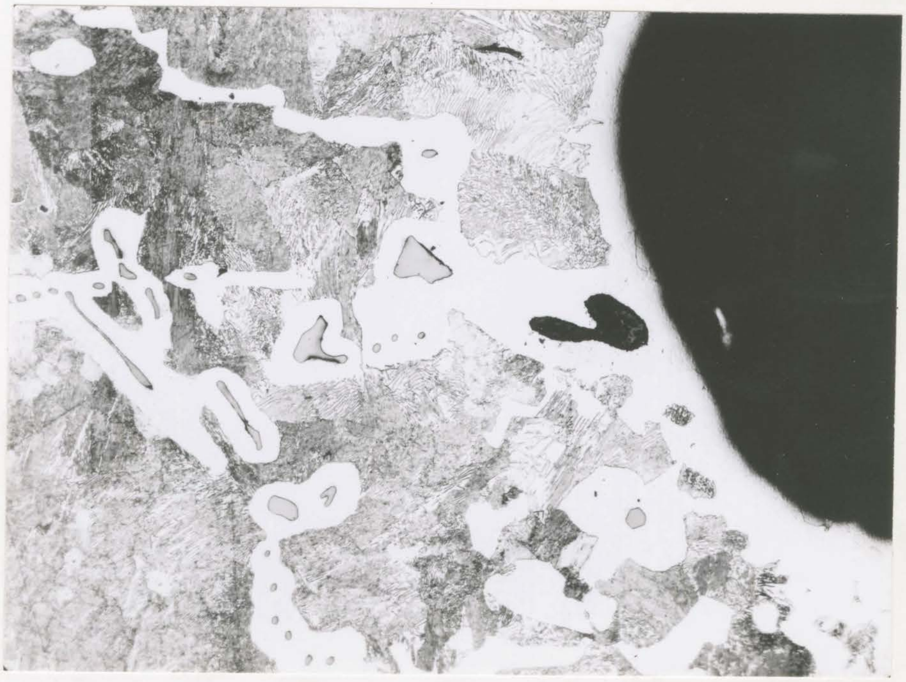

FIGURE 5.7.2 Specimen 2, Austenitized and Slowly Cooled. Ferrite Regions Surrounding MnS Inclusions. Section Parallel to Growth Direction. Picral Etch. X200.

FIGURE 5.7.3 Segregation Patterns in Fe-13 wt% Mn-0.25 wt% S Alloy Revealed by Sulphide Tinting. X50.

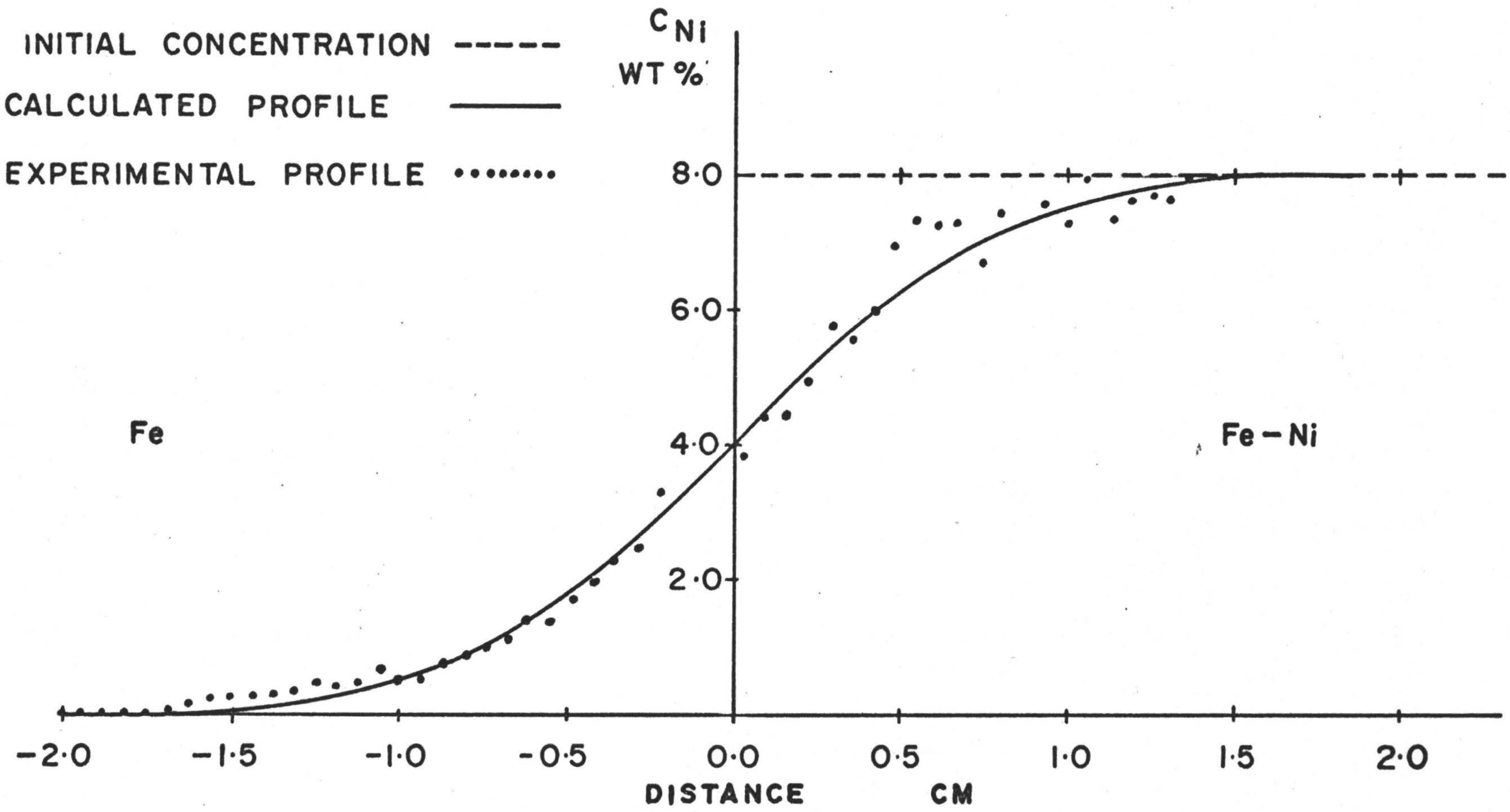

FIGURE 6.1.1 Calculated and Experimental Concentration Profiles of Ni in the Fe/Fe-8 wt% Ni Diffusion Couple of Convection Experiment.

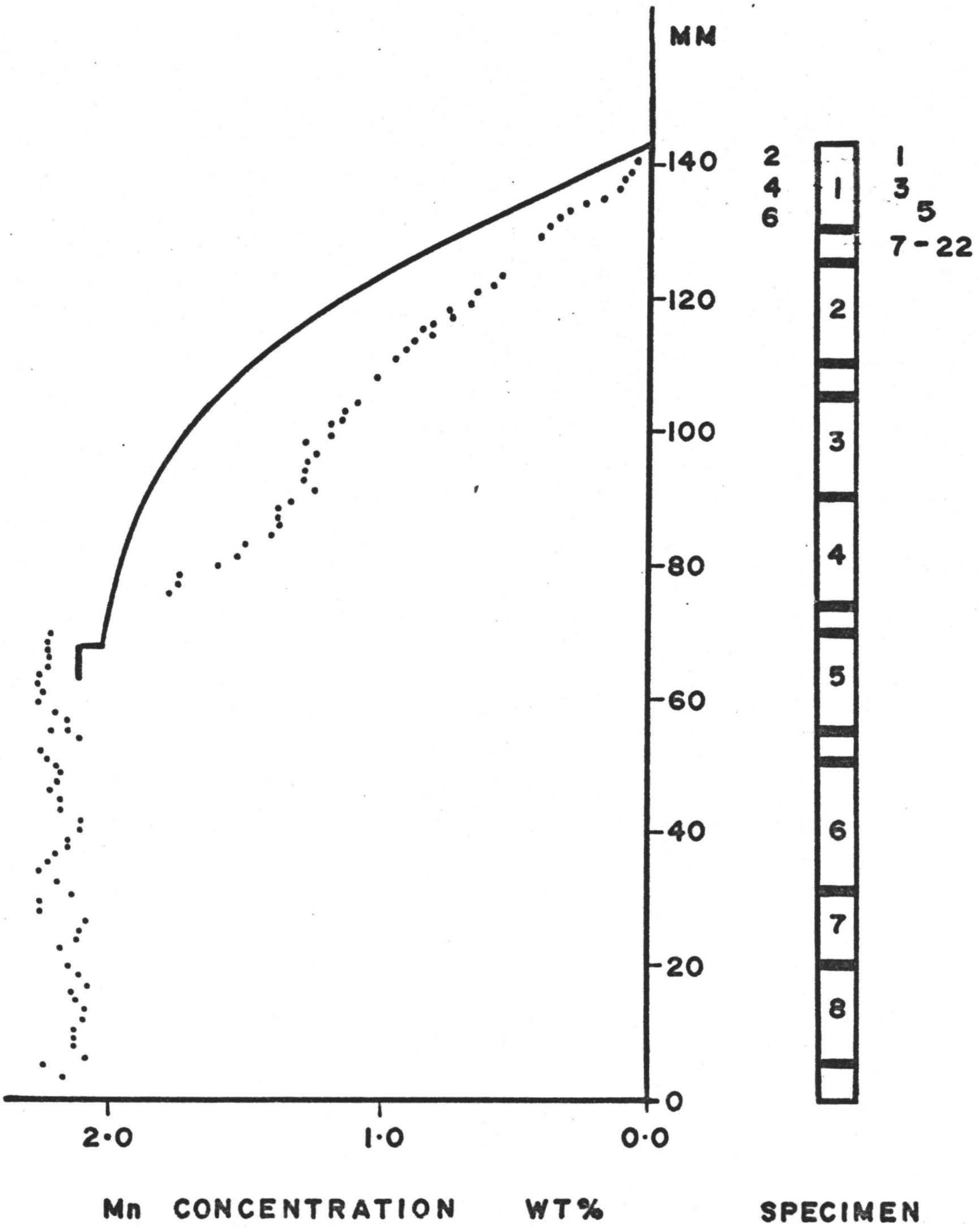

FIGURE 6.2.1 Specimen 1. Manganese Concentration of Matrix and Location of Inclusions Listed in Table 6.4.1.

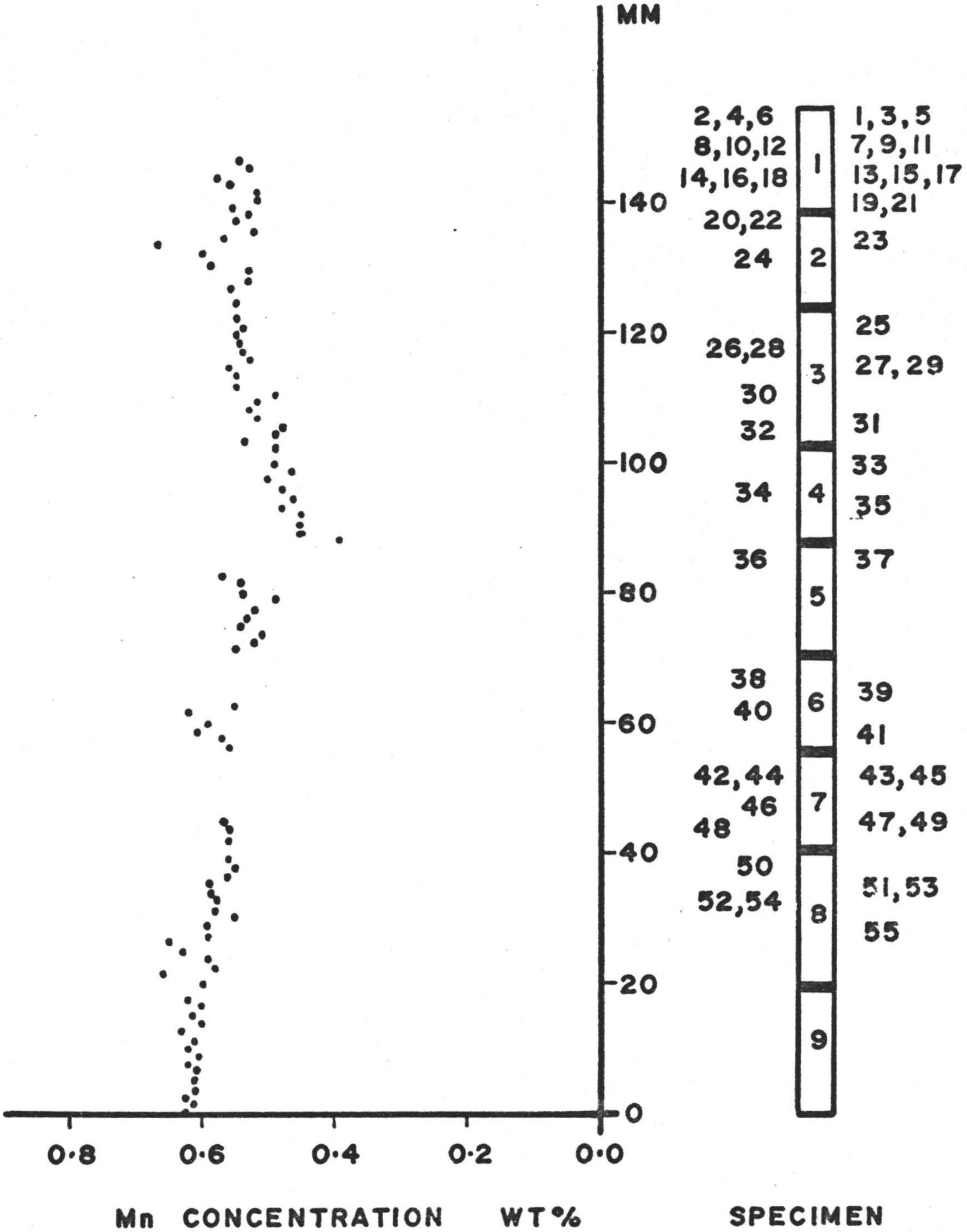

FIGURE 6.2.2 Solidified Specimen 2. Manganese Concentration of Matrix and Location of Inclusions Listed in Table 6.4.1.

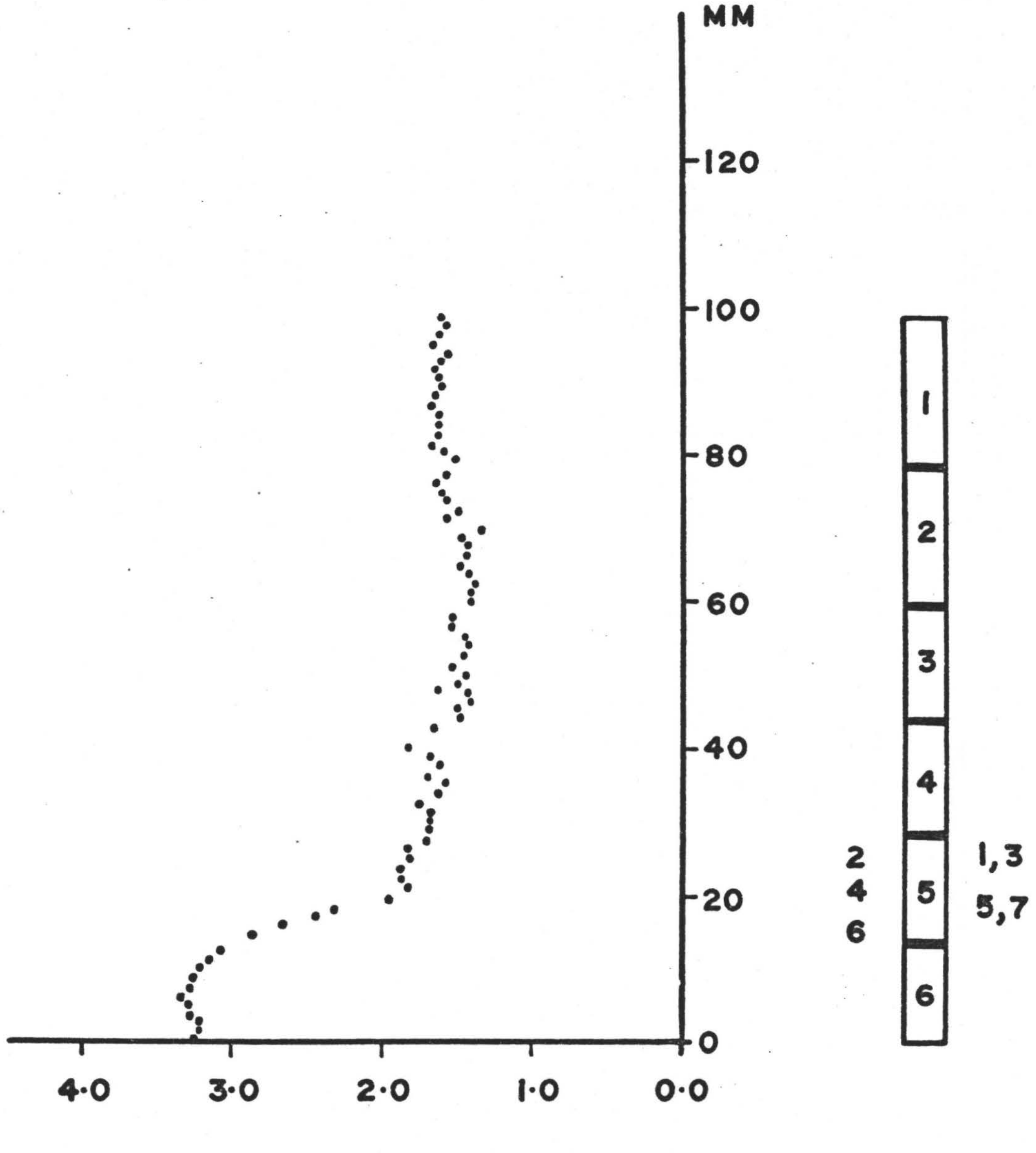

FIGURE 6.2.3 Solidified Specimen 5. Manganese Concentration of Matrix and Location of Inclusions Listed in Table 6.4.1.

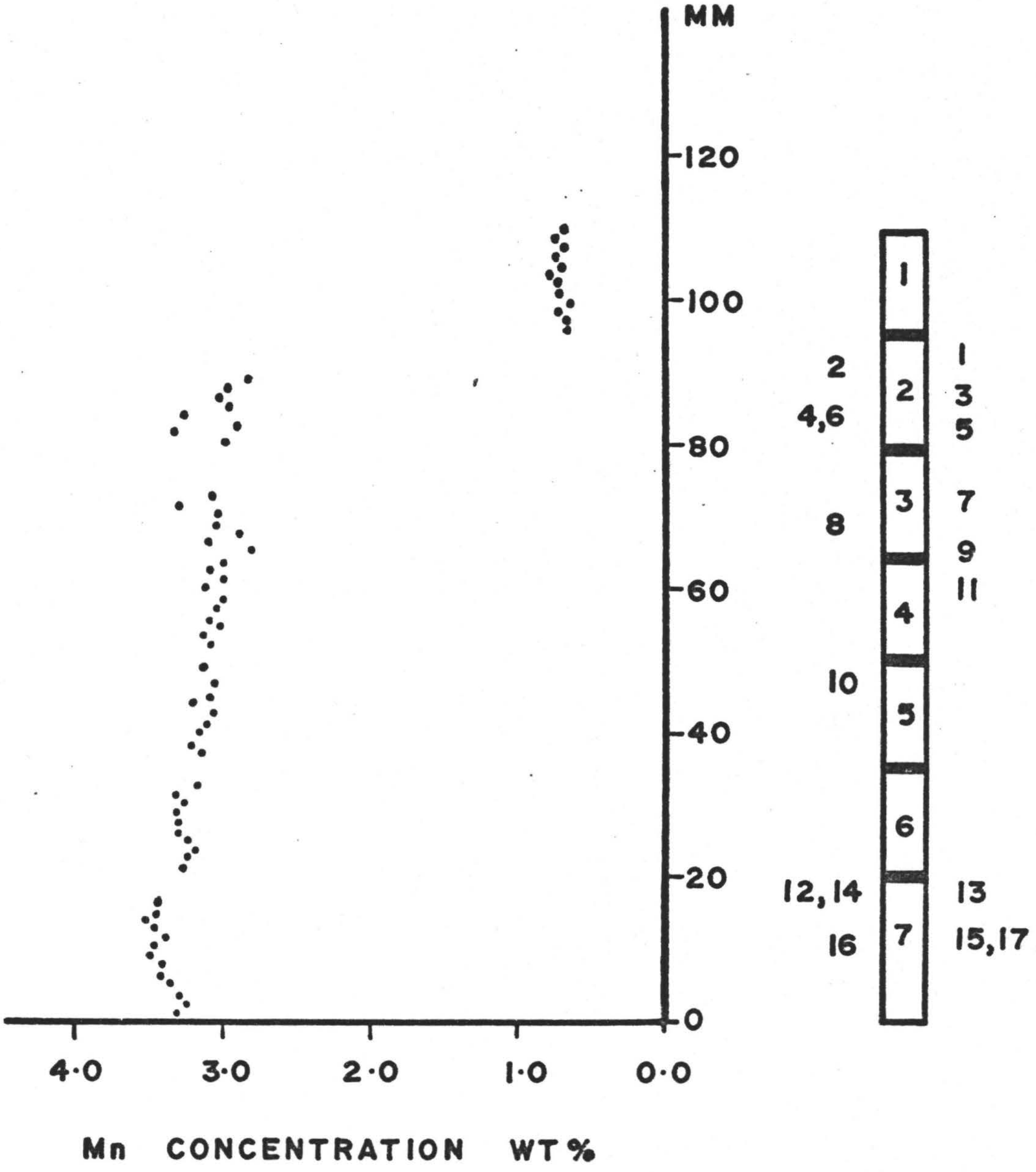

FIGURE 6.2.4 Solidified Specimen 6. Manganese Concentration of Matrix and Location of Inclusions Listed in Table 6.4.1.

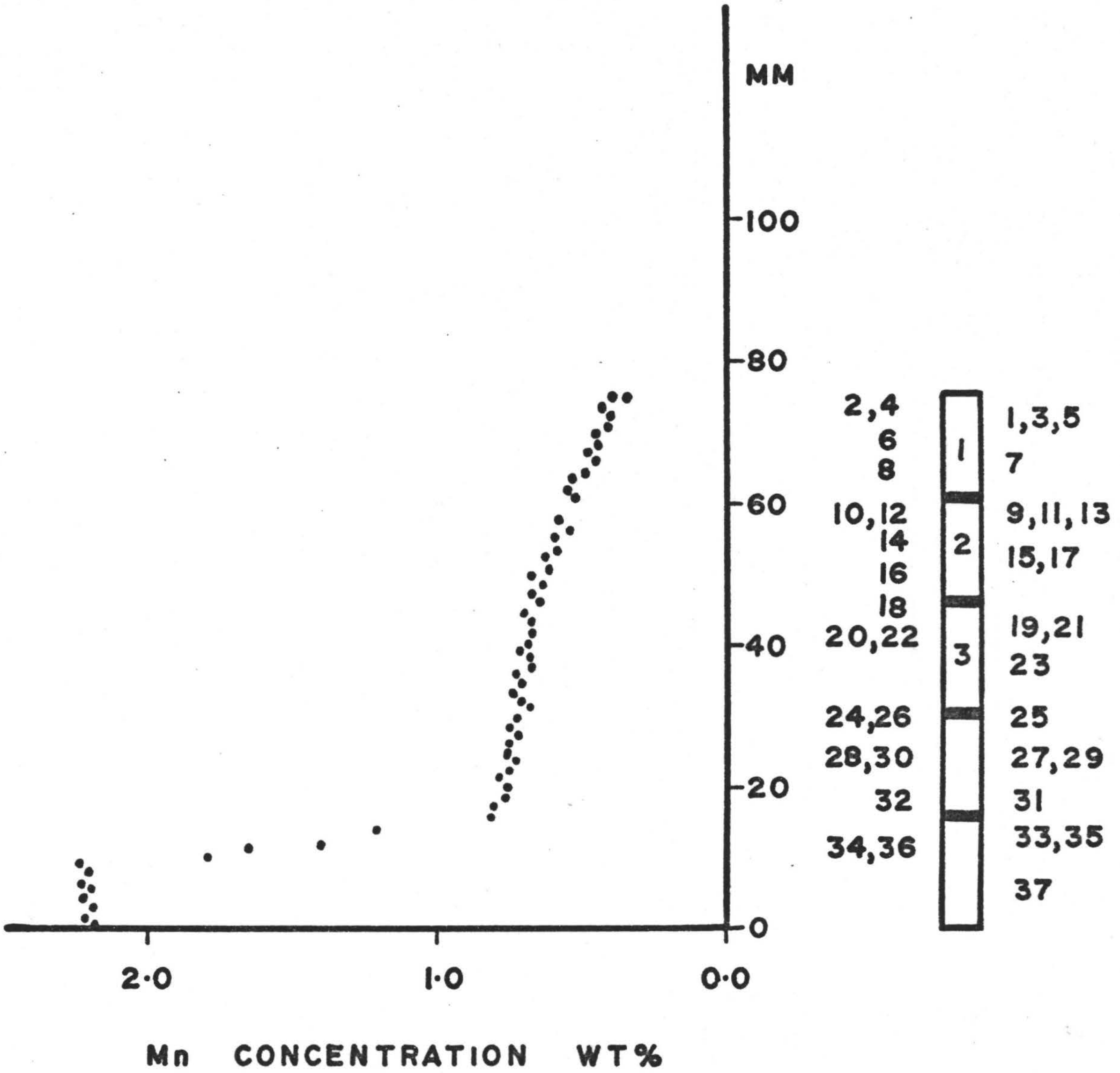

FIGURE 6.2.5 Solidified Specimen 7. Manganese Concentration of Matrix and Location of Inclusions Listed in Table 6.4.1.

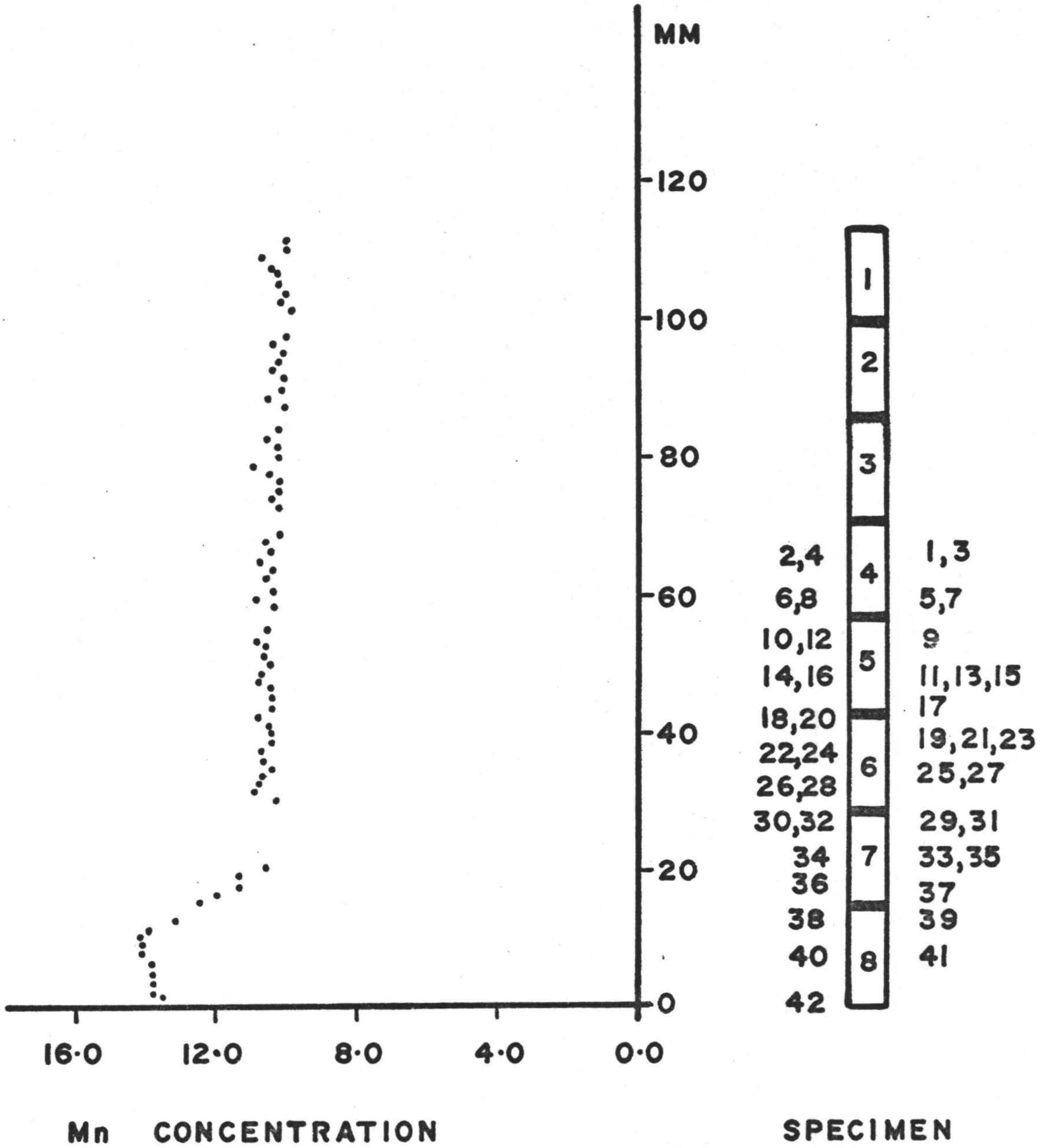

FIGURE 6.2.6 Solidified Specimen 9. Manganese Concentration of Matrix and Location of Inclusions Listed in Table 6.4.1.

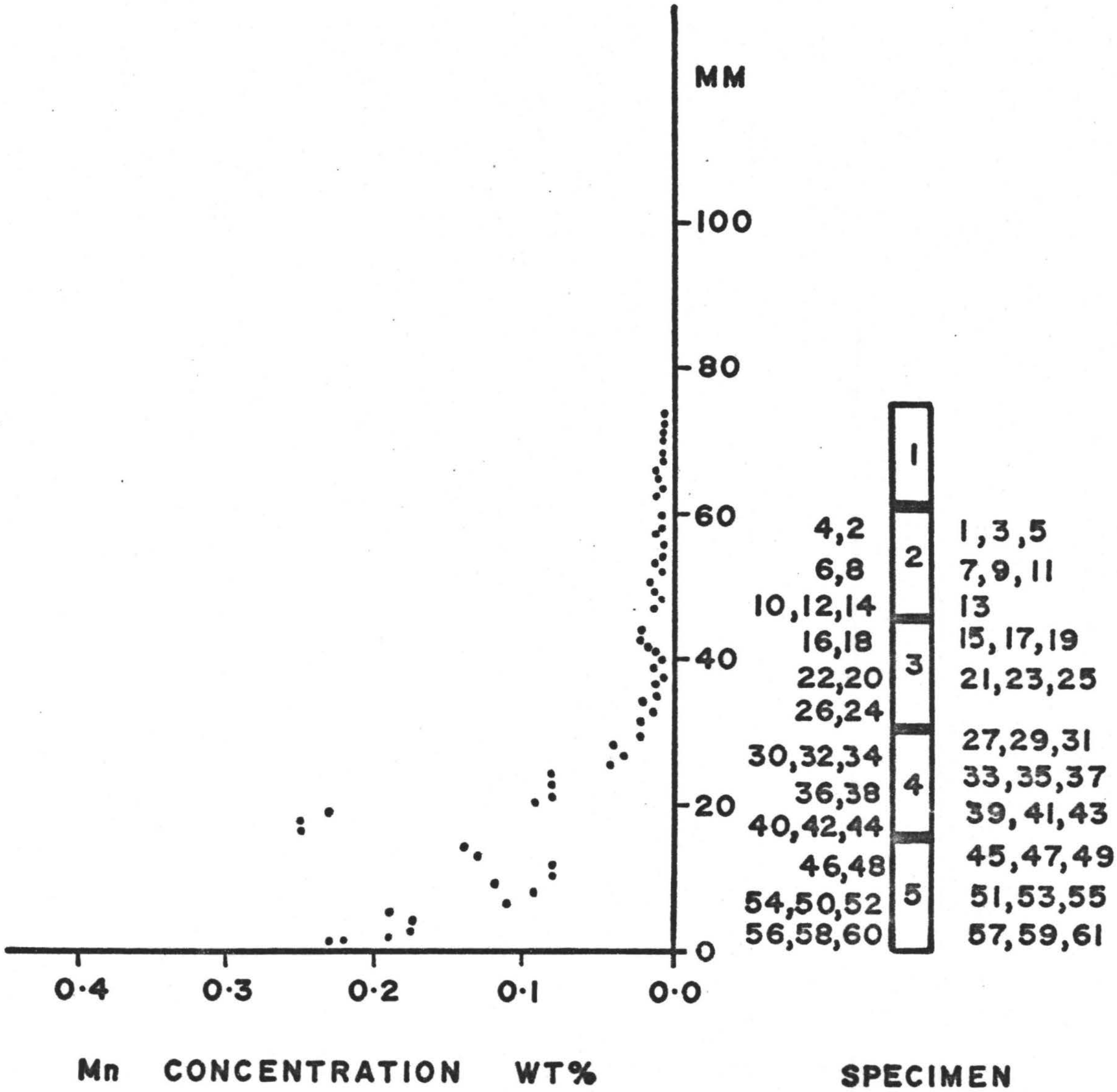

FIGURE 6.2.7 Solidified Specimen 10. Manganese Concentration of Matrix and Location of Inclusions listed in Table 6.4.1.

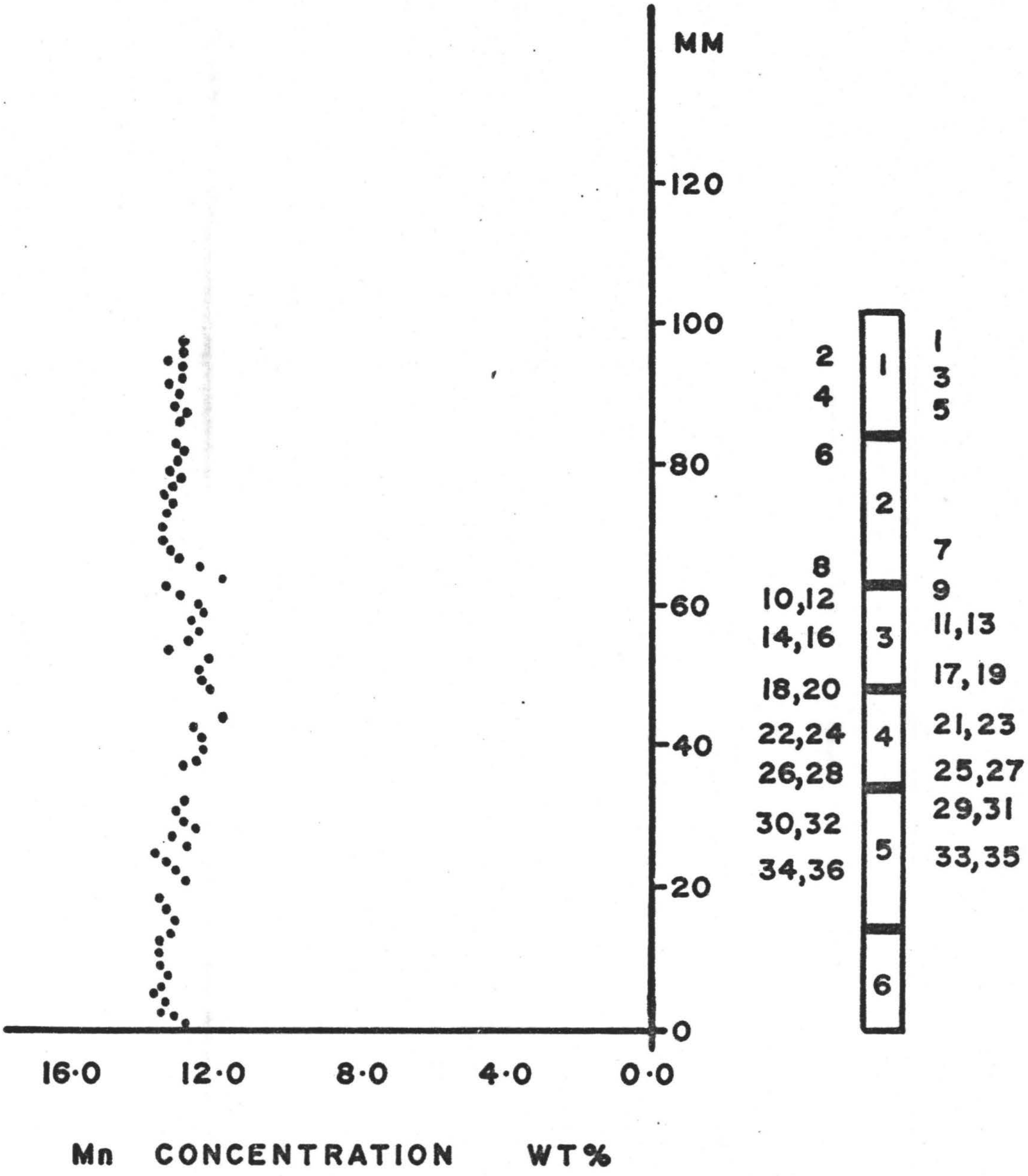

FIGURE 6.2.8 Solidified Specimen 13. Manganese Concentration of Matrix and Location of Inclusions Listed in Table 6.4.1.

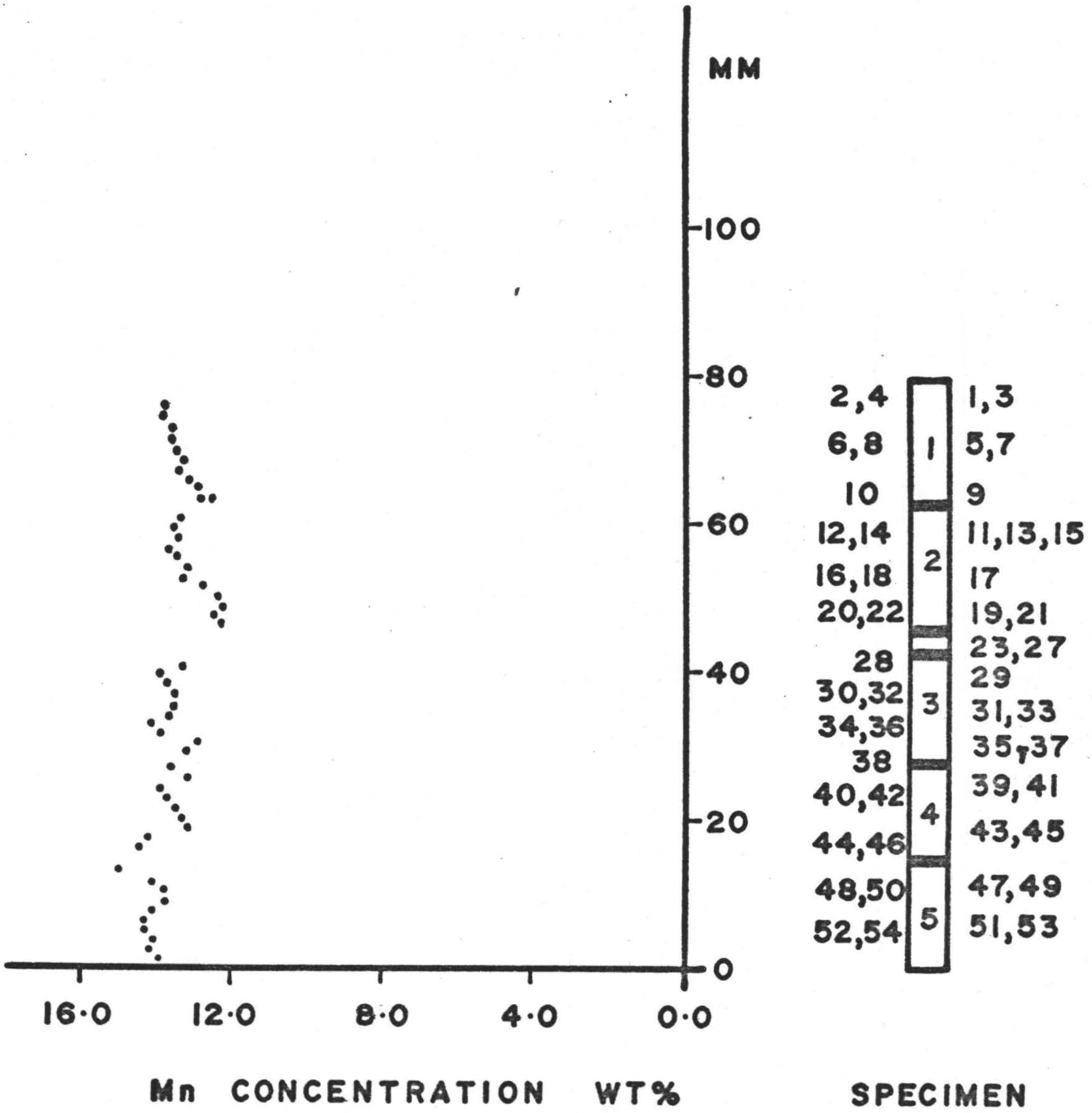

FIGURE 6.2.9 Solidified Specimen 14. Manganese Concentration of Matrix and Location of Inclusions Listed in Table 6.4.1.

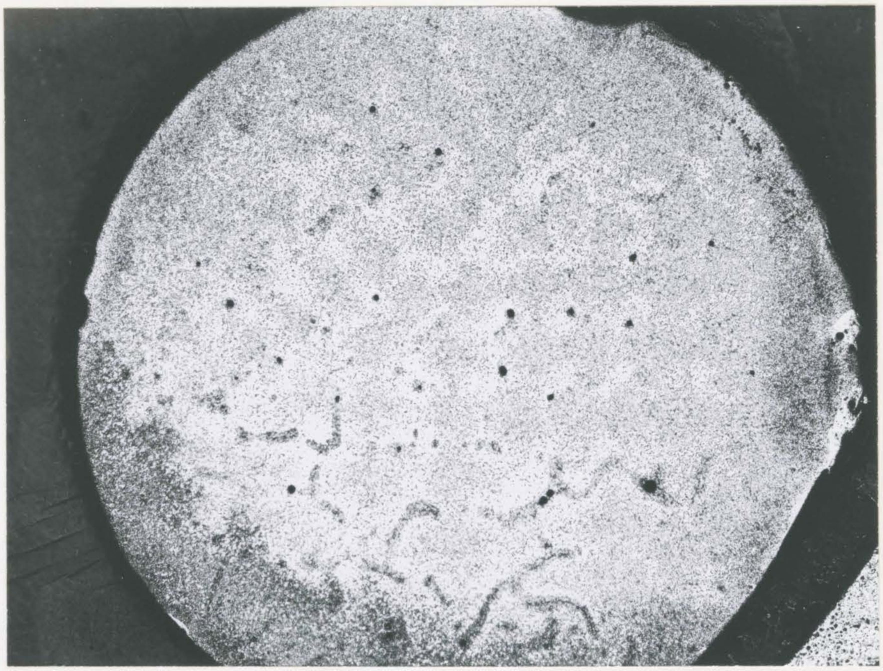

FIGURE 6.3.1 Specimen 21. Section Normal to Growth Direction. Picral Etch. X20.

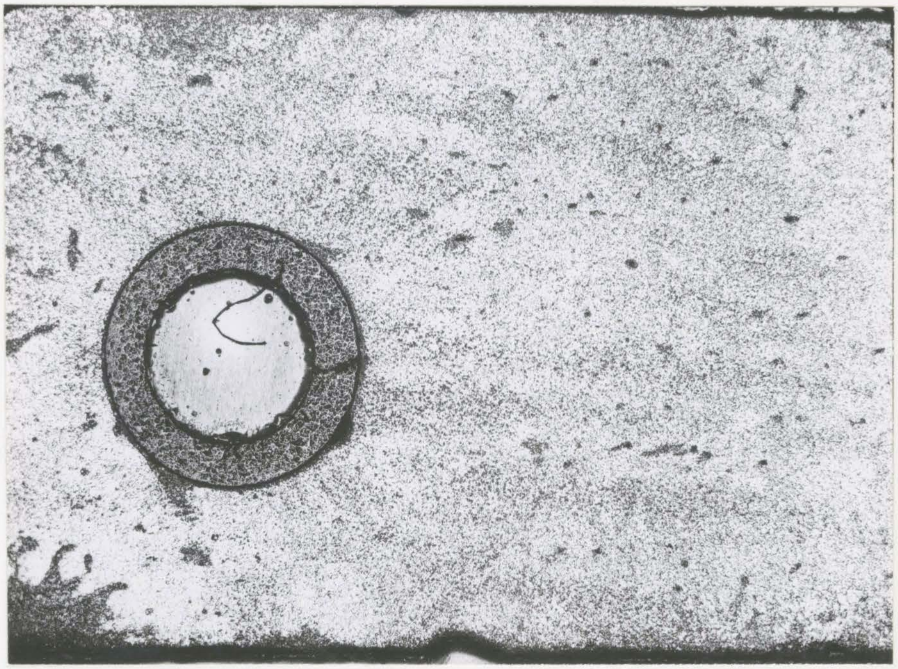

FIGURE 6.3.2 Specimen 21. Section Parallel to Growth Direction. Alumina Thermocouple Protection Sheath Is Embedded in Specimen. Picral Etch. X20.

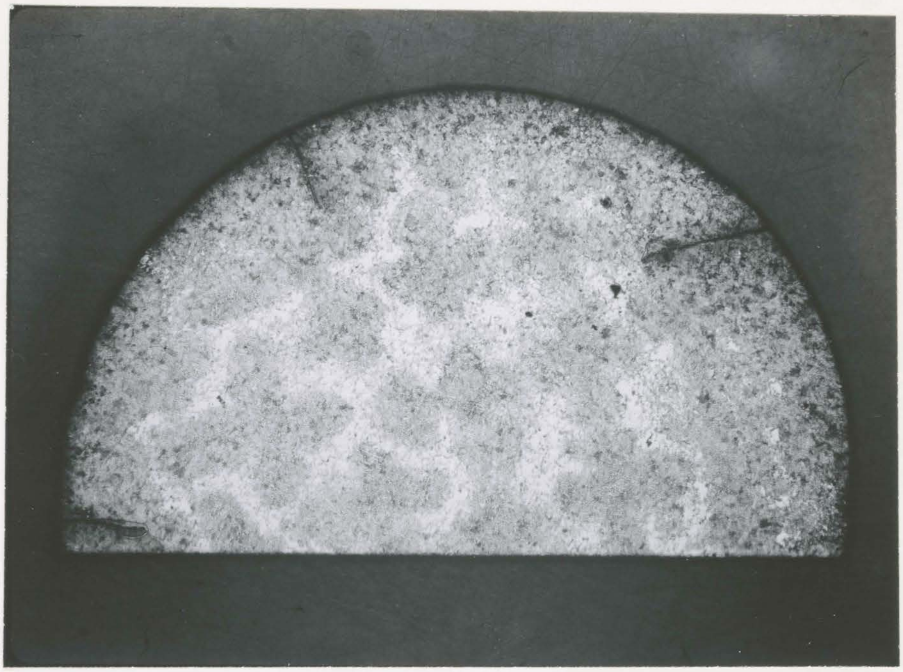

FIGURE 6.3.3 Specimen 6. Fe-3 wt% Mn-0.005 wt% S-0.4 wt% C. Section Normal to Growth Direction. Orthophenol and Picral Etch. X20.

FIGURE 6.3.4 Same as Above. Section Parallel to Growth Direction.

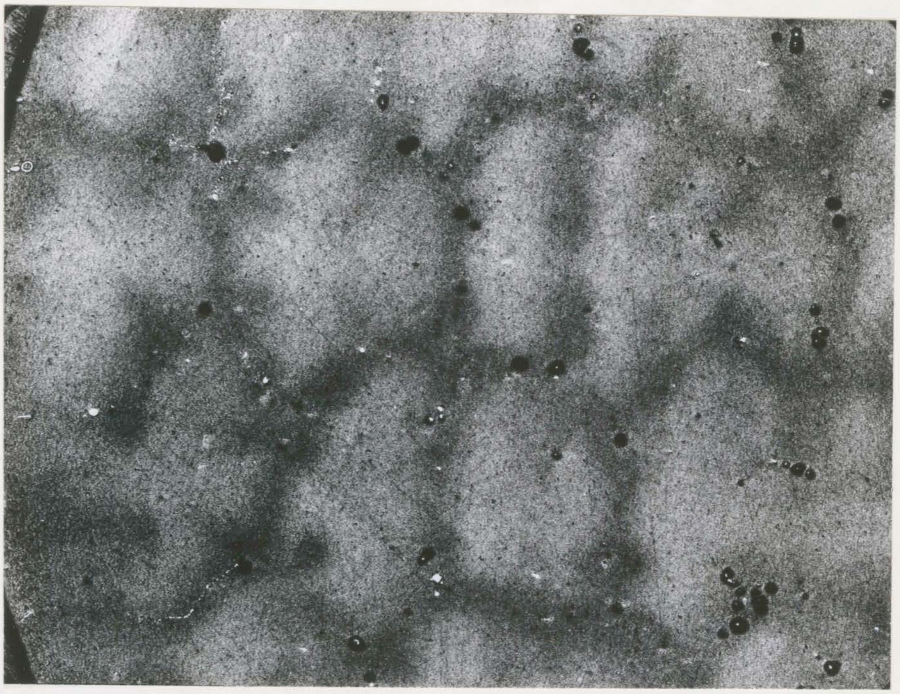

FIGURE 6.3.5 Specimen 9. Section Normal to Growth Direction. Sulphide Tint. X50.

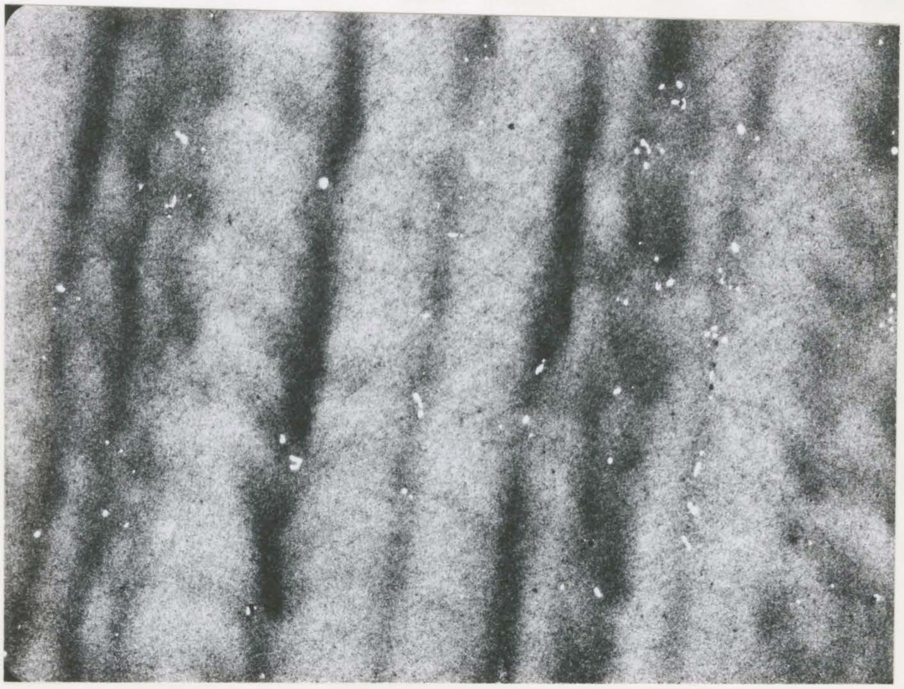

FIGURE 6.3.6 Same as Above. Section Parallel to Growth Direction.

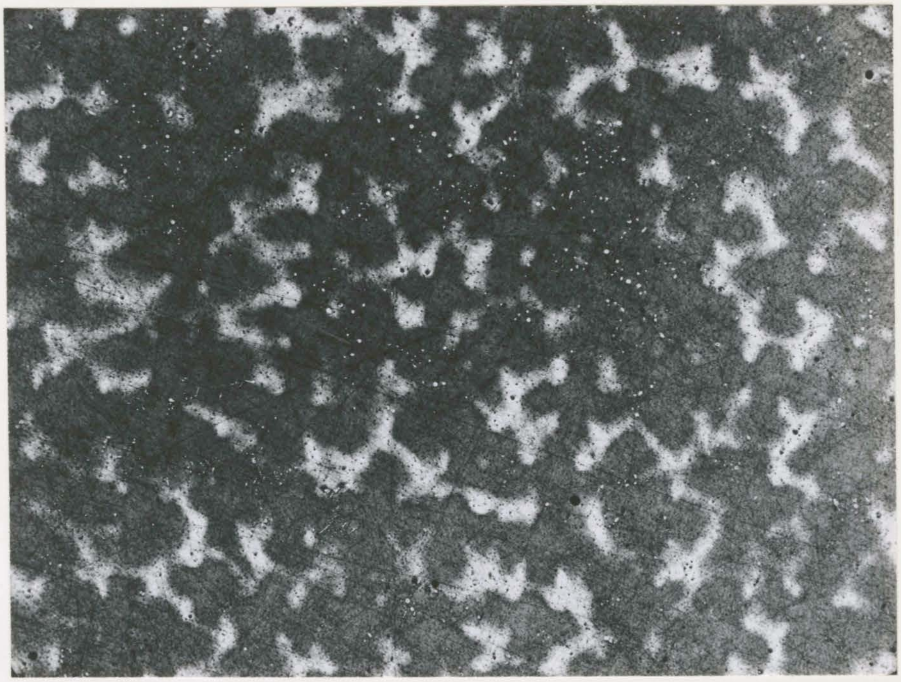

FIGURE 6.3.7 Specimen 13. Fe-15 wt% Mn-0.25 wt% S. Section Normal to Growth Direction of Primary Dendrite Arms. Sulphide Tint. X50.

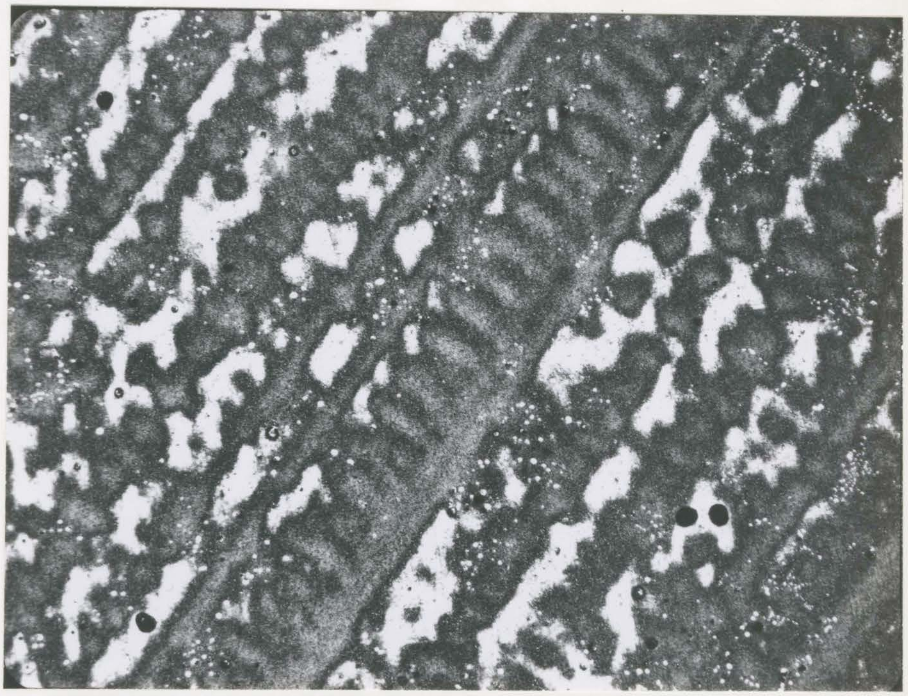

FIGURE 6.3.8 Same as Above. Section Parallel to Macroscopic Growth Direction.

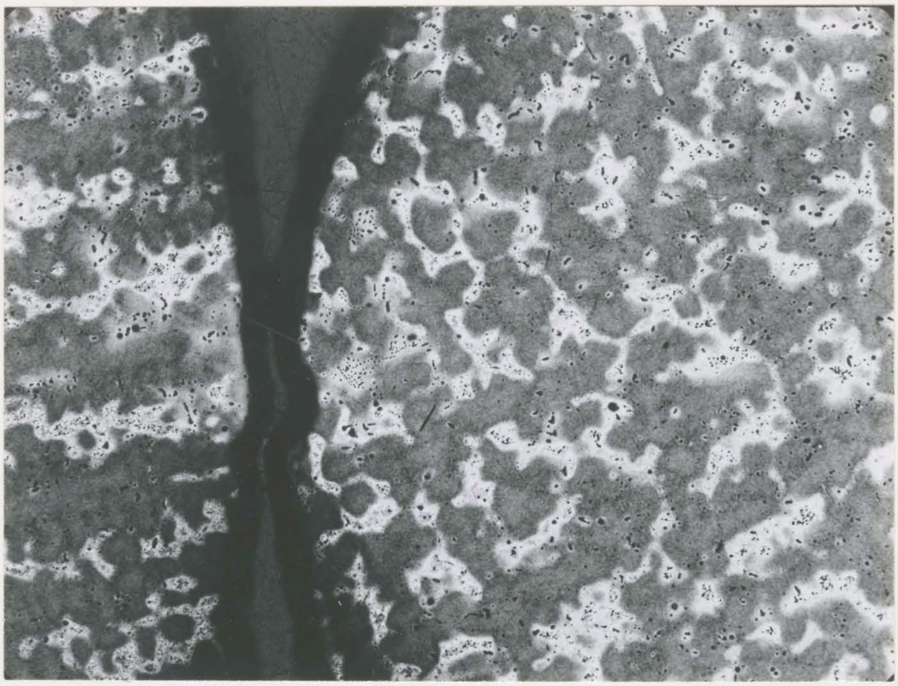

FIGURE 6.3.9 Specimen 14. Section Normal to Growth Direction. Sulphide Tint. X50.

FIGURE 6.3.10 Same as Above. Section Parallel to Growth Direction.

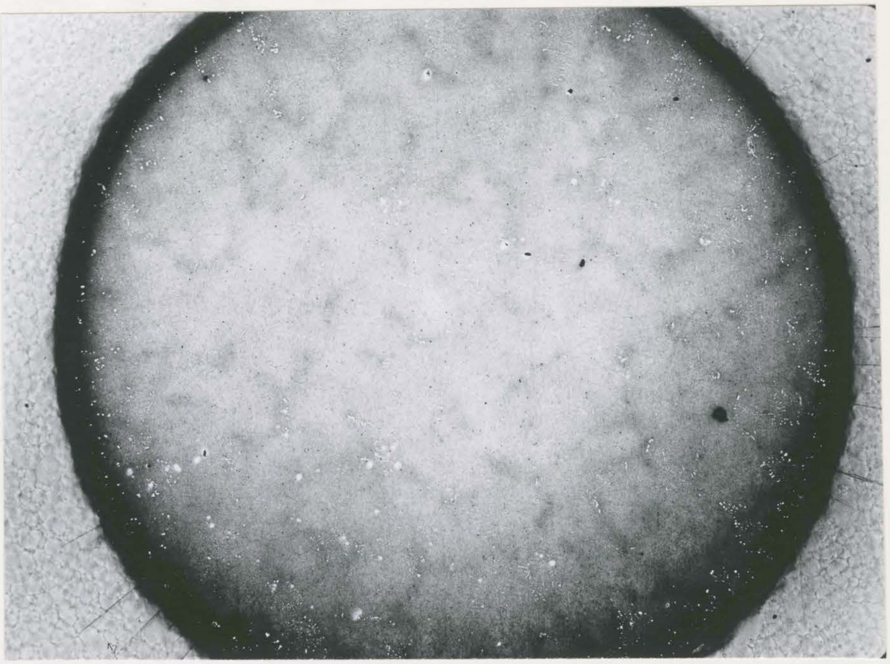

FIGURE 6.3.11 Specimen 24. Fe-10 wt% Mn-0.25 wt% S. Section Normal to Growth Direction. Growth Rate: 50 mm/hr. Sulphide Tint. X20.

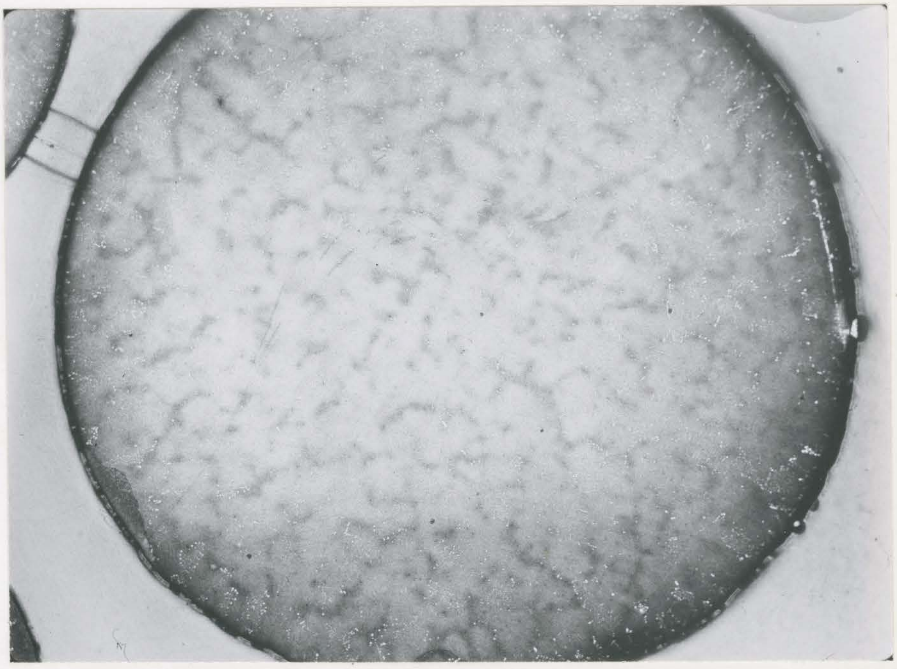

FIGURE 6.3.12 Same Specimen as Above. Growth Rate: 100 mm/hr.

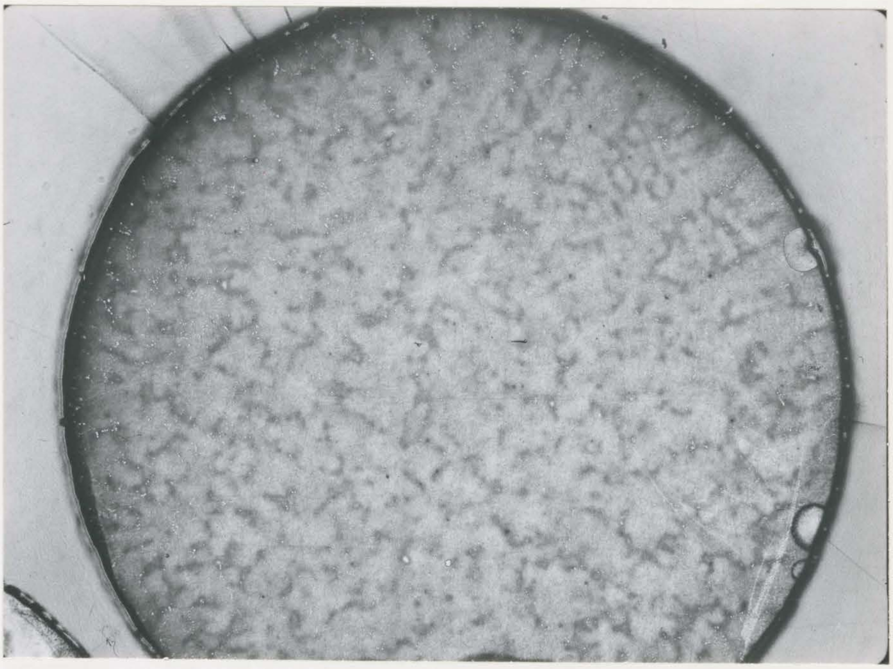

FIGURE 6.3.13 Same Specimen as in Figure 6.3.11. Growth Rate: 200 mm/hr.

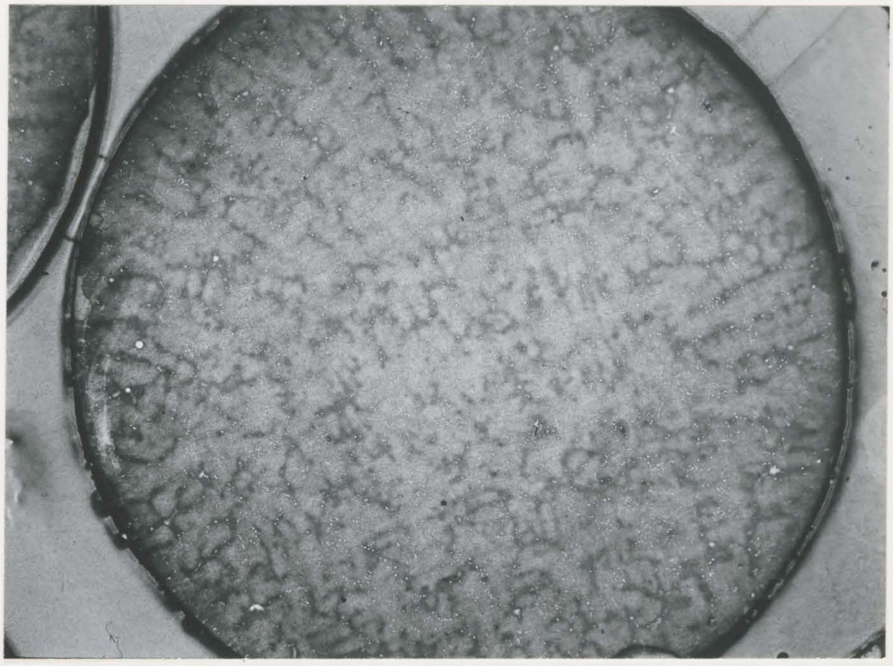

FIGURE 6.3.14 Same Specimen as in Figure 6.3.11. Growth Rate: 400 mm/hr.

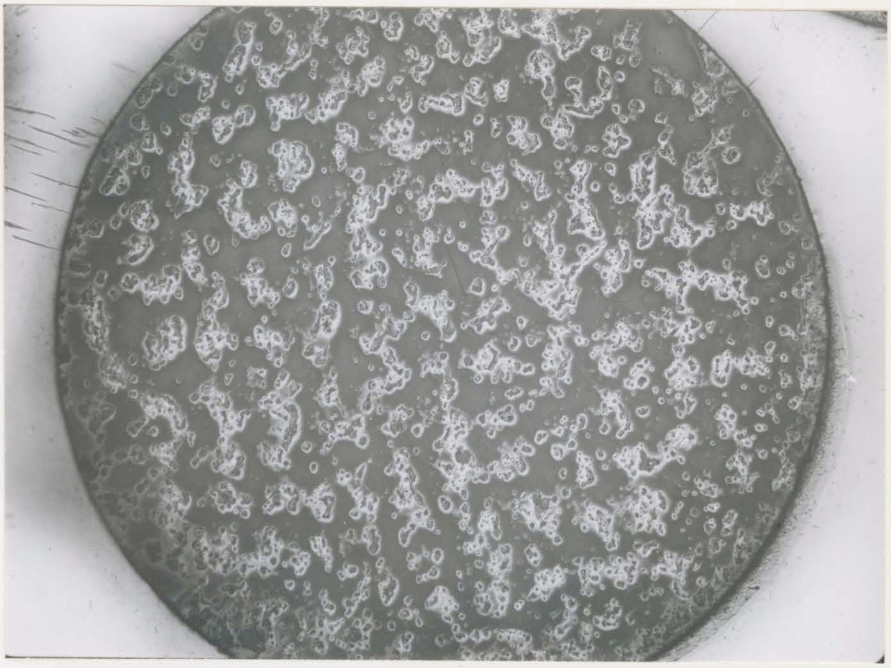

FIGURE 6.3.15 Specimen 25. Fe-13 wt% Mn-0.25 wt% ZrO_2. Growth Rate: 50 mm/hr. Normal Section. Sulphide Tint. X20.

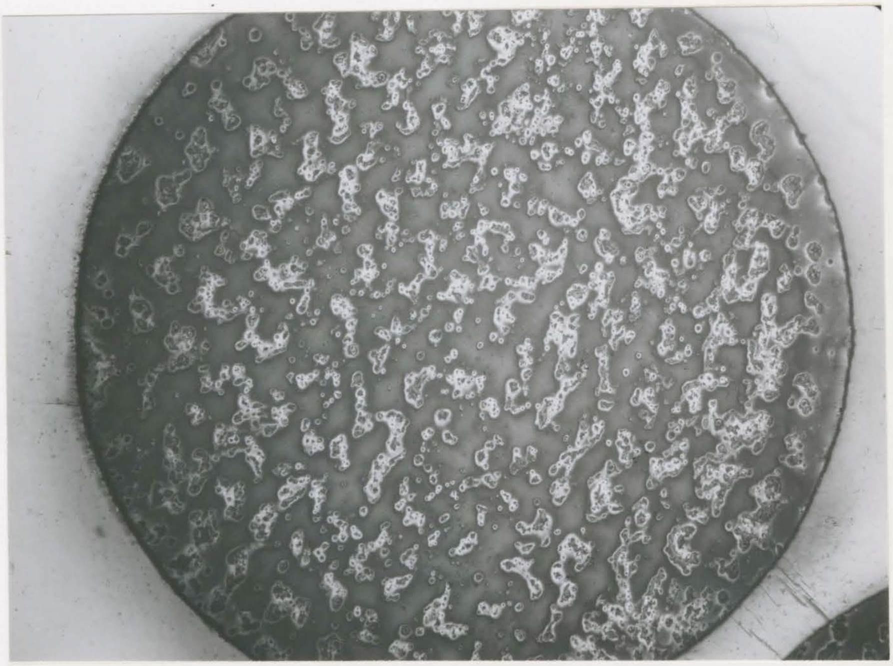

FIGURE 6.3.16 Same Specimen and Growth Conditions as Above, but Different Cross-Section.

FIGURE 6.3.17 Specimen 25. Fe-13 wt% Mn-0.25 wt% ZrO_2. Growth Rate: 100 mm/hr. Normal Section. Sulphide Tint. X20.

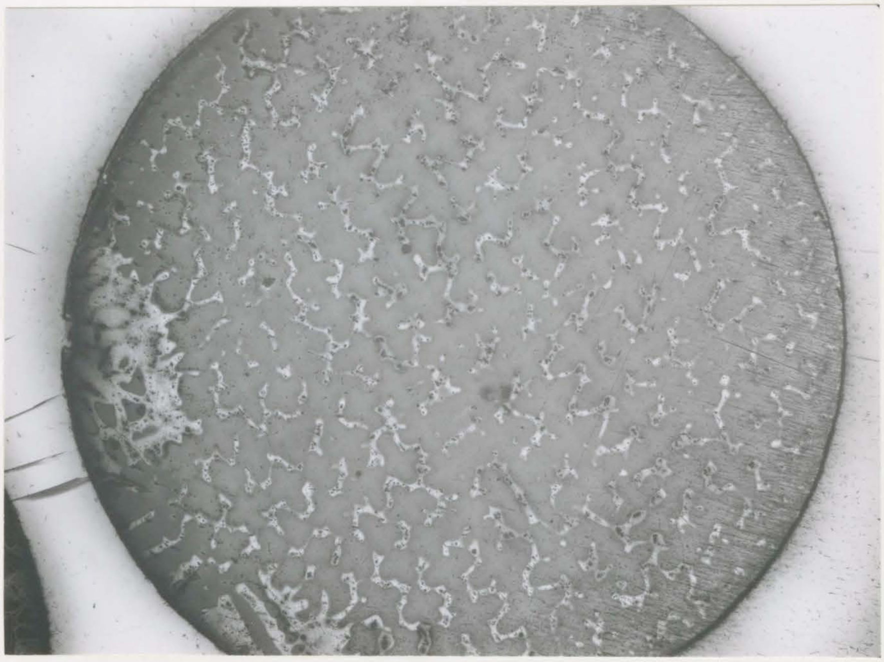

FIGURE 6.3.18 Same Specimen and Growth Conditions as Above, but Different Cross-Section.

FIGURE 6.3.19 Specimen 25. Fe-13 wt% Mn - 0.25 wt% ZrO_2. Growth Rate : 100 mm/hr. Parallel Section. Sulphide Tint. X20.

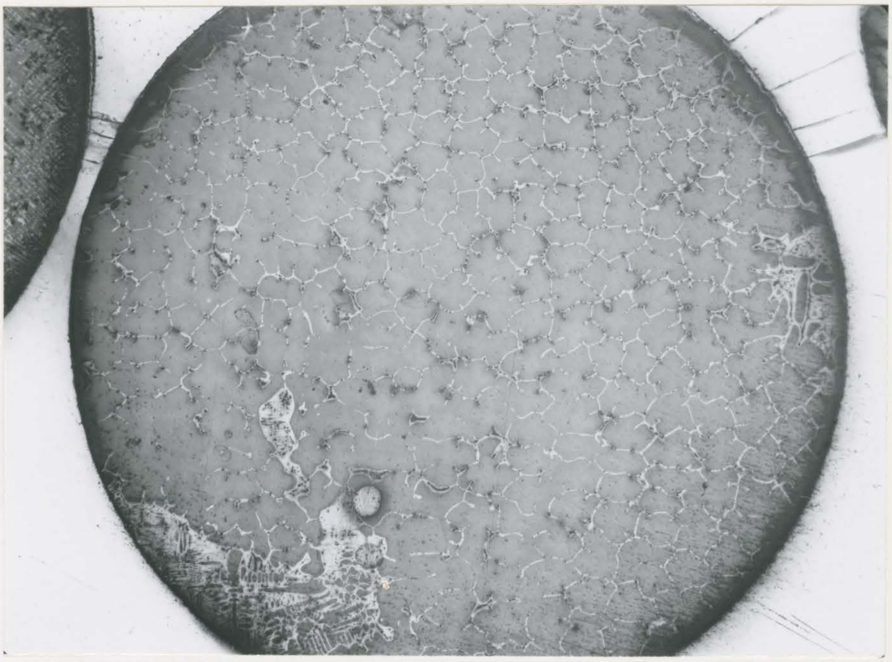

FIGURE 6.3.20 Specimen 25. Fe-13 wt% Mn-0.25 wt% ZrO_2. Normal Section of Transient State Region. Sulphide Tint. X20.

FIGURE 6.3.21 Specimen 25. Fe-13 wt% Mn-0.25 wt% ZrO_2. Normal Section in Quenched Liquid Ahead of Solid-Liquid Interface. Sulphide Tint. X20.

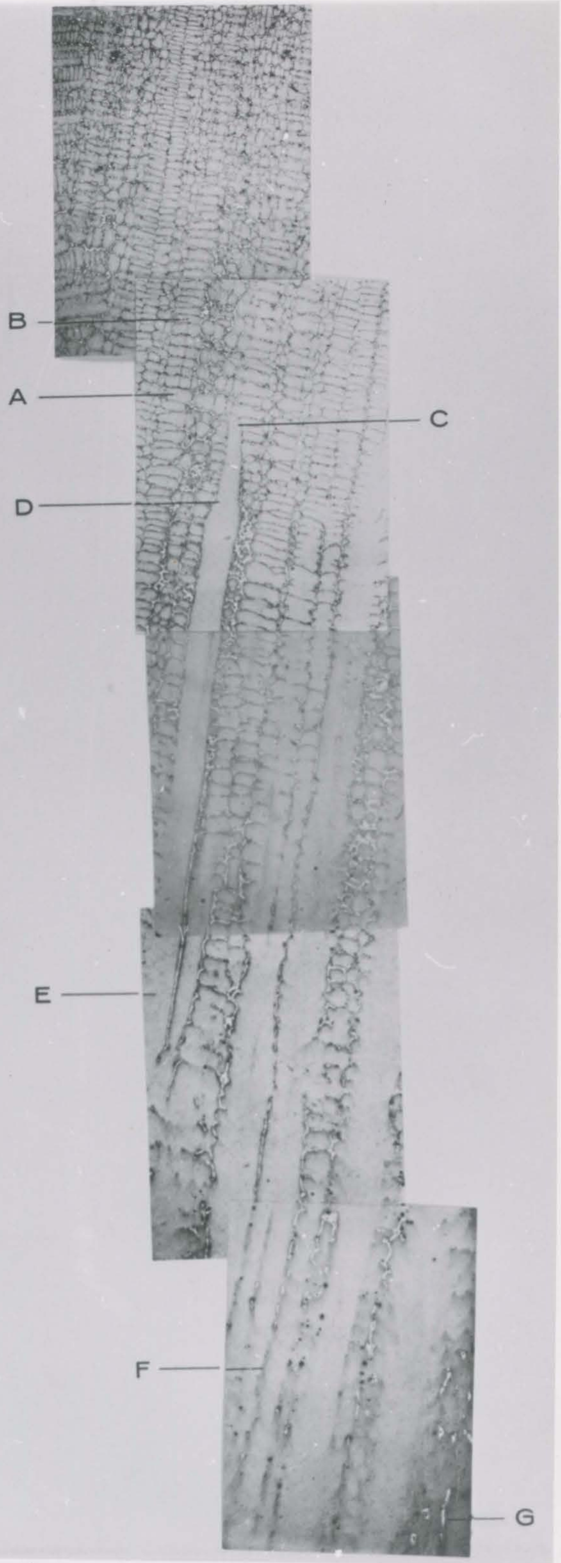

FIGURE 6.3.22 Specimen 9. Fe-13 wt% Mn-0.25 wt% S. Growth Rate: 50 mm/hr. Section Parallel to Macroscopic Growth Direction near Final Position of Primary Arm Tips. The Quenched Liquid Is at the Top (Note Horizontal Dendrites at Top Left) and the Region Solidified under Controlled Conditions at the Bottom. Sulphide Tint. X15.

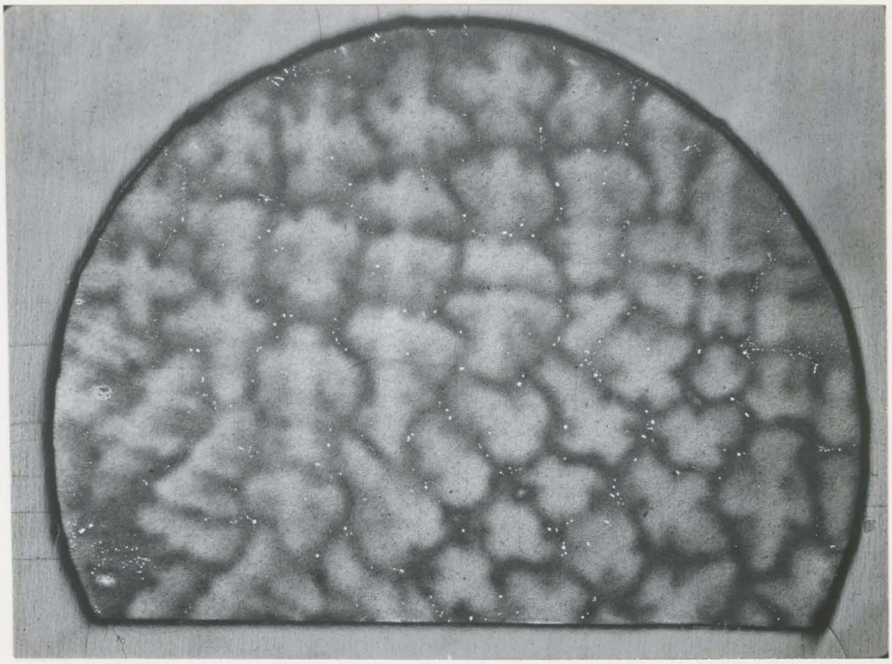

FIGURE 6.3.23 Specimen 9. Fe-13 wt% Mn-0.25 wt% S. Growth Rate: 50 mm/hr. Normal Section of Region Below Point G in Figure 6.3.22. Sulphide Tint. X20.

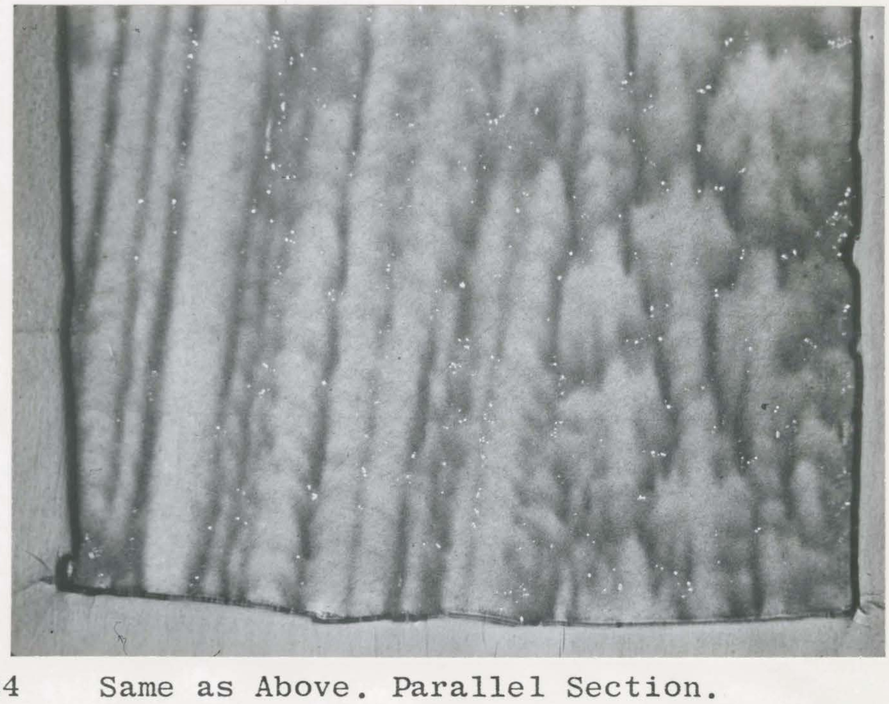

FIGURE 6.3.24 Same as Above. Parallel Section.

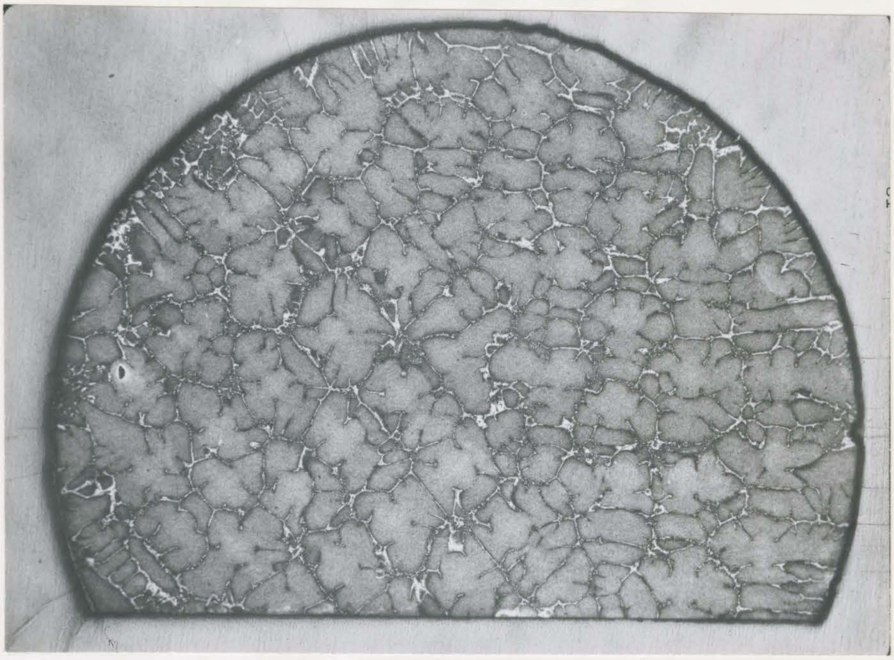

FIGURE 6.3.25 Specimen 9. Fe-13 wt% Mn-0.25 wt% S. Normal Section at the Level of Point C in Figure 6.3.22. Sulphide Tint. X20.

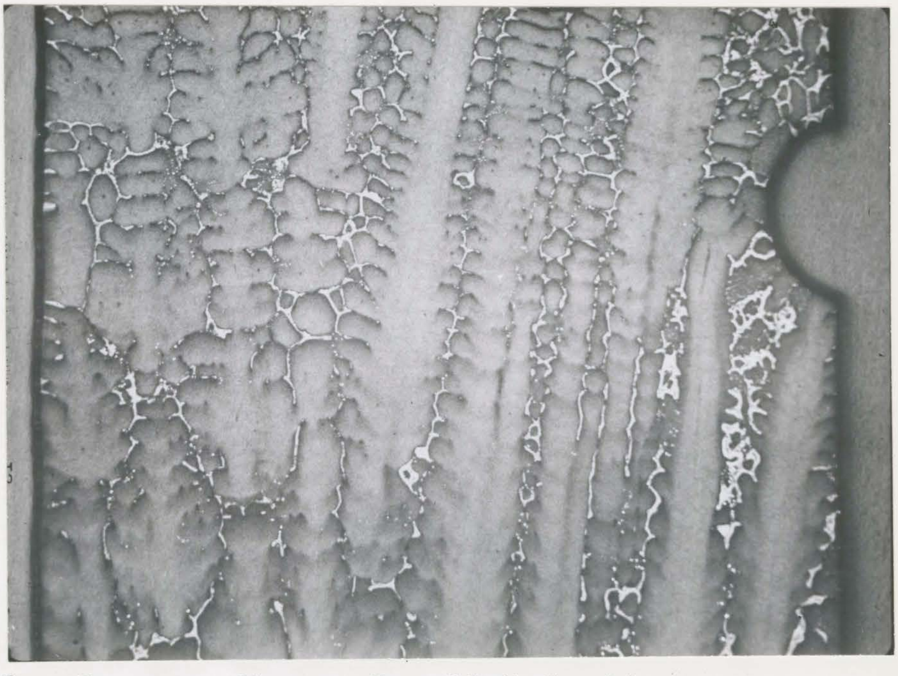

FIGURE 6.3.26 Same as Above. Parallel Section.

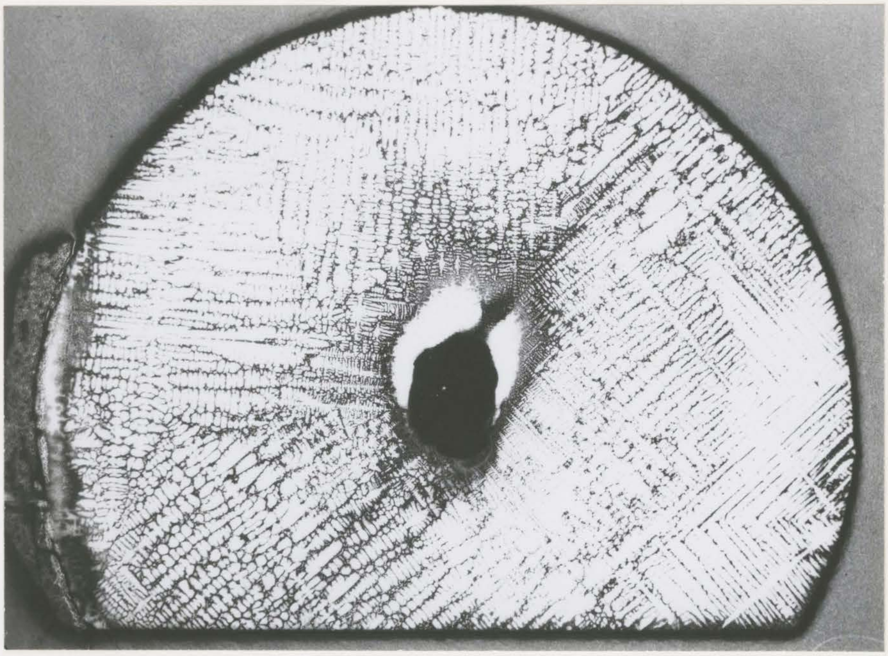

FIGURE 6.3.27 Specimen 9. Fe-13 wt% Mn-0.25 wt% S. Normal Section of Quenched Liquid Region. Sulphide Tint. X20.

FIGURE 6.3.28 Same as Above. Parallel Section.

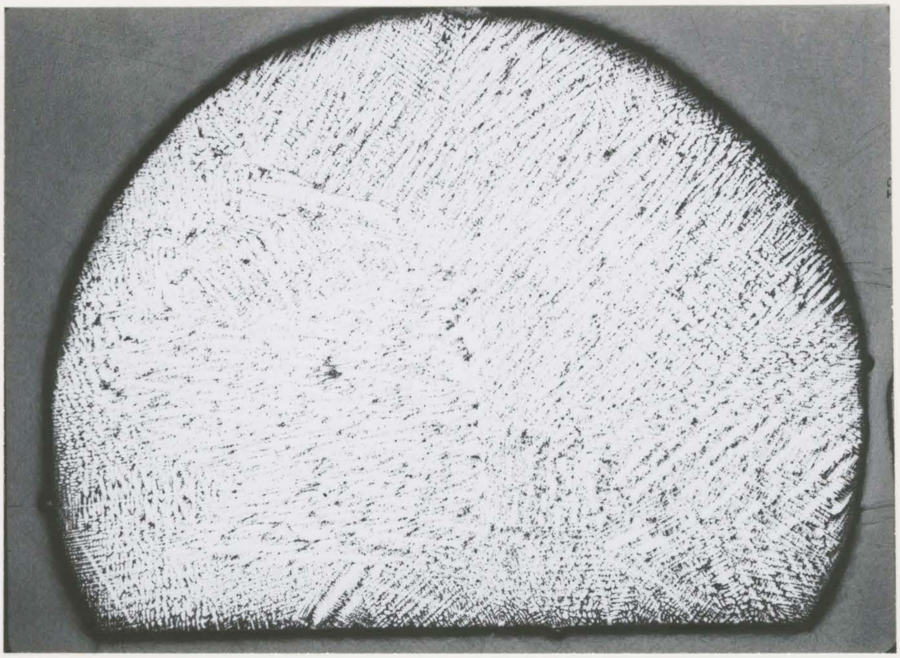

FIGURE 6.3.29 Specimen 9. Fe-13 wt% Mn-0.25 wt% S. Normal Section of Quenched Liquid Region. Sulphide Tint. X20.

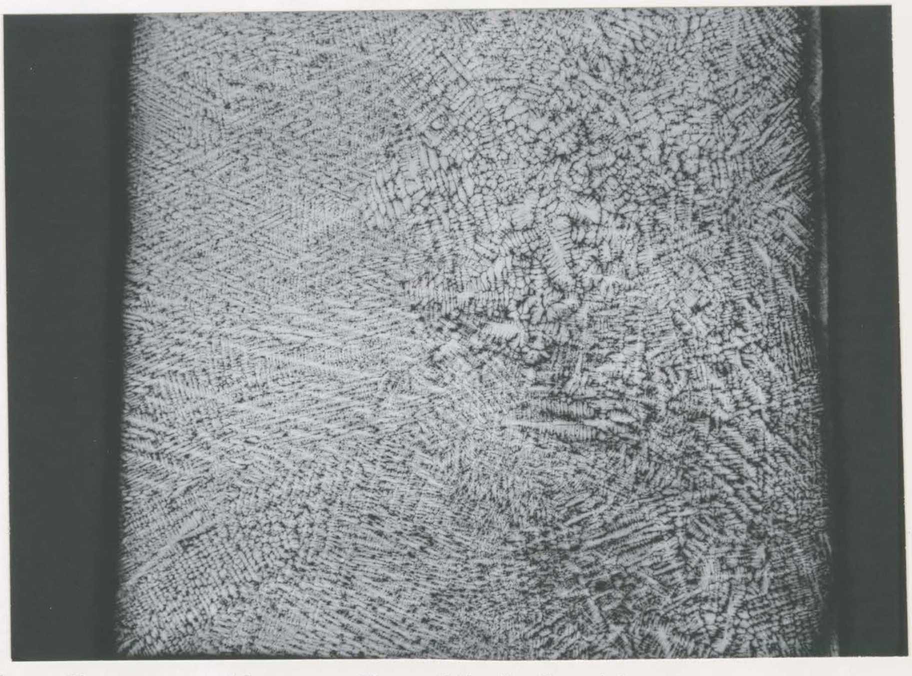

FIGURE 6.3.30 Same as Above. Parallel Section.

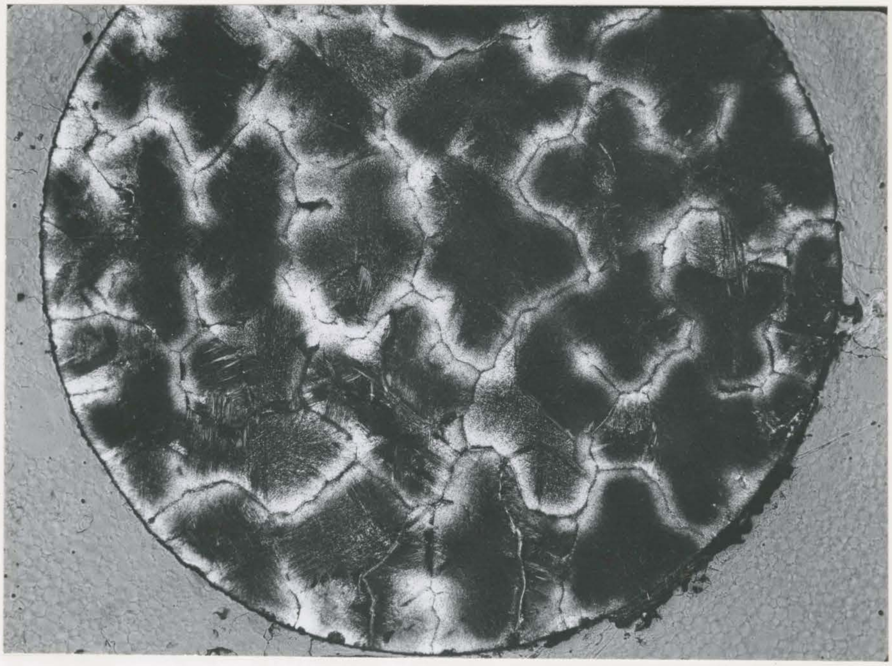

FIGURE 6.3.31 Specimen 23. Fe-0.03 wt% S-0.4 wt% C. Section Normal to Growth Direction. Quenched Liquid Region Located 2 cm Ahead of the Final Solid-Liquid Interface. The Dendrite Cores Contain Martensite and the Interdendritic Region, Martensite, Retained Austenite and Iron Sulphide Films. Nital Etch. X20.

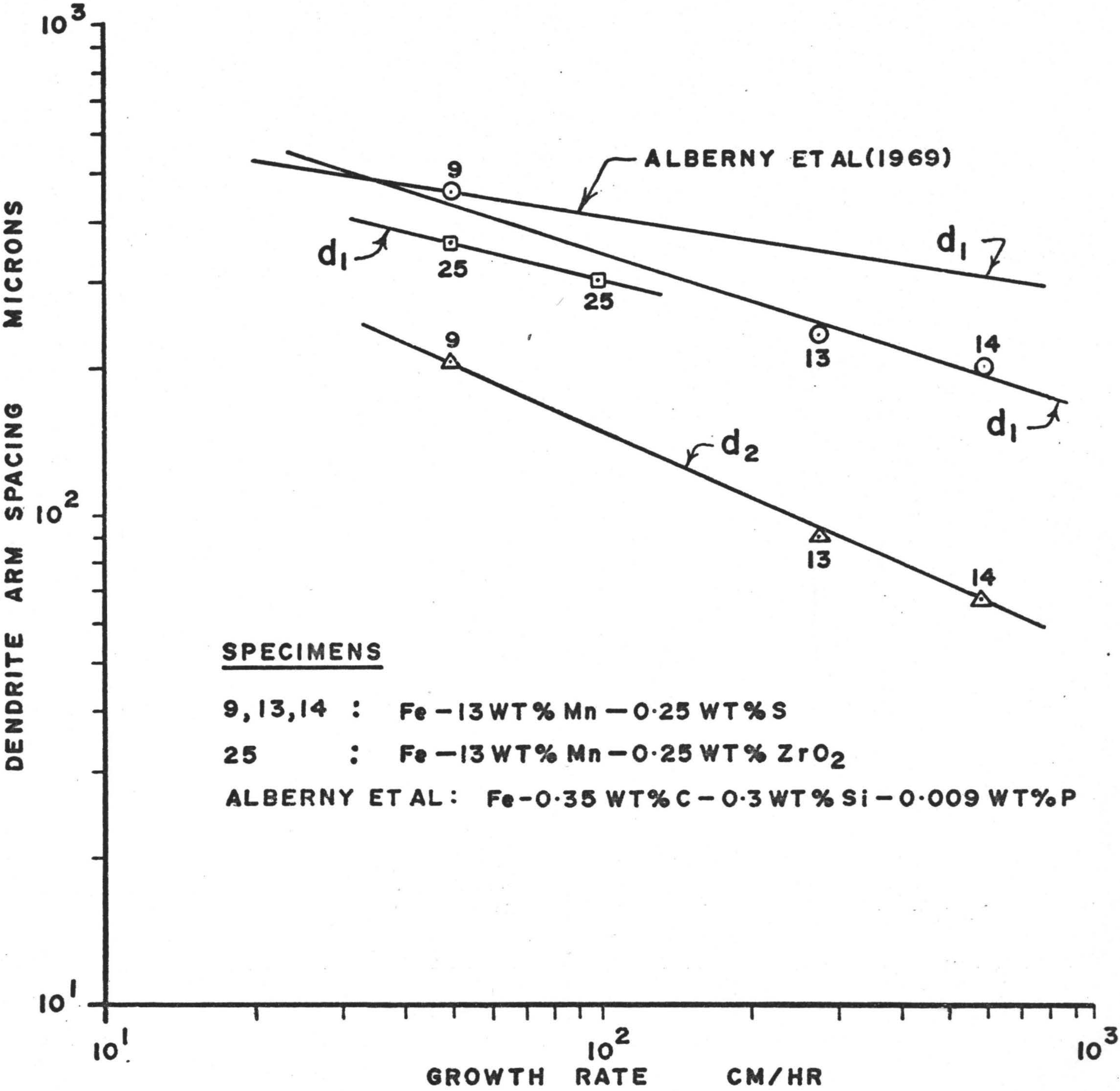

FIGURE 6.3.32 Relationships Between Primary and Secondary Dendrite Arm Spacings (d_1 and d_2) and Growth Rate for Various Iron-Base Alloys.

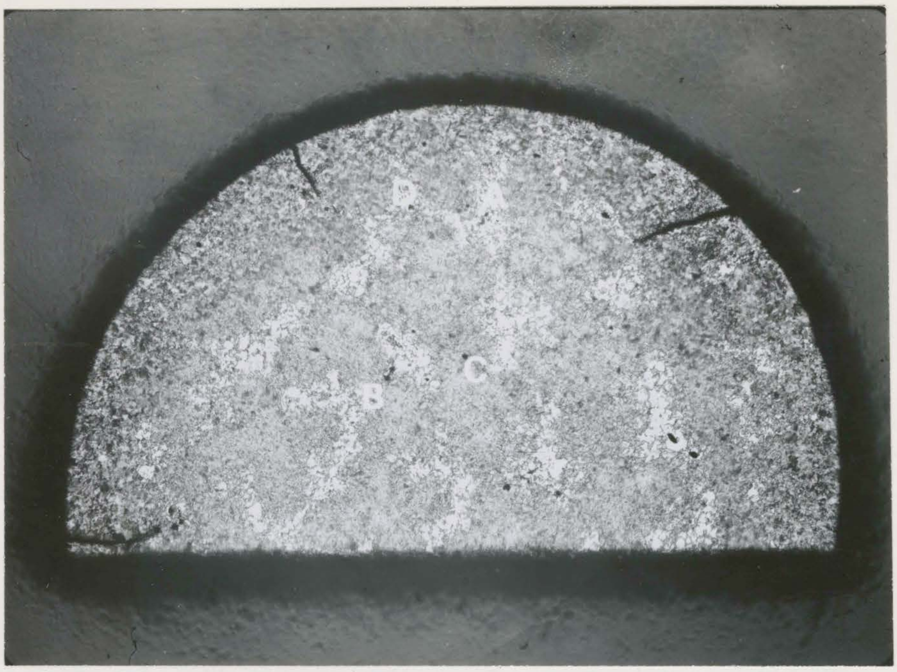

FIGURE 6.3.33-a Cross-Section of Specimen 6. X20.
1000 microns = ├──────┤

FIGURE 6.3.33-b Distribution of Manganese along a
[x] Path (A⟶B) and a [+] Path (C⟶D).

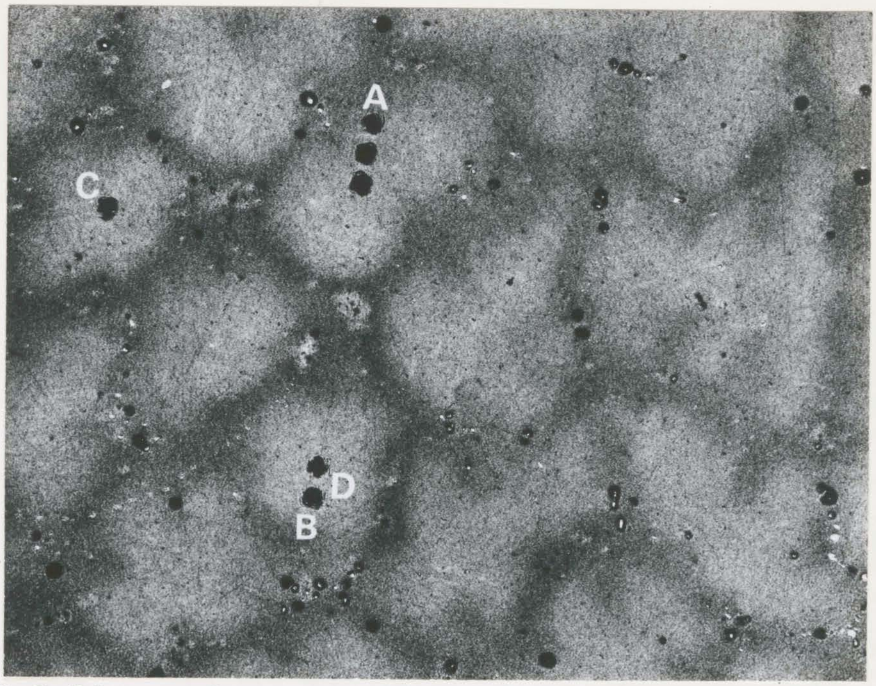

FIGURE 6.3.34-a Cross-Section of Specimen 9. X50.
100 microns = ⊢⊣

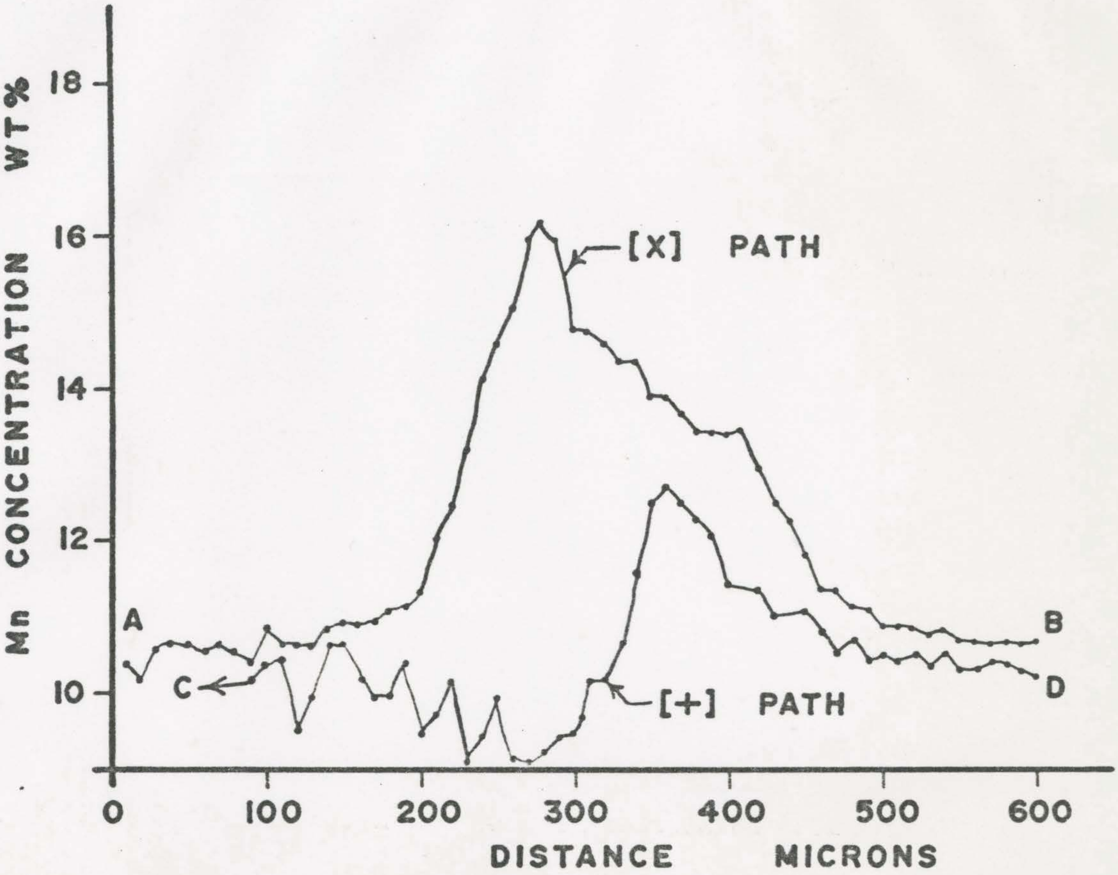

FIGURE 6.3.34-b Distribution of Manganese along a [x] Path (A⟶D) and a [+] Path (C⟶D).

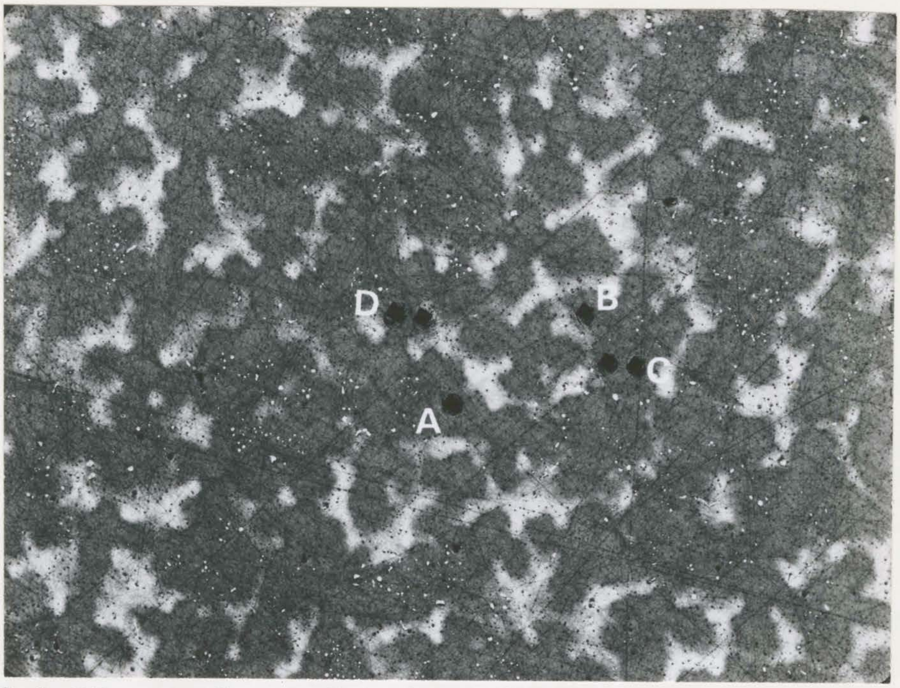

FIGURE 6.3.35-a Cross-Section of Specimen 13. X50. 100 microns = ⊢⊣

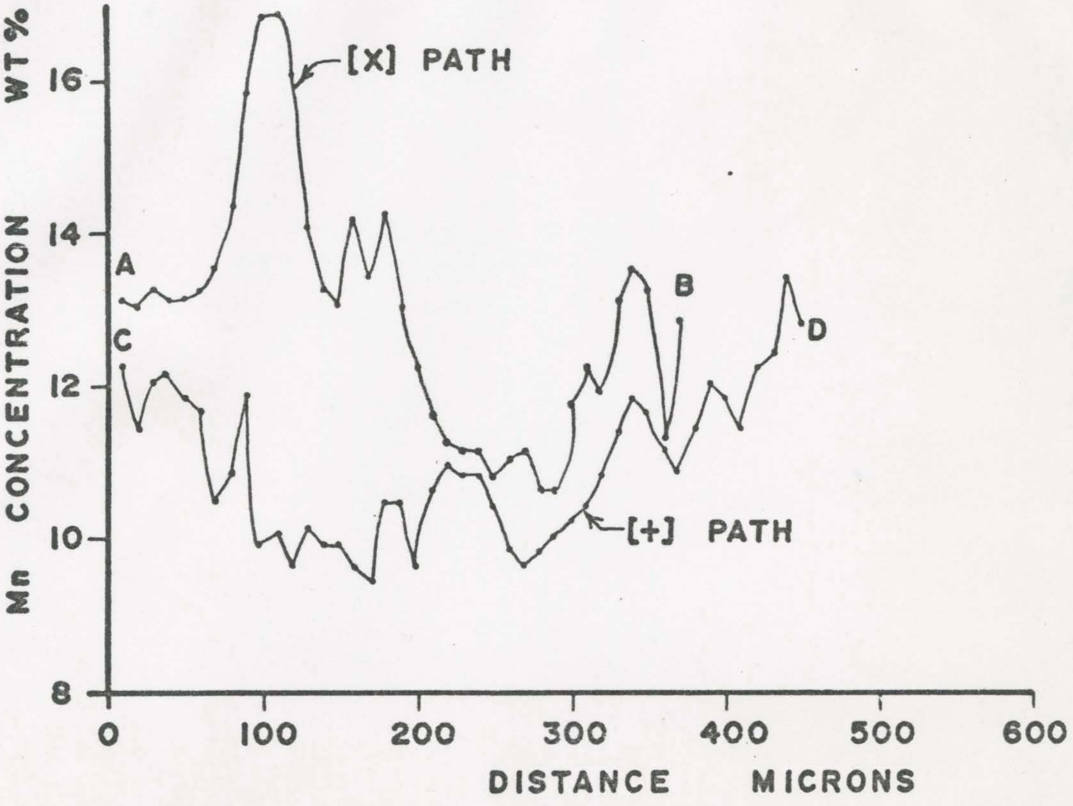

FIGURE 6.3.35-b Distribution of Manganese Along a [x] Path (A ⟶ B) and a [+] Path (C ⟶ D).

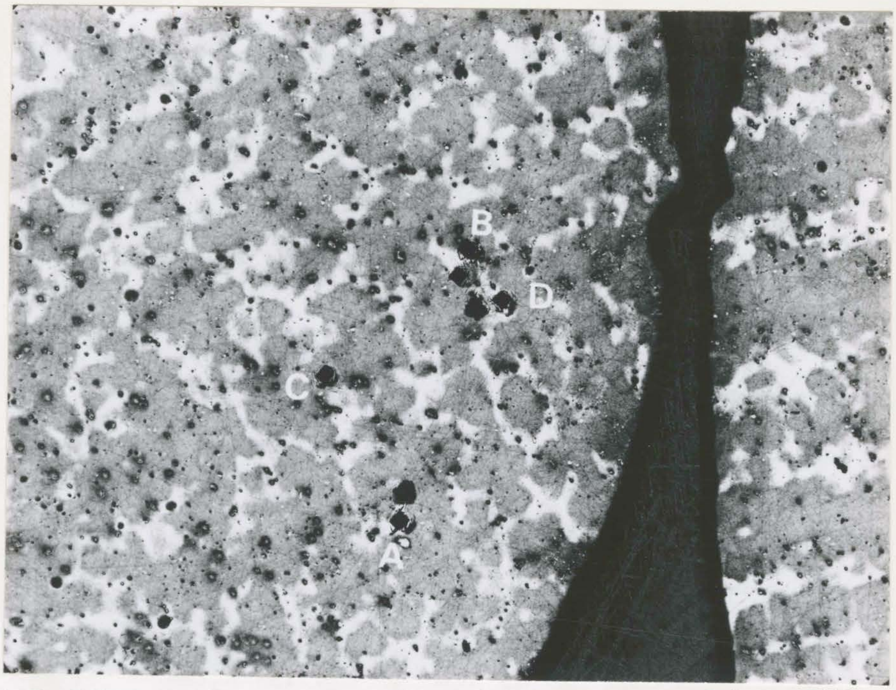

FIGURE 6.3.36-a Cross-Section of Specimen 14. X50.
100 microns = ⊢—⊣

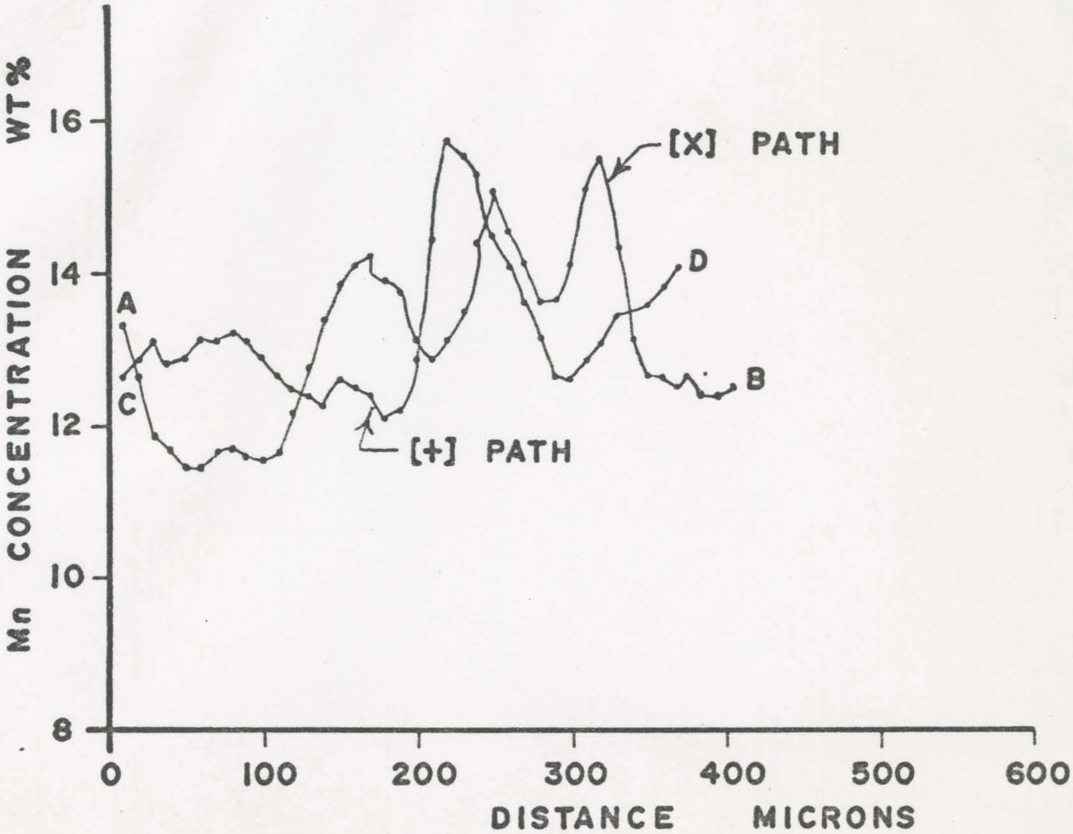

FIGURE 6.3.36-b Distribution of Manganese Along a [X] Path (A → B) and a [+] Path (C → D)

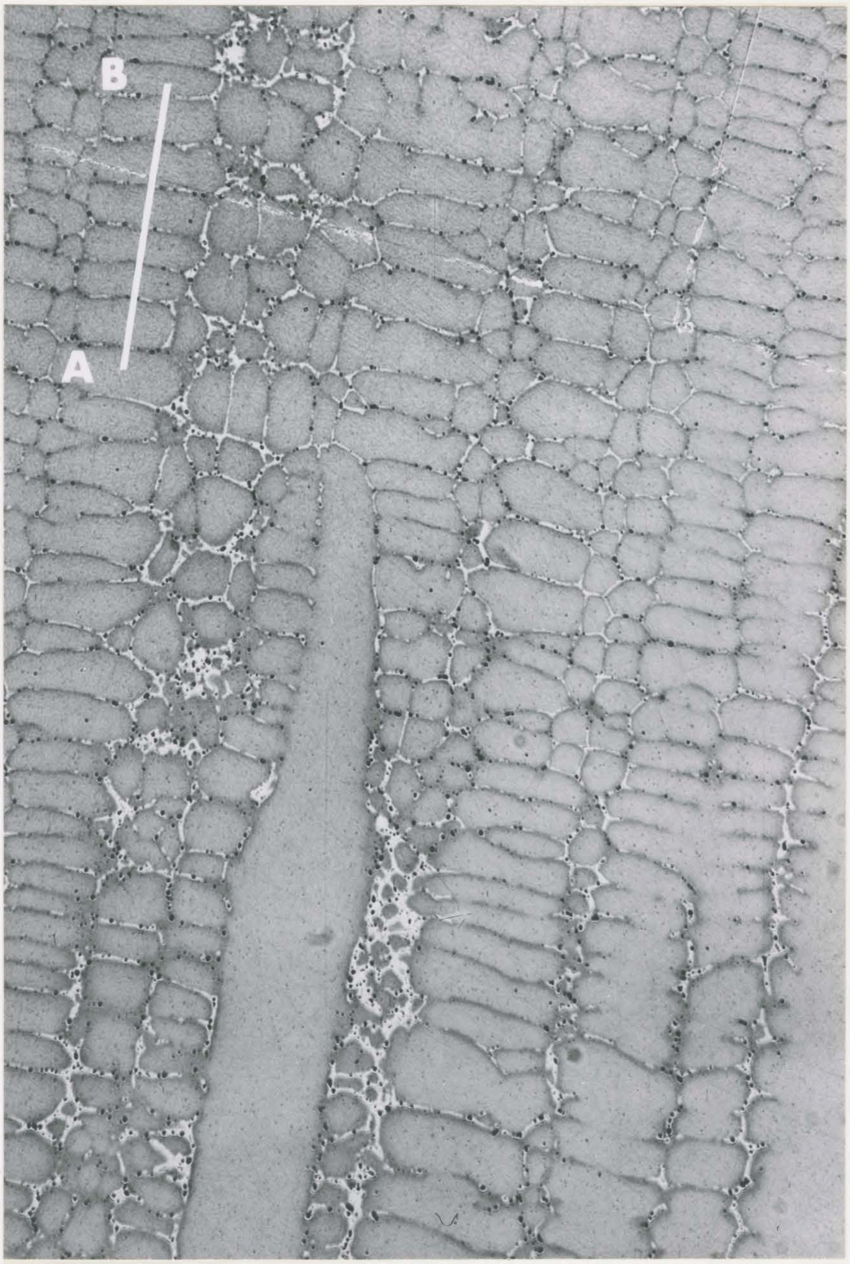

FIGURE 6.3.37 Micrograph Shows Dendrite Arms in the Vicinity of Primary Arm Tips Just Prior to Quenching. The Electron Probe Trace A-B for Microanalysis of Mn Is Also Indicated. Section Parallel to Growth Direction. Sulphide Tint. X45.

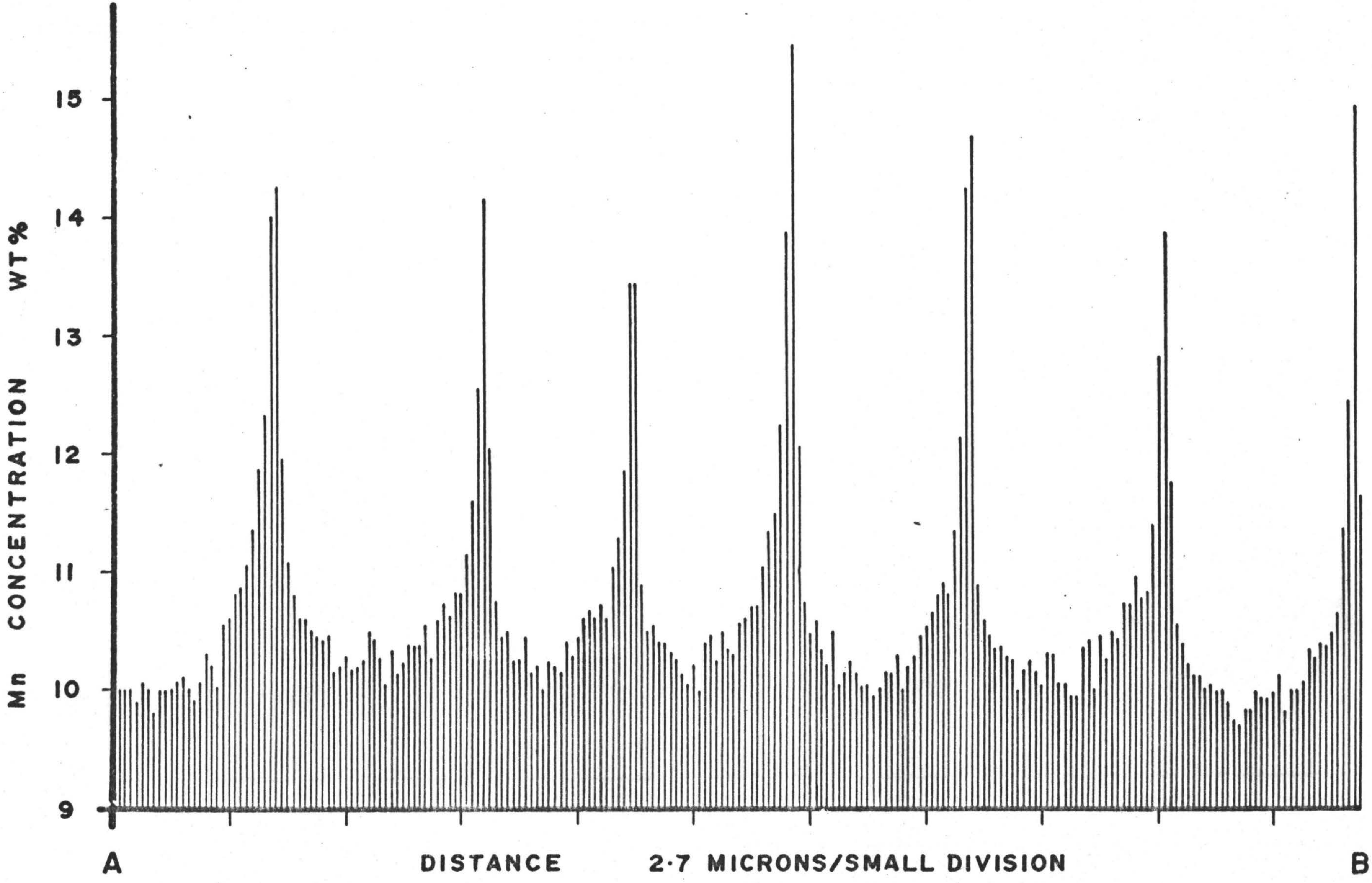

FIGURE 6.3.38 Manganese Segregation in Group of Cells Marked in Figure 6.3.37. Note the Brace-like $\underbrace{\hphantom{xxxx}}$ Distribution of Mn.

FIGURE 6.4.1 Specimen 12. Inclusions in Cell Boundaries. No Sulphur Was Detected. Longitudinal Section. Unetched. X200.

FIGURE 6.4.2 Specimen 10. (Fe, Mn) (S, O) Inclusions. Longitudinal Section. Unetched. X200.

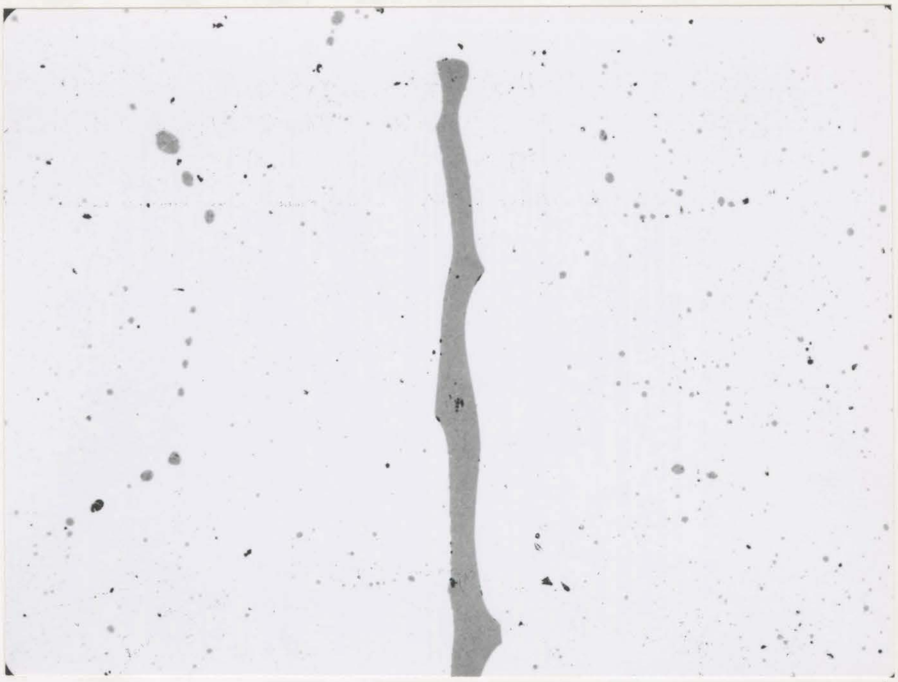

FIGURE 6.4.3 Specimen 10. (Fe, Mn) (S, O) Inclusions. Longitudinal Section. Unetched. X200.

FIGURE 6.4.4 Specimen 1. (Fe, Mn) (S, O) Inclusions. Longitudinal Section. Unetched. X200.

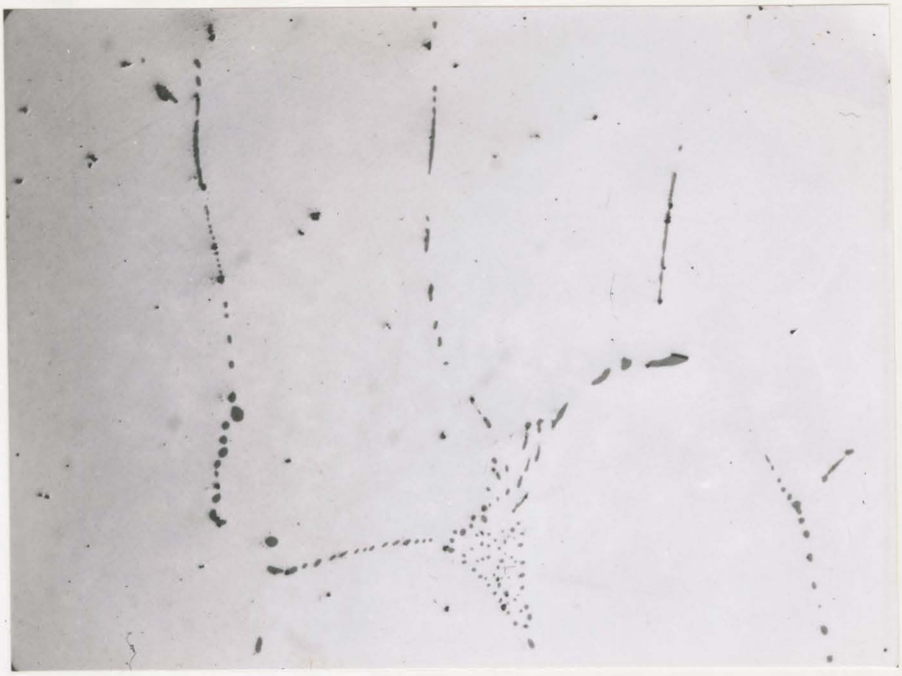

FIGURE 6.4.5 Specimen 2. Formation of MnS Inclusions in Steady-State Region. Unetched. X200.

FIGURE 6.4.6. Specimen 2. "Sinusoidal" MnS Inclusions in Steady-State Region. Unetched. X800.

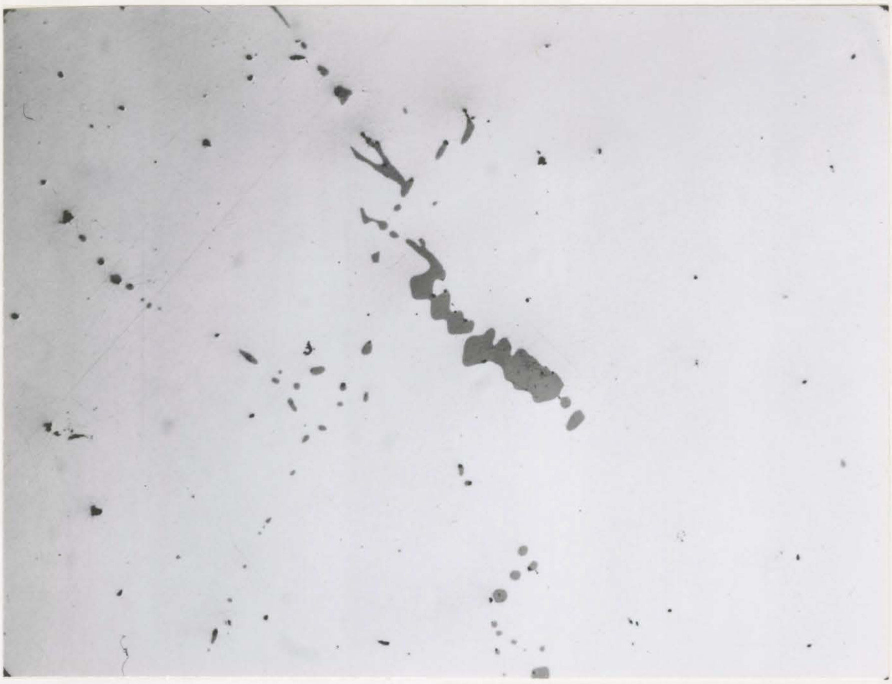

FIGURE 6.4.7 Specimen 2. "Sinusoidal" MnS Inclusions Near Initial Position of Solid-Liquid Interface. Unetched. X200.

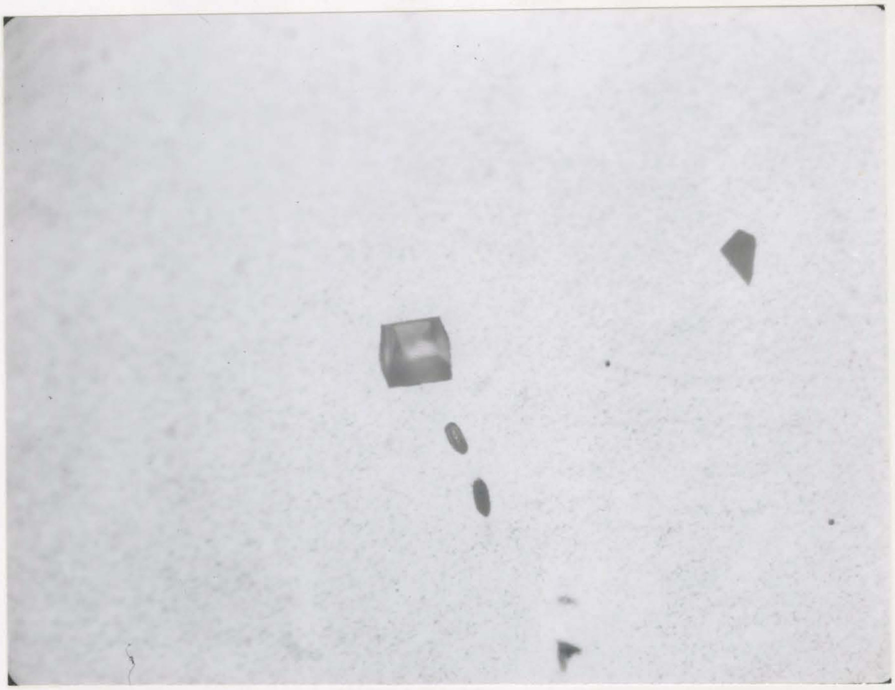

FIGURE 6.4.8 Specimen 5. Translucent Angular Inclusions. Longitudinal Section. Unetched. X800.

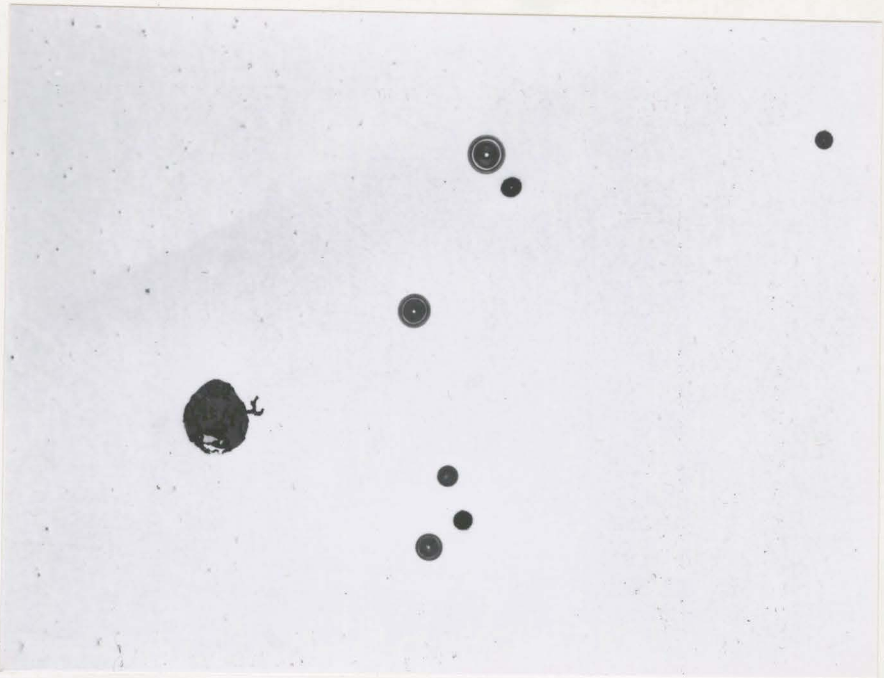

FIGURE 6.4.9 Specimen 5. Translucent and Opaque Inclusions. Longitudinal Section. Unetched. X200.

FIGURE 6.4.10 Specimen 6. Typical Angular and Isolated MnS Inclusion. Unetched. X200.

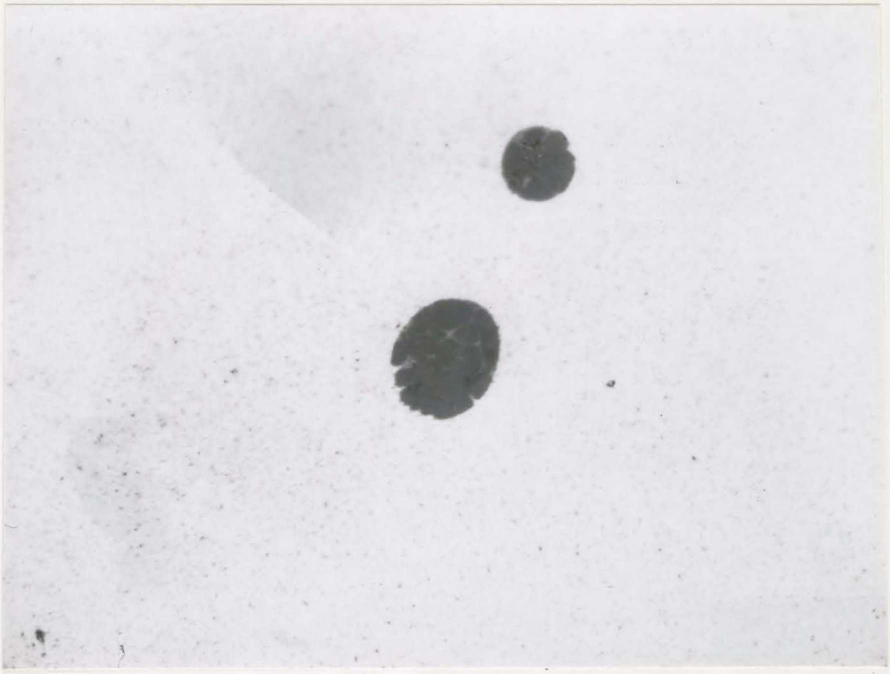

FIGURE 6.4.11 Specimen 7. (Fe, Mn) (S, O) Duplex Inclusions. Longitudinal Section. Unetched. X800.

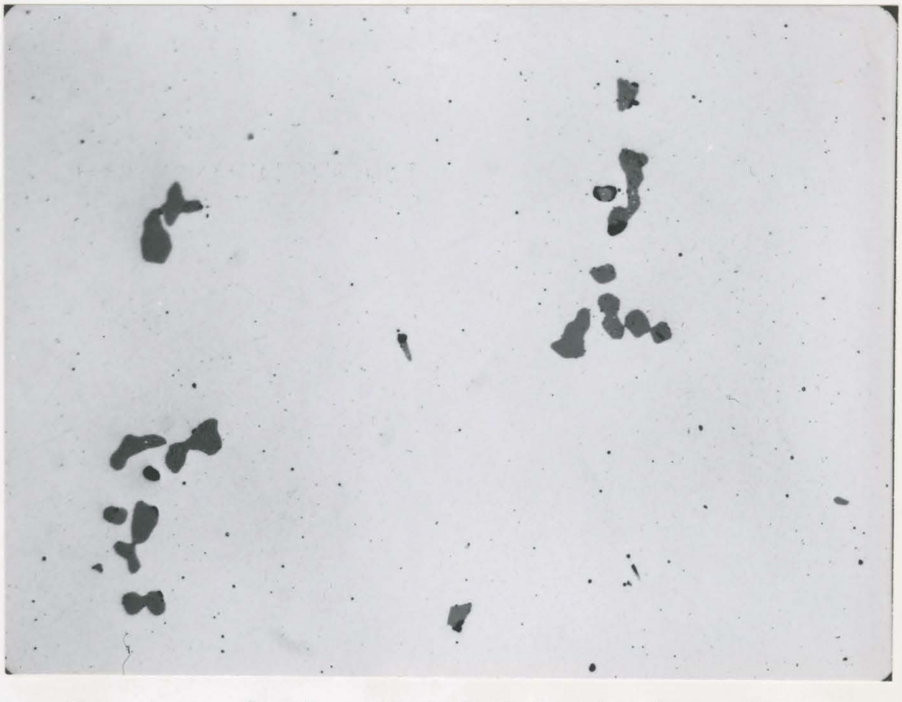

FIGURE 6.4.12 Specimen 9. Faceted MnS Inclusions Near Initial Position of Solid-Liquid Interface. Unetched. X200.

FIGURE 6.4.13 Specimen 9. Detail of MnS Inclusion Near Initial Position of Solid-Liquid Interface. Unetched. X800.

FIGURE 6.4.14 Specimen 9. MnS Inclusions in Region Immediately Below Initial Position of Solid-Liquid Interface. The Inclusions Are Relatively Numerous and Small, and Elongated in the Direction of Mechanical Working. Unetched. X200.

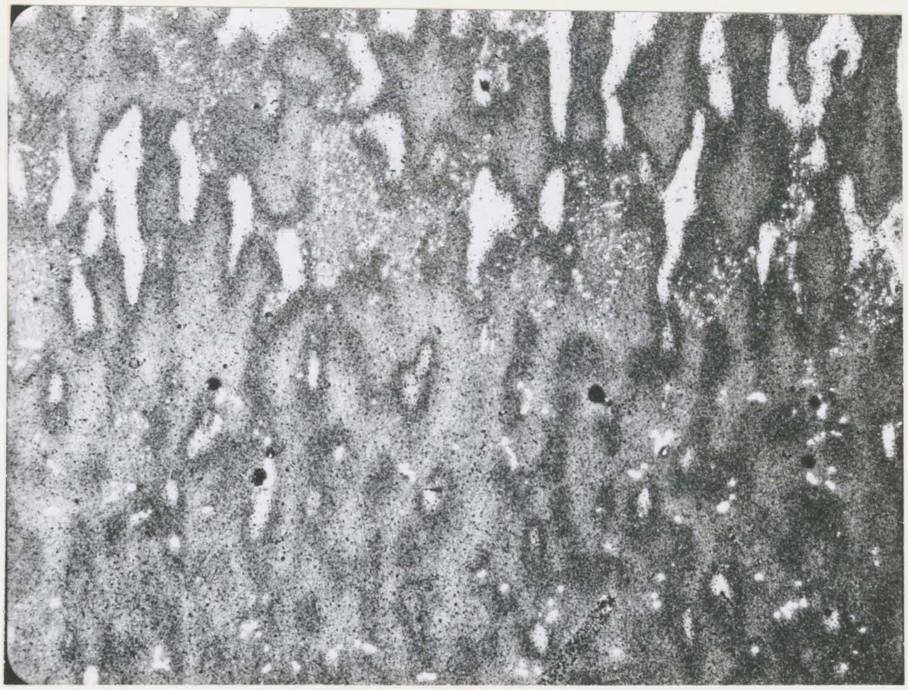

FIGURE 6.4.15 Specimen 13. MnS Inclusions and Segregation Pattern Near Original Position of Interface. Sulphide Tint. X50.

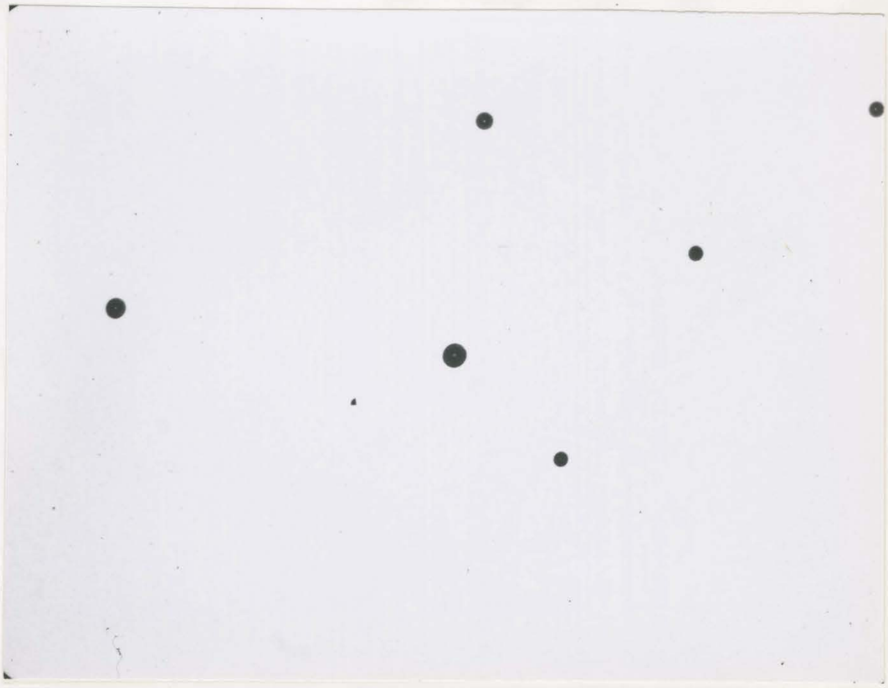

FIGURE 6.4.16 Specimen 12. Translucent Inclusions Containing Iron and Oxygen, but no Manganese or Sulphur. Longitudinal Section. Unetched. X200.

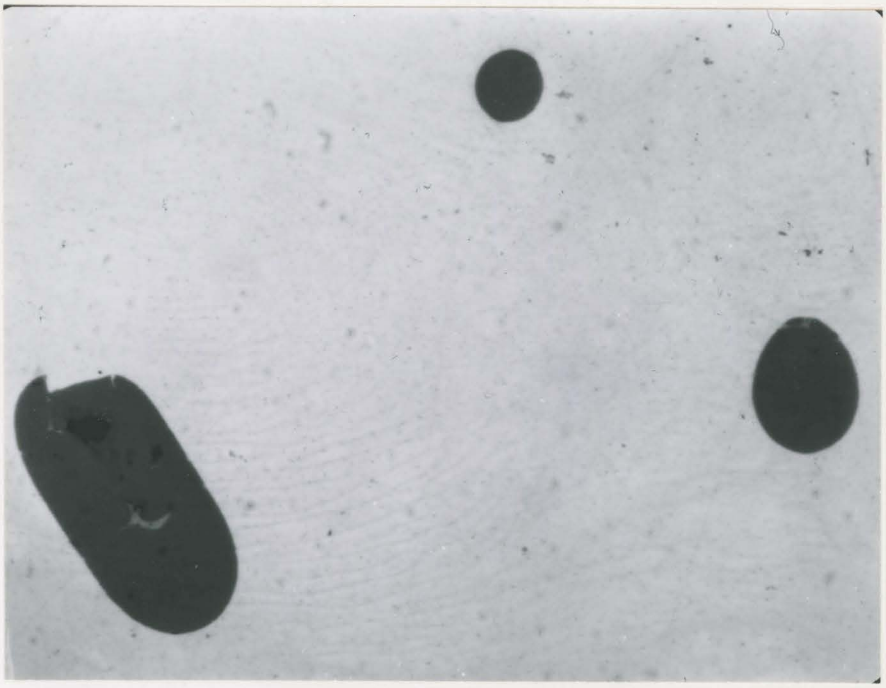

FIGURE 6.4.17 Specimen 1. Fe-3 wt% Mn-0.005 wt% S Alloy. Duplex Inclusions. Unetched. X1000.

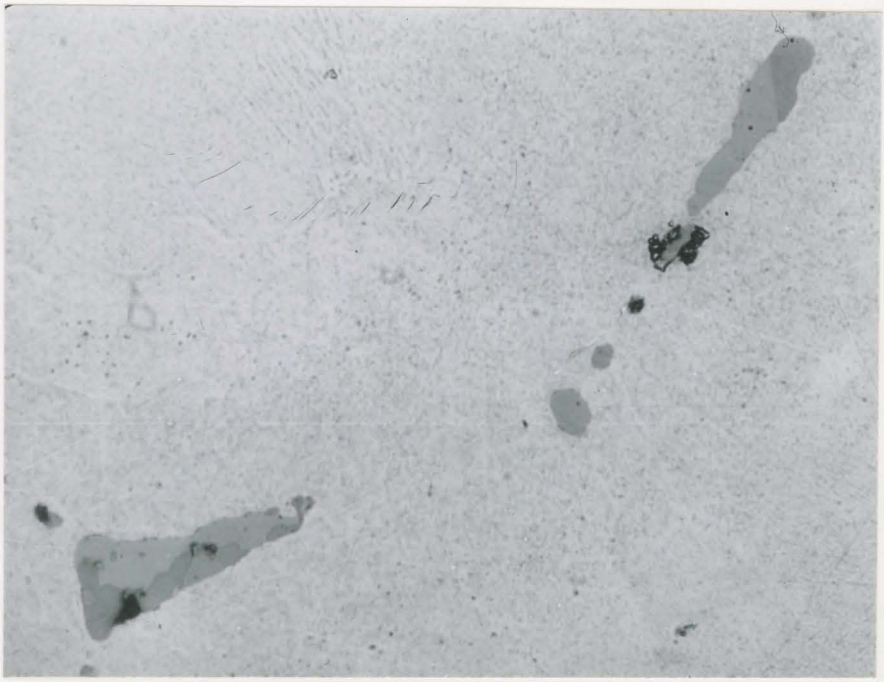

FIGURE 6.4.18 Specimen 2. Fe-0.5 wt% Mn-0.03 wt% S-0.4 wt% C Alloy. Duplex Inclusions. Unetched. X1000.

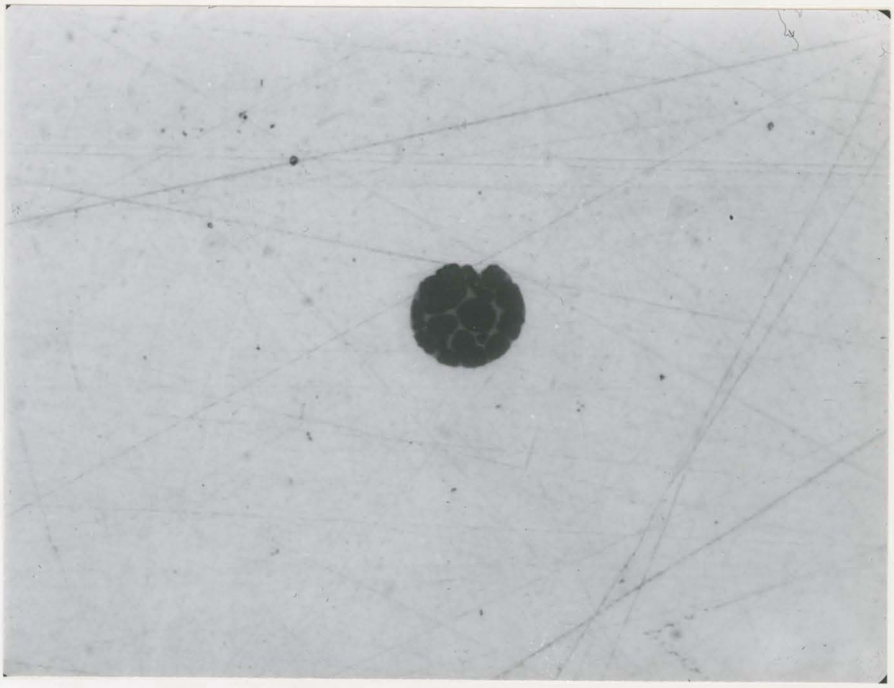

FIGURE 6.4.19 Specimen 7. Fe-3 wt% Mn-0.005 wt% S Alloy. Duplex Inclusion. Unetched. X1000.

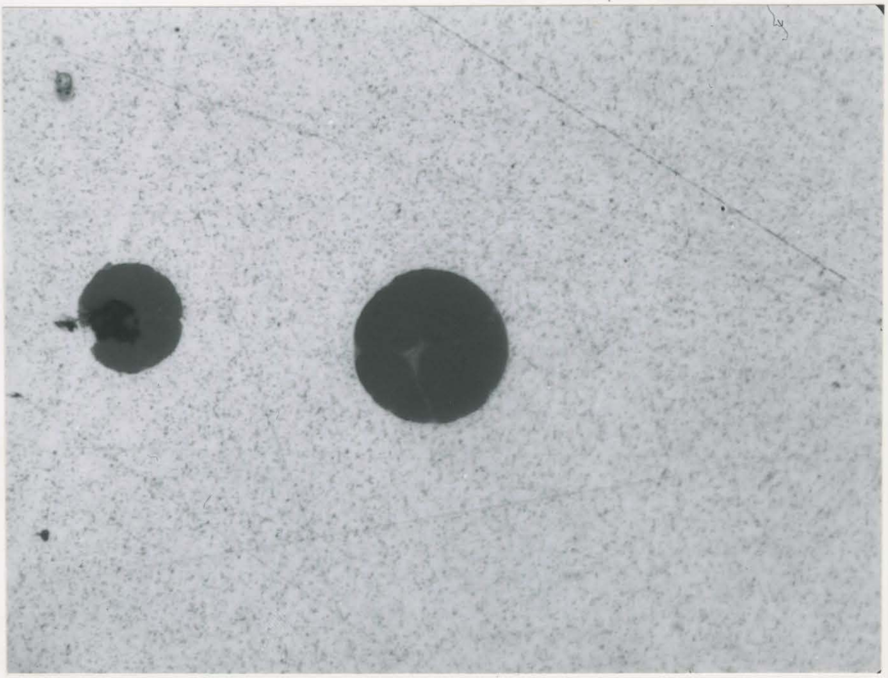

FIGURE 6.4.20 Specimen 10. Fe-0.5 wt% Mn-0.03 wt% S Alloy. Duplex Inclusions. Unetched. X1000.

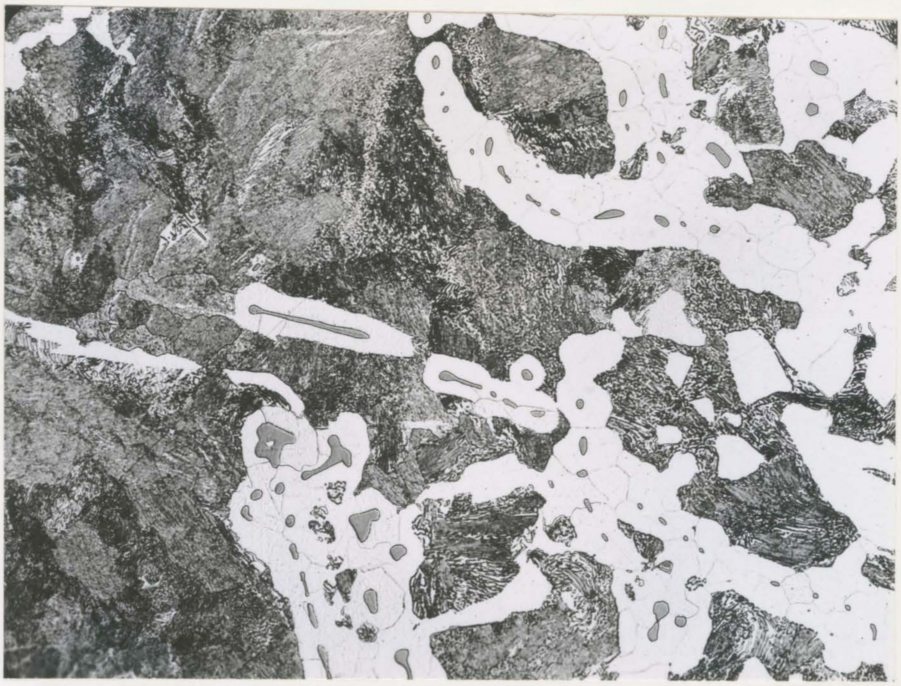

FIGURE 6.4.21 Specimen 2. Fe-0.5 wt% Mn-0.03 wt% S-0.4 wt% C Alloy. Medium Grey Inclusions Surrounded by Ferrite. Specimen Was Austenitized and Slowly Cooled. Nital Etch. X200.

FIGURE 6.4.22 Specimen 23. Fe-0.03 wt% S-0.4 wt% C Alloy. Tan-Coloured FeS Inclusion; There Is no Marked Correlation Between the Ferrite Regions (White) and the Position of the Inclusion. X400.

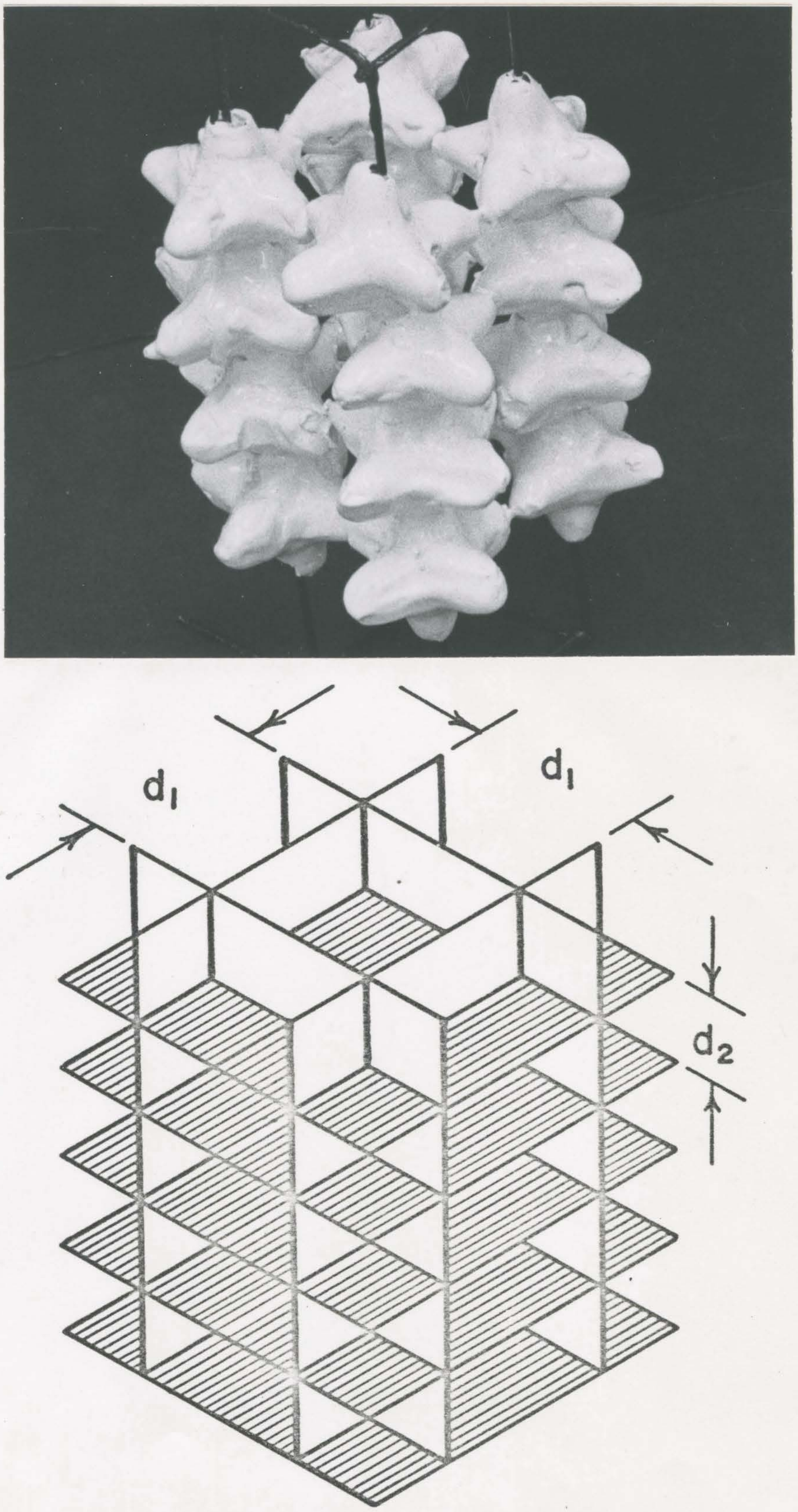

FIGURE 7.1.1 Wax Model and Isometric Sketch of Dendritic Skeleton Showing Primary and Secondary Arm Spacings d_1 and d_2 in Open Type of Structure.

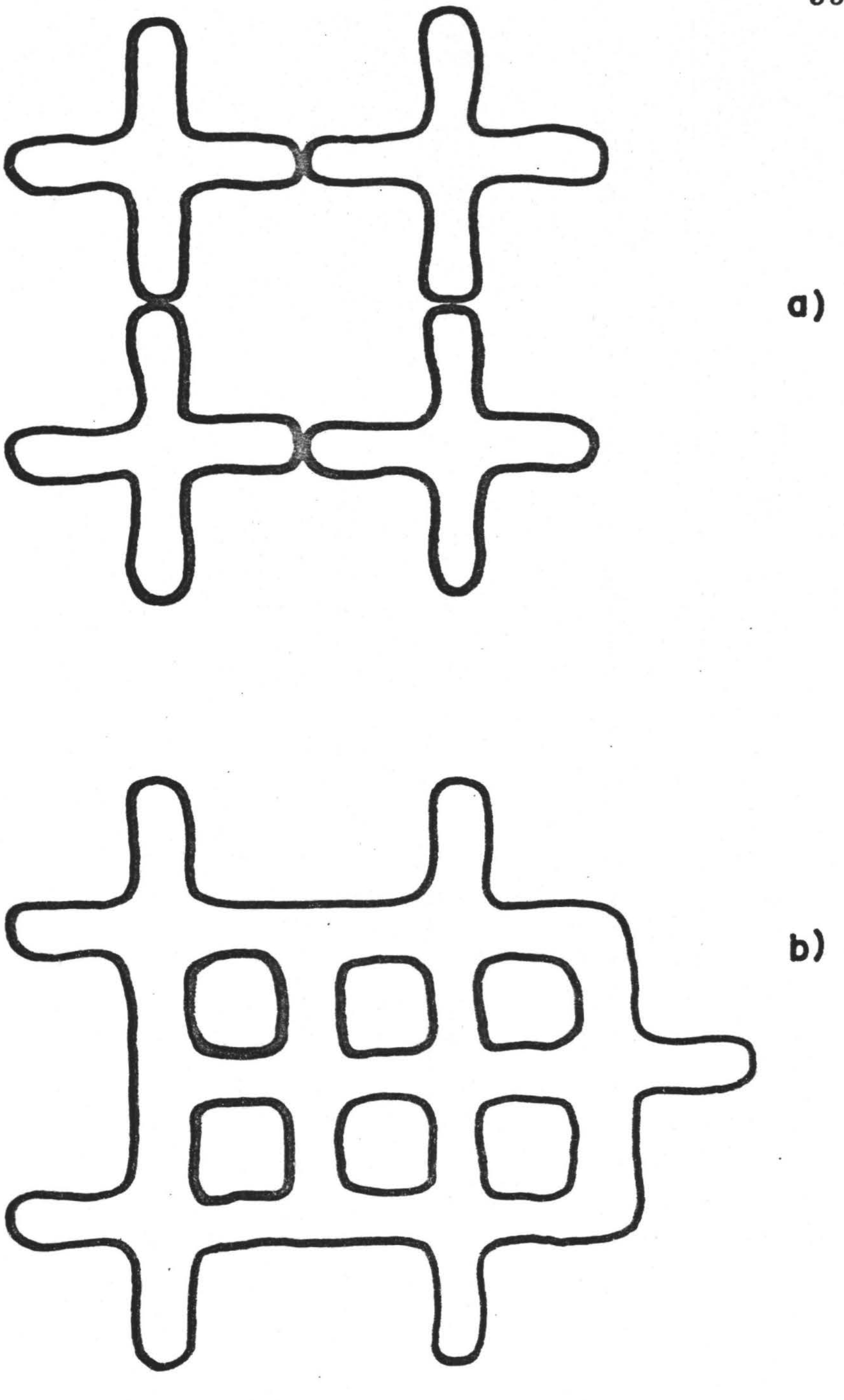

FIGURE 7.1.2 Two-Dimensional Solidification Structures. a) Open Structure b) Close-Packed Structure. The Area of a Segregation Cell in the latter Structure Is One-Quarter the Area of a Cell in the Former Structure.

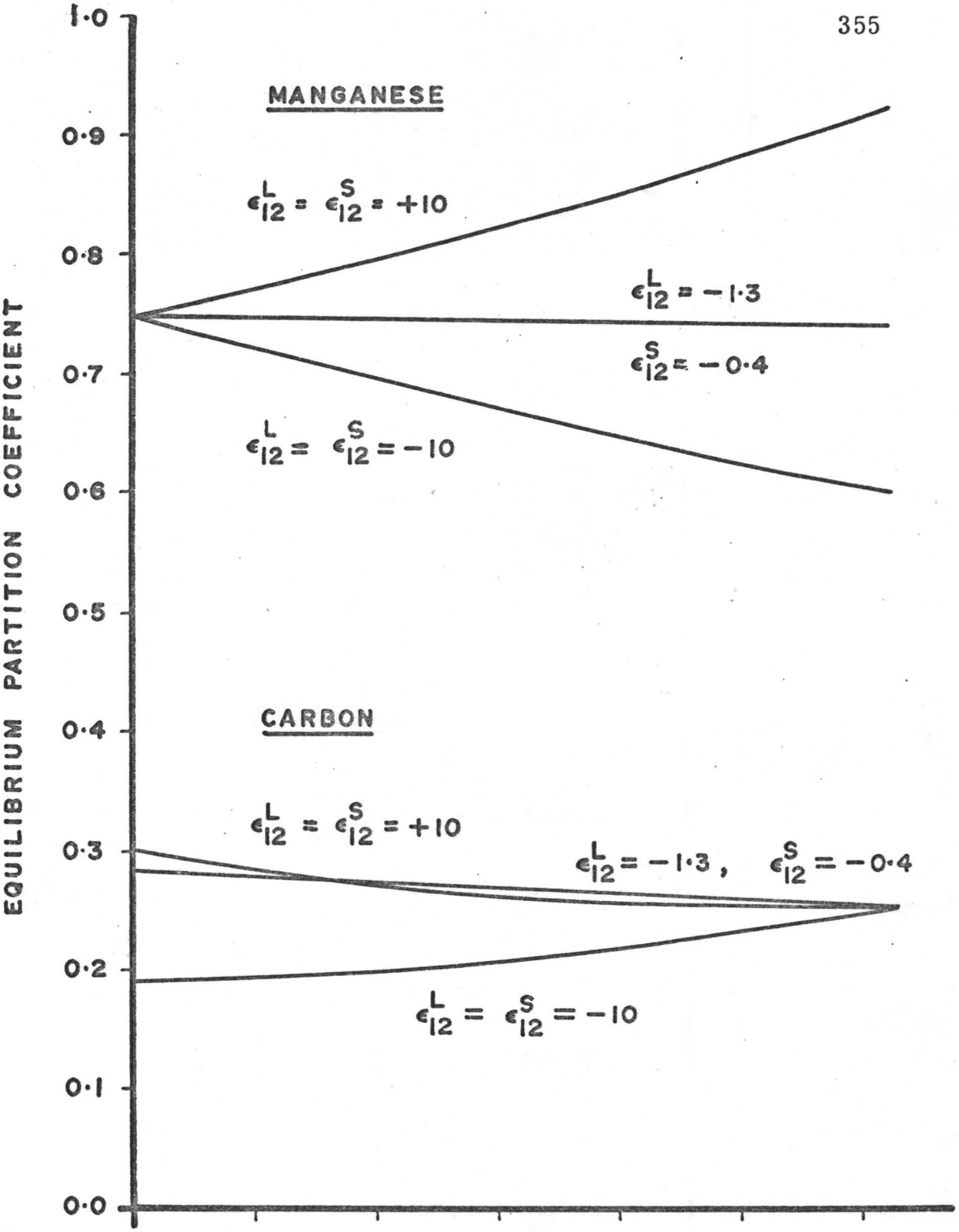

FIGURE 7.1.3 Calculated Variation of Manganese and Carbon Equilibrium Partition Coefficients with Cross-Interaction Parameters and Carbon Concentration in the γ_{Fe} + Liquid System at 1490°C.

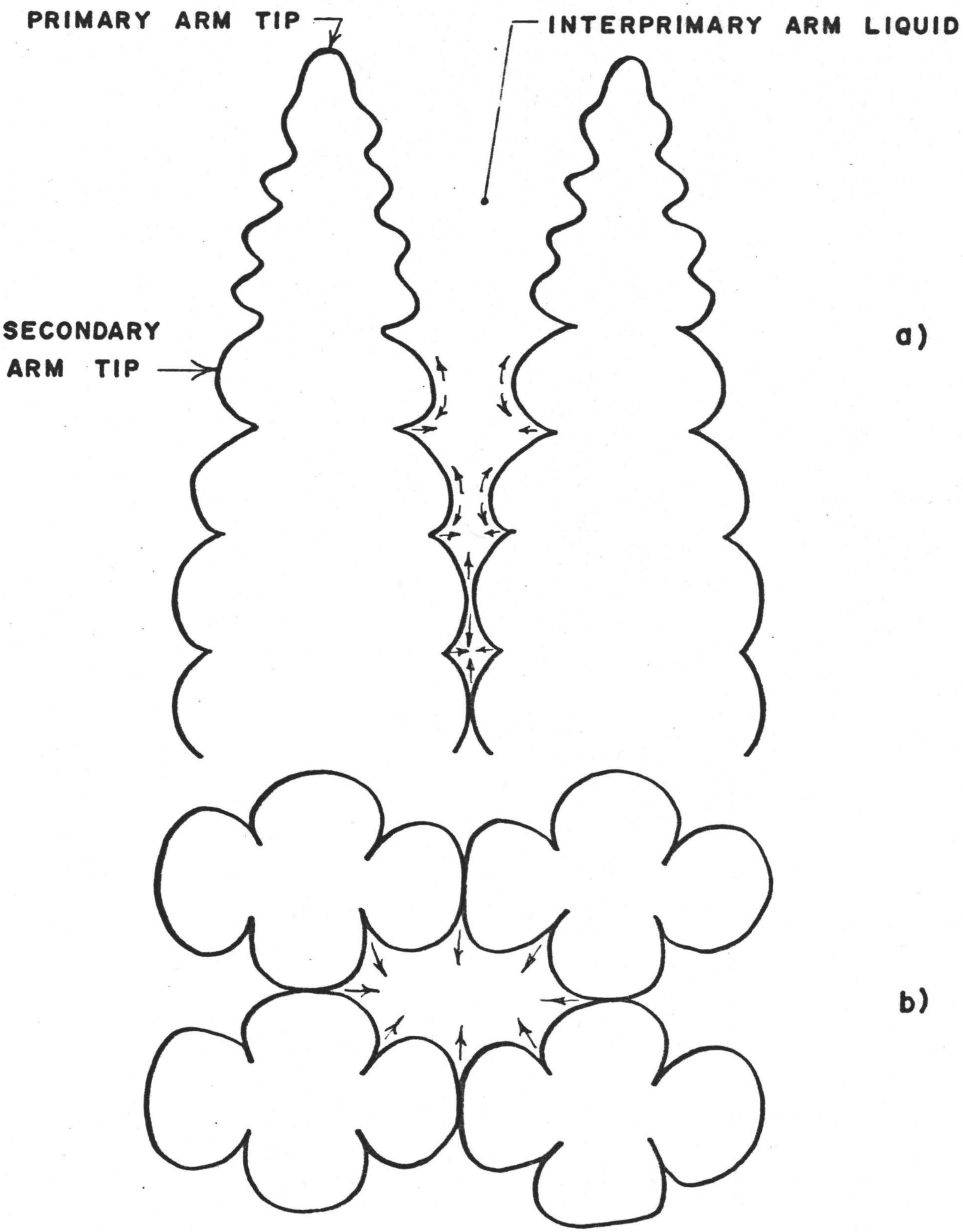

FIGURE 7.1.4 Sketch of Longitudinal Section a) and Transverse Section b) of Primary Dendrite Arms Growing into the Liquid Phase. This Sketch Corresponds Roughly to Figure 6.3.22. The Solute Flow Is Indicated by Arrows.

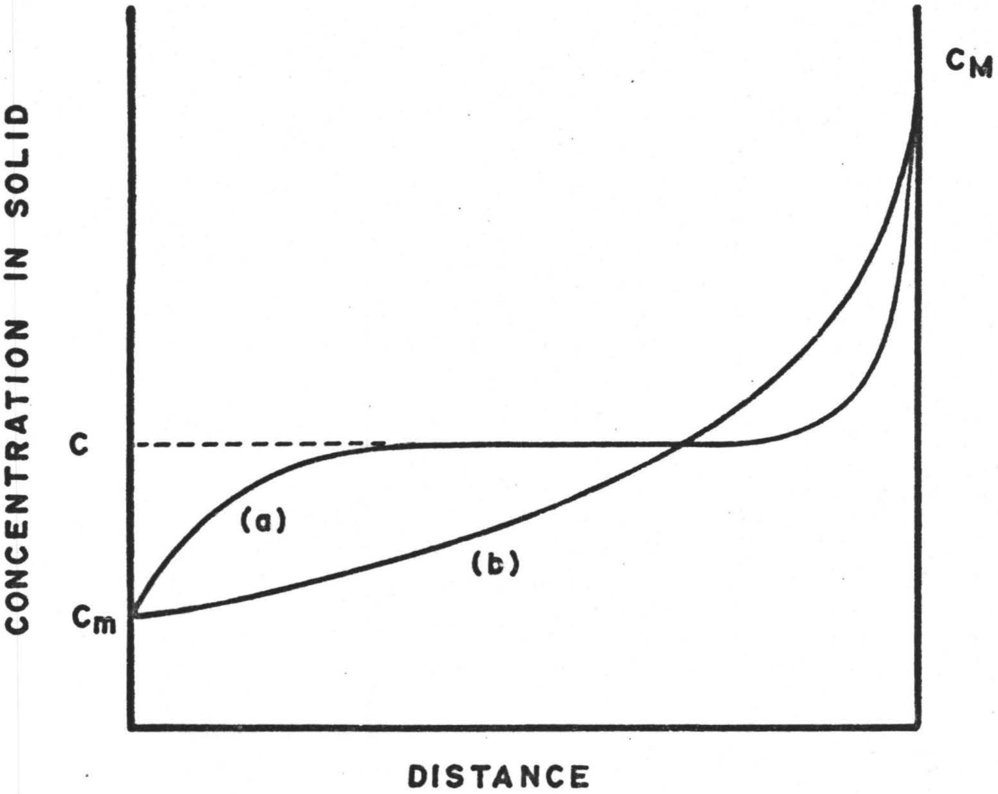

FIGURE 7.1.5 Solute Distributions in the Solid Phase.
a) Relatively High Cooling Rate in which Case the Solute Builds up at the Solid-Liquid Interface during Solidification.
b) Relatively Low Cooling Rate in which Case the Solute Concentration in the Liquid Phase Is Uniform during Solidification.
The Degree of Segregation Is Greater in Case b) than in Case a). However the Segregation ratios, $I_S = C_M/C_m$, Are Similar in Both Cases.

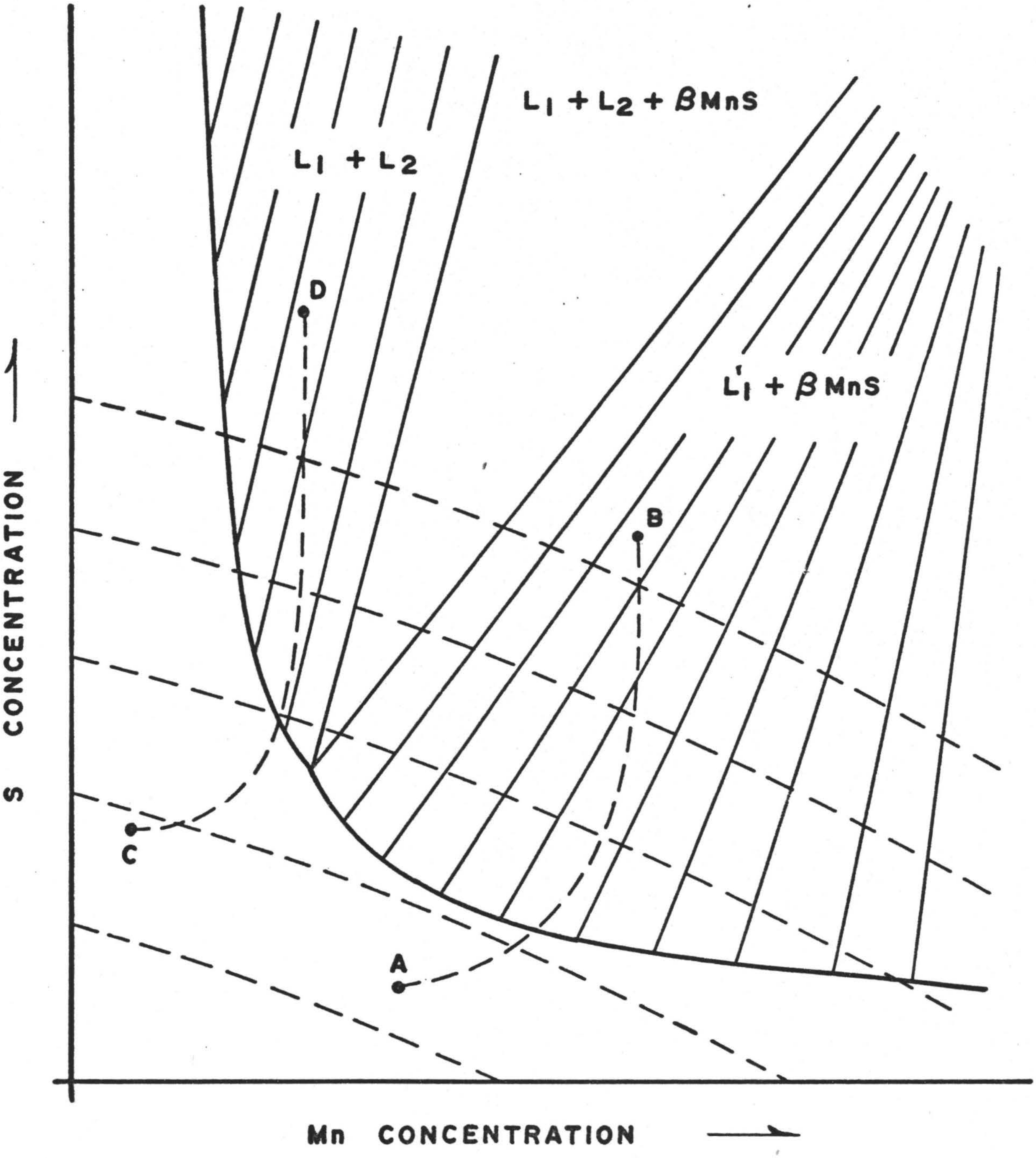

FIGURE 7.2.1. Segregation Trajectories of Two Alloys of Average Composition, Given by Points A and C, along Metastable Extensions of the Iron Liquidus Surface (Broken Lines). The Metastable Extensions of the Liquid FeS (L_2), Liquid Iron (L_1' and L_1) and Solid MnS (βMnS) Equilibria Taken from Figure 2.2.4-d Are also Shown.

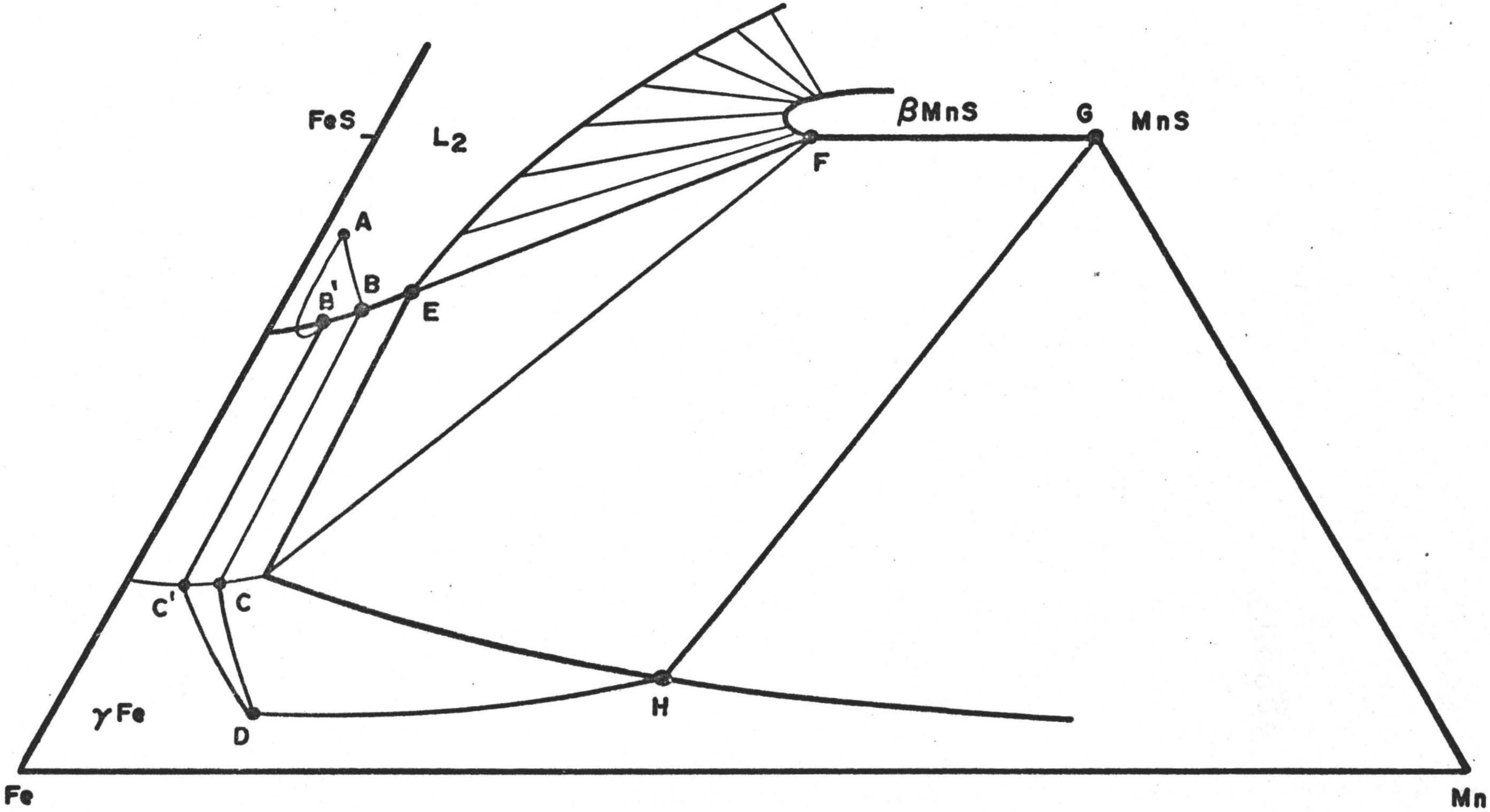

FIGURE 7.2.2 Schematic Version of the Fe-Mn-S Isotherm at 1300°C Presented in Figure 2.2.5, Showing Several Diffusion Paths Relating to the Transformation of FeS Inclusions into MnS Inclusions.